FUNDAMENTALS AND NEW APPLICATIONS OF ELECTROCHEMICAL PROMOTION IN CATALYSIS

A DISSERTATION
SUBMITTED TO THE UNIVERSITY OF CAMBRIDGE
FOR THE DEGREE OF
DOCTOR OF PHILOSOPHY

Federico José Williams
King's College, Cambridge

Department of Chemistry
University of Cambridge
15 October, 2000

Declaration

The work described in this thesis is in its entirety the original work of the author except where specific reference is made to other sources. Moreover, this dissertation includes no work done in collaboration, except where explicitly stated, and has not been submitted in whole or in part for any other qualification at this or any other university. The contents of this thesis contain no more than sixty thousand words.

Federico José Williams
Cambridge, 15 October 2000

Acknowledgements

I would like to thank Professor Richard Lambert for his enthusiastic supervision, wise advice, unconditional support over the past three years, and much more besides. I am also grateful to Mintcho Tikhov and Alejandra Palermo for their expert assistance and many helpful discussions. I would also like to thank Celso Aldao for useful and entertaining discussions. Special thanks are extended to Samuel Tracey, Sebastian Günther, Luca Gregoratti and Maya Kiskinova for their invaluable assistance at Elettra, the synchrotron radiation source in Trieste, Italy. I am also indebted to Norman MacLeod for his skillful assistance during surface area measurements and for useful discussions.

I acknowledge financial support from Fundación YPF in the form of a 'José A. Estenssoro' scholarship. I also acknowledge financial support from Fundación Antorchas and British Council Argentina. I would like to thank the Board of Graduate Studies of the University of Cambridge for the 'Lundgren' research award and Cambridge Overseas Trust for financial support. I am finally very grateful to King's College for the award of an scholarship, a travel grant and a 'Ferris Fund' award.

Summary

Electrochemical promotion (EP) is a new way of controlling catalytic performance. It is implemented by depositing porous thin film metal catalysts on solid electrolyte supports where they act as both a catalyst and a working electrode of an electrochemical cell. The technique entails electrochemical pumping of ions from the solid electrolyte to the surface of the catalytically active metal film with which it is in contact. In short, controlling the potential difference of the electrochemical cell controls the coverage of promoters on the catalyst while a catalytic reaction is taken place. Thus, it provides a unique method for studying promotion in heterogeneous catalysis.

My research has focused on elucidating the phenomena that underlie the EP effect. The resulting advances in fundamental understanding have been used to exploit EP as a tool to study alkali promotion in new applications in heterogeneous catalysis and to diversify the catalytic chemistry that can be addressed by EP. Thus, we have used conventional and spatially resolved *in situ* photoelectron spectroscopic data to demonstrate that EP of thin film metal catalysts deposited on solid electrolyte supports is the result of the spillover phenomena at the three phase boundary between the electrolyte, the catalyst and the gas phase. Ions from the electrolyte are discharged at the catalyst/electrolyte interface and migrate to cover the catalyst surface whose properties are thereby strongly altered. This is the first time that such advanced spectroscopic techniques have been brought to bear on this fascinating and complex problem. Reactor measurements along with post-reaction photoelectron spectroscopies were used in order to: (i) establish the mechanism of reaction, (ii) determine the mode of promoter action and (iii) identify the chemical state of the promoter phase, in the Na-promoted catalytic control of toxic emissions. Very large increases both in activity and in selectivity of the catalysts were achieved and point the way towards further developments and possible

applications. Finally, the use of EP as a mechanistic probe in surface catalysed polymerisation reactions has been demonstrated for the first time, broadening the range of utility of the extraordinary phenomenon of EP.

List of Publications

The following is a list containing the scientific publications that form the basis of this thesis and arise from the work of the author.

[i] F. J. Williams, C. M. Aldao, A. Palermo and R. M. Lambert, A Monte Carlo simulation of the CO+NO reaction on Na-promoted platinum, Surface Science **412/413**, 174–183 (1998).

[ii] F. J. Williams, A. Palermo, M. S. Tikhov and R. M. Lambert, First demonstration of *in situ* electrochemical control of a base metal catalyst: Spectroscopic and kinetic study of the CO+NO reaction over Na-promoted Cu, Journal of Physical Chemistry B **103**, 9960–9966 (1999).

[iii] F. J. Williams, A. Palermo, M. S. Tikhov and R. M. Lambert, The origin of Electrochemical Promotion in heterogeneous catalysis: Photoelectron spectroscopy of solid state electrochemical cells, Journal of Physical Chemistry B **104**, 615–621 (2000).

[iv] R. M. Lambert, F. J. Williams, A. Palermo and M. S. Tikhov, Modelling alkali promotion in heterogeneous catalysis: *in situ* electrochemical control of catalytic reactions, Topics in Catalysis **13**, 91–98 (2000).

[v] R. M. Lambert, A. Palermo, F. J. Williams and M. S. Tikhov, Electrochemical Promotion of catalytic reactions using alkali ion conductors, Solid State Ionics, **136**, 677–685 (2000).

[vi] F. J. Williams and R. M. Lambert, A study of sodium promotion in Fischer-Tropsch synthesis: electrochemical control of a ruthenium model catalyst, Catalysis Letters, **70**, 9–14 (2000).

[vii] F. J. Williams, A. Palermo, M. S. Tikhov and R. M. Lambert, Electrochemical promotion by sodium of the rhodium-catalysed NO+CO reaction, Journal of Physical Chemistry B, **104**, 11883–11890 (2000).

[viii] F. J. Williams, A. Palermo, M. S. Tikhov and R. M. Lambert, Electrochemical promotion by sodium of the rhodium-catalysed reduction of NO by propene: kinetics and spectroscopy, Journal of Physical Chemistry B, **105**, 1381–1388 (2001).

[ix] F. J. Williams, M. S. Tikhov, A. Palermo, N. MacLeod and R. M. Lambert, Electrochemical promotion of rhodium-catalysed NO reduction by CO and by propene in the presence of oxygen, Journal of Physical Chemistry B, **105**, 2800–2808 (2001).

[x] F. J. Williams, A. Palermo, M. S. Tikhov and R. M. Lambert, Mechanism of alkali promotion in heterogeneous catalysis under realistic conditions: application of electron spectroscopy and electrochemical promotion to the reduction of NO by CO and by propene over rhodium, Surface Science, in press.

[xi] F. J. Williams and R. M. Lambert, A Monte Carlo study of sodium promotion in the reduction of NO by CO over Rh(111), Chemical Physics Letters, to be submitted.

Contents

CHAPTER 1

Setting the scene

The research undertaken in this work deals with the phenomenon of *electrochemical promotion* and its scope is to describe the fundamentals of the effect and to explore its uses in new applications. The main objective of this chapter is to introduce the different concepts that provide the basis of the research presented in this dissertation. Therefore this chapter will describe the motivation and the relevant background.

We will demonstrate that electrochemical promotion can be used as an extraordinary tool to study the effects of alkali promoters in catalysis. We shall therefore introduce the subject of *alkali promotion in heterogeneous catalysis*. Furthermore, we will use EP to study the conversion of noxious molecules emitted from automobile gas exhausts into innocuous species. There is, therefore, a section discussing *automotive emission control*.

The phenomenon of electrochemical promotion requires the use of ion conducting solid materials. It follows from this that an introduction to *solid electrolytes* and their applications in solid state electrochemistry is necessary. Of course, the subject of electrochemical promotion deserves both description of the main research performed in the field and discussion of its relevance. This, as well as the scope of this dissertation will be presented at the end of the chapter.

1.1 Alkali promotion in heterogeneous catalysis

A catalyst can be defined as a substance which increases the rate of a chemical reaction without itself being consumed [1]. Heterogeneous catalysts are of vital technological importance, being responsible for the manufacture of virtually the entire output of the

modern chemical industry. They also play an increasingly important role in protecting the environment [2], where for example they transform toxic substances into harmless molecules. Catalysts for heterogeneous reactions consist mainly of small metal particles dispersed on high surface area supports, for example the industrial catalyst used to convert ethylene to ethylene oxide consists of Ag particles dispersed on Al_2O_3. However, the structure and composition of practical supported metal catalysts are relatively complex and they are usually optimised by empirical means to improve their catalytic properties, e. g. activity and selectivity.

The catalytic activity of a catalyst is a measure of the amount of reactants that have been converted into products and is usually expressed by the rate of the desired catalytic reaction, e. g. the number of product molecules per active site per second, r. The catalytic selectivity is a characteristic related to the fact that in most cases, the catalytic reaction converts the reactant into many products where only one of them is the desired one. Consequently, the selectivity of a catalyst is defined as the fraction of reactant molecules converted to the desired product, e. g. i, and is expressed by the ratio $r_i / \sum r_j$.

Desirable properties in catalysts are a very high catalytic activity and selectivity and long-term stability. In order to achieve these requisites, catalysts are usually modified by introducing additives. When this results in an improvement of the activity and/or selectivity of the catalyst, the additives are called promoters. Very often metal catalysts are promoted with alkali metal additives. In fact, there are more than forty catalytic reactions of industrial importance that are promoted by alkalis [3]. Well known examples include the Haber–Bosch synthesis of ammonia from N_2 and H_2 which displays an increased activity on alkali promotion, the Fischer–Tropsch synthesis of hydrocarbons from CO and H_2 that exhibits improved selectivity to longer chain hydrocarbons and the ethylene epoxidation catalyst that becomes more selective.

There has been therefore a great interest in the study of heterogeneous catalysts and in particular in the alkali promotion phenomena. Two main approaches can be identified in the way heterogeneous catalysts are studied. The first is related to the needs of the chemical industry and its prime concern is the development, typically through trial and error procedures, of practical catalysts that operate efficiently under realistic conditions. The second aspect of catalytic studies has been the attempt to understand at an atomic level the fundamental nature of the catalytic process. This approach involves using surface science techniques that allow the study of the gas/solid interface on well defined model systems, typically single crystals.

As a consequence, surface science studies have been extensively dedicated to coadsorption experiments on single crystal metal surfaces modified by alkali atoms. These model experiments play a significant role in understanding the contribution of various factors to the alkali-promotion phenomena. The purpose of this section is to summarise what has been achieved by surface science model studies [4, 5]. Therefore, we will briefly discuss the general aspects of (i) the adsorption of alkali metals on well-defined transition metal surfaces and (ii) the interaction of these adsorbed alkali metals with subsequently adsorbed molecular species. Finally, we will introduce the model put forward to explain the experimental observations.

1.1.1 Alkali metal adsorption

The single valence electron of alkali metals is weakly bound; hence, the alkali metals are very electropositive elements (the alkali metals have ionisation potentials in the range 3.9–5.4 eV). When adsorbed on a transition metal surface a partial electron transfer from the alkali metal to the transition metal occurs. Consequently, the alkali species itself becomes partially ionic and forms a dipole layer. This causes a work function decrease, where the work function ϕ is the amount of energy required to take one electron from just inside the solid to a point just outside across its dipole layer [6]. The lower the ionisation potential of the alkali metal, the larger the dipole moment of the adsorbed alkali metal and thus the induced work function change [7].

The general dependence of the alkali-induced decrease in work function on alkali coverage is the following. First, there is a strong linear decrease in work function with increasing alkali coverage, followed by a rather broad minimum, after which the work function increases until it approaches the level of the bulk alkali in question at completion of the first overlayer. This general trend is independent of temperature up to adsorption temperatures below the onset of desorption of the first alkali layer (300–350 K depending on the type of alkali metal) and can be understood as follows. The extent of electron transfer is dependent on the alkali coverage: as the coverage increases the electrostatic repulsion among the positively charged atoms increases causing the charge transfer to lessen. This depolarisation means that the charge transfer per adsorbed alkali metal atom is not constant but decreases with coverage, hence leading to the observed levelling of the work function versus coverage [8].

Since the work function varies with the potential difference across the dipole layer then its value depends on the particular surface point that is being examined [9]. Microscopically, the work function near the adsorbed alkali metal atom is *locally* decreased leaving the potential of the rest of the surface unchanged [4]. This means that the lateral

range of the alkali induced charge redistribution within the surface is rather short (up to next nearest neighbours) [5]. This point has obvious consequences on the range of alkali promotion and will be discussed below.

The maximum amount of alkali metal that can be adsorbed on metal surfaces (saturation coverage) depends strongly on the temperature. For example, multilayers of sodium on Ni(111) start desorbing at 370 K. The desorption traces of Na taken from different initial coverages also show that the desorption temperatures ranges from 400 K at about monolayer coverage to $\geq$ 900 K at low sodium coverage (0.02) [7].

Because of the large dipole moments of the adsorbed alkali metals, there is a repulsive interaction between these species. Thus, ordered two-dimensional structures have been observed [10]. This is a function of alkali coverage and temperature: the higher the coverage the higher can be the temperature where order prevails. The surface mobility of adsorbed alkali metals is very high at $T > 100$ K. So that to achieve ordering of the adlayer at low coverages, the temperature has to be low, otherwise only a disordered phase is present.

1.1.2 Coadsorption of alkali metal and gas molecules

What follows summarises experimental results found in the literature on the effect of alkali metal atoms on coadsorbed molecules. We will concentrate primarily on systems in which CO is the coadsorbate since it has received the most attention. Moreover, we will also discuss the effect of alkalis on coadsorbed NO due to the relevance this system has in the work presented in this dissertation.

Coadsorption of CO with alkalis has been widely studied using a large number of experimental techniques by a large number of authors [4, 5]. The major findings common to a great number of single crystal surfaces are:

[i] The presence of an alkali on a metal surface raises the desorption temperature of CO. The desorption temperature increase is generally interpreted as evidence for a substantial strengthening of the substrate−CO bond in the presence of an alkali metal. The saturation coverage of CO is increased by the presence of alkalis with respect to the clean surface.

[ii] The addition of CO to an alkali-precovered surface results in an increase in the work function, even for those systems in which CO causes a work function decrease on the clean surface (e. g. CO/Pt and CO/Cu). The CO-induced work function increase is ascribed to backdonation of metal electrons into the CO $2\pi^*$ molecular orbital. The CO-induced work function change for the alkali promoted surface is

much larger than for the clean surface. This indicates a larger backdonation due to alkali promotion.

[iii] Infrared spectroscopy shows that alkali coadsorption decreases the vibrational frequency of the C−O bond, thus indicating the weakening of the intramolecular bond [11]. This observation can be rationalised in terms of an alkali-increased occupancy of the CO $2\pi^*$ antibonding molecular orbital, which results in the intramolecular bond weakening and thus lowers the activation energy for dissociation. In some cases the alkali-induced weakening of the C−O bond promotes the dissociation of the CO molecule, these include: Na, K, Cs/Ni(100) and K, Na/Al(100) [5]. No CO dissociation is detected on alkali-promoted Pt(111), Rh(111), Ru(0001), Pd(100), Ni(111), Cu(100) and Cu(110), although all experimental data indicate the same induced weakening of the C−O bond [5, 12].

[iv] X-ray photoemission spectroscopy measurements have shown that when CO is coadsorbed with an alkali metal on a transition metal surface, a decrease by 1eV in the binding energy of both C 1s and O 1s core levels is generally observed, compared with CO adsorbed on the clean surface. The decrease in binding energy of the CO core levels in the promoted system is consistent with a model in which the alkali-CO interaction involves charge transfer from the alkali to coadsorbed CO, either directly or through the substrate.

The coadsorption of NO with alkali has broadly similar results to those encountered with CO. This is, on alkali promotion: (i) the saturation coverage of NO increases, (ii) the desorption temperature of NO increases hence the strength of the metal−NO bond increases and (iii) the N−O intramolecular bond is weakened. These observations are usually explained as an alkali-enhanced electron donation to the $2\pi^*$ orbital of the NO molecule (see discussion below). The increased occupancy of the $2\pi^*$ orbital can cause dissociation of the NO molecule. Alkali-induced NO dissociation was observed when NO is coadsorbed on the following alkali-promoted surfaces: Na/Ag(110) [13], Na/Ag(111) [14], Rb/Ag(111) [15], K/Pt(111) [16, 17], Na/Pt(111) [18], Na/Rh(100) [19], K/Rh(100) [20, 21], K/Rh(111) [22–25] and Cs/Ru(10$\bar{1}$0) [26].

The above measurements indicate that the alkali−CO interaction is *short-range* in nature. In most studies in which the alkali and CO coverages are varied conveniently, it can be seen that 2 different CO states are generally available, one in which the CO properties are very similar, if not identical, to those of the clean (unpromoted) surface, and one in which the CO is significantly perturbed by the presence of the alkali. This is, if the alkali coverage is low enough, two states are clearly distinguished, a promoted

state and a second CO state virtually identical to CO adsorbed on the clean surface. Most theoretical calculations of alkali interactions have predicted a very short-range interaction (see below), this is certainly consistent with the results summarised above. However, it has been also proposed [27] that the alkali−CO interaction involves a *long-range* component. Therefore, it was suggested [11] that the interaction of an alkali with a coadsorbed molecule such as CO consists of a short-range and a long-range interaction. The short-range interaction is the primary promotion interaction whereas the long-range interaction is much weaker. This view was experimentally tested. Using photoemission of adsorbed Xe atoms, Wandelt and coworkers [28] measured the surface potential around a potassium atom on Rh(111). They observed a decrease in surface potential around the potassium that recover to almost its unpromoted value within about 4–5 Å. Thus, showing that the work function depends very strongly on the lateral distance from the adatom. The same trends were observed for potassium on ruthenium [29]. Therefore, these experimental results support a short-range interaction.

1.1.3 Models of promotion

The experimental observations described above can be explained in terms of the alkali-enhanced backdonation in the $2\pi^*$ molecular orbital of CO. Alkali modifiers increase the backdonation due to their ability to transfer electrons to the metal. This causes an increase in the strength of the metal−CO bond and weakens the C−O bond reducing the activation energy for dissociation. The increase in occupancy of the $2\pi^*$ molecular orbital of CO due to coadsorbed potassium has been *directly* observed by Lee *et al.* [30] by use of spectroscopic methods, thus supporting strongly this view. Furthermore, electron-withdrawing additives, such as sulphur, act in an opposite manner, and strengthen the CO bond, thus becoming poisons for catalytic reactions involving the dissociation of adsorbed CO [31].

Lang *et al.* [32] showed using theoretical calculations that the negative electrostatic potential caused by the charge transfer from the alkali atom to the substrate gives rise to a down-shift of the molecular CO levels relative to the Fermi level including the $2\pi^*$ antibonding level, which then increases its occupancy. This model predicts a short-range interaction, expecting sites up to nearest-neighbours to an alkali atom to be much more affected than sites further away. Many other theoretical models have been put forward to explain the promotion phenomena. A detail discussion is beyond the scope of this dissertation. A more detailed discussion could be found in the review by Bonzel [4]. However, it is worth mentioning that the different models suggest various different types of interactions between the alkali atom and the coadsorbed molecule, e. g.

indirect (through metal) charge transfer or direct electron transfer through a covalent bond. Nevertheless, there is one common feature in all of them: the increased occupation of the CO $2\pi^*$ molecular orbital. This increase is responsible for the experimental observations as discussed above.

1.2 Automotive emission control

Air pollution is mainly due to nitrogen oxides, sulphur oxides, carbon monoxide, hydrocarbons and carbon dioxide. Although these molecules are emitted in natural processes, the large excess produced nowadays disturbs the natural cycles resulting in acid rain, photochemical smog and global warming.

Carbon dioxide, for instance, is an essential component in photosynthesis, but the large amount produced by the combustion of fossil fuel is thought to be responsible for the enlarged greenhouse effect, which results in global warming. Other molecules that contribute to this greenhouse effect by accumulation in the air are N_2O and chlorinated fluorocarbons. Another product of the combustion of fossil fuels is CO, which is formed at incomplete combustion conditions. Carbon monoxide has serious health consequences since it inhibits O_2 uptake in blood by attaching to haemoglobin with higher affinity. Besides CO, several hydrocarbons are products of incomplete combustion. Hydrocarbons are toxic and cause photochemical smog. Briefly, photochemical smog refers to the formation of oxidation products by interaction of hydrocarbons and nitrogen oxides with sunlight, which cause respiratory problems, eye irritation and plant damage. Sulphur oxides originate from the combustion of sulphur containing fuels. It is toxic and causes acid rain by reaction with water (H_2SO_4). Nitrogen oxides are predominantly emitted as NO, NO_2 and N_2O and have a direct noxious effect on health. They also participate in photochemical pollution as well as in acid rain formation (HNO_3). They are formed in the combustion of nitrogen containing fuels and in the reaction between N_2 and O_2 present in air at high temperatures.

Most of these pollutants originate from stationary sources, like power plants and chemical plants and from mobile source like automobiles, aircrafts and ships. Automobile emissions is one of the major sources of carbon monoxide, hydrocarbons and nitrogen oxides emissions [2]. Therefore, they are legislated in order to limit the emission of carbon monoxide, hydrocarbons and nitrogen oxides to minimise their effect on environment and human health.

1.2.1 Three-way catalysts

The most commonly applied solution for the reduction of C_xH_y, CO and NO is the catalytic convertor, which is placed in the exhaust pipe of automobiles. The hydrocarbons in the exhaust gas are a mixture of olefins, paraffins and aromatics[1]. The method of catalytic removal of all three pollutants is to oxidise the hydrocarbon and CO and to reduce the NO,

$$2\,CO + O_2 \rightarrow 2\,CO_2 \tag{1.1}$$

$$C_xH_y + (x + y/4)\,O_2 \rightarrow x\,CO_2 + (y/2)\,H_2O \tag{1.2}$$

$$2\,NO + 2\,CO \rightarrow N_2 + 2\,CO_2 \tag{1.3}$$

$$(2x + y/2)\,NO + C_xH_y \rightarrow (x + y/4)\,N_2 + x\,CO_2 + (y/2)\,H_2O \tag{1.4}$$

Noble metal catalysts are very active at these reactions. Pt based catalysts are very active at oxidation of CO and hydrocarbons, but less efficient at NO reduction. Pd catalysts are also active in oxidation reactions but are more susceptible to lead and sulphur and sinter more rapidly in reducing atmospheres. Rh catalysts are very efficient in the catalytic reduction of NO [33].

The first generation of catalytic convertors consisted of platinum and palladium supported on alumina and transformed CO and hydrocarbons into CO_2 and H_2O (no attempt was made to remove NO). After more stringent regulations concerning NO emission, a dual-bed convertor was developed, in which separate reduction and oxidation catalysts were used. The first catalyst was active for the reduction of NO and the second one for oxidising both CO and hydrocarbons. This system required reducing exhaust gas composition (rich fuel conditions) on the first catalyst and an additional air entrance on the second catalyst in order to favour the oxidation processes. However, the efficiency to eliminate NO was very limited: NO was reduced to NH_3 on the first catalyst, which was further transformed to NO on the second catalyst [34]. Since then, C_xH_y, CO and NO are removed simultaneously over one catalytic system, the noble metal based three-way catalyst (TWC). The name 'three-way catalyst' is based on the fact that the catalyst promotes the removal of all three pollutants [35].

A typical TWC consists mainly in a combination of noble metals (Pt, Pd and Rh) dispersed on an alumina support stabilised by barium and lanthanum oxides. The catalyst also contains ceria, which is added to store oxygen under oxidising conditions (lean conditions). The simultaneous conversion of all three pollutants only occurs in a

[1] However auto exhaust catalysts are usually tested in a microreactor using propene as a substitute of the real mixture of hydrocarbons.

small range of gas exhaust composition around stoichiometry, i. e. the concentrations of oxidants and reductants present on the gas exhaust are equal. Under rich conditions, high NO reduction activity is obtained but the C_xH_y and CO conversion decreases strongly due to insufficient amount of O_2 to achieve full oxidation into CO_2 and H_2O. On the other hand, under lean conditions, the C_xH_y and CO activity is high, whereas the NO reduction activity is low. So, high NO, CO and C_xH_y conversions are only obtained in the operating region around stoichiometry. This is achieved as follows. The exhaust is monitored by an oxygen sensor which indicates if excess oxygen is present. Feedback from this to the fuel injection system controls the air/fuel ratio fed to the engine, which maintains the exhaust at conditions for which the catalyst is effective.

Maximum conversions of 95% and average conversions of about 80% have been reported for NO reduction and CO and C_xH_y oxidation [36]. However, these high conversion levels are only reached above 573 K. Therefore, the pollutants are not converted while the catalyst reaches this temperature. An additional disadvantage of TWC is the production of N_2O. Thus it is important that the catalyst is already active at low temperature with a high selectivity towards N_2 formation rather than N_2O.

1.2.2 Lean-burn catalysts

The TWC has been successful in controlling exhaust emissions from conventional petrol engines which operate close to stoichiometric conditions as discussed above. However, the exhaust from lean burn petrol engines and diesel engines contains excess oxygen. Under these net-oxidising conditions the three way catalysts are no longer effective for NO control. It is therefore of great importance to develop catalyst technologies that will allow NO reduction in lean environments. The search for catalysts for this reaction has not yet been successful and consequently is a subject of considerable research.

Several technologies have been developed to reduce NO under lean conditions. They include: NO decomposition, selective catalytic reduction and NO storage and reduction [34]. However, one of the most promising methods employed is the selective catalytic reduction of nitric oxide by hydrocarbons under excess oxygen conditions [37],

$$\mathrm{NO} + \mathrm{hydrocarbon} + \mathrm{O_2} \quad \rightarrow \quad \mathrm{N_2} + \mathrm{CO_2} + \mathrm{H_2O}. \tag{1.5}$$

Various catalytic systems have been examined for this reaction. They include: metal-exchanged zeolites, supported transition metal oxides and supported noble metals. Platinum group metal catalysts supported on metal oxides appear to be favourable for the reduction of NO. This is mainly due to their excellent hydrothermal stability and their

resistance to poisoning by SO_2. However, these catalysts have some shortcomings, such as the fact that they are only active in a narrow temperature range. This is due to the fact that platinum group metals are good combustion catalysts, resulting in a narrow temperature range between the onset of reaction and complete oxidation of the reductant. After the reductant is consumed conversion of NO to NO_2 occurs and the extent of NO conversion falls with increasing temperature. Another problem with these catalysts is that a large portion of NO is reduced to N_2O, a pollutant itself, rather than harmless N_2. The fraction of total NO converted to N_2O reported in the literature depends on the catalyst, conditions and reductant used, but lies in the range of 40 to 75% for Pt catalysts and 10 to 60% for Rh catalysts [38].

1.3 Solid electrolytes

High ionic conductivity in solids is a widely recognised phenomenon. Most ionic solids show significant levels of ionic conductivity only at very high temperatures, as the melting point is approached. However, there are materials that exhibit high ionic conductivity at temperatures well below melting and often as low as room temperature. Such compounds are known as solid electrolytes although they are also called superionic conductors and fast ion conductors to stress the fact that they are solids with liquid-like ionic conductivities.

To be useful as a solid electrolyte an ionic conductor should have high ionic conductivity with zero electronic conduction, it should also be chemically inert to the gas environment and thermally stable. In the particular case of alkali ion conductors, β" alumina fulfills all three requirements, being therefore, the preferred material for applications dealing with alkali conductors [39]. The next subsection deals with the sodium ion conductor solid electrolyte used in this work and includes discussion of its structure and properties. The wide range of solid electrolyte applications is examined in the final subsection.

1.3.1 Sodium β" alumina

Sodium β" alumina is a non-stoichiometric ceramic oxide containing Al_2O_3, Na_2O and small amounts of MgO and/or Li_2O. It has a layered structure in which densely packed blocks alternate with open conduction planes containing the mobile Na^+ ions. The idealised structure of the unit cell of β" alumina is shown in figure 1.1a. The oxide packing arrangement comprises close packed layers in a cubic close packed, ABC, stacking sequence, which continues throughout the structure including the conduction planes. The

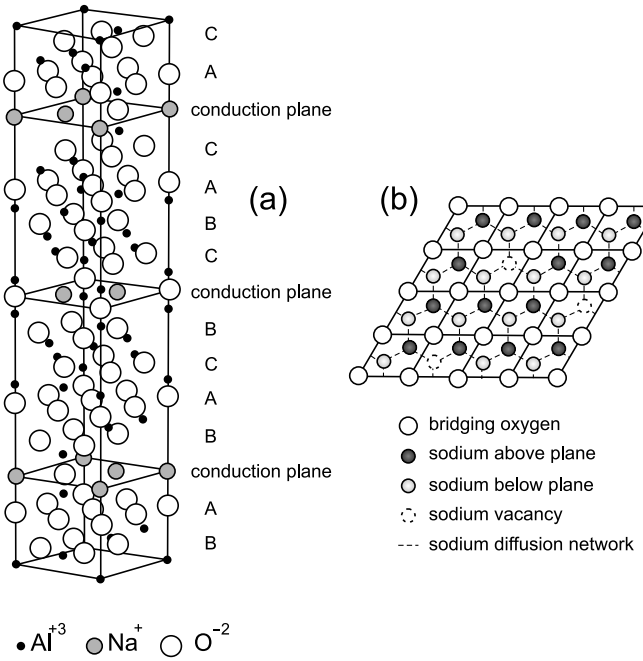

Figure 1.1: (a) Sodium β" alumina crystalline structure showing alternating conduction planes and closed packed blocks, redrawn from reference [39]. (b) Section through the conduction plane.

close packed blocks are four oxide layers thick and contain Al^{+3} ions (and Li^{+}, Mg^{+2} ions) distributed over tetrahedral and octahedral sites. These sites are too small to accommodate the Na^{+} ions which, instead, reside in the conduction planes. Adjacent close packed oxide blocks are held one layer apart by Al−O−Al units. Alternate sodium ion sites lie above and below the plane through the centre of the bridging oxygen ions as made clear in figure 1.1b.

The high conductivity arises because the sodium ions are able to move around within the conduction planes but cannot penetrate the dense oxide blocks. Therefore, the β" alumina is a two-dimensional Na^{+} ion conductor. This means that the conductivity of a given crystal is anisotropic. However polycrystalline β" alumina exhibits isotropic conductivity due to the random arrangement of the anisotropically conducting grains. The conduction mechanism is regarded as a vacancy process. This mechanism involves the motion of a sodium vacancy through the conduction plane by successive sodium ion hops in the direction opposite to vacancy motion [40]. The idealised structure drawn in figure 1.1a has two sodium ions per unit cell conducting plane thus there are no sodium vacancies and there is no ionic conductivity [39]. In reality, the β" structure is always sodium ion deficient and the structure is thus stabilised by the presence of ions such as Li^{+} and/or Mg^{+2}. These dopant ions occupy vacant aluminium sites generating

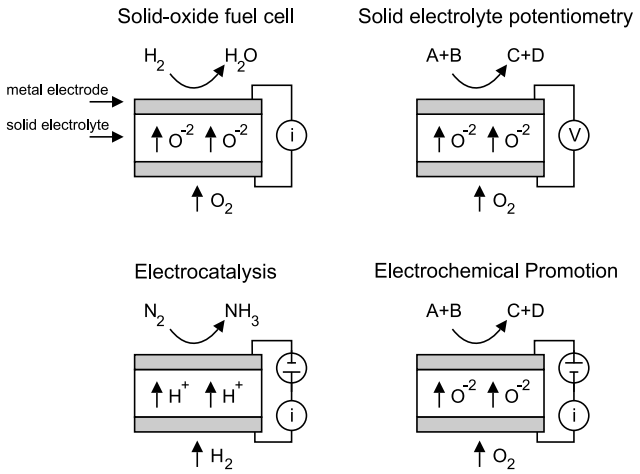

Figure 1.2: Schematic diagram showing different applications of solid state electrochemical cells.

Na^+ vacancies in the conduction plane and therefore conductivity arises as shown in figure 1.1b.

Sodium β" alumina shows high ionic conductivity at temperatures as low as room temperature and it is unstable at temperatures in excess of 1823 K [39]. Furthermore, under the range of temperatures and gas mixtures explored in this work (373–773 K), the solid electrolyte is chemically inert and thermally stable. However, it should be noted that there is a restriction in the maximum voltage that can be applied across the solid electrolyte. At a given temperature there is a voltage threshold above which the electrolyte suffers gross physical damage [41]. This phenomenon is known as *voltage breakdown* and is due to the dielectric breakdown of a thin sodium ion depletion layer at the positive electrode face.

1.3.2 Applications

From the initial discovery of high ionic conductivity has grown a surprising diversity of applications using solid electrolytes. Solid electrolytes are used in the construction of solid state electrochemical cells, which consist of two porous metal electrodes in contact with a solid electrolyte. Although solid electrolyte cells are most widely used in solid-state batteries [42] and in chemical sensors [43], they can also play an important role in the field of heterogeneous catalysis [44–46].

Figure 1.2 shows an schematic diagram that depicts some applications of solid state electrochemical cells, namely, fuel cells, solid electrolyte potentiometry, electrocatalysis and electrochemical promotion. A brief description of these systems will be given in the

text that follows.

Fuel cells are electrochemical cells that convert chemical energy directly into electrical energy. Thus, they are galvanic cells since they produce electricity as a result of an spontaneous reaction. One of the electrodes of the cell is exposed to the fuel, e. g. H_2 [47], CO [42], CH_4 [48], or hydrocarbons [49], whereas the other electrode is exposed to oxygen or air. Since the electrodes are exposed to different gas environments the cell also serves as a chemical separator. The solid electrolyte used in solid-oxide fuel cells is an oxygen conductor. The O^{-2} conductor used in most of the applications is yttria-stabilised zirconia (YSZ), i. e. a solid electrolyte made of Y_2O_3 and ZrO_2. The electrolyte shows good ionic conductivity in the range 573–1673 K, thus solid-oxide fuel cells operate within this temperature range. The principle of operation of the cell involves reduction of molecular O_2 at the cathode (the electrode at which the reduction occurs), diffusion of the O^{-2} through the electrolyte, and oxidation of the fuel at the anode (the electrode where the oxidation takes place).

Whereas fuel cells are used to generate electrical power while generating inexpensive chemicals (H_2O and/or CO_2), they can also be used for simultaneous generation of useful chemicals and electricity [50]. This was first shown by Vayenas and Farr [51] when they showed that a solid-oxide fuel cell with Pt based electrodes can quantitatively convert NH_3 to NO with simultaneous generation of electrical power. Subsequent work has shown that with the appropriate catalytic anodes several other exothermic reactions of industrial importance can be carried out successfully using solid-oxide fuel cells [52]. These include the oxidations of H_2S to SO_2 [53] and of methanol to formaldehyde [54].

In its pioneering work Wagner proposed the use of solid electrolytes to measure *in situ* the thermodynamic activity of oxygen on metal catalysts [55]. Since then it has been implemented in many catalytic reactions and the technique is now known as Solid Electrolyte Potentiometry [44]. The steady-state oxygen activity in a metal catalyst can be obtained from the measured potential difference (the zero-current cell potential, E, also called the electromotive force or emf of the cell) of the following cell,

reference gas, reference electrode | YSZ | metal catalyst, reacting mixture.

Id est the cell consist of two porous metal electrodes interfaced with an oxygen-ion-conducting solid electrolyte, one of the electrodes is exposed to a reacting mixture and therefore serves as a catalyst for the reaction under study. The other electrode is exposed to a reference gas (e. g. ambient air). The thermodynamic activity of adsorbed oxygen on the metal catalyst can be related with the measured potential difference of the cell through the Nernst equation [44, 45], and therefore it can be determined continuously during the surface reaction. The same principle is applied in oxygen sensors in which

changes in the partial pressure of oxygen can be determined from the measured potential difference in a solid state electrochemical cell.

Solid electrolyte cells can also be used to carry out electrocatalytic reactions. Unlike its application as a fuel cell in this case the cell works as an electrolytic cell in which the rate of a catalytic reaction is modified in a faradaic manner by the flow of current. Figure 1.2 illustrates the case of ammonia synthesis [56] using the following arrangement:

$$H_2,\ Pd \mid SCY \mid Pd,\ N_2$$

where SCY is a solid electrolyte that exhibits high protonic conductivity. Current application from an external source at atmospheric pressure and 570 °C results in production of NH_3. The rate of NH_3 formation is equal to the rate of electrochemical hydrogen supply ($I/2F$) thus the effect is faradaic. The same idea has been previously applied in the decomposition of nitric oxide [57, 58] and in methane production [59, 60]. The common feature in these cases is that the rate of the catalytic reaction is modified in a *faradaic* way, i. e. the change in reaction rate is equal or smaller than the change in current.

Perhaps the most interesting application of solid electrolyte cells stems from the effect of electrochemical promotion, where the effect of the current on a catalytic reaction is *non-faradaic*. The phenomenon was discovered by Stoukides and Vayenas [61] when they were studying the following electrocatalytic reaction,

$$O_2,\ Ag \mid YSZ \mid Ag,\ C_2H_4,\ O_2.$$

Note that in this case (as in the case of Solid Electrolyte Potentiometry) there is a catalytic reaction taking place in one of the electrodes under open circuit conditions (when there is no current flowing). The reaction is the silver catalysed formation of ethylene oxide (desired product) and of CO_2 and H_2O (undesired products). Stoukides and Vayenas found that the increase in the rate of ethylene oxide and complete oxidation upon current application was more than two orders of magnitude greater than the rate of electrochemical supply of oxygen to the catalyst. Thus, the effect was highly non-faradaic. Moreover, they observed that the effect was reversible, i. e. interrupting the current resulted in a decrease of the reaction rates to their open circuit values. Furthermore, they also showed that the selectivity towards ethylene oxide formation rather than CO_2 production was increased when oxygen was electrochemically pumped to the catalyst. Therefore, the catalytic properties of the silver catalyst were improved during electrochemical oxygen pumping. The authors also observed the same effects of oxygen pumping during propylene oxidation on silver [62]. They proposed that the phenomenon was due to surface oxidation of the silver catalyst, although later on their interpretation changed.

Table 1.1: Electrochemical Promotion studies using alkali conductors.

Reactants	Products	Catalyst	T(°C)	$\rho^{\dagger}$	Reference
C_2H_4, O_2	C_2H_4O, CO_2, H_2O	Ag	240–260	$3^{a,b}$	[63, 64]
H_2, C_2H_2	C_2H_4, C_2H_6	Pt	100–320	0.11^{a}	[65]
H_2, C_6H_6	C_6H_{12}	Pt	130	0.13	[66]
CO, O_2	CO_2	Pt	300–450	8^{b}	[67]
C_2H_4, O_2	CO_2, H_2O	Pt	290–470	10^{b}	[68–70]
C_3H_6, O_2	CO_2, H_2O	Pt	340	2.3^{b}	[71]
NO, CO	CO_2, N_2O, N_2	Pt	350	6^{a}	[72]
NO, H_2	N_2O, N_2, H_2O	Pt	375	30^{a}	[73]
NO, CH_4	CO_2, N_2O, N_2, H_2O	Pt	400	$6^{a,b}$	[74]
NO, C_2H_4	CO_2, N_2O, N_2, H_2O	Pt	400	∞	[75]
NO, C_3H_6	CO_2, N_2O, N_2, H_2O	Pt	375	$7^{a,b}$	[76]
NO, C_3H_6, O_2	CO_2, N_2O, N_2, H_2O	Pt	400	$1.2^{a,b}$	[74]
NO, CO	CO_2, N_2O, N_2	Rh	307	3^{a}	this work
NO, CO, O_2	CO_2, N_2O, N_2	Rh	322	1.4^{a}	this work
NO, C_3H_6	CO_2, N_2O, N_2, H_2O	Rh	350	2.4^{a}	this work
NO, C_3H_6, O_2	CO_2, N_2O, N_2, H_2O	Rh	350	1.8^{a}	this work
NO, CO	CO_2, N_2O, N_2	Cu	375	66^{a}	this work
CO, H_2	hydrocarbons	Ru	200	0.28^{a}	this work

† Rate enhancement factor ρ defined as the ratio of the promoted r to the unpromoted $r_\circ$ catalytic rates, i. e. $\rho = r/r_\circ$

[a] Alkali-induced change in product selectivity.

[b] Reaction rates *versus* catalyst potential show a volcano behaviour.

1.4 Electrochemical Promotion

After the discovery of the non-faradaic effect described above, Vayenas examined his finding further and realised that it was a general phenomenon, i. e. that the catalytic activity and selectivity of metal surfaces can be modified reversibly by interfacing the metal with a solid electrolyte and by supplying or removing ionic species to or from the catalyst surface [77]. This is accomplished by applying a potential between the conductive catalyst film and a second metal film (counter electrode) also interfaced with the solid electrolyte, thus causing a controlled migration of promoting ions from the solid electrolyte onto the catalyst surface. Since the changes in catalytic reaction rates exceed the rate of ionic species transport to or from the catalyst surface, then the effect is non-faradaic and consequently it was first called non-faradaic electrochemical modification of catalytic activity (NEMCA) [77]. Later on, Pritchard named the effect electrochemical promotion (EP) [78].

The effect has been demonstrated for more than 50 catalytic reactions on Pt, Pd,

Rh, Ag, Ni, IrO_2 or RuO_2 deposited on O^{-2}, F^-, Na^+, K^+ or H^+ conducting solid electrolytes. Most of the studies have been performed using either YSZ (oxygen conductors) or Na β"alumina (sodium conductors) solid electrolytes. Table 1.1 shows all the EP studies reported in the literature carried out using alkali conductors. Furthermore, it has been shown that the phenomenon also occurs in aqueous solutions [79]. The subject has been repeatedly reviewed by Vayenas and coworkers [80–90].

In this section the main features of EP are briefly outlined and the origin of the effect is discussed in the light of surface spectroscopic investigations.

1.4.1 The electrochemical cell

The typical experimental arrangement used to perform EP experiments is illustrated in figure 1.3 for the case of alkali conductors. It consists of three metallic electrodes interfaced with a solid electrolyte. The electrode where the catalytic reaction of interest $A + B \rightarrow C + D$ is taking place is called the working electrode (W). A galvanostat-potentiostat (G-P) is used to either flow constant currents (I) between the catalyst and the counter electrode (C) or to apply a constant potential difference, V_{WR}, between the working electrode and the reference electrode (R). The potential of the working electrode measured relative to the reference electrode with a high impedance voltemeter (no current flows through that circuit) V_{WR} is also called catalyst potential.

The working electrode serves both as an electrode and as a catalyst for the heterogeneous reaction under study. In this design, the so called 'single pellet' design [91], the counter and reference electrodes are exposed to the reactive gas mixture. Therefore they must be catalytically inactive and chemically inert, in practice this is achieved by using gold films [92].

A true reference electrode must have a constant potential. In EP cells with oxide ion conductors a porous metallic electrode exposed to oxygen or air can serve as a true reference electrode. Its potential, is fixed via the equilibrium between O^{-2} in the solid electrolyte and O_2 in the gas phase at a well defined partial pressure. Also, if the reference electrode is exposed to the same gas mixture as the working electrode then it can still act as a true reference electrode only to the extent that no reaction is catalysed on its surface and that the potential setting reaction is still the one between O^{-2} in the solid electrolyte and O_2 in the gas phase. Gold electrodes satisfy these criteria to a satisfactory extent.

In EP cells with Na^+ conductors a true reference electrode should be in contact with molten sodium or a suitable Na alloy. This design is not practical and therefore was never used in EP applications. Instead, the reference electrode is exposed to the same

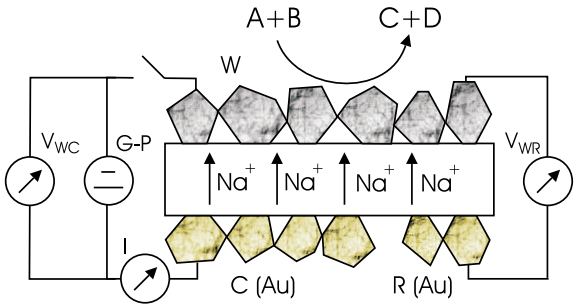

Figure 1.3: Schematic diagram showing the solid state electrochemical cells used in EP applications

gas mixture as the catalyst electrode. Changes in the gas composition are expected to lead to changes in the state and amount of sodium on the surface of the reference electrode and therefore in the reference electrode work function and potential. Thus the electrode should be termed pseudo-reference electrode. However, in the EP literature the term reference electrode is used instead. Although the potential of the reference electrode changes to some extent with gas composition, for a fixed gas composition it gives a valid reference point. This is best shown by the reversibility of the effect with V_{WR} which in turns provides strong evidence supporting the use of this configuration.

1.4.2 The EP effect

The phenomenon of EP is observed upon applying an electrical potential to the metal catalyst (thus changing V_{WR}). In the particular case of using Na β" alumina, current then flows between the working and counter electrodes corresponding, to the following cathodic reaction:

$$\mathrm{Na}^{+}(\beta\text{"alumina}) + \mathrm{e}^{-}(\mathrm{W}) \quad \rightarrow \quad \mathrm{Na}\ (\mathrm{W}). \tag{1.6}$$

This occurs until the amount of Na 'pumped' to the catalyst causes the value of V_{WR} to reach the desired value, at which point the current vanishes provided there are no losses of sodium species from the surface, either by desorption or reaction. The adsorbed Na atoms diffuse over the entire catalyst surface and induce changes in its catalytic properties. The value of the catalyst potential can be reversed so that the reverse anodic reaction occurs. Then Na species on the catalyst surface migrate into the solid electrolyte until the required new value of V_{WR} is achieved. Therefore, the promoter level on the catalyst surface can be varied reversibly, any given level being maintened by fixing the value of V_{WR}.

X-ray photoemission spectroscopy (XPS) has provided conclusive experimental evidence for the reversible spillover of sodium ions. Thus showing that electrochemically controlled pumping of sodium ions is the origin of electrochemical promotion when using alkali conducting solid electrolytes. Lambert *et al.* [76] have shown that the intensity of the Na 1s XP spectra increased when V_{WR} of the cell, Pt | Na β"alumina | Au, was decreased under ultra-high vacuum conditions. Furthermore, they also demonstrated using XPS that electropumped Na is identical in behaviour and in chemical state with Na supplied to the Pt surface by vacuum deposition from a Na evaporation source. Scanning Tunneling Microscopy (STM) was also used to demonstrate the phenomenon. Makri *et al.* [93] interfaced a Pt(111) single crystal with a Na β"alumina solid electrolyte using a Pt paste. They showed using an atmospheric pressure STM that negative current application pumped Na from the electrolyte to the Pt(111) surface and that positive current application reversed the process.

Although the origin of the EP effect is easily understood when using alkali conductors as discussed above, its nature when using oxygen conductors is particularly intriguing. The main difference between using oxygen conductors rather than sodium conductors in an EP application, is that oxygen, unlike sodium, is at the same time a reactant. So, how can pumping oxygen to the catalyst modify in a non-faradaic manner the rate of a catalytic reaction that involves oxygen? Several studies have been performed with the aim of answering this question. Vayenas and coworkers used XPS and temperature-programmed desorption (TPD) to study Pt | YSZ catalyst surfaces under electrochemical control [94–96]. They found that, electrochemical oxygen pumping to the catalyst resulted in the presence of two XPS-resolved oxygen species on the Pt surface, chemisorbed oxygen (O 1s binding energy at 530.4 eV) and negatively charged oxygen species (lower O 1s binding energy than chemisorbed oxygen, 528.8 eV) denoted, $O^{\delta-}$. They also found that $O^{\delta-}$ species: (i) does not form via adsorption of molecular oxygen from the gas phase, (ii) is less reactive to H_2 or CO than regular chemisorbed oxygen and (iii) is more strongly bonded to the catalyst surface than regular chemisorbed oxygen (TPD desorption peak at 750–780 K against 675–685 K for regular oxygen). Therefore, they proposed that the spillover $O^{\delta-}$ species act as promoter species of catalytic reactions whereas the weakly bonded regular chemisorbed oxygen species participates of the catalytic reactions. Supplying $O^{\delta-}$ species to the catalyst surface increases its work function (forming an effective electrochemical double layer) and thus it weakens the chemisorptive bond of electron acceptor adsorbates and strengthens the chemisorptive bond of electron donor adsorbates. This is, $O^{\delta-}$ spillover species behave in an opposite manner as alkali (electropositive) promoters. As a consequence,

they proposed that the EP effect when using oxygen conductors is due to controlled electrochemical pumping of $O^{\delta-}$ species to the catalyst surface.

Imbihl and coworkers also studied the Pt | YSZ interface using XPS [97]. In agreement with the result from Vayenas they found that electrochemically induced oxygen spillover species are formed on the Pt surface upon applying a positive potential. However, they also found that this spillover species is *identical* to regular chemisorbed oxygen given that their O 1s binding energies are equal. This latter result is at variance with the XPS study performed by Vayenas, where a partially negatively charged species has been postulated based on the finding of a lower O 1s binding energy. To explain this discrepancy Imbihl argued as follows. (i) different oxygen coverages and hence different O 1s binding energies have been reached upon electrochemical pumping in the two sets of experiments due to different sample temperatures and due to different structural properties of the Pt/YSZ interfaces. (ii) the Patras samples might contain chemical contaminants which can interact and affect the binding energy of coadsorbed oxygen.

Vayenas and coworkers also measured the work function changes of Pt catalyst films deposited on YSZ induced upon electrochemical supply or removal of O^{-2} to or from the catalyst surface [98]. They found that the change in catalyst work function equals the change in catalyst potential,

$$e\Delta V_{\mathrm{WR}} = \Delta\phi_{\mathrm{W}}. \tag{1.7}$$

Moreover, Vayenas also claims the theoretical validity of this equality [82].

Other research groups also studied the changes in work function of metallic electrodes deposited on YSZ. Zipprich *et al.* [99] have observed deviations from the equality while Emery *et al.* [100] and Wodiunig [101] failed to observed the equality. Most strikingly, Poppe and coworkers [102] did not observe any changes in work function upon changing V_{WR} in the Pt/YSZ samples they prepared, however they did observe the 1:1 relation when using Pt/YSZ samples supplied by Vayenas. Deviations from equation (1.7) have also been observed by the Patras group [103].

It is evident that these experimental results question the theoretical validity of equation (1.7). In fact, Parsons criticised equation (1.7) arguing that the assumption made by Vayenas on its derivation is unjustified [104, 105]. The lack of agreement regarding the theoretical validity of equation (1.7) does not affect the empirical observations that provide the basis of the EP effect. Electrochemical Promotion is due to the controlled electrochemical pumping of promoter species to the catalyst surface from a solid electrolyte. This promoter species modify the catalyst work function, however its change might not be equal to the change in catalyst potential, which instead reflects the change

in potential across the catalyst/electrolyte interface.

1.5 Scope of this dissertation

The research discussed in this dissertation has the following aims: (i) to study the fundamentals of EP using spectroscopic methods, (ii) to exploit EP as a tool to study alkali promotion in new applications in heterogeneous catalysis and (iii) to diversify the catalytic chemistry that can be addressed by EP.

The desire to understand the EP phenomenon in as much detail as possible motivated the first part of this investigation. Therefore, firstly, we focused on elucidating the phenomena that underlie the EP effect. Thus, chapter 3 describes a fundamental photoelectron spectroscopic study of the EP cells used in the catalytic studies performed in this work.

Although low-pressure surface science studies provide a description of the fundamental processes taking place during alkali promotion, the correlation between these results and the catalytic surface reactions calls for kinetics measurements maintained at high pressures. Thus, the second part of the investigation was motivated by this need to model alkali promotion under realistic conditions. Therefore, EP was used as a tool to control *in situ* the level of alkali promoters on the catalyst surface while the catalytic reaction of interest is taking place. This work was carried out by combining ultrahigh vacuum surface characterisation with an atmospheric pressure microreactor in which the kinetics of the catalytic reaction is studied. Since the UHV chamber is equipped with an atmospheric reaction cell that allows simulation of the different situations encounter in the microreactor then the surface composition can be monitored at various stages of reaction. This combined approach thus bridges conventional kinetic reactor studies and UHV surface adsorption studies, giving insight into the chemical state of the surface under conditions approaching those used in catalysis. This method was used to study alkali promotion in the following environmentally and technologically important reactions:

i. The catalytic reduction of nitric oxide by carbon monoxide or propene in the absence and presence of oxygen over rhodium catalysts. Described in chapters 4, 5, and 6.

ii. The catalytic reduction of nitric oxide by carbon monoxide over copper catalysts. Described in chapter 7.

iii. Fischer-Tropsch synthesis over ruthenium catalysts. Described in chapter 8.

The principal questions of interest for the different catalytic systems were:

What is the reaction mechanism?

What is the mode of promoter action?

What are the different surface species present on the catalyst surface under reaction conditions? How do they change in the alkali-promoted regime?

What is the most likely chemical state of the alkali metal during the reaction?

The study of the response of activity and selectivity to controlled changes in promoter levels as well as the systematic determination of surface composition for different relevant catalytic conditions lead us to propose answers to the questions framed above.

Bibliography

[1] J. M. Thomas and W. J. Thomas, *Principles and practice of heterogeneous catalysis*, VCH, Weinheim, 1996.

[2] G. Ertl, H. Knözinger, and J. Weitkamp, editors, *Environmental catalysis*, Wiley-VCH, Weinheim, 1999.

[3] W. D. Mross, Alkali doping in heterogeneous catalysis, Catalysis Reviews Science and Engineering **25**, 591–637 (1983).

[4] H. P. Bonzel, Alkali-metal-affected adsorption of molecules on metal surfaces, Surface Science Reports **8**, 43–125 (1987).

[5] M. P. Kiskinova, *Poisoning and promotion in catalysis based on surface science concepts and experiments*, volume 70 of *Studies in surface science and catalysis*, Elsevier Science, Amsterdam, 1992.

[6] C. Herring and M. H. Nichols, Thermionic Emission, Reviews of Modern Physics **21**, 185–269 (1949).

[7] R. L. Gerlach and T. N. Rhodin, Binding and charge transfer associated with alkali metal adsorption on single crystal nickel surfaces, Surface Science **19**, 403–426 (1970).

[8] R. W. Verhoef and M. Asscher, The work function of adsorbed alkalis on metals revisited: a coverage-dependent polarisability approach, Surface Science **391**, 11–18 (1997).

[9] K. Wandelt, The local work function: concepts and implications, Applied Surface Science **111**, 1–10 (1997).

[10] R. D. Diehl and R. McGrath, Structural studies of alkali metal adsorption and coadsorption on metal surfaces, Surface Science Reports **23**, 43–171 (1996).

[11] D. Heskett, The interaction range in alkali metal-promoted systems, Surface Science **199**, 67–86 (1988).

[12] J. Kiss, G. Klivényi, K. Révéz, and F. Solymosi, Photoelectron spectroscopic studies on the dissociation of CO on potassium-dosed Rh(111) surface, Surface Science **223**, 551–568 (1989).

[13] R. A. Marbrow and R. M. Lambert, Chemisorption and surface reactivity of nitric oxide on clean sodium-dosed Ag(110), Surface Science **61**, 317–328 (1976).

[14] P. J. Goddard, J. West, and R. M. Lambert, Adsorption, coadsorption and reactivity of sodium and nitric oxide on Ag(111), Surface Science **71**, 447–461 (1978).

[15] P. J. Goddard and R. M. Lambert, Surface crystallography of rubidium on Ag(111) and the chemical reactivity of nitric oxide on rubidium-dosed Ag, Surface Science **79**, 93–108 (1979).

[16] E. L. Garfunkel, J. J. Maj, J. C. Frost, M. H. Farias, and G. A. Somorjai, Interaction of potassium with π-electron orbital containing molecules on Pt(111), Journal of Physical Chemistry **87**, 3629–3635 (1983).

[17] M. Kiskinova, G. Pirug, and H. P. Bonzel, Interaction of NO with potassium promoted Pt(111), Surface Science **140**, 1–17 (1984).

[18] I. R. Harkness and R. M. Lambert, Chemisorption and reactivity of nitric oxide on Na-dosed platinum(111), Journal of the Chemical Society, Faraday Transactions **93**, 1425–1429 (1997).

[19] H. Höchst and E. Colavita, The interaction of CO, NO and O_2 with sodium-promoted Rh(100) surfaces, Journal of Vacuum Science and Technology A **4**, 1442–1445 (1986).

[20] L. J. Whitman and W. Ho, The kinetics and mechanisms of alkali metal-promoted dissociation: a time resolved study of NO adsorption and reaction on potassium-precovered Rh(100), Journal of Chemical Physics **89**, 7621–7645 (1988).

[21] L. J. Whitman and W. Ho, How potassium promotes dissociation of NO on Rh(100), Journal of Vacuum Science and Technology A **6**, 880–882 (1988).

[22] L. Bugyi and F. Solymosi, Interaction of NO with potassium and boron contaminated Rh surfaces, Journal of Vaccum Science and Technology A **5**, 863–864 (1987).

[23] L. Bugyi and F. Solymosi, Adsorption and decomposition of NO on potassium promoted Rh(111), Vacuum **37**, 194–194 (1987).

[24] L. Bugyi and F. Solymosi, Interaction of NO with clean and K-dosed Rh(111) surfaces. I. AES, TDS and work function studies, Surface Science **188**, 475–489 (1987).

[25] L. Bugyi, J. Kiss, K. Révéz, and F. Solymosi, Interaction of NO with clean and K-dosed Rh(111) surfaces. II. EELS and PES studies, Surface Science **233**, 1–11 (1990).

[26] H. J. Zhang, Z. J. Yan, H. Y. Li, P. M. He, S. N. Bao, J. Wang, C. Y. Xu, and Y. B. Xu, Thermal desorption spectroscopy study of NO adsorption on clean and Cs-precovered Ru($10\bar{1}0$) surfaces, Acta Physica Synica **49**, 577–580 (2000).

[27] R. A. de Paola, J. Hrbek, and F. M. Hoffmann, Potassium promoted C−O bond weakening on Ru(001). I. Through-metal interaction at low potassium precoverage, Journal of Chemical Physics **82**, 2484–2498 (1985).

[28] T. V. W. Janssens, G. R. Castro, K. Wandelt, and J. W. Niemantsverdriet, Surface potential around potassium promoter atoms on Rh(111) measured with photoemission of adsorbed Xe, Kr and Ar, Physical Review B **49**, 14599–14609 (1994).

[29] K. Market and K. Wandelt, The short range of the electronic promoter effect of potassium, Surface Science **159**, 24–34 (1985).

[30] J. Lee, C. P. Hanrahan, J. Arias, R. M. Martin, and H. Metiu, Detection by metastable quenching spectroscopy of enhanced back-donation from Ni(111) surface to the $2\pi^*$ orbital of chemisorbed CO, caused by coadsorption of potassium, Physical Review Letters **51**, 1803–1806 (1983).

[31] D. W. Goodman, Model catalytic studies over metal single crystals, Accounts of Chemical Research **17**, 194–200 (1984).

[32] N. D. Lang, S. Holloway, and J. K. Nørskov, Electrostatic adsorbate-adsorbate interactions: the poisoning and promotion of the molecular adsorption reaction, Surface Science **150**, 24–38 (1985).

[33] M. Shelef and G. W. Graham, Why rhodium in automotive three-way catalysts?, Catalysis reviews science and engineering **36**, 433–457 (1994).

[34] A. Fritz and V. Pitchon, The current state of research on automotive lean NO_x catalysis, Applied Catalysis B: Environmental **13**, 1–25 (1997).

[35] K. C. Taylor, Nitric oxide catalysis in automotive exhaust systems, Catalysis reviews science and engineering **35**, 457–481 (1993).

[36] K. C. Taylor, Catalysts in cars, Chemtech **20**, 551–555 (1990).

[37] M. D. Amiridis, T. Zhang, and R. J. Farrauto, Selective catalytic reduction of nitric oxide by hydrocarbons, Applied Catalysis B: Environmental **10**, 203–227 (1996).

[38] R. Burch and T. C. Watling, The effect of promoters on Pt/Al_2O_3 catalsysts for the reduction of NO by C_3H_6 under lean-burn conditions, Applied Catalysis B: Environmental **11**, 207–216 (1997).

[39] P. T. Moseley, The solid electrolyte: properties and characteristics, in *The sodium sulfur battery*, edited by J. L. Sudworth and A. R. Tilley, pages 19–77, Chapman and Hall, New York, 1985.

[40] G. C. Farrington and J. L. Briant, Fast ionic transport in solids, Science **204**, 1371–1379 (1979).

[41] A. Hooper, Electrical breakdown in beta-alumina ceramics, Transactions and Journal of the British Ceramic Society **79**, 134–138 (1980).

[42] K. P. Jagannathan, S. K. Tiku, H. S. Ray, A. Ghosh, and E. C. Subbarao, Technological applications of solid electrolytes, in *Solid electrolytes and their applications*, edited by E. C. Subbarao, pages 201–259, Plenum Press, New York, 1980.

[43] W. Göpel, New materials and transducers for chemical sensors, Sensors and Actuators B **18-19**, 1–21 (1994).

[44] M. Stoukides, Applications of solid electrolytes in heterogeneous catalysis, Industrial Engineering Chemistry Research **27**, 1745–1750 (1988).

[45] H.-G. Lintz and C. G. Vayenas, Solid ion conductors in heterogeneous catalysis, Angewandte Chemie International Edition **28**, 708–715 (1989).

[46] M. Stoukides, Solid-electrolyte membrane reactors: current experience and future outlook, Catalysis reviews science and engineering **42**, 1–70 (2000).

[47] R. F. Service, Bringing fuel cells down to earth, Science **285**, 682–685 (1999).

[48] E. Murray, T. Tsai, and S. A. Barnett, A direct-methane fuel cell with a ceria-based anode, Nature **400**, 649–651 (1999).

[49] S. D. Park, J. M. Vohs, and R. J. Gorte, Direct oxidation of hydrocarbons in a solide-oxide fuel cell, Nature **404**, 265–267 (2000).

[50] C. G. Vayenas, S. I. Bebelis, and C. C. Kyriazis, Cogeneration: electricity + chemicals. Part 1: solid electrolytes?, Chemtech **21**, 422–428 (1991).

[51] C. G. Vayenas and R. D. Farr, Cogeneration of electric energy and nitric oxide, Science **208**, 593–594 (1980).

[52] C. G. Vayenas, Catalytic and electrocatalytic reactions in solid oxide fuel cells, Solid State Ionics **28-30**, 1521–1539 (1988).

[53] I. V. Yentekakis and C. G. Vayenas, Chemical cogeneration in solid electrolyte cells: the oxidation of H_2S to SO_2, Journal of the Electrochemical Society **136**, 996–1002 (1989).

[54] S. Neophytides and C. G. Vayenas, Chemical cogeneration in solid electrolyte cells: the oxidation of CH_3OH to H_2CO, Journal of the Electrochemical Society **137**, 839–845 (1989).

[55] C. Wagner, Adsorbed atomic species as intermediates in heterogeneous catalysis, Advances in Catalysis **21**, 323–381 (1970).

[56] G. Marnellos and M. Stoukides, Ammonia synthesis at atmospheric pressure, Science **282**, 98–100 (1998).

[57] S. Pancharatnam, R. A. Huggins, and D. M. Mason, Catalytic decomposition of nitric oxide on zirconia by electrolytic removal of oxygen, Journal of the Electrochemical Society **122**, 869–875 (1975).

[58] T. M. Gür and R. A. Huggins, Decomposition of nitric oxide on zirconia in a solid-state electrochemical cell, Journal of the Electrochemical Society **126**, 1067–1075 (1979).

[59] T. M. Gür and R. A. Huggins, Methane synthesis by a solid-state ionic method, Science **219**, 967–969 (1983).

[60] T. M. Gür and R. A. Huggins, Methane synthesis over transition metal electrodes in a solid state ionic cell, Journal of Catalysis **102**, 443–446 (1986).

[61] M. Stoukides and C. G. Vayenas, The effect of electrochemical oxygen pumping on the rate and selectivity of ethylene oxidation on polycrystalline silver, Journal of Catalysis **70**, 137–146 (1981).

[62] M. Stoukides and C. G. Vayenas, Electrocatalytic rate enhancement of propylene epoxidation on porous silver electrodes using a zirconia oxygen pump, Journal of Catalysis **131**, 839–845 (1984).

[63] A. Palermo, A. Hussain, and R. M. Lambert, Triply-promoted ethene epoxidation: NO_x promotion of the Ag-catalysed reaction in the presence of alkali and chlorine under electrochemical control, Catalysis Letters (2000), in press.

[64] C. Karavasilis, S. Bebelis, and C. G. Vayenas, *In situ* controlled promotion of catalytst surfaces via NEMCA: the effect of Na on the Ag-catalysed ethylene epoxidation in the presence of chlorine moderators, Journal of Catalysis **160**, 205–213 (1996).

[65] S. Tracey, J. P. Holgado-Vazquez, A. Palermo, and R. M. Lambert, *In situ* electrochemical promotion by sodium of the selective hydrogenation of acetylene over platinum, Journal of Catalysis **179**, 231–240 (1998).

[66] C. A. Cavalca and G. L. Haller, Solid electrolytes as active catalyst supports: electrochemical modification of benzene hydrogenation activity on Pt/β"(Na)Al_2O_3, Journal of Catalysis **177**, 389–395 (1998).

[67] I. V. Yentekakis, G. Moggridge, C. G. Vayenas, and R. M. Lambert, *In situ* controlled promotion of catalyst surfaces via NEMCA: the effect of Na on the Pt-catalysed CO oxidation, Journal of Catalysis **146**, 292–305 (1994).

[68] C. G. Vayenas, S. Bebelis, and M. Despotopoulou, Non-faradaic electrochemical modification of catalytic activity. 4. The use of β"Al_2O_3 as the solid electrolyte, Journal of Catalysis **128**, 415–435 (1991).

[69] I. R. Harkness, C. Hardacre, R. M. Lambert, I. V. Yentekakis, and C. G. Vayenas, Ethylene oxidation over platinum: *in situ* controlled promotion using Na-β" alumina and studies with a Pt(111)/Na model catalyst, Journal of Catalysis **160**, 19–26 (1996).

[70] P. D. Petrolekas, S. Brosda, and C. G. Vayenas, Electrochemical promotion of Pt catalyst electrodes deposited on $Na_3Zr_2Si_2PO_{12}$ during ethylene oxidation, Journal of Catalysis **160**, 205–213 (1996).

[71] N. C. Filkin, M. S. Tikhov, A. Palermo, and R. M. Lambert, A kinetic and spectroscopic study of the *in situ* electrochemical promotion by sodium of the platinum-catalysed combustion of propene, Journal of Physical Chemistry A **103**, 2680–2687 (1999).

[72] A. Palermo, R. M. Lambert, I. R. Harkness, I. V. Yentekakis, O. Mar'ina, and C. G. Vayenas, Electrochemical promotion by Na of the platinum-catalysed reaction between CO and NO, Journal of Catalysis **161**, 471–479 (1996).

[73] O. A. Mar'ina, I. V. Yentekakis, C. G. Vayenas, A. Palermo, and R. M. Lambert, *In situ* controlled promotion of catalyst surface via NEMCA: the effect of Na on the Pt-catalysed NO reduction by H_2, Journal of Catalysis **166**, 218–228 (1997).

[74] N. C. Filkin, *Electrochemical promotion of environmentally important catalytic reactions*, PhD thesis, University of Cambridge, Cambridge, 1997.

[75] I. R. Harkness and R. M. Lambert, Electrochemical promotion of the NO + ethylene reaction over platinum, Journal of Catalysis **152**, 211–214 (1995).

[76] I. V. Yentekakis, A. Palermo, N. C. Filkin, M. S. Tikhov, and R. M. Lambert, *In situ* electrochemical promotion by sodium of the platinum-catalysed reduction of NO by propene, Journal of Physical Chemistry B **101**, 3759–3768 (1997).

[77] C. G. Vayenas, S. Bebelis, and S. Neophytides, Non-faradaic electrochemical modification of catalytic activity, Journal of Physical Chemistry **92**, 5083–5085 (1988).

[78] J. Pritchard, Electrochemical Promotion, Nature **343**, 592–593 (1990).

[79] S. G. Neophytides, D. Tsiplakides, P. Stonehart, M. M. Jaksic, and C. G. Vayenas, Electrochemical enhancement of a catalytic reaction in aqueous solution, Nature **370**, 45–47 (1994).

[80] C. G. Vayenas, S. Bebelis, S. Neophytides, and I. V. Yentekakis, Non-faradaic electrochemical modification of catalytic activity in solid electrolyte cells, Applied Physics A **49**, 95–103 (1989).

[81] C. G. Vayenas, S. Bebelis, and C. C. Kyriazis, Cogeneration: electricity + chemicals. Part 2: Nonfaradaic catalysis, Chemtech **21**, 500–501 (1991).

[82] C. G. Vayenas, S. Bebelis, I. V. Yentekakis, and H.-G. Lintz, Non-faradaic electrochemical modification of catalytic activity: a status report, Catalysis Today **11**, 303–442 (1992).

[83] C. G. Vayenas, S. Ladas, S. Bebelis, I. V. Yentekakis, S. Neophytides, Y. Jiang, C. Karavasilis, and C. Pliangos, Electrochemical promotion in catalysis: Non-faradaic electrochemical modification of catalytic activity, Electrochimica Acta **39**, 1849–1855 (1994).

[84] C. G. Vayenas, I. V. Yentekakis, S. Bebelis, and S. G. Neophytides, *In Situ* controlled promotion of catalyst surfaces via solid electrolytes: the NEMCA effect, Berichte der Bunsen Gesellschaft Physical Chemistry Chemical Physics **99**, 1393–1401 (1995).

[85] C. G. Vayenas and S. G. Neophytides, Electrochemical activation of catalysis: *In Situ* controlled promotion of catalyst surfaces, in *Catalysis*, volume 12, pages 199–253, The royal society of chemistry, 1996.

[86] C. G. Vayenas, M. M. Jaksic, S. I. Bebelis, and S. G. Neophytides, The electrochemical activation of catalytic reactions, in *Modern Aspects of Electrochemistry*, edited by J. O. Bockris, B. E. Conway, and W. R. E. White, volume 29, pages 57–202, Plenum Press, New York, 1996.

[87] C. G. Vayenas and I. V. Yentekakis, Electrochemical modification of catalytic activity, in *Handbook of heterogeneous catalysis*, edited by G. Ertl, H. Knötzinger, and J. Weitkamp, volume 8, pages 1310–1325, Wiley-VCH, Weinheim, 1997.

[88] C. G. Vayenas and S. Bebelis, Electrochemical promotion, Solid State Ionics **94**, 267–277 (1997).

[89] C. G. Vayenas and S. Bebelis, Electrochemical promotion of heterogeneous catalysis, Catalysis Today **51**, 581–594 (1999).

[90] S. Bebelis, M. Makri, A. Buekenhoudt, J. Luyten, S. Brosda, P. Petrolekas, C. Pliangos, and C. G. Vayenas, Electrochemical activation of catalytic reactions using anionic, cationic and mixed conductors, Solid State Ionics **129**, 33–46 (2000).

[91] I. V. Yentekakis and S. Bebelis, Study of the NEMCA effect in a single-pellet catalytic reactor, Journal of Catalysis **137**, 278–283 (1992).

[92] B. Hammer and J. K. Nørskov, Why gold is the noblest of all the metals, Nature **376**, 238–240 (1995).

[93] M. Makri, C. G. Vayenas, S. Bebelis, K. H. Besocke, and C. Cavalca, Atomic resolution STM imaging of electrochemically controlled reversible promoter dosing of catalysts, Surface Science **369**, 351–359 (1996).

[94] S. Ladas, S. Kennou, S. Bebelis, and C. G. Vayenas, Origin of non-faradaic electrochemical modification of catalytic activity, Journal of Physical Chemistry **97**, 8845–8848 (1993).

[95] S. G. Neophytides and C. G. Vayenas, TPD and cyclic voltammetric investigation of the origin of electrochemical promotion in catalysis, Journal of Physical Chemistry **99**, 17063–17067 (1995).

[96] S. G. Neophytides, D. Tsiplakides, and C. G. Vayenas, Temperature programmed desorption of oxygen from Pt films interfaced with Y_2O_3-doped ZrO_2, Journal of Catalysis **178**, 414–428 (1998).

[97] B. Luerßen, S. Günter, H. Marbach, M. Kiskinova, J. Janek, and R. Imbihl, Photoelectron spectromicroscopy of electrochemically induced oxygen spillover at the Pt/YSZ interface, Chemical Physics Letters **316**, 331–335 (2000).

[98] S. Ladas, S. Bebelis, and C. G. Vayenas, Work function measurements on catalyst films subject to *in situ* electrochemical promotion, Surface Science **251/252**, 1062–1068 (1991).

[99] W. Zipprich, H.-D. Wiemhöfer, U. Vohrer, and W. Göpel, *In situ* photoelectron spectroscopy of oxygen electrodes on stabilised zirconia, Berichte der Bunsen Gesellschaft Physical Chemistry Chemical Physics **99**, 1406–1413 (1995).

[100] D. A. Emery, P. H. Middleton, and I. S. Metcalfe, The effect of electrochemical current pumping on the work function of solid electrolyte supported catalysts, Surface Science **405**, 308–315 (1998).

[101] S. Wodiunig, *Electrochemical Promotion of RuO_2 catalysts for the gas phase combustion of ethylene*, PhD thesis, École Polytechnique Fédérale de Lausanne, Lausanne, 2000.

[102] J. Poppe, S. Völkening, A. Schaak, E. Schütz, J. Janek, and R. Imbihl, Electrochemical promotion of catalytic CO oxidation on Pt/YSZ catalysts under low pressure conditions, Physical Chemistry Chemical Physics **1**, 5241–5249 (1999).

[103] C. Raptis, T. Badas, D. Tsiplakides, C. Pliangos, and C. G. Vayenas, Electrochemical promotion of NO reduction by C_3H_6 on Rh/YSZ catalyst-electrodes and investigation of the origin of the promoting action using TPD and WF measurements, in *12th International congress on catalysis*, edited by A. Corma, F. V. Melo, S. Mendioroz, and J. L. G. Fierro, volume 130B of *Studies in Surface Science and Catalysis*, pages 1283–1287, Elsevier, Amsterdam, 2000.

[104] R. Parsons, Book reviews, Journal of Electroanalytical Chemistry **422**, 202–203 (1997).

[105] R. Parsons, Comment on the paper entitled 'On the work function of the gas exposed electrode surfaces in solid state electrochemistry', Journal of Electroanalytical Chemistry **486**, 91 (2000).

CHAPTER 2

Methodology

2.1 X-ray photoelectron spectroscopy

X-ray photoelectron spectroscopy (XPS) is based on the photoelectric effect: a solid that is irradiated with photons of sufficiently high frequency emits electrons. The key to photoelectron spectroscopy is detection of the emitted photoelectrons and measurement of their kinetic energy distribution. Figure 2.1 shows a schematic diagram of the XPS process: an X-ray photon of energy $h\nu$ causes the emission of a core or valence electron with kinetic energy E_{kin}. Energy conservation requires that:

$$E_{\mathrm{kin}} = h\nu - E_{\mathrm{B}} - \phi \tag{2.1}$$

where ϕ is the sample's work function and E_{B} is the binding energy of the electron and is given by the difference between the total energies of the final state (with N-1 electrons) and the initial state (with N electrons):

$$E_{\mathrm{B}} = E_{\mathrm{f}} - E_{\mathrm{i}}. \tag{2.2}$$

However, since the sample is in electrical contact with the spectrometer (their Fermi levels are equal) then the measured kinetic energy of a photoelectron E'_{kin} is given by [1]:

$$E'_{\mathrm{kin}} = h\nu - E_{\mathrm{B}} - \phi_{\mathrm{sp}} \tag{2.3}$$

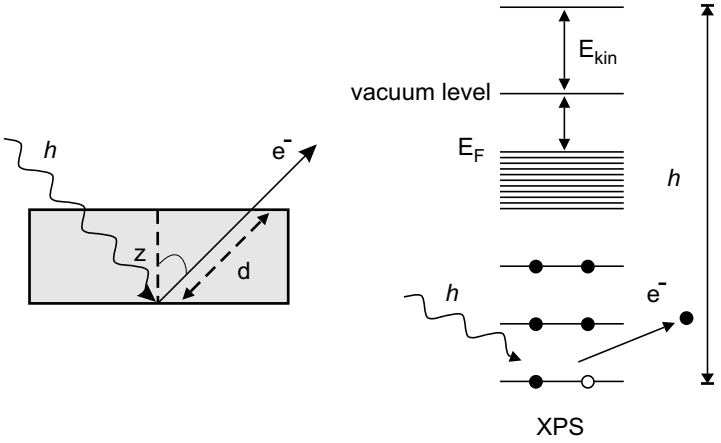

Figure 2.1: The diagram on the left illustrates the emission of photoelectrons at an angle θ with respect to the surface normal. The electrons are emitted from atoms located a distance z below the surface and have to travel a distance d through the solid before being detected. The diagram on the right illustrates the XPS process.

where ϕ_{sp} is the work function of the spectrometer and E_{B} is the binding energy of the electron with respect to the Fermi level of the sample E_{F}. As the photon energy of the X-rays ($h\nu$) and ϕ_{sp} are known and E'_{kin} is determined experimentally, the calculation of the electron binding energy is a simple matter.

2.1.1 Surface sensitivity

A key aspect of XPS is its surface sensitivity, i. e. the vast majority of detected signal comes from the surface region of the sample. Why is XPS surface sensitive? The x-rays employed to emit electrons penetrate $\sim 10^{-6}$ m into the sample. Thus the electrons are emitted from atoms in the solid at various depths below its surface. Only those electrons which leave the solid and still have their initial characteristic energy (kinetic energy immediately after photon excitation) contribute to the elastic (no energy loss) peaks observed in the photoelectron spectroscopy spectrum. On the other hand, the electrons which have lost energy before being detected contribute to the background of the spectrum (or to the satellite structure, see below for discussion). The process by which an electron can lose energy as it travels through the solid is known as 'inelastic scattering'. Briefly, there are three main processes by which the photoelectrons lose energy: (i) excitation of lattice vibrations, these losses are so small (of the order of a few tens of meV) that they are usually not detected, (ii) excitation of a second electron from its ground state to an empty state in the solid or alternatively ionisation of a level with the ejection of another photoelectron (iii) plasmon excitations (collective oscillations of

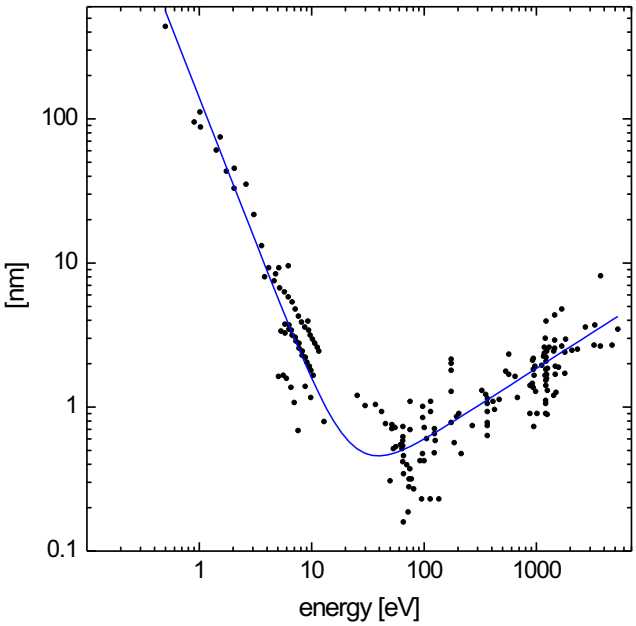

Figure 2.2: Mean free path of electrons in solids as a function of their energy. From Seah and Dench [2].

conduction band electrons) [3].

The inelastic mean free path λ is a measure of the average distance traveled by an electron through a solid before it is inelastically scattered. It can be defined by equation (2.4) which gives the probability of the electron traveling a distance d through the solid (or an electron being emitted from a distance z below the surface at an angle θ with respect to the surface normal) without undergoing any inelastic collisions [4];

$$P = \exp(-d/\lambda) = \exp(-z/\cos(\theta)\lambda). \tag{2.4}$$

From equation (2.4) it is clear that the larger the distance to be traveled inside the solid, the lower the probability of escaping the solid without loosing energy. The mean free path depends on the initial kinetic energy of the electron and, although it also depends on the solid concerned, is very similar for most elements. The relationship between the mean free path and photoelectron energy is graphically represented in figure 2.2. It is evident that low energy electrons (10-1000 eV) have a very short mean free path in a solid ($\leq$ 10 Å), i. e. they can travel very short distances through the solid before they can lose energy. This means that any experimental technique such as photoelectron spectroscopy which involves the generation and detection of electrons of such energies will be surface sensitive. The inelastic mean free path curve exhibits a minimum for electrons of kinetic energy around 50-100 eV. At lower energies the probability of inelastic

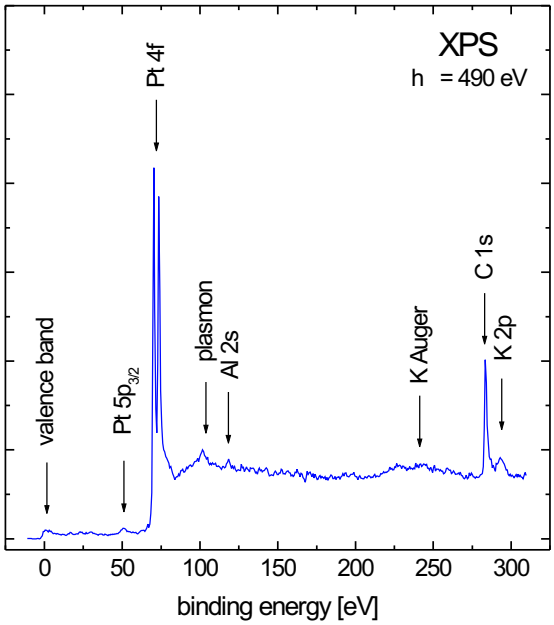

Figure 2.3: Typical XPS spectrum obtained for a Pt/K β"alumina EP sample.

scattering decreases since an electron has insufficient energy to cause plasmon excitation and consequently λ increases. At higher energies, the scattering becomes dominated by plasmon-creation which slowly becomes weaker as the energy increases and thus λ increases [5].

As discussed above, photoelectron spectroscopy is surface sensitive due to the inelastic scattering of the emitted electrons. How can we change the degree of surface sensitivity? One possibility would be to ensure that the electrons being detected have kinetics energies corresponding to the minimum in the mean free path curve. In order to achieve this, the photon energy needs to be adjusted to give the photoelectrons the desired kinetic energy. This requires the use of a tunable photon source like synchrotron radiation sources. Another possibility would be to collect the electrons at a more grazing angle. From equation (2.4) it is clear that as θ increases, the probability of undergoing inelastic scattering for electrons emitted at z increases, therefore the surface sensitivity is increased.

2.1.2 General features of the spectra

The core atomic levels of each element are associated with a characteristic binding energy. Therefore the presence of peaks at particular energies indicates the presence of a specific element in the sample under study. For example, figure 2.3 shows the XPS

Table 2.1: Spectroscopic notation used in XPS.

n	l	j	X-ray level	spectroscopic level
1	0	1/2	K	$1s$
2	0	1/2	L_1	$2s$
2	1	1/2	L_2	$2p_{1/2}$
2	1	3/2	L_3	$2p_{3/2}$
3	0	1/2	M_1	$3s$
3	1	1/2	M_2	$3p_{1/2}$
3	1	3/2	M_3	$3p_{3/2}$
3	2	3/2	M_4	$3d_{3/2}$
3	2	5/2	M_5	$3d_{5/2}$
...	...	...	...	...
4	3	5/2	N_6	$4f_{5/2}$
4	3	7/2	N_7	$4f_{7/2}$

spectrum of a Pt/K β" alumina EP sample. The spectrum was acquired with a photon energy of 490 eV using a synchrotron radiation source. Peaks due to K, Pt, C and Al are readily assigned if one consults binding energy tables [6]. In addition to the expected photoelectron peaks, the spectrum contains peaks due to Auger electrons as well. The latter arise from deexcitation of the core hole by an Auger transition (see below). Photoelectron peaks are labeled according to the quantum numbers of the level from which the electron originates. Table 2.1 summarises the spectroscopic nomenclature. As can be seen from figure 2.3, the characteristic XPS peaks are superimposed on a background of inelastically scattered electrons that increases as the binding energy increases (kinetic energy decreases). The intensity of the different peaks depends on two factors: (i) the concentration of the element within the sampled region and (ii) the probability of the core level being ionised when irradiated by a photon, i. e. the photoionisation cross-section.

Closer inspection of the spectrum in figure 2.3 shows that emission from some levels, e. g. Pt 4f, does not give rise to a single photoemission peak, but a doublet. Figure 2.4 shows that the Pt 4f emission is in fact split into two peaks. This arises from spin-orbit coupling effects in the final state. In the initial state the Pt 4f level is completely full and therefore has no total spin. However, the removal of an electron from the 4f level by photoionisation creates an unpaired electron spin in the final state. The interaction of the spin momentum (s) and the orbital angular momentum (l) of the electron, i. e. spin-orbit coupling, gives rise to two final levels that differ in energy and in degeneracy [6]. The two levels are characterised by the total angular momentum $j = l + s$, in this

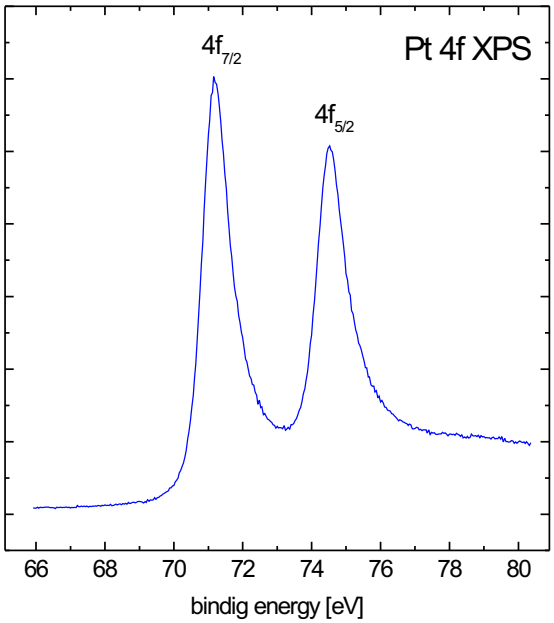

Figure 2.4: Pt 4f XPS spectrum of a Pt/K β"alumina EP sample.

particular case the coupling of $l = 3$ and $s = 1/2$ gives j values of 7/2 and 5/2. The lowest energy final state is the one with maximum j and the relative intensities of the two peaks reflects the degeneracies of the final states $(2j + 1)$. This spin-orbit splitting is of course not present in s levels ($l = 0$), but is seen with p, d and f core-levels which all show characteristic spin-orbit doublets.

2.1.3 Satellite structure of the spectra

As well as the generation of core photoelectron lines in XPS, certain outgoing photoelectrons undergo characteristic energy losses as they are ejected from the atom due to the enhanced probability for loss of a specific amount of energy. Such well defined losses should not be confused with the general cascade of inelastic collisions that occur once the electron has been ejected and give rise to the observed background, but involve promotion of electrons within the atom to a higher level; the resulting loss of kinetic energy by the photoelectron is observed in the XPS spectrum as a minor peak to the high binding energy side of the characteristic core level. Such phenomena include shake up/off processes and plasmon excitation.

Shake up/off processes

Shake up/off processes are caused by the reorganisation of the valence electrons following the photoemission event. In the case of the shake up process a valence electron is

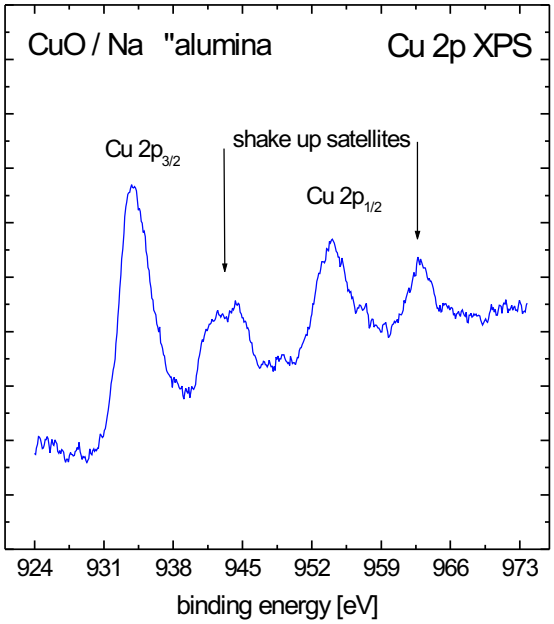

Figure 2.5: Cu 2p XPS spectrum of a CuO/Na β"alumina EP sample showing the shake up satellites.

excited into a higher energy level. The energy required for this transition is lost by the primary emitted photoelectron and consequently a satellite structure appears at the higher binding energy side of the main core level peak. Figure 2.5 shows the shake up satellites appearing in the Cu 2p spectrum of a CuO/Na β"alumina EP sample. It should be noted that the satellite is absent in metallic Cu and Cu_2O, therefore it is very useful as a fingerprint of the oxidation state of this element. A related occurrence is that of shake off in which the valence electron is ejected completely from the atom leading to a doubly ionised system. Such losses occur as a very broad feature within the large background of inelastically scattered electrons and therefore yield no spectroscopic information.

Plasmon excitations

Plasmon losses result from the collective oscillations of electrons in the conduction band brought about by the outgoing electron which suffers a discrete energy loss, the plasmon frequency (or multiples of this value), observed as a characteristic series of peaks on the high binding energy side of the main core line. Figure 2.3 shows a typical plasmon loss observed on the high binding energy side of the Pt 4f peak in the wide XPS spectrum of a Pt/K β"alumina EP sample.

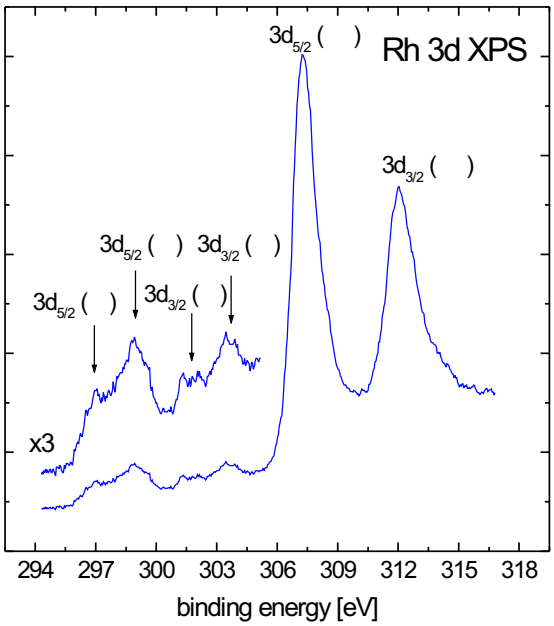

Figure 2.6: Rh 3d XPS spectrum of a Rh/Na β"alumina EP sample showing the Mg x-ray satellites.

X-ray satellites

The laboratory photon sources used to generate photoelectrons do not consist merely of a characteristic X-ray line, but some minor X-ray components at higher photon energies. The unmonochromatised Mg source used in this work consists of a main X-ray emission of photon energy $h\nu = 1253.6\,\text{eV}$ and width 0.7 eV ($K\alpha_{1,2}$) and satellite lines of smaller intensity [6]. The most important satellites are the $K\alpha_3$ and $K\alpha_4$ lines situated at 8.4 eV and 10.2 eV higher photon energy with 8% and 4% relative intensity respectively. Therefore, for each photoelectron peak that results from the $K\alpha_{1,2}$ photons there is a family of minor peaks at lower binding energies. Figure 2.6 shows the X-ray satellite features present in the Rh 3d XPS spectrum of a Rh/Na β"alumina EP sample.

Asymmetric metal core levels

This feature is closely related to shake up processes and is due to the high density of unfilled states above the Fermi level in metals. Shake up transitions can occur to these states resulting not in discrete satellite features but rather a high binding energy tail accompanying the core level peak. This feature is easily observed in figures 2.4 and 2.6 in the Pt 4f and Rh 3d spectra of Pt and Rh Na/β" alumina EP samples respectively.

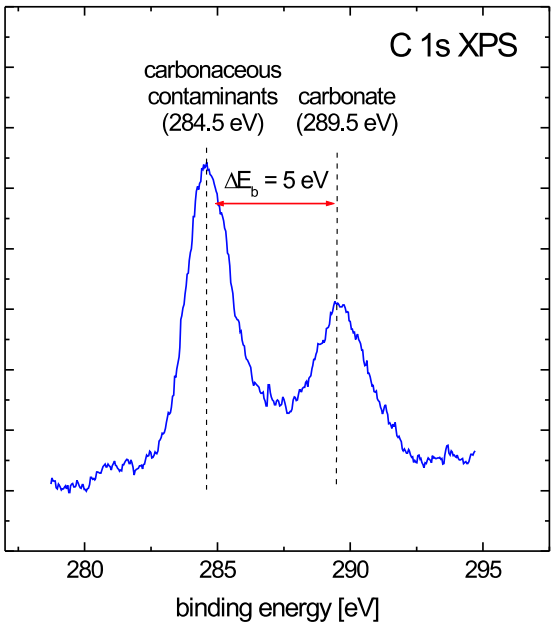

Figure 2.7: C 1s XPS spectrum showing the chemical shift.

2.1.4 Peak position

Equation (2.2) defines the binding energy as the energy difference between the final state of the system containing the core hole and the initial neutral ground state. As a consequence, the binding energy of a photoelectron contains information on the state of the atom before photoionisation (the initial state) and on the core-ionised atom left behind after the emission of an electron (the final state). Therefore, a shift of peak position in a photoelectron spectrum can be due to both initial state and final state effects.

Initial state effects

The binding energy of the photoelectrons shows variations for a particular element and energy level depending on the exact chemical environment of the atom. Thus, a very important aspect of XPS is its ability to determine the binding energy difference between two or more inequivalent chemical environments of the same element, this is the so-called XPS chemical shift. The physical basis of the chemical shift effect is illustrated by equation (2.5):

$$\Delta E_{\mathrm{B}} = E_{\mathrm{i}}^{(2)} - E_{\mathrm{i}}^{(1)} = k(q_{\mathrm{i}}^{(2)} - q_{\mathrm{i}}^{(1)}) + (V_{\mathrm{i}}^{(2)} - V_{\mathrm{i}}^{(1)}) \tag{2.5}$$

where ΔE_B is the binding energy change due to a change in chemical environments (1 and 2), E_i is the binding energy of a particular core level on atom i, q_i is the charge on atom i and V_i is the electrostatic potential experienced by atom i [6]. It is clear that a binding energy change can be due to a change in the charge of the atom or in the potential experienced by the atom. In general, it is found, that the binding energy of an electron in any orbital of an atom increases as the oxidation state of the atom increases. Also, as the atom looses valence electrons (the bond with other atom becomes more polar or ionic) the binding energy of the remaining electrons increases. The chemical shift is illustrated in figure 2.7 which shows the C 1s XPS spectrum of a bulk sodium carbonate sample. The low binding energy contribution to the spectrum is due to a contamination overlayer present on the specimen surface, consisting mainly of hydrocarbon fragments.

Final state effects

If we assume that after a photoemission event the energy of the remaining electrons is the same as in the initial state before emission of the photoelectron (i. e. the system remains 'frozen'), then the binding energy is simply equal to the negative orbital energy of the emitted electron ($\varepsilon < 0$) [1]:

$$E_B = -\varepsilon. \tag{2.6}$$

However, the above approximation (called Koopmans' Theorem) is not correct since after a photoemission event, the remaining electrons in the final state feel the presence of the core hole and as a result they relax to lower the total energy of the system. The relaxation process causes a reduction in the binding energy of the ejected electron. Thus the binding energy is not equal to the energy of the orbital from which the photoelectron is emitted; the difference is caused by the reorganisation of the remaining electrons when an electron is removed from a core level [1]:

$$E_B = -\varepsilon - E_{relax}. \tag{2.7}$$

The relaxation energy has two contributions: the intra-atomic relaxation is due to rearrangement of electrons in the orbitals of the excited atom and the extra-atomic relaxation arises by additional screening of the core hole by the surrounding of this atom in the solid. When interpreting binding energy shifts with equation (2.5) we are assuming that relaxation energies do not vary significantly from one chemical environment to another.

Other features besides relaxation effects are final state effects. These include, spin-orbit coupling and shake up/off processes. These final state effects give rise to splitting

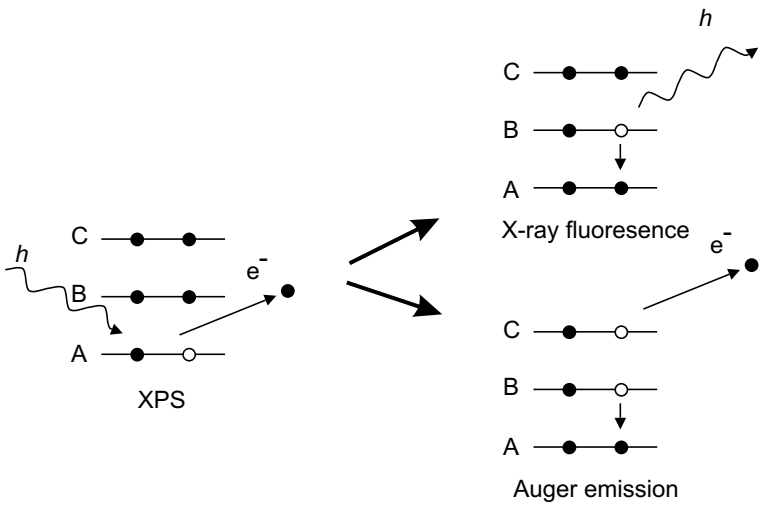

Figure 2.8: Schematic diagram of the processes available for the decay of the core hole.

of peaks and the appearance of satellite peaks as discussed above.

2.1.5 The fate of core holes

Figure 2.8 shows the two pathways available for the decay of a core hole: X-ray fluorescence and Auger electron emission. Each mechanism involves the neutralisation of the core hole by an electron from a higher level. The hole in A is filled by an electron from B releasing an amount of energy $E_A - E_B$. In the case of X-ray fluorescence, excess energy is released by the emission of an X-ray photon with energy given by,

$$h\nu = E_A - E_B. \tag{2.8}$$

In the case of Auger emission, excess energy causes the emission of an electron with a kinetic energy characteristic of the emitting atom, (thus resulting in a doubly ionised system)

$$E_{kin} = E_A - E_B - E_C^{'} \tag{2.9}$$

where $E_C^{'}$ is the binding energy of the C level in the presence of a hole in B, and is therefore different from the ground state binding energy E_C [6]. The Auger electrons are inevitably analysed along with the photoelectron signal and therefore appear on the XP spectrum, often providing important complementary information. The Auger transitions can be distinguished from the XPS peaks because the kinetic energy of the Auger electrons is independent of the photon energy.

2.1.6 Line broadening effects

The width of an XPS peak ΔE, defined as the full width at half maximum (FWHM), is determined by the inherent width of the core level ΔE_{n}, the width of the X-ray line ΔE_{p} and the resolution of the electron analyser ΔE_{a}. Assuming that all components have a Gaussian line shape it is given by,

$$\Delta E = (\Delta E_{\mathrm{n}}^2 + \Delta E_{\mathrm{p}}^2 + \Delta E_{\mathrm{a}}^2)^{1/2}. \tag{2.10}$$

The laboratory X-ray source used in this work, Mg $K\alpha$, has a line width of 0.7 eV. The inherent line width of a core level is a direct consequence of the uncertainty principle

$$\Delta E_{\mathrm{n}} \cdot \Delta t \geq \frac{h}{4\pi} \tag{2.11}$$

where $h = 4.1357 \times 10^{-15}\,\mathrm{eV} \cdot \mathrm{s}$ is Planck's constant and Δt is the lifetime of the core hole. Since Δt is typically between 10^{-14} and 10^{-15} s we would expect from equation (2.11) a natural photoelectron line width of the order of 0.4 eV. The resolution achieved in this work has typical values between 1 and 2 eV depending on the above parameters.

2.1.7 Quantification

XPS was not only used to determine the species present on the surface of the catalysts studied in this work, but also it was used to estimate their surface concentrations. Depending on whether the adsorbate is present on submonolayer quantities or it forms a thick film over the substrate, different equations should be used to estimate the adsorbate surface concentration. When the adsorbate is present in small quantities (less than a monolayer) and after assuming that it does not attenuate the substrate signal, its surface concentration can be estimated using the equation due to Carley and Roberts [7],

$$\vartheta_{\mathrm{a}} = \frac{KE_{\mathrm{a}}}{KE_{\mathrm{s}}} \times \frac{I_{\mathrm{a}}}{I_{\mathrm{s}}} \times \frac{\mu_{\mathrm{s}} N \lambda_{\mathrm{s}} \rho_{\mathrm{s}} \cos\theta}{\mu_{\mathrm{a}} M_{\mathrm{s}}} \tag{2.12}$$

where,

ϑ_{a} = adatom surface coverage ($\mathrm{atom} \cdot \mathrm{cm}^{-2}$)
KE = kinetic energy of the photoelectrons
θ = angle of collection of the photoelectrons with respect to the sample normal
μ = photoelectron cross section
I = integrated peak intensity
N = Avogadro's number

λ_s = inelastic mean free path of the substrate photoelectrons

M_s = molar mass of the substrate

ρ_s = density of the substrate

On the other hand, when the adsorbate forms a thick film over the substrate its thickness can be estimated from the attenuation of the substrate signal using the following equation [6],

$$I = I_\circ \exp\left(-\frac{d}{\lambda \cos\theta}\right) \tag{2.13}$$

where,

I = integrated substrate intensity when overlayer is present

$I_\circ$ = integrated intensity of the clean substrate

d = film thickness

λ = inelastic mean free path of photoelectrons

The inelastic mean free path in equations (2.12) and (2.13) have been taken from the calculations of Penn [8], whereas the photoionisation cross section in equation (2.12) have been taken from the calculations of Yeh and Lindau [9].

Equations (2.12) and (2.13) are valid for an ideally flat substrate, however our EP samples are very rough, i. e. the surface area is typically two orders of magnitude greater than the geometrical area (see below). Therefore the calculated quantities should only be taken as a rough estimation.

2.1.8 Spatial resolution

The spatial resolution of photoelectron spectroscopy is given by the area of the sample irradiated by the X-ray beam. For example, the laboratory X-ray beam used in this work irradiates an area of $\sim 1\,\mathrm{cm}^2$ over the sample, thus yielding an average of the chemical composition over that area. However, if the photon beam is focused to submicron dimensions over the sample and the sample is scanned across its surface then a chemical map of the sample can be obtained. This technique is called Scanning Photoemission Microscopy (SPEM) and uses synchrotron radiation since the required photon flux to obtain a measurable signal should be concentrated into a microspot of about $10^{-2}\,\mu\mathrm{m}^2$. We have performed SPEM experiments at the ESCA microscopy beamline on the ELETTRA X-ray synchrotron photon source in Trieste, a detailed description of the technique can be found elsewhere [10].

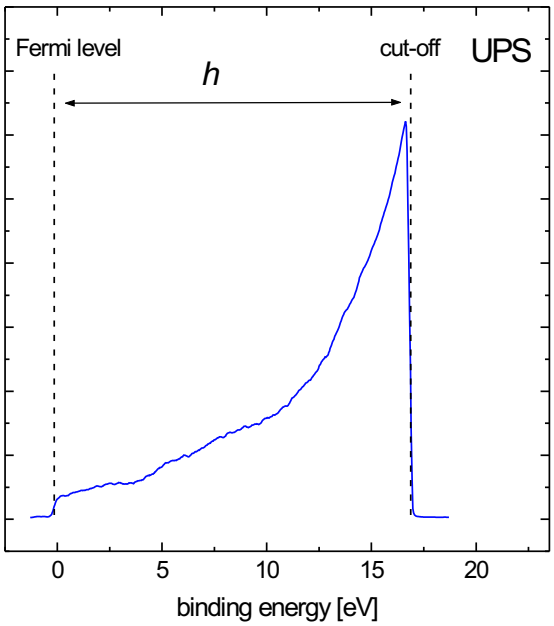

Figure 2.9: UPS spectrum of a Rh/Na β"alumina EP sample.

2.2 Work function measurements

Photoelectron spectroscopy can be performed using ultraviolet radiation instead of X-rays, in this case the technique is called Ultraviolet Photoelectron Spectroscopy (UPS). The low photon energy employed in UPS ensures that only valence electrons are photoemitted. UPS has been utilised to measure the work function of our EP samples.

Figure 2.9 shows a UPS spectrum of a Rh/Na β"alumina EP sample. The low binding energy onset of the spectrum is due to the density of states at the Fermi level and provides a convenient zero for the binding energy scale. Most of the intensity at higher binding energy is due to secondary electrons. These are photoelectrons which have suffered energy loss while travelling through the solid. The cut-off point corresponds to electrons which had just enough kinetic energy to overcome the work function of the substrate. Therefore, those electrons contributing to the high binding energy cut-off in the spectrum have zero kinetic energy $E_{\mathrm{kin}}^{\mathrm{cut-off}} = 0$. On the other hand, electrons from the Fermi level posses the highest kinetic energy (their binding energy is zero) $E_{\mathrm{kin}}^{\mathrm{Fermi}} = h\nu - \phi$. Hence, the width of the UPS spectrum $\Delta E = E_{\mathrm{kin}}^{\mathrm{Fermi}} - E_{\mathrm{kin}}^{\mathrm{cut-off}}$ equals $h\nu - \phi$, and therefore, the work function becomes:

$$\phi = h\nu - \Delta E \tag{2.14}$$

The width of the spectrum in figure 2.9 is $\Delta E = 16.6\,\mathrm{eV}$ and since the photon energy

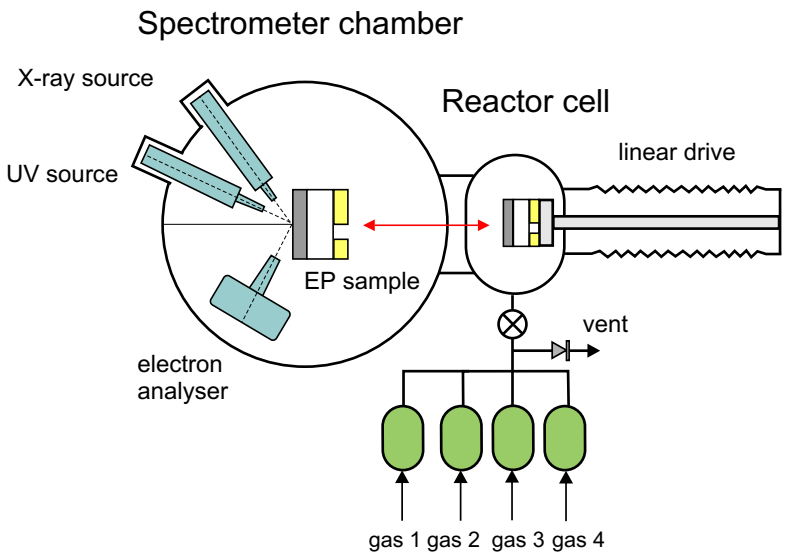

Figure 2.10: Schematic diagram of the spectrometer system. The EP sample is mounted on a linear drive that allows translation between the reaction cell and the spectrometer chamber.

was $h\nu = 21.2\,\text{eV}$ then equation (2.14) gives a work function of 4.6 eV for the Rh EP sample. This value is in reasonable agreement with the work function for polycrystalline Rh of 4.9 eV reported in the literature [11].

2.3 Implementation of photoelectron spectroscopies

Photoemission measurements were performed using a VG ADES 400 ultrahigh vacuum (base pressure $< 10^{-10}$ Torr) spectrometer system. This was equipped with a UV-source (He gas discharge), an X-ray source (Mg $K\alpha$), an hemispherical electron analyser and a reaction cell as shown in figure 2.10. The reaction cell allowed exposing the EP sample to a reactive gas atmosphere at reaction temperatures. When the gate between the spectrometer chamber and reaction cell was closed reactant gases could be introduced into the reaction cell at up to atmospheric pressure, whilst maintaining UHV in the spectrometer chamber. A controlled mixture of reactants can be leaked into the reaction cell using a set of electronic mass flow controllers and valves.

The EP sample holder was mounted on a manipulator that allowed translation between the reaction cell and the spectrometer chamber. The electrochemical cell was mounted on a sample holder made from a machinable ceramic and containing embedded electrically insulated nichrome filaments that allowed resistively heating of the sample. The temperature was monitored by a thermocouple connected to the working electrode and all electrical connections were made of gold. This set-up is illustrated in figure 2.11.

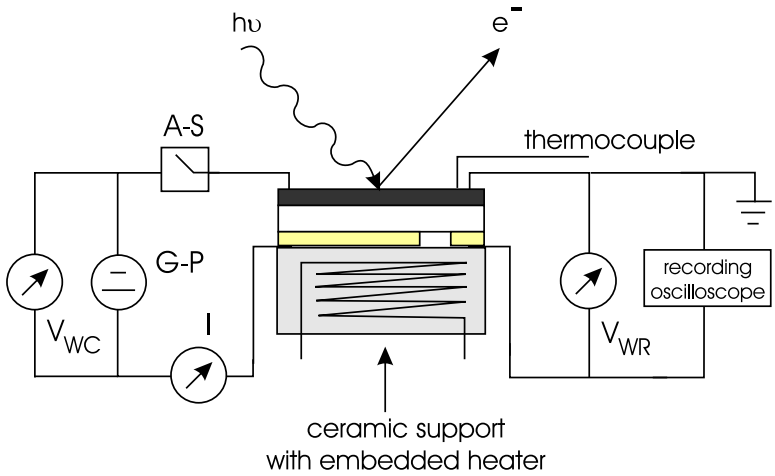

Figure 2.11: Sample holder and electrochemical cell (three electrode arrangement) used for the *in situ* XPS and UPS measurements and for the post-reaction XPS measurements.

The design of the sample holder and the transfer arm allowed heating of the sample and application of electrical potentials, in both the reaction cell and spectrometer chamber.

This set-up was employed to perform two distinct photoemission measurements: (i) the spillover of promoter species was studied as a function of catalyst potential with the EP sample at elevated temperature and with potentials applied and (ii) the species present on the working electrode (catalyst) surface were monitored as a function of gas composition and catalyst potential after exposing the EP sample to a reactive gas atmosphere at reaction temperatures in the reaction cell. The first set of experiments are *in situ* measurements performed under potentiostatic control to study the origin of the EP effect, whereas the second set are post-reaction experiments performed to shed some light regarding the different species present on the catalyst surface under reaction conditions.

2.3.1 *In situ* experiments

In these experiments, the EP sample is transfered from the reaction cell to the spectrometer chamber, where at elevated temperatures UP and XP spectra were acquired *in situ* as a function of catalyst potential under ultrahigh vacuum conditions. XP spectra were acquired at a constant pass energy of 20 eV using an un-monochromated Mg $K\alpha$ (1253.6 eV) source operated at 11 kV and 20 mA. Quoted binding energies are referred to the Au $4f_{7/2}$ emission at 84 eV from the Au wire that formed the electrical connection to the working electrode. Work function changes were determined by measuring the change in secondary electron cut-off in the UP spectrum relative to the Fermi edge. UP

spectra were recorded using He I radiation (21.21 eV) and a constant pass energy of 2 eV. During acquisition of the UP spectra the analyser was positioned at 7° with respect to the surface normal and the working electrode was biased −9.5 V with respect to ground. XP spectra were recorded with the working electrode grounded and the analyzer at 35° with respect to the sample normal.

Ohmic drop measurements

The goal of these *in situ* experiments is to relate the potential difference between the working and reference electrodes V_{WR} with the surface coverage of promoter species present on the working electrode surface. However, V_{WR} might contain a potential due to the resistance of the solid electrolyte, the so called ohmic drop [12], which should be subtracted from V_{WR} in order to determine its true value. The ohmic drop was determined using the current interruption technique [12]. This is based on the fact that upon a sudden interruption of the current, the ohmic drop decays almost instantaneously (within 10^{-6} s) whereas the potential of the working electrode decays with a much longer time constant. Current interruption was achieved by means of an analogue switch (ADG201HS) with a response time of 50 ns. A digital oscilloscope was use to record the ohmic drop. The results showed that the ohmic drop contribution to V_{WR} could be neglected under all conditions. That is, the V_{WR} values reported in this work are true values.

2.3.2 Post-reaction XPS

Post-reaction XP/AE spectra were obtained after exposing the catalyst film to the same conditions of temperature and reactant partial pressures as those used in the EP microreactor (see below). During exposure of the catalyst to the reaction mixture, the V_{WR} conditions were such that the catalyst film was either (i) unpromoted or (ii) Na-promoted. The spectra were acquired by the following procedure: (i) the sample temperature was lowered to 330 K in reaction gas and (ii) open circuit conditions were imposed when the sample temperature was below 350 K, i.e. when Na mobility was low. The object of this procedure was to 'freeze out' the surface conditions pertaining to the catalytically active surface. This procedure has been employed with success in the past [13].

2.3.3 Synchrotron experiments

Synchrotron experiments were performed at the ESCA microscopy beamline on the ELETTRA light source, Trieste, Italy. The photon beam, provided by a spherical grating

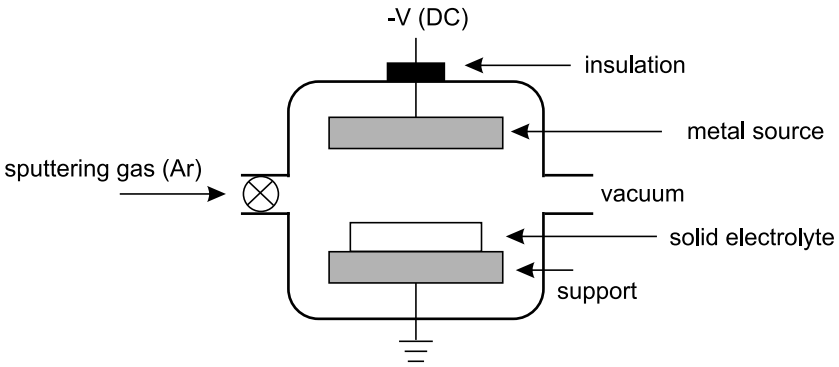

Figure 2.12: Schematic diagram showing the sputtering system.

monochromator, was demagnified in the scanning photoemission microscope (SPEM) to a spot of 0.15 μm diameter using a zone plate optical system. Photoelectrons were collected with an hemispherical analyzer mounted at 70° with respect to the sample normal and the incident photon beam. All experiments were performed with the working electrode grounded and at a photon energy of 490 eV. The SPEM operated in two modes: imaging and spectroscopic. Elemental mapping was performed by scanning the sample with respect to the focused beam with the analyzer tuned to the desired kinetic energy. In spectroscopic mode, core or valence spectra could be recorded from microspots on features selected from the elemental maps.

2.4 The EP sample

2.4.1 Sample preparation

The EP samples used were all made in the same basic configuration. A thin porous, pollycrystalline metallic film is deposited on one of the faces of a wafer of a Na β"alumina solid electrolyte by means of direct current (DC) sputtering in an Ar atmosphere. This film forms the catalytically active working electrode of the electrochemical cell. The opposite side of the wafer carries a gold counter electrode and a gold reference electrode, also deposited by DC sputtering. Thus, we have a solid electrolyte electrochemical cell with a three-electrode arrangement described in the previous chapter.

As mention above all the metallic films were deposited on the solid electrolyte using a DC sputtering deposition technique [14]. The objective of this deposition process is to transfer atoms from a metal source to the solid electrolyte where film formation and growth proceeds atomistically. The atoms are removed from a solid metal surface (source) through impact of gaseous ions (Ar^+).

Table 2.2: Different EP samples used.

EP Sample	WE	CE, RE	length (cm)×width (cm)×height (cm)
Rh1[a]	Rh	Au	$2 \times 2 \times 0.1$
Rh2[b]	Rh	Au	$0.3 \times 1 \times 0.1$
Cu1[c]	Cu	Au	$2 \times 2 \times 0.1$
Cu2[c]	Cu	Au	$2 \times 2 \times 0.1$
Cu3[d]	Cu	Au	$1 \times 1 \times 0.1$
Cu4[e]	Cu	Au	$1 \times 1 \times 0.1$
Ru1[f]	Ru	Au	$4.5 \times 1.5 \times 0.1$

[a] Used in the spectroscopic experiments discussed in chapters 3-6.
[b] Used in the reactor experiments discussed in chapters 4-6.
[c] Used in the spectroscopic experiments discussed in chapters 3 and 7.
[d] Used in the synchrotron experiments discussed in chapter 3.
[e] Used in the reactor experiments discussed in chapters 7.
[f] Used in the reactor experiments discussed in chapters 8.

Figure 2.12 shows a schematic diagram of the sputtering system employed to deposit the metallic electrodes onto the solid electrolyte. The metal source is a plate of the material to be deposited and it is connected to the negative terminal of a DC power supply. The solid electrolyte is placed on a grounded support facing the metal source. After evacuation of the chamber a constant pressure of argon is introduced. A negative potential is applied to the metal source. This results in the formation of argon cations which are accelerated toward the source, striking with its surface and ejecting metal atoms from it through momentum transfer. These atoms enter and pass through the region containing argon ions, atoms and electrons to eventually deposit on the solid electrolyte. Consequently, a metal film grows on the solid electrolyte.

Various parameters can be controlled in this process: negative potential applied (V), argon pressure (P_{Ar}), distance between the metal source and the solid electrolyte (d), and deposition time (t). The combination of these that produces useful EP samples was found by a systematic trial and error approach. The parameters typically employed were: $V = 900\,\mathrm{V}$, $P_{\mathrm{Ar}} = 2 \times 10^{-1}\,\mathrm{mbar}$, $d = 1\,\mathrm{cm}$ and $t = 120\,\mathrm{min}$. It should be noted that the temperature was not controlled during the deposition of the films. It is also worthwhile noting that prior deposition of the film, the metal source was extensively sputtered in order to avoid potential contamination from species present on the metal plate surface. Also before deposition, the first layers of the solid electrolyte were mechanically removed in order to eliminate potential contaminants that might be adsorbed on its surface.

Na β" alumina EP samples containing either Rh, Cu or Ru catalyst films (working

electrode, WE) and Au counter and reference electrodes (CE, RE) have been used in this work. Rh, Au and Cu were all deposited using DC sputtering in Ar. Ru was deposited by thermal decomposition of a solution of $Ru_3(CO)_{12}$ in acetone at 573 K in a nitrogen atmosphere.

The geometrical dimensions of the EP samples changed according to the activity of the catalyst film. This is, the lower the catalyst film activity the greater the geometrical area of the sample (and consequently the catalyst surface area) needed to be in order to obtain measurable reaction rates. The Rh, Cu and Ru EP samples employed have therefore distinct dimensions. Table 2.2 shows a list of all the samples used.

The Na β"alumina used was donated by Beta Research and Development. Rh, Cu and Au metal films were deposited from 99.99% purity metal plates provided by Johnson Matthey. The $Ru_3(CO)_{12}$ complex was provided by Professor Brian F. G. Johnson.

2.4.2 Sample characterisation

The EP samples were characterised by XRD, XPS and surface area measurements. XRD data were obtained on a Philips PW1877 automated powder diffractometer, using Cu K_α source ($\lambda = 1.54056\,\text{Å}$). All spectra were taken over a range $20^\circ < 2\vartheta < 70^\circ$ and referenced to the JCPDS database. Figure 2.13 shows typical XRD pattern from (i) the bare Na β" alumina wafer, (ii) the metal catalyst film deposited on one face and (iii) the gold film deposited on the other face. The rhodium, gold, copper and ruthenium patterns show peaks characteristic of the relevant metal (triangles) and additional peaks due to the underlying β" alumina (circles).

The bottom spectra in figures 2.14a and 2.14b correspond to the Cu 2p and C 1s XP spectra of the Cu1 EP sample immediately after preparation. The binding energies indicate that the film consisted of metallic copper (Cu $2p_{3/2}$ at 932.6 eV) and that the only observable impurity was elemental carbon (C 1s at 284 eV). In order to remove the carbon the sample was treated with oxygen in the reaction cell ($P_{O_2} = 0.2\,\text{mbar}$, $T = 350^\circ\text{C}$ and $V_{WR} = 1000\,\text{mV}$ for 15 minutes) follow by hydrogen ($P_{H_2} = 0.2\,\text{mbar}$, $T = 350^\circ\text{C}$ and $V_{WR} = 1000\,\text{mV}$ for 30 minutes). The spectra resulting after a successive treatment are shown in figures 2.14a and 2.14b. Removing the carbon from the copper film resulted in a 57% increase of the Cu signal and a 88% decrease in the carbon signal. The film remained metallic copper after the oxidation-reduction cycle.

Figures 2.14c and 2.14d show the Rh 3d and C 1s XP spectra of the Rh1 EP sample after preparation. The binding energies indicate that the film consisted of metallic rhodium (Rh $3d_{5/2}$ at 307.3 eV) and that the only observable impurity was elemental carbon (C 1s at 284 eV). Cleaning the rhodium film with the treatment described above

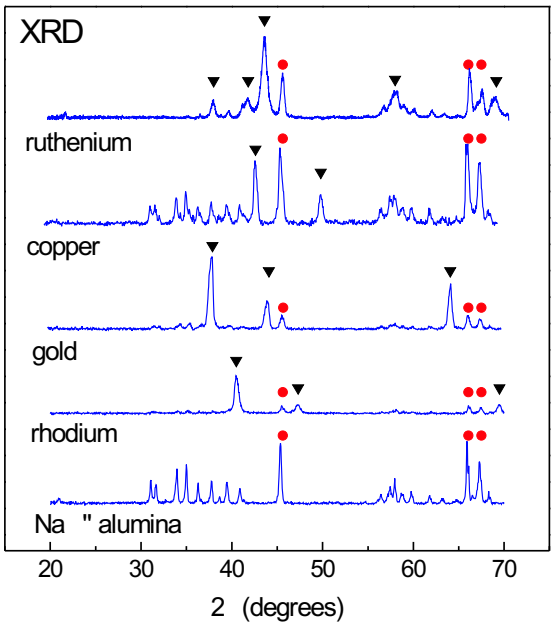

Figure 2.13: XRD patterns from the bare Na β" alumina, the metal catalyst film subsequently deposited on one face and the gold film deposited on the other face.

resulted in a 37% increase of the Rh signal and a 81% decrease in the carbon signal, with no detectable oxidation of the rhodium surface.

The active metal area of the rhodium catalysts was determined using two different methods: (i) the CO methanation technique developed by Komai *et al.* [15] and (ii) the electrochemical technique developed by Ladas *et al.* [16]. Before measuring the surface area the sample was calcined in oxygen and reduced with hydrogen at 573 K in order to generate a clean metal surface.

The first method is based on the conversion of chemisorbed CO to methane on metal sites. Briefly, the method involves: (i) adsorbing CO at room temperature on the metal surface, (ii) reacting the adsorbed CO molecules with H_2 to form methane and (iii) detecting the number of CH_4 molecules produced. On the basis of the number of methane molecules detected which gives the amount of adsorbed CO and assuming a one-to-one CO to surface Rh ratio the catalyst surface area can be estimated. Table 2.3 shows the estimated catalyst surface areas of the different Rh samples used.

The second technique involves measuring galvanostatic transients. A fixed negative current was applied between the working and counter electrodes (i.e. sodium pumping to the catalyst) while measuring the resulting changes in catalyst potential as a function

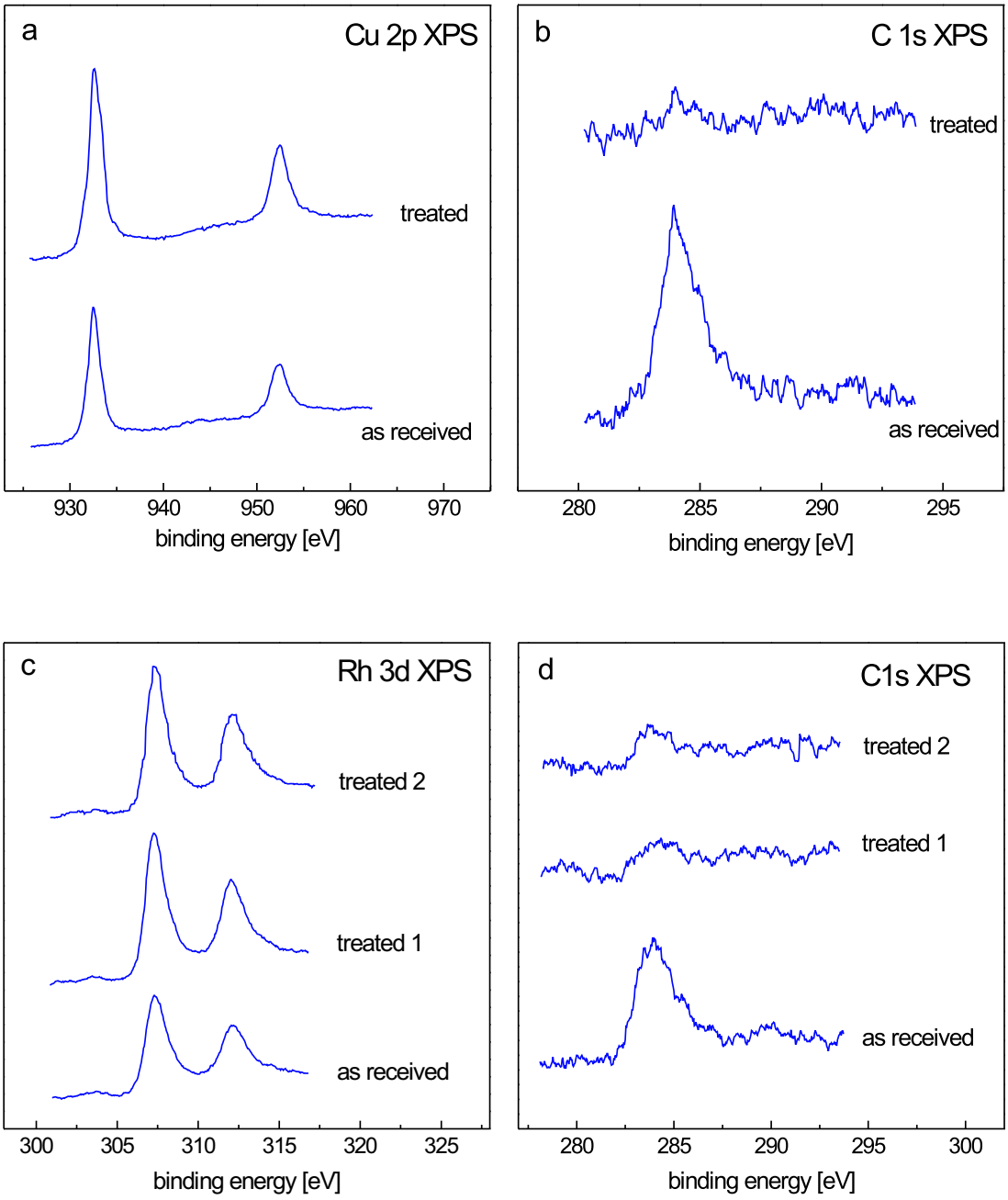

Figure 2.14: XP spectra showing the effect of pretreatments on the amount of carbon on copper and rhodium catalysts. (a) Cu 2p spectra, (b) C 1s spectra, (c) Rh 3d spectra and (d) C1s spectra.

Table 2.3: Surface area measurements of the different rhodium EP samples used.

Rhodium EP Sample	Geometrical area (cm^2)	Surface area (μmol Rh)
Rh1	4	1.5 ($\sim$560 cm^2)†
Rh2	0.3	0.1 ($\sim$37.6 cm^2)†
Rh3	1	0.32 ($\sim$120.5 cm^2)†

† Estimated using a surface metal atom density of 1.6×10^{15} atom cm^{-2} which corresponds to the {111} plane of Rh.

of time. It can be shown using Faraday's Law and the Helmholz equation [16] that:

$$A = \frac{P_\circ I}{\varepsilon_\circ \dfrac{\mathrm{d}\phi}{\mathrm{d}t}} \tag{2.15}$$

Where A is the catalyst surface area (m^2), $P_\circ$ is the initial dipole moment of Na on Rh (1.7×10^{-29} C m [17]), I (C s^{-1}) is the current applied between the working and counter electrodes, $\varepsilon_\circ = 8.85 \times 10^{-12}$ $C^2J^{-1}m^{-1}$. $\mathrm{d}\phi/\mathrm{d}t$ is the initial slope of the work function *versus* time curve. As we can not determine $\mathrm{d}\phi/\mathrm{d}t$ experimentally, we measured $e\mathrm{d}V_{\mathrm{WR}}/\mathrm{d}t$ and used the relationship between $e\mathrm{d}V_{\mathrm{WR}}$ and $\mathrm{d}\phi$ obtained experimentally (see chapter 3 for discussion). Inserting the measured values in equation (2.15) yields a Rh1 surface area of $\sim$552 cm^2. This is equivalent to 1.4 μmol Rh, in good agreement with the value measured by CO methanation (1.5 μmol Rh).

The surface area of the copper sample used in the microreactor experiments (Cu4) was estimated measuring galvanostatic transients as described above. This yields a surface area of $\sim$68 cm^2.

EP samples characterisation indicate that the catalyst is a rough metallic film. Its surface area is typically two orders of magnitude greater than its geometrical area. Furthermore, the only observable impurity present on its surface is elemental carbon and it can be successfully removed by oxidation-reduction cycles.

2.5 The EP Microreactor

The microreactor used is an atmospheric pressure well-mixed flow reactor. Figure 2.15 shows a diagram of the microreactor. The sample was mounted in a quartz vessel, which was suspended in a small tube furnace. A flow of reactant gases in hellium carrier was passed into the quartz vessel and hence over the sample, the flows of the gases being accurately controlled with electronic mass flow controllers (Brooks 5850TR). Quantitative

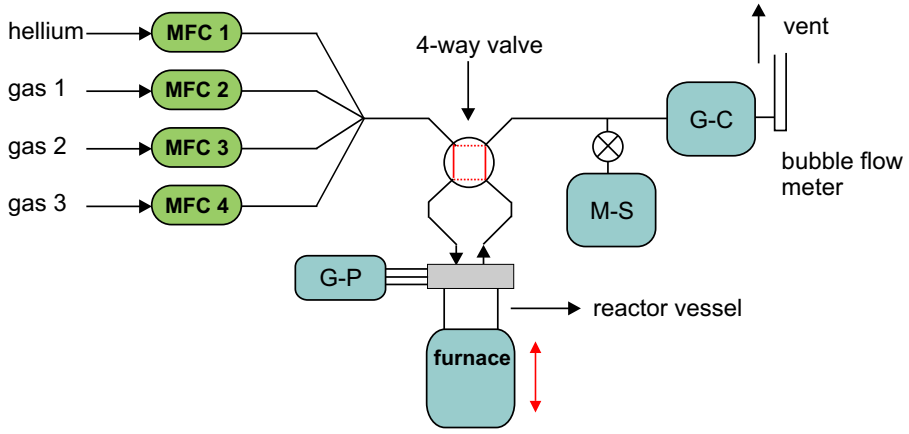

Figure 2.15: Schematic diagram of the microreactor.

measurement of reactants and products was achieved using on-line gas chromatography (Shimadzu GC-14B) and on-line mass spectrometry (Balzers QMG 064) after performing calibrations using gases of known concentration. The GC columns used were subject to appropriate thermal conditioning prior use and suitable temperature and valve switching programmes enabled the separation of all (product and reactant) gases. A four-way valve was used to either direct the gas flow through the reactor vessel to measure reaction products, or to bypass the reactor to permit measurement of the inlet concentrations and hence calculate reactant conversions. The mass spectrometer was mounted in a small stainless steel vacuum system pumped by a small turbomolecular/rotary pump combination, base pressure $< 10^{-9}$ Torr. A Negretti needle valve was used to leak flow from the gas line into the vacuum to a total pressure of 10^{-6} Torr (when flowing pure He) as measured by a Bayard Alpert ionisation gauge.

The reactor vessel is shown schematically in figure 2.16 and is a quartz tube, closed at one end, diameter 2 cm and volume 50 cm^3. It is clampled and sealed at the open end by a stainless steel head and viton O-rings. The head contains channels for circulating cooling water, feedthroughs and two 1/8" stainless steel tubes for gas flow. Feedthroughs allowed the electrodes of the sample to be connected to the galvanostat-potentiostat (Ionic Systems) via catalytically inert gold wires, and for use of a thermocouple to monitor the temperature of the sample.

Two distinct set of experiments have been performed using the EP microreactor. The dependence of steady state reaction rates has been studied as a function of: (i) catalyst potential V_{WR} at constant reactants partial pressure and temperature, and (ii) reactants partial pressure at constant catalyst potential and temperature. In the first set of experiments, the gas composition fed to the reactor is fixed, whereas in the second set

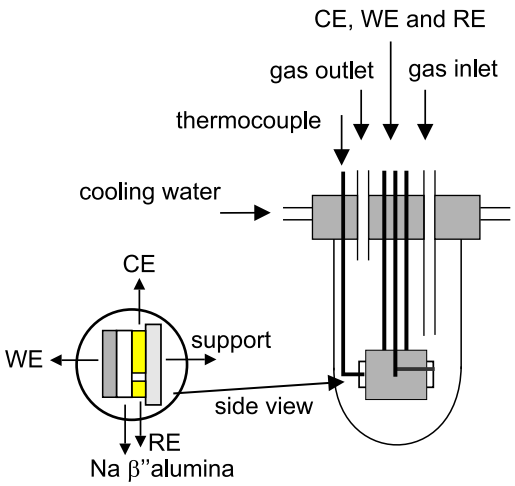

Figure 2.16: Scheme of the reactor vessel.

it was adjusted to give constant values of the required reactants partial pressure in the outlet of the reactor. The well-mixed behaviour of the reactor meaning that these outlet pressures were the values throughout the reactor vessel. All experiments were carried out at atmospheric pressure and constant flow rate. Reactant conversion was restricted to $< 20\%$ in order to avoid mass transfer limitations. Control experiments were carried out in which the total flow was varied by a given factor in order to verify that the observed changes in activity were indeed due to changes in actual surface reaction rates, unaffected by mass transfer limitations.

Bibliography

[1] G. Ertl and J. Küppers, *Low energy electrons and surface chemistry*, VCH, Weinheim, 1985.

[2] M. P. Seah and W. A. Dench, Quantitative electron spectroscopy of surfaces: a standard data base of electron inelastic mean free paths in solids, Surface and Interface Analysis **1**, 2–11 (1979).

[3] M. Prutton, *Introduction to surface physics*, Oxford University Press, Oxford, second edition, 1994.

[4] M. W. Roberts, Photoelectron spsectroscopy and surface chemistry, in *Advances in catalysis*, edited by D. D. Eley, H. Pines, and P. B. Weisz, volume 29, pages 55–95, Academic Press, New York, 1980.

[5] D. P. Woddruff and T. A. Delchar, *Modern techniques of surface science*, Cambridge University Press, Cambridge, second edition, 1994.

[6] D. Briggs and M. P. Seah, editors, *Practical surface analysis*, volume 1 Auger and X-ray photoelectron spectroscopy, Wiley, New York, second edition, 1990.

[7] A. F. Carley and M. W. Roberts, An X-ray photoelectron spectroscopic study of the interaction of oxygen and nitric oxide with aluminium, Proceedings of the Royal Society London A **363**, 403–424 (1978).

[8] D. R. Penn, Quantitative chemical analysis by ESCA, Journal of Electron Spectroscopy and Related Phenomena **9**, 29–40 (1976).

[9] J. J. Yeh and I. Lindau, Atomic subshell photoionisation cross sections and asymmetry parameters: $1 \leq Z \leq 103$, Atomic Data and Nuclear Data Tables **32**, 1–155 (1985).

[10] M. Kiskinova, M. Marsi, E. di Fabrizio, and M. Gentili, Synchrotron radiation scanning photoemission microscopy: instrumentation and application in surface science, Surface Review and Letters **6**, 265–286 (1999).

[11] H. B. Michaelson, The work function of the elements and its peridiocity, Journal of Applied Physics **48**, 4729–4733 (1977).

[12] I. S. Metcalfe, Solid electrolyte electrochemical cells for catalyst sensing, in *Catalysis*, volume 13, pages 1–36, The royal society of chemistry, 1997.

[13] N. C. Filkin, *Electrochemical promotion of environmentally important catalytic reactions*, PhD thesis, University of Cambridge, Cambridge, 1997.

[14] M. Ohring, *The materials science of thin films*, Academic Press, New York, 1992.

[15] S. Komai, T. Hattori, and Y. Murakami, CO-H_2 tritation for the determination of super small metal surface area, Journal of Catalysis **120**, 370–376 (1989).

[16] S. Ladas, S. Bebelis, and C. G. Vayenas, Work function measurements on catalyst films subject to *in situ* electrochemical promotion, Surface Science **251/252**, 1062–1068 (1991).

[17] C. M. Mate, C. T. Kao, and G. A. Somorjai, Carbon monoxide induced ordering of adsorbates on the Rh(111) crystal surface: importance of surface dipole moments, Surface Science **206**, 145–168 (1988).

CHAPTER 3

The origin of electrochemical promotion

3.1 Introduction

The catalytic activity and selectivity of metal catalysts is often deliberately altered by addition of so-called promoters, frequently alkali metals [1]. Understanding promoter action and the associated reaction mechanisms by application of surface science methods to model systems is an important goal in current research [2, 3]. Electrochemical Promotion (EP) provides *in situ* control of promoter coverage at the surface of working metal catalysts under reaction conditions. It may therefore be used to address these key issues in a novel way.

EP involves electrochemical pumping of promoter species (e. g. Na) to or from a solid electrolyte (Na β" alumina in the present case) from or to a porous film metal catalyst with which it is in contact. By varying the catalyst potential with respect to a reference electrode (potentiostatic control) one may reversibly alter the alkali coverage and consequently the catalytic behaviour of the metal surface. Thus we have a means for the systematic investigation of certain aspects of promoter action in a manner that was previously not possible. We have exploited this unique aspect of EP to elucidate the mechanism of alkali promotion in a variety of important metal-catalysed reactions including NO reduction (Chapters 4-7) and Fischer-Tropsch synthesis (Chapter 8). However, before discussing these results, it is a necessary prerequisite to establish the nature of the phenomena underlying the EP effect.

Although electrochemical pumping of promoter species has been shown previously as discussed in the first chapter, there has been no clear systematic study of the reversible

dependence of promoter coverage with catalyst potential. This reversible electrochemical control of promoter species is the key assumption made in interpreting the EP reactor data. Addressing this important point, to understand the phenomenon in as much detail as possible, is the principal aim of the present chapter.

X-ray and ultraviolet photoelectron spectroscopies (XPS, UPS) have been used to study the phenomena that underlie the EP effect. Specifically, we have investigated the electrochemical pumping of Na at the Na β" alumina/metal (M) interface where the electrode reaction is:

$$Na^{+}_{(\beta\text{"alumina})} + e^{-}_{(\text{metal})} \quad \rightleftarrows \quad Na_{(\text{metal})} \tag{3.1}$$

and M is either Rhodium or Copper. These systems were chosen to demonstrate the nature of the EP effect because they were used to study the effect of sodium on reactions catalysed by either Rh or Cu as discussed in the following chapters.

3.2 Experimental methods

The procedures used for sample preparation and characterisation have been described in chapter 2. UPS and XPS measurements were performed under UHV conditions (base pressure $< 10^{-10}$ Torr) in a VG ADES 400 UHV spectrometer system. Synchrotron experiments were performed at the ESCA microscopy beamline on the ELETTRA light source, Trieste, Italy. Details regarding sample mounting, manipulation and data acquisition are also given in chapter 2. All XP spectra are recorded with the working electrode grounded.

Sample Rh1 was used to carried out the spectroscopic experiments involving Rh EP cells. In contrast, three different Cu samples have been employed when studying Cu EP cells. XPS was carried out using Cu1, work function changes using Cu2 and synchrotron experiments using Cu3.

The temperature chosen for these spectroscopic experiments was the same as that used in the metal-catalysed reactions under EP conditions (see chapters 4 and 7). Note that the experiments span a range of V_{WR} values. Larger excursions were not possible because they would necessitate application of large values V_{WC} - the voltage applied between the metal working electrode and the Au counter electrode. These leads to electrolytic decomposition of the solid electrolyte accompanied by evolution of oxygen gas, detected mass spectrometrically.

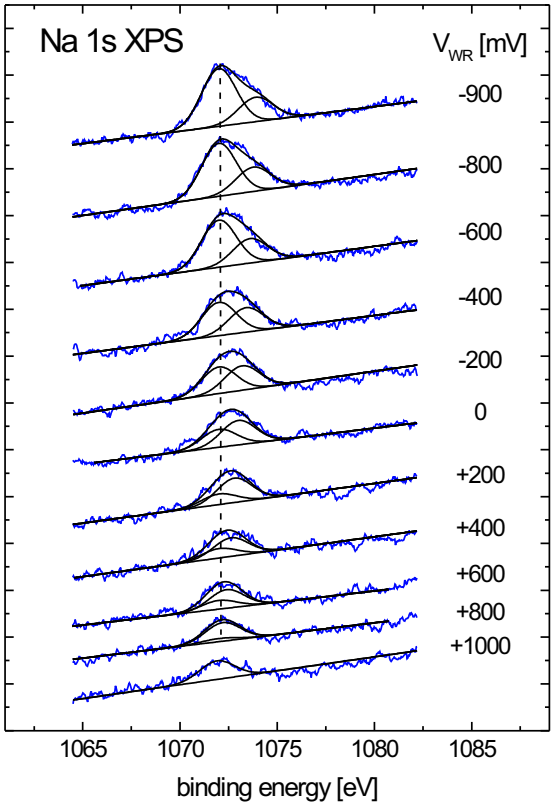

Figure 3.1: Na 1s XP spectra showing the effect of catalyst potential on sodium coverage of the Rh film under UHV conditions at 580 K.

3.3 Rh EP sample

We start describing the spectroscopic consequences of Na pumping to the Rhodium surface of a Rh | Na β" alumina | Au EP sample.

3.3.1 XP spectroscopy

Figure 3.1 shows Na 1s XP spectra obtained at 580 K as a function of catalyst potential V_{WR} under ultra high vacuum conditions. The +1000 mV spectrum corresponds to the electrochemically-cleaned sample; increasingly negative values of V_{WR} correspond to increasing amounts of electro-pumped Na on the catalyst surface. These observations confirm that EP works by supplying alkali promoter species to the catalyst surface. The spectral behaviour was reversible and reproducible as a function of V_{WR}, consistent with the reversible and reproducible catalytic response under reaction conditions at atmospheric pressure (see chapter 4 for example). Note the residual Na 1s emission from the electrochemically-cleaned sample. In order to understand this, recall that the rhodium film is both thin and porous. The Na 1s emission therefore comprises two

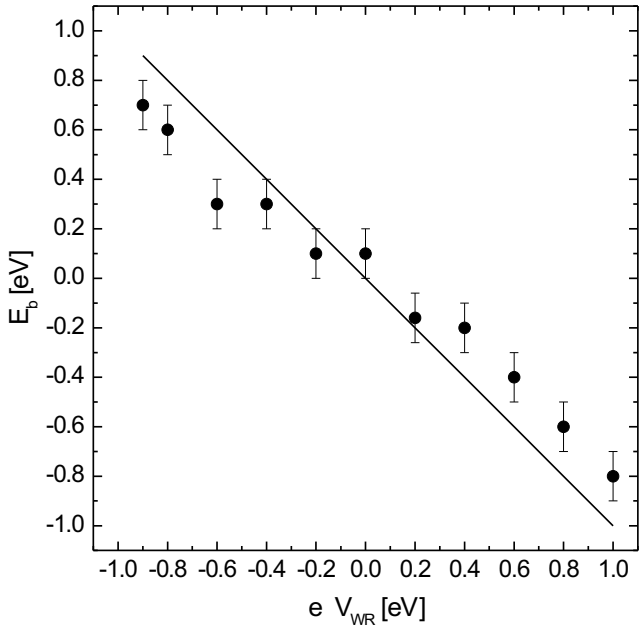

Figure 3.2: Binding energy shift of the Na 1s component due to Na in the solid electrolyte as a function of the change in V_{WR}.

components, one due to the Na present on the surface of the Rh film, the other due to Na present in the underlying β"alumina electrolyte which was visible to XPS through the cracks and pores in the metal film. The component due to the Na on the Rh catalyst exhibits invariant binding energy E_{b} (Rh film is grounded) and increases in intensity with decreasing V_{WR}. In contrast with this, the other component exhibits constant intensity and a systematic shift in apparent binding energy ΔE_{b}. This shift is numerically equal to the change in V_{WR}, as shown in Figure 3.2 where the apparent binding energy shift of the Na component ascribed to the Na β"alumina has been plotted against ΔV_{WR}. These results confirm that this component of the Na 1s emission arises from the solid electrolyte whose electrostatic potential differs from that of the Rh film by the amount ΔV_{WR}.

The filled circles in figure 3.3 show the integrated intensity of the Na 1s emission from the component associated with the Rh surface *versus* V_{WR}. For $V_{\mathrm{WR}} < 1000\,\mathrm{mV}$, decreasing the catalyst potential causes a linear increase of the sodium coverage with potential. It is significant that over this same regime, the work function also varies linearly with V_{WR} (figure 3.3 and see below). A value for the sodium coverage ϑ_{Na} may be estimated from the integrated Na 1s intensity of the component associated with the Rh surface by making use of the relationship derived by Carley and Roberts [4]. In this manner, the highest Na coverage achieved ($V_{\mathrm{WR}} = -900\,\mathrm{mV}$, figure 3.1) corresponds to

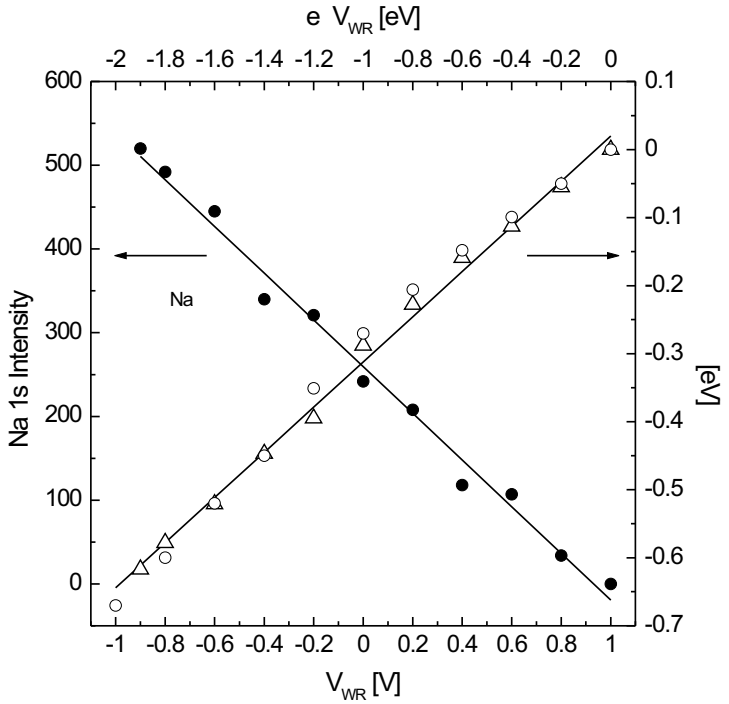

Figure 3.3: Integrated Na 1s XP intensity due to sodium on the rhodium surface and associated work function change of the rhodium film as a function of V_{WR}.

$2.84 \times 10^{15}\,\mathrm{atom/cm^2}$, equivalent to ~ 1.7 monolayers (ML). Where 1 ML is defined as one sodium adatom per substrate atom. Such a coverage of sodium should attenuate the Rh 3d XPS signal by $\sim 50\%$ relative to that from the sodium free surface; however no such attenuation was observed. The reason for this apparent discrepancy is that the equation used to estimate ϑ_{Na} is valid for an ideally flat substrate, whereas our samples are very rough. Thus it gives an overestimate of the actual sodium coverage, because the true metal surface area is much greater than the geometrical area of the Rh film. We may take this roughness factor into account in order to produce a more realistic estimate of the sodium coverage by applying a simple correction factor. This factor is just the geometrical surface area divided by the true metal area. The resulting calculated sodium coverage at $V_{\mathrm{WR}} = -900\,\mathrm{mV}$ is then 0.013 ML, in good agreement with the observed lack of attenuation of the Rh XPS intensity. It is also in good accord with the linear dependence of work function on sodium coverage, as discussed below.

3.3.2 Work function changes

Work function data provide complementary information about the surface processes occurring during the spillover of electro-pumped Na. In figure 3.3, the open circles show

the work function change $\Delta\phi$ when the catalyst potential is systematically decreased from +1000 mV to −1000 mV at 580 K; the open triangles show corresponding data obtained when the process was reversed, i. e. when the catalyst potential was increased from −1000 mV to +1000 mV. Thus the value of $\Delta\phi$ corresponding to a particular value of V_{WR} is independent of sample history. This indicates that (i) the spillover process is reversible and (ii) a given V_{WR} corresponds to a given sodium coverage.

It is apparent from figure 3.3 that $\Delta\phi$ varies linearly with both catalyst potential and ϑ_{Na}. This is a clear indication that we are in the low alkali coverage regime, where such behaviour is to be expected [5]. Specifically, ϑ_{Na} must be less than ~ 0.1 ML [6]. The maximum sodium coverage achieved in the experiments whose results are illustrated in figure 3.3 caused a work function decrease of −0.65 eV. Comparison with single crystal data obtained for the Rh(111)/Na system [6] indicates that in the present case $V_{WR} = -900$ mV corresponds to $\vartheta_{Na} \sim 0.025$ ML, i. e. about twice the value based on XPS intensity analysis. This is a satisfactory level of agreement. For present purposes, the key point is that two independent methods indicate that our experimental data span the range $0 < \vartheta_{Na} <\sim 0.02$.

3.4 Cu EP sample

We now describe the spectroscopic consequences of Na pumping to the Copper surface of a Cu | Na β" alumina | Au EP sample.

3.4.1 XP spectroscopy

Figure 3.4 shows Na 1s XP spectra obtained at 623 K as a function of catalyst potential V_{WR} under UHV conditions. The +700 mV spectrum corresponds to the electrochemically cleaned sample; decreasing V_{WR} from +700 mV to −600 mV results in an increase in the amount of Na present on the catalyst surface. It should be noted that the spectrum at $V_{WR} = +400$ mV was acquired after the one at $V_{WR} = -600$ mV. Thus, reversing the pumping process, i. e. increasing V_{WR} from −600 mV to +400 mV restores the amount of Na present on the catalyst surface. This reversibility is in line with the reversible and reproducible catalytic response observed under reaction conditions at atmospheric pressure (see chapter 7). As in the previous case, the Na 1s emission envelope comprises two components, one due to the Na present on the surface of the Cu film, the other due to Na in the β"alumina electrolyte which is visible through the cracks and pores in the metal film. The component due to Na on the Cu catalyst exhibits invariant binding energy (Cu film is grounded) and increases in intensity with decreasing V_{WR}, as one

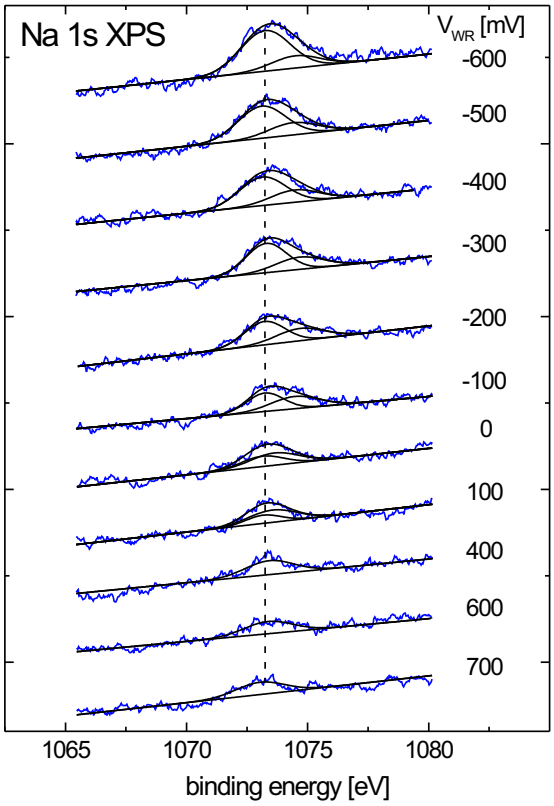

Figure 3.4: Na 1s XP spectra showing the effect of catalyst potential on sodium coverage of the Cu film under UHV conditions at 623 K.

would expect. The other component exhibits constant intensity and a systematic shift in apparent binding energy ΔE_b. This shift is numerically equal to the change in V_WR (i. e. the change in catalyst potential), nicely confirming that the corresponding Na 1s emission arises from the solid electrolyte whose electrostatic potential differs from that of the Cu film by the amount ΔV_WR. The numerical correspondence between ΔV_WR and ΔE_b is made even more apparent by the results presented in figure 3.5. The apparent binding energy shift of the Na component ascribed to the Na β" alumina has been plotted against ΔV_WR. These results confirm beyond doubt the interpretation offered above.

Figure 3.6 shows the integrated intensity of the Na 1s emission from the component associated with the Cu surface against V_WR. Two points are very apparent. Firstly, there is a region ($\sim$ +700 to $\sim$ +300 mV) in which decreasing the catalyst potential does not pump XPS-detectable Na on the Cu surface. Secondly, for $V_\mathrm{WR} <\sim$ +300 mV, decreasing the catalyst potential causes a linear increase of the Na 1s XPS area. The first observation implies that at $\sim$ +300 mV the Cu surface has been fully depleted of Na by electro-pumping. The second observation is equally interesting: once detectable

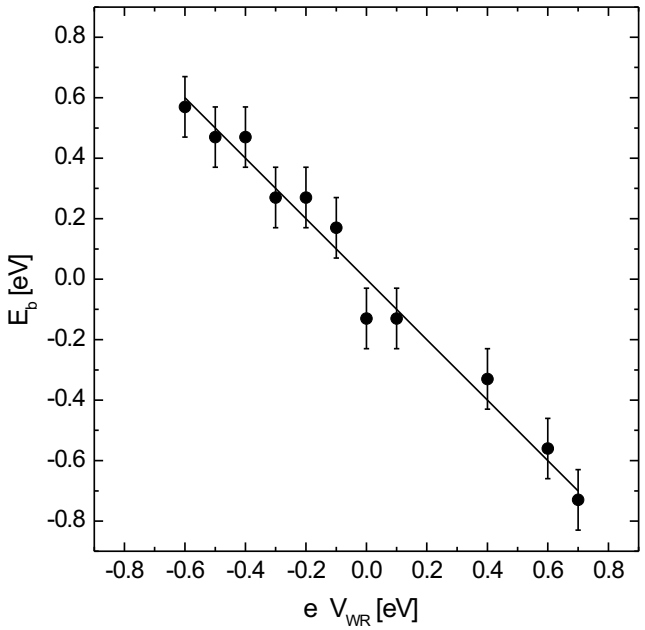

Figure 3.5: Binding energy shift of the Na 1s component due to Na in the solid electrolyte as a function of the change in V_{WR}.

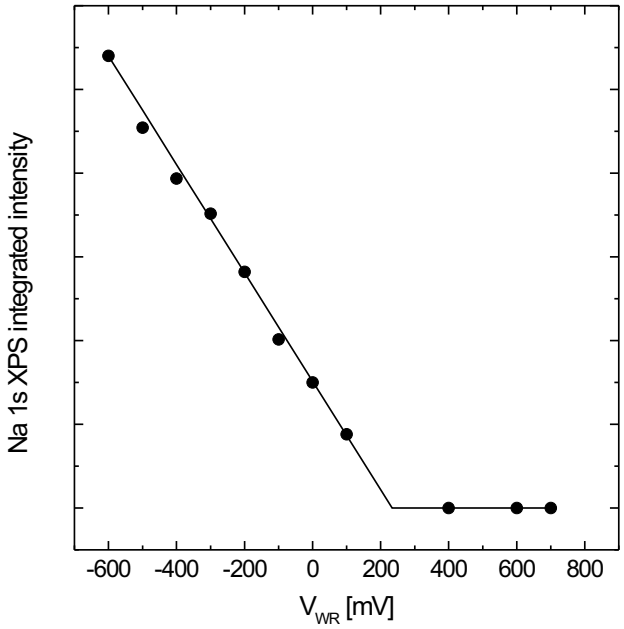

Figure 3.6: Integrated Na 1s XP intensity due to sodium on the copper surface as a function of V_{WR}.

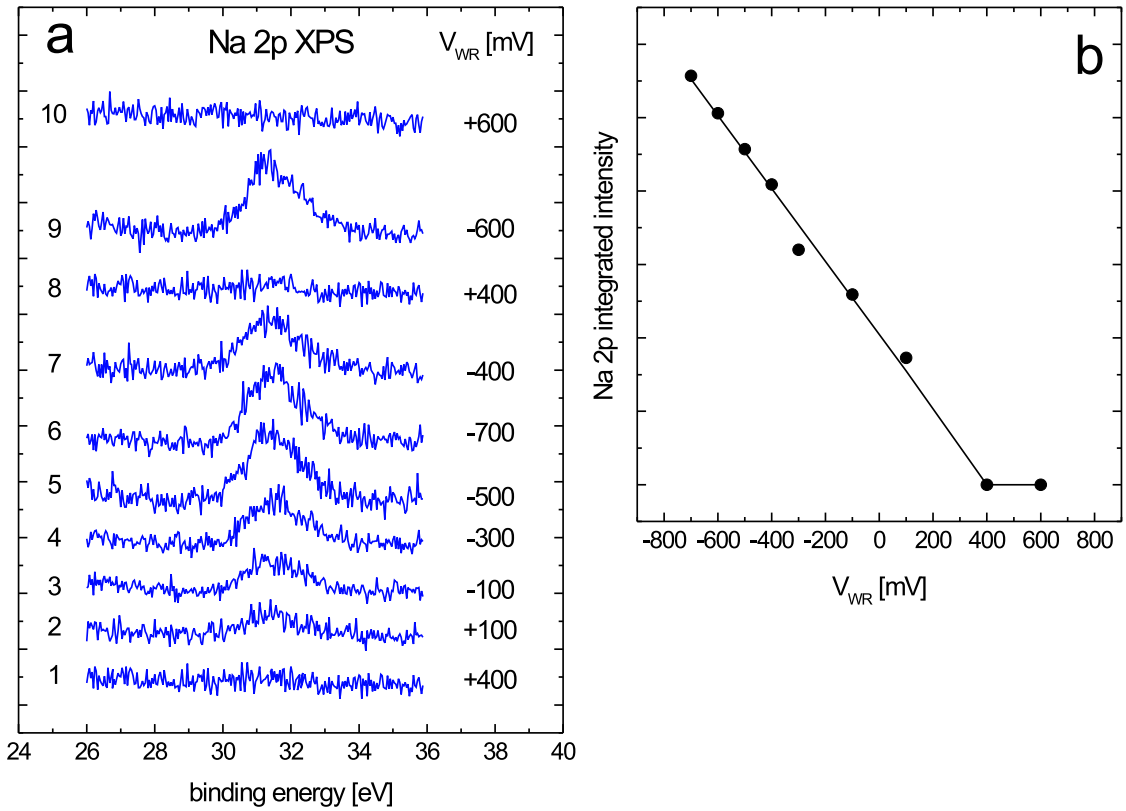

Figure 3.7: (a) Synchrotron core level spectroscopy: grazing electron exit Na 2p spectra as a function of V_{WR}. (b) Integrated Na 2p intensity from sodium on copper *versus* V_{WR}.

Na is present on the Cu surface, the Na coverage changes linearly with V_{WR}. This is in excellent accord with the synchrotron data presented below.

Figure 3.7a shows synchrotron Na 2p XP spectra as a function of V_{WR} at T = 523 K. In this case it is evident that the component due to the Na present on the Na β" alumina is not detected. Only a single component is visible in the Na 2p emission. This exhibits invariant BE and grows in intensity as the catalyst potential is decreased (spectra 1–6). On the basis of the preceding arguments, we assign it to Na on the Cu surface. The reversibility of Na transport is made clear in figure 3.7a. Spectra were recorded in the time sequence 1–10 during which the Na coverage increased progressively as V_{WR} was altered from +400 mV (spectrum 1) to −700 mV (spectrum 6). Switching to −400 mV (spectrum 7) decreased the amount of Na to a coverage intermediate between spectra 4 (−300 mV) and 5 (−500 mV). A further increase to +400 mV (spectrum 8) immediately cleaned the surface of Na; switching to −600 mV (spectrum 9) gave a coverage intermediate between spectra 5 and 6; switching to +600 mV again generated a clean surface (spectrum 10). That is, for a given value of V_{WR}, there was a specific

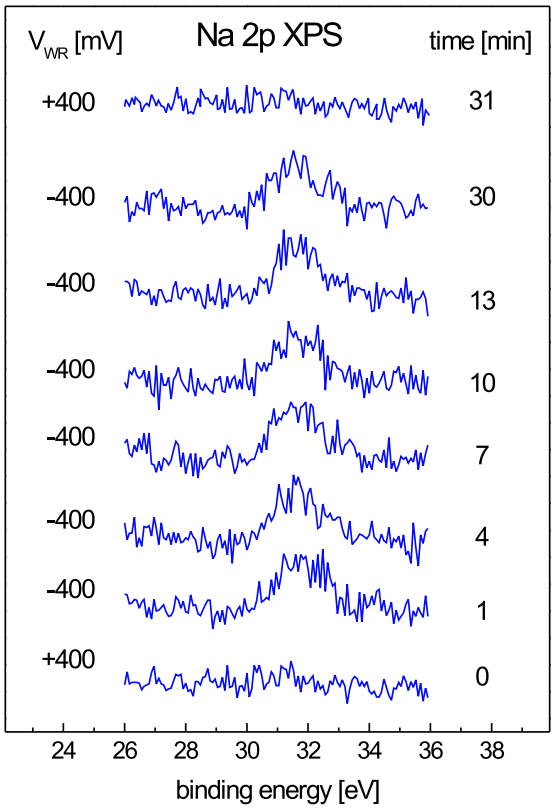

Figure 3.8: Synchrotron core level spectroscopy: grazing electron exit Na 2p spectra as a function of time for different values of V_{WR}.

amount of Na present on the Cu surface.

Unlike the laboratory XP spectra, the synchrotron measurement strongly discriminates against Na 2p photoelectrons from the underlying solid electrolyte. This is due to two factors, one relating to the incident photons, the other to the emitted electrons, as follows. (i) The X-ray beam diameter was only 0.15 μm. Since the beam was adjusted so as to impinge on top of a Cu particle, the underlying electrolyte is effectively shielded from incident photons. (ii) The photoelectrons were detected at grazing exit angle (70° with respect to the sample normal) which enhances the surface sensitivity of the measurement.

Figure 3.7b shows the dependence of the integrated raw Na 2p emission intensity on catalyst potential. The behaviour replicates that of the Na 1s intensity extracted for the invariant component in the spectra obtained with a laboratory source (figure 3.6). Decreasing V_{WR} from ~ 600 mV to ~ 400 mV caused no increase in the Na 2p intensity. Further decrease in V_{WR} caused a linear increase in the Na coverage. This threshold behaviour is also apparent in the $\Delta\phi$ data (see later) and in the catalytic response of the system (see chapter 7). It is discussed below.

In order to check whether or not the measured Na coverages corresponded to true steady-state values, we attempted to study the time dependence of the spillover process. Figure 3.8 shows a time sequence of Na 2p XP spectra obtained as V_{WR} was switched from +400 mV (electrochemically cleaned surface) to −400 mV (Na pumped to Cu surface) and back again to +400 mV (Na pumped away from Cu). The acquisition time per spectrum was ~ 1 minute. It is apparent that the Na spillover and reverse spillover processes took place in less than one minute, after which the Na coverage remained constant with time. Therefore, we were not able to study the time dependence of the spillover process.

The spectroscopic data may be used to estimate Na surface coverages: the data presented in figure 3.6 yield a maximum Na concentration of 4.1×10^{14} atom/cm^2 for $V_{\mathrm{WR}} = -600$ mV and the data presented in Figure 3.7b yield a maximum Na concentration of 3.4×10^{14} atom/cm^2 at $V_{\mathrm{WR}} = -700$ mV. Thus the agreement between the calculated maximum sodium concentrations for two independent sets of data is good. If we assume a density of substrate atoms of 1.8×10^{15} atom/cm^2 (corresponding to Cu(111)) then the data in Figures 3.6 and 3.7b correspond to maximum sodium coverages of 0.22 and 0.18 monolayers, respectively. Note however that the estimation is valid for an ideally flat substrate. Our samples are rough. Therefore, we are overestimating the sodium coverage, because the true metal surface area is greater than the geometrical area covered by Cu. A more precise estimate of the maximum achievable sodium coverage is provided by work function measurements, as discussed below.

3.4.2 Elemental mapping by SPEM

The scanning photoemission microscope (SPEM) operated in two modes: imaging and spectroscopic. The synchrotron results discussed above were obtained in spectroscopic mode, i. e. by recording core level spectra from microspots on the sample. Elemental mapping was performed by scanning the sample with respect to the focused beam with the analyzer tuned to the desired kinetic energy.

By tuning the analyzer to the Cu 3d or Na 2p photoelectrons and scanning the sample, we obtained intensity maps which reflect the distribution of the elements at the surface with spatial resolution of 0.15 μm, as a function of V_{WR} with the sample held at 523 K. Since we are dealing with rough surfaces the raw photoelectron maps are a mixture of chemical information (spatial variation in the chemical composition) and topographical effects [7, 8]. The topographical effects arise from the facts that the emitted photoelectrons are detected over a solid angle centered along a certain direction and that the surface is not perfectly flat. Consequently, the angle between the surface

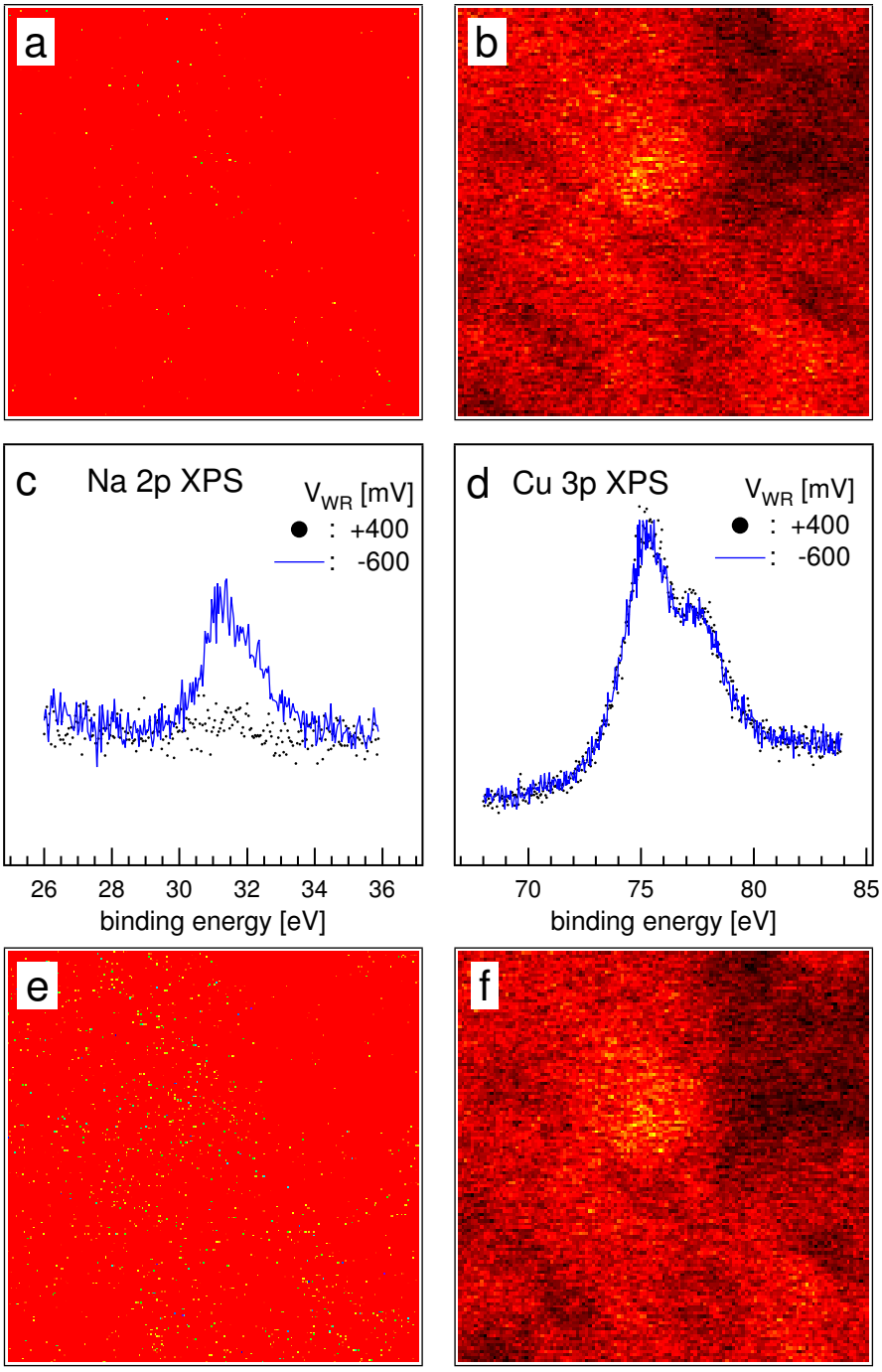

Figure 3.9: $25 \times 25\,\mu m^2$ photoelectron intensity maps. (a) Na $2p_{3/2}$ at $V_{WR} = +400\,mV$, (b) Cu $3d_{5/2}$ at $V_{WR} = +400\,mV$, (c) and (d) XP microspot spectra taken at the center of the images, (e) Na $2p_{3/2}$ at $V_{WR} = -600\,mV$, (f) Cu $3d_{5/2}$ at $V_{WR} = -600\,mV$.

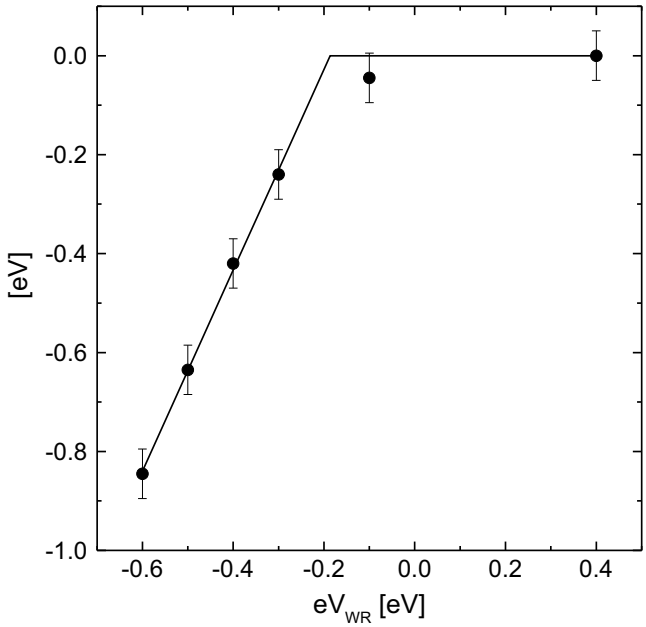

Figure 3.10: Work function changes of the Cu working electrode as a function of V_{WR}.

normal and the detection axis, which affects the intensity of the measured photoemission yield, changes from point to point. To our knowledge, these are the first measurements of their kind. We present them because they suggest that certain conclusions may be drawn tentatively. Clearly further developments along these lines would be desirable.

Figure 3.9 shows $25\mu\mathrm{m} \times 25\mu\mathrm{m}$ typical Cu $3\mathrm{d}_{5/2}$ and Na $2\mathrm{p}_{3/2}$ intensity maps taken at 523 K for two V_{WR} values: +400 mV (Na-free surface) and −600 mV (sodium coverage ~ 0.06 monolayers). The spectra in figures 3.9c and 3.9d where taken from a microspot located at the centre of each image. These spectra show that: (i) at +400 mV there is no detectable sodium at the point of analysis, (ii) at −600 mV there is sodium present at this point. Figures 3.9b and 3.9f show Cu $3\mathrm{d}_{5/2}$ intensity maps for $V_{\mathrm{WR}} = +400$ mV and −600 mV respectively. The bright feature identifies a Cu-rich region, probably a large Cu crystallite, whereas the dark features could be due to cracks on the Cu surface or to shadowing of the Cu particles. These two images show that there was no thermal drift during the experiments - an important point when evaluating the significance of the Na maps. Figures 3.9a and 3.9e show the Na $2\mathrm{p}_{3/2}$ maps corresponding to figures3.9b and 3.9f respectively. Qualitatively, these images indicate that the amount of surface Na has been increased by electro-pumping.

3.4.3 Work function changes

Work function measurements provide valuable complementary information about the surface processes occurring during spillover of electro-pumped Na. Figure 3.10 shows the work function changes of the copper film as a function of the ohmic-drop free potential V_{WR} at 623 K. The overall behavior mirrors that of the Na 1s and Na 2p Xp intensities (Figures 3.4 and 3.7). As with the XP intensities, the work function exhibits fully reversible dependence on V_{WR}. Two features are again noteworthy. First, there is a range of V_{WR} (+400 mV to −100 mV) over which no changes in work function occur. Second, for $V_{\mathrm{WR}} < -100\,\mathrm{mV}$, decreasing V_{WR} (i. e. pumping Na to Cu) causes a linear decrease in the work function. The first observation implies that at $\sim -100\,\mathrm{mV}$ the Cu surface was fully depleted of Na by electro-pumping. Given the linear dependence of Na XP intensities on V_{WR} above the threshold, the second observation implies that we are dealing with submonolayer coverages of Na on Cu where $\Delta\phi$ varies linearly with ϑ_{Na}. Specifically, over the range of our measurements, it must be the case that $\vartheta_{\mathrm{Na}} < 0.3$ monolayers. In fact, if we make use of the published $\Delta\phi$ data for Na/Cu(111) it is straightforward to estimate the maximum value of ϑ_{Na} achieved under our conditions. This corresponds to $V_{\mathrm{WR}} = -600\,\mathrm{mV}$, at which point the measured $\Delta\phi$ is −0.85 eV with respect to the clean surface value. This is equivalent to $\vartheta_{\mathrm{Na}} = 0.06$ monolayers on the basis of a pure Cu(111) surface. It should be a realistic estimate for our polycrystalline Cu sample which is composed of large particles ($\sim 5\mu$m) whose external surfaces will be dominated by (111) planes.

3.5 The relationship between $e\Delta V_{\mathrm{WR}}$ and $\Delta\phi_{\mathrm{W}}$

The relationship between the change in the ohmic-drop free potential difference between the working and reference electrodes ($e\Delta V_{\mathrm{WR}}$) and the change in the work function of the working electrode ($\Delta\phi_{\mathrm{W}}$) is a somewhat controversial subject. On one hand, Vayenas *et al.* [9] have derived the following expression:

$$e\Delta V_{\mathrm{WR}} = \Delta\phi_{\mathrm{W}}. \tag{3.2}$$

and have validated it experimentally [10]. On the other hand, Zipprich *et al.* [11] have observed deviations from the equality while Emery *et al.* [12] and Wodiunig [13] failed to observed the equality. Most strikingly, Poppe and coworkers [14] did not observe any changes in work function upon changing V_{WR} in the Pt/YSZ samples they prepared, however they did observe the 1:1 relation when using Pt/YSZ samples supplied

by Vayenas. Deviations from equation (3.2) have also been observed by the Patras group [15]. As is apparent from figures 3.3 and 3.10, although we observed a linear relationship between $e\Delta V_{\mathrm{WR}}$ and $\Delta\phi_{\mathrm{W}}$ in a range of catalyst potentials, we failed to observe the 1:1 correspondence predicted by equation (3.2).

It is most unlikely that the cause of these discrepancies is to be related to differences in measuring technique. With a patchy sample (as in the present case) the methods used to measure work function changes (UPS cut-off and the Kelvin probe method) provide an area-averaged value for the work function. Furthermore, the two methods average over similar areas of the sample surface.

Metcalfe and co-workers have investigated these discrepancies [12, 16, 17]. They showed that the relationship between working-electrode work function and working-electrode potential is highly dependent on temperature and working-electrode morphology. They also showed that for any change in catalyst potential

$$e\Delta V_{\mathrm{WR}} = \Delta\phi_{\mathrm{W}} + e\Delta\psi_{\mathrm{W}} \tag{3.3}$$

where $\Delta\psi_{\mathrm{W}}$ is the change in outer (Volta) potential. They argued that equation (3.3) is valid when there is significant loss of spillover species from the surface, either by desorption or reaction. Equation (3.2) was taken to correspond to the case where there is true thermodynamic equilibrium between the promoter species in the electrolyte and those spilt over onto the metal catalyst surface. Thus the relative rates of spillover to the catalyst and removal from the catalyst of promoter species define two limiting cases. If the kinetics of electrochemical supply are fast whereas the rate of loss of spillover species from the surface is relatively slow then $e\Delta V_{\mathrm{WR}} = \Delta\phi_{\mathrm{W}}$. Conversely, if the electrochemical process is slow and the rate of loss of spillover surface species is fast then $e\Delta V_{\mathrm{WR}} = e\Delta\psi_{\mathrm{W}}$, since the coverage of spillover species will be negligible and will not appreciably modify the metal surface work function. Thus equation (3.3) may be thought to describe the behaviour in the general case, while equation (3.2) describes a limiting case.

Thus, within this framework, a finite steady state desorption rate for Na from the Cu or Rh surface could provide an explanation for the deviations we observed from equation (3.2). However, at very low alkali coverages and under vacuum conditions, such as those used here, Na desorption from transition metal surfaces commences at $\sim 800\,\mathrm{K}$ (Pt(111) [18], Ru(001) [19]) or $\sim 700\,\mathrm{K}$ (Cu(111) [20], Ni(111) [21]). Although there is no reported value for the saturation coverage of Na on Rh(111) at 580 K, data for closely related systems indicate that it is highly unlikely that significant desorption occurs at 580 K for $\vartheta_{\mathrm{Na}} \sim 0.025\,\mathrm{ML}$ [22]. Thus the evidence indicates that Metcalfe's

model fails to provide an explanation for the observed deviation from equation (3.2).

The theoretical validity of equation (3.2), claimed many times in the literature by Vayenas (see for example reference [23] and references therein), have been recently questioned by Parsons [24, 25], who argued that the assumption made by Vayenas on its derivation is unjustified, and by Imbihl [26], who argued that there are no obvious theoretical reasons for such an identity. This indicates that there are no theoretical reasons to expect that it should hold for our samples, as our experimental results indeed confirm.

3.6 Uncoupling of V_{WR} and ϑ_{Na}

For the Rh EP sample, over the range of V_{WR} values explored, both the sodium coverage and catalyst work function changed linearly and reversible with catalyst potential. However, this was only observed within a range of V_{WR} values with the Cu EP samples. In fact, for three different Cu samples using three different experimental techniques we obtained the same results. (i) there is a range of V_{WR} values over which no Na is present on the surface of the copper. (ii) after a certain threshold value of V_{WR} is exceeded V^{*}_{WR}, both the Na coverage and the Cu work function vary linearly with decreasing catalyst potential as in the Rh case. The reason for the different behaviour of Rh and Cu samples remains to be clarified, although it seems at least possible that it is connected with differences in electrode morphology and electrode/electrolyte interface (whose properties determine the change in catalyst potential).

Why, under some conditions is ϑ_{Na} linked to V_{WR}, whereas under others, it is not?

First, it should by noted that this observation implies that at V^{*}_{WR} the Cu surface has been fully depleted of Na by electro-pumping. Thus, a further increase of catalyst potential is not expected to modify ϑ_{Na} at the Cu surface since its already zero. Second, this observation is in good agreement with reactor studies of the $CO + O_2$ [27], $CO + NO$ [28], $NO + C_2H_4$ [29], $O_2 + C_2H_4$ [30], $NO + C_3H_6$ [31] and $NO + H_2$ [32] reactions over Pt under EP conditions. These show that over a certain range of V_{WR} the catalytic rate remains at a constant unpromoted value. Then, beyond the threshold V^{*}_{WR} value, the rate increases strongly as V_{WR} continues to decrease.

The underlying causes for the eventual disentanglement of ϑ_{Na} and V_{WR} might be understood as follows. In the cell,

$$(+)\ \mathrm{M}\ |\ \mathrm{Na}\ \beta\text{''}\ \text{alumina}\ |\ \mathrm{Au}\ (-)$$

an externally imposed DC voltage (V_{WC}), which is small compared to the electrolyte decomposition potential and is negative in the gold counter electrode side, will result in Na^{+} ions migrating to the Au. However, since O^{-2} ions are unable to discharge

at the M | Na β" alumina interface then this interface will behave like a capacitor. This behaviour of solid interfaces has been observed in the past [33] and is not directly accessible to the experimental methods we employ. All of them, including the catalytic reaction itself, are probes of the gas/solid or vacuum/solid interface.

Finally it should be noted, that the threshold in V_{WR} for Na-induced work function decrease does not coincide with the threshold in V_{WR} for the appearance of XP detectable Na. This difference probably reflects differences in the electrode/electrolyte interface between Cu samples. Such differences would be expected to lead to shifts in the V_{WR} scale but they do not affect our interpretation of the results.

3.7 Conclusions

1. The coverage of electro-pumped Na on a thin film Rh or Cu catalyst contacted with a sodium ion conducting solid electrolyte is determined by the catalyst potential; the effect is fully reversible.

2. The Na coverage and Rh work function scale linearly with catalyst potential. The sodium coverage varies from 0 to $\sim$0.02 monolayer.

3. The Na coverage and Cu work function scale linearly with catalyst potential. The Na coverage varies from zero to $\sim$0.06 monolayer.

4. The time constants of these spill over and reverse spill over processes is short compared with one minute. Photoelectron microscopy suggests that the spatial distribution of the Na on the Cu is relatively uniform.

5. At sufficiently high values of catalyst potential V_{WR}, this quantity is uncoupled from the Na coverage, work function and catalytic performance of the working electrode.

6. Electrochemical promotion of heterogeneously catalysed reactions is due to the potential-controlled sodium coverage on the catalyst surface.

Bibliography

[1] W. D. Mross, Alkali doping in heterogeneous catalysis, Catalysis Reviews Science and Engineering **25**, 591–637 (1983).

[2] H. P. Bonzel, Alkali-metal-affected adsorption of molecules on metal surfaces, Surface Science Reports **8**, 43–125 (1987).

[3] M. P. Kiskinova, *Poisoning and promotion in catalysis based on surface science concepts and experiments*, volume 70 of *Studies in surface science and catalysis*, Elsevier Science, Amsterdam, 1992.

[4] A. F. Carley and M. W. Roberts, An X-ray photoelectron spectroscopic study of the interaction of oxygen and nitric oxide with aluminium, Proceedings of the Royal Society London A **363**, 403–424 (1978).

[5] R. W. Verhoef and M. Asscher, The work function of adsorbed alkalis on metals revisited: a coverage-dependent polarisability approach, Surface Science **391**, 11–18 (1997).

[6] C. M. Mate, C. T. Kao, and G. A. Somorjai, Carbon monoxide induced ordering of adsorbates on the Rh(111) crystal surface: importance of surface dipole moments, Surface Science **206**, 145–168 (1988).

[7] M. Marsi, L. Casalis, L. Gregoratti, S. Günther, A. Kolmakov, J. Kovac, D. Lonza, and M. Kiskinova, ESCA microscopy at Elettra: what is like to perform spectromicroscopy experiments on a third generation synchrotron radiation source, Journal of Electron Spectroscopy and Related Phenomena **84**, 73–83 (1997).

[8] M. Marsi, L. Casalis, L. Gregoratti, S. Günther, A. Kolmakov, J. Kovac, D. Lonza, and M. Kiskinova, Artefact formation in scanning photoelectron emission microscopy, Ultramicroscopy **75**, 35–51 (1998).

[9] C. G. Vayenas, S. Bebelis, I. V. Yentekakis, and H.-G. Lintz, Non-faradaic electrochemical modification of catalytic activity: a status report, Catalysis Today **11**, 303–442 (1992).

[10] S. Ladas, S. Bebelis, and C. G. Vayenas, Work function measurements on catalyst films subject to *in situ* electrochemical promotion, Surface Science **251/252**, 1062–1068 (1991).

[11] W. Zipprich, H.-D. Wiemhöfer, U. Vohrer, and W. Göpel, *In situ* photoelectron spectroscopy of oxygen electrodes on stabilised zirconia, Berichte der Bunsen Gesellschaft Physical Chemistry Chemical Physics **99**, 1406–1413 (1995).

[12] D. A. Emery, P. H. Middleton, and I. S. Metcalfe, The effect of electrochemical current pumping on the work function of solid electrolyte supported catalysts, Surface Science **405**, 308–315 (1998).

[13] S. Wodiunig, *Electrochemical Promotion of RuO_2 catalysts for the gas phase combustion of ethylene*, PhD thesis, École Polytechnique Fédérale de Lausanne, Lausanne, 2000.

[14] J. Poppe, S. Völkening, A. Schaak, E. Schütz, J. Janek, and R. Imbihl, Electrochemical promotion of catalytic CO oxidation on Pt/YSZ catalysts under low pressure conditions, Physical Chemistry Chemical Physics **1**, 5241–5249 (1999).

[15] C. Raptis, T. Badas, D. Tsiplakides, C. Pliangos, and C. G. Vayenas, Electrochemical promotion of NO reduction by C_3H_6 on Rh/YSZ catalyst-electrodes and investigation of the origin of the promoting action using TPD and WF measurements, in *12th International congress on catalysis*, edited by A. Corma, F. V. Melo, S. Mendioroz, and J. L. G. Fierro, volume 130B of *Studies in Surface Science and Catalysis*, pages 1283–1287, Elsevier, Amsterdam, 2000.

[16] D. A. Emery, R. J. C. Luke, P. H. Middleton, and I. S. Metcalfe, Electrochemical enhancement of carbon monoxide oxidation over yttria-stabilized zirconia supported platinum catalysts. I. Effect of catalyst morphology on kinetic behavior, Journal of the Electrochemical Society **146**, 2188–2193 (1999).

[17] D. A. Emery, P. H. Middleton, and I. S. Metcalfe, Electrochemical enhancement of carbon monoxide oxidation over yttria-stabilized zirconia supported platinum catalysts. II. Effect of catalyst morphology on catalyst work function, Journal of the Electrochemical Society **146**, 2194–2198 (1999).

[18] I. R. Harkness, *A comparative study of alkali doping and electrochemical promotion for the control of the catalytic chemistry of platinum*, PhD thesis, University of Cambridge, Cambridge, 1994.

[19] D. L. Doering and S. Semancik, Low temperature ordering of sodium overlayers on Ru(001), Surface Science **129**, 177–191 (1983).

[20] D. Tang, D. McIlroy, X. Shi, C. Su, and D. Heskett, The structure of Na overlayers on Cu(111) at room temperature, Surface Science **255**, L497–L503 (1991).

[21] R. L. Gerlach and T. N. Rhodin, Binding and charge transfer associated with alkali metal adsorption on single crystal nickel surfaces, Surface Science **19**, 403–426 (1970).

[22] R. D. Diehl and R. McGrath, Structural studies of alkali metal adsorption and coadsorption on metal surfaces, Surface Science Reports **23**, 43–171 (1996).

[23] C. G. Vayenas and S. Bebelis, Electrochemical promotion of heterogeneous catalysis, Catalysis Today **51**, 581–594 (1999).

[24] R. Parsons, Book reviews, Journal of Electroanalytical Chemistry **422**, 202–203 (1997).

[25] R. Parsons, Comment on the paper entitled 'On the work function of the gas exposed electrode surfaces in solid state electrochemistry', Journal of Electroanalytical Chemistry **486**, 91 (2000).

[26] J. Janek, M. Rohnke, B. Luerßen, and R. Imbihl, Promotion of catalytic reactions by electrochemical polarization, Physical Chemistry Chemical Physics **2**, 1935–1941 (2000).

[27] I. V. Yentekakis, G. Moggridge, C. G. Vayenas, and R. M. Lambert, *In situ* controlled promotion of catalyst surfaces via NEMCA: the effect of Na on the Pt-catalysed CO oxidation, Journal of Catalysis **146**, 292–305 (1994).

[28] A. Palermo, R. M. Lambert, I. R. Harkness, I. V. Yentekakis, O. Mar'ina, and C. G. Vayenas, Electrochemical promotion by Na of the platinum-catalysed reaction between CO and NO, Journal of Catalysis **161**, 471–479 (1996).

[29] I. R. Harkness and R. M. Lambert, Electrochemical promotion of the NO + ethylene reaction over platinum, Journal of Catalysis **152**, 211–214 (1995).

[30] I. R. Harkness, C. Hardacre, R. M. Lambert, I. V. Yentekakis, and C. G. Vayenas, Ethylene oxidation over platinum: *in situ* controlled promotion using Na-β" alumina and studies with a Pt(111)/Na model catalyst, Journal of Catalysis **160**, 19–26 (1996).

[31] I. V. Yentekakis, A. Palermo, N. C. Filkin, M. S. Tikhov, and R. M. Lambert, *In situ* electrochemical promotion by sodium of the platinum-catalysed reduction of NO by propene, Journal of Physical Chemistry B **101**, 3759–3768 (1997).

[32] O. A. Mar'ina, I. V. Yentekakis, C. G. Vayenas, A. Palermo, and R. M. Lambert, *In situ* controlled promotion of catalyst surface via NEMCA: the effect of Na on the Pt-catalysed NO reduction by H_2, Journal of Catalysis **166**, 218–228 (1997).

[33] D. O. Raleigh, Interphase phenomena in solid electrochemical cells, in *Fast ion transport in solids*, edited by W. van Gool, pages 477–485, North-Holland, Amsterdam, 1973.

CHAPTER 4

The Rh–catalysed reduction of nitric oxide by carbon monoxide

4.1 Introduction

The metal-catalysed heterogeneous reduction of CO by NO has been investigated over many years under a wide range of conditions and by means of a variety of catalyst types including single crystals [1], polycrystalline foils and wires [2, 3], and oxide-supported metals [4, 5]. The earliest study carried out on single crystal surfaces under ultra high vacuum conditions was that of Lambert and Comrie [6] who examined the reaction on Pt(111) and Pt(110). More recently Zaera *et al.* [7–11] and Belton *et al.* [12–17] have investigated the reaction on single crystal surfaces of rhodium using molecular beam techniques and atmospheric pressure conditions, respectively. A comprehensive review of the reaction over rhodium surfaces is available [18]. The motivation for much current work on this topic derives, at least in part, from the important role played by the CO + NO reaction in practical automotive catalytic converters [19]; our contribution to this subject involves the application of alkali promotion using electrochemical methods, as indicated in the present and following chapters.

Lambert and coworkers have shown that on Pt surfaces promotion by (electrochemically supplied) Na greatly enhances both activity and selectivity towards N_2 production in the CO + NO reaction [20]. A mechanistic model was proposed and subsequently supported by Monte Carlo calculations [21]. This work eventually led to the development of highly active and selective alkali-promoted Pd and Pt dispersed catalysts [22, 23]. Most recently, MacLeod *et al.* have shown that Pt/γ-alumina dispersed catalysts exhibit strong promotion by Na under simulated exhaust gas conditions [24].

The efficacy of alkalis in promoting activity and selectivity in NO reduction over Pt and Pd derives from alkali-induced NO dissociation on these metal surfaces, which otherwise are not very efficient for NO dissociation. In this respect, clean Rh surfaces are much more efficient than both Pt and Pd, and this indeed is why Rh is a vital component in automotive catalytic converters [25]. However, the mechanism of Rh-catalysed NO reduction by CO remains controversial.

The present work is principally motivated by the following questions. Can the catalytic performance of Rh be usefully enhanced by alkali promotion? What can alkali promotion reveal about the reaction mechanism? As we have shown in the previous chapter, EP provides *in situ* control of promoter concentration at the surface of a rhodium metal catalyst. We now describe the catalytic consequences of Na pumping to the Rh surface. We find that alkali promotion is effective in enhancing the catalytic performance of Rh and the data point to NO dissociation as the rate-limiting step.

4.2 Experimental methods

EP samples for catalytic testing and spectroscopic analyses were prepared by depositing a rhodium metal film on one face of a Na β" alumina wafer: this constituted the catalyst (working electrode). Gold counter and reference electrodes were deposited on the other face, all three electrodes being deposited by DC sputtering of Rh or Au in argon. These EP samples were characterised by XRD, XPS and surface area measurements, as discussed in chapter 2.

Reactor measurements were performed in the well-mixed reactor operated at atmospheric pressure described in chapter 2. Inlet and exit gas analysis was carried out by a combination of on-line gas chromatography (Shimadzu-14B; molecular sieve 13X and Haysep-N columns) and on-line mass spectrometry (Balzers QMG 064). N_2, N_2O, CO and CO_2 were measured by gas chromatography, and NO was monitored continuously by mass spectrometry after performing the necessary calibrations. NO (Distillers MG) and CO (Distillers MG) were diluted in ultrapure He (99.996%) and fed to the reactor by mass flow controllers (Brooks 5850 TR). The total flow rate was kept constant in all experiments at $34 \times 10^{-5}\,\mathrm{mol{\cdot}s^{-1}}$ (500 $\mathrm{cm^3(STP)/min}$), with partial pressures P_{NO} and P_{CO} of $0.2 - 1.8$ and $0.3 - 1.1\,\mathrm{kPa}$, respectively, with added helium giving a total pressure of 1 atm in every case. Reactant conversion was restricted to $< 15\%$ in order to avoid mass transfer limitations. Control experiments were carried out in which the total flow was varied by a factor of 5 in order to verify that the observed changes in activity were indeed due to changes in actual surface reaction rates, unaffected by mass

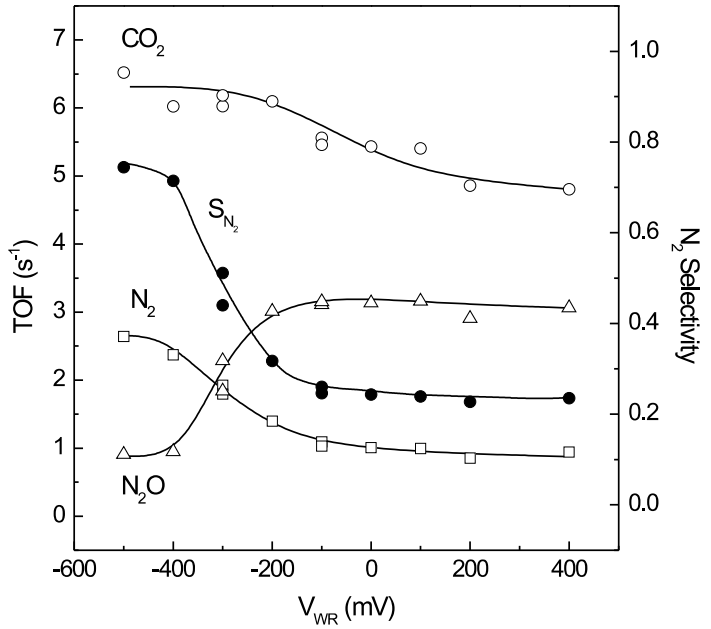

Figure 4.1: Effect of catalyst potential V_{WR} on the CO_2, N_2, and N_2O formation rates and on nitrogen selectivity. Conditions: $T = 580\,\mathrm{K}$, $P^{\circ}_{\mathrm{NO}} = P^{\circ}_{\mathrm{CO}} = 1\,\mathrm{kPa}$.

transfer limitations. Nitrogen and carbon mass balances always closed to within 5%.

4.3 Effect of catalyst potential on reaction rates

Figure 4.1 shows typical steady-state (potentiostatic) rate data obtained at one atmosphere pressure and 580 K for constant inlet pressures of NO and CO, $P^{\circ}_{\mathrm{CO}} = P^{\circ}_{\mathrm{NO}} = 1\,\mathrm{kPa}$. Turnover frequencies (TOF) are expressed as molecules of product per Rh surface atom per second. It is apparent that the CO_2, N_2O and N_2 turnover frequencies are dependent on catalyst potential, and the observed behaviour was fully reversible with V_{WR}. Also shown in figure 4.1 is the dependence of N_2 selectivity on V_{WR}, where the former quantity is defined as

$$S_{\mathrm{N_2}} = \frac{r_{\mathrm{N_2}}}{r_{\mathrm{N_2}} + r_{\mathrm{N_2O}}}. \tag{4.1}$$

Equation (4.1) shows that the nitrogen selectivity gives the probability that a nitric oxide molecule is converted to nitrogen (the desired product) as opposed to nitrous oxide (the undesired product). These data show that the rates of CO_2 and N_2 production increase with decreasing V_{WR}, whereas the N_2O rate decreases. Thus the system exhibits pronounced electrochemical promotion: Na induces an increase in overall activity and in N_2 production at the expense of N_2O production, resulting in an increase in nitrogen selectivity from 24% to 80%. The rate enhancement ratios (ρ) defined as the ratio

of the maximum promoted rates to the unpromoted rates are as follows: $\rho_{CO_2} = 1.4$, $\rho_{N_2} = 3.1$ and $\rho_{N_2O} = 0.3$. The observed changes in turnover frequencies and in nitrogen selectivity were fully reversible, i. e. returning V_{WR} to the initial value restored all the reaction rates to their initial values. It is worth noting that our TOF values for the unpromoted Rh film are very similar to those reported for the CO + NO reaction over Rh(111) under similar conditions of temperature and reactant pressures [13, 16]. This provides additional validation for our estimate of the surface area of the rhodium film described in chapter 2.

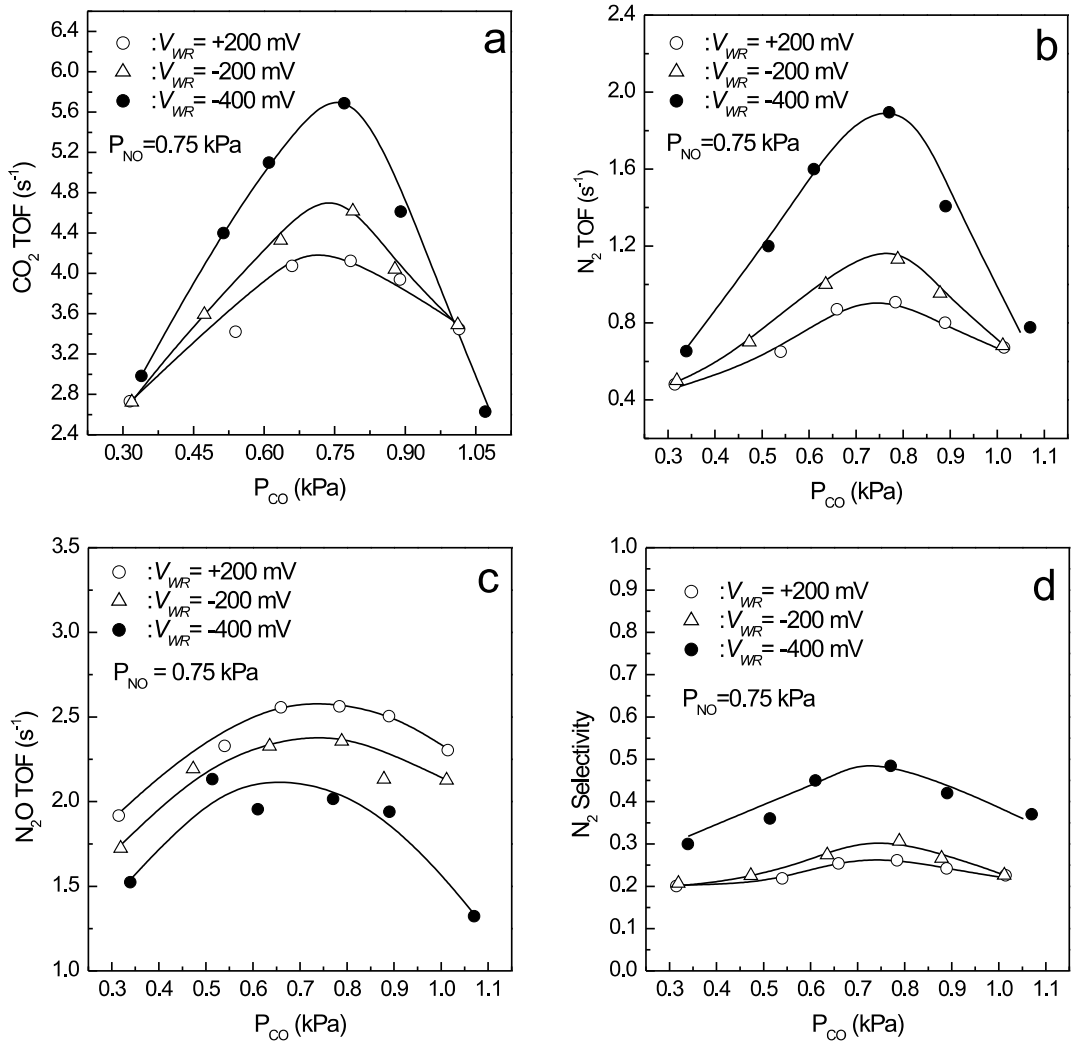

Figure 4.2: Effect of partial pressure of CO P_{CO} on the rates of CO_2 (a), N_2 (b), and N_2O (c) formation and on the selectivity of NO reduction to nitrogen(d), at three different fixed catalyst potentials. $T = 580\,\mathrm{K}$, $P_{\mathrm{NO}} = 0.75\,\mathrm{kPa}$.

4.4 Effect of reactant partial pressures on reaction rates

The dependence of the CO_2, N_2 and N_2O reaction rates on P_{CO} at fixed P_{NO} for three different values of catalyst potential is illustrated in figures 4.2a−4.2c. $V_{WR} = +200\,mV$ corresponds to the clean Rh surface (unpromoted rate) while $V_{WR} = -200\,mV$ and $V_{WR} = -400\,mV$ correspond to promoted surfaces with progressively increased sodium loadings. Figure 4.2d shows the corresponding nitrogen selectivity data: it is apparent that the highest selectivities to nitrogen production always occur in the presence of the highest Na loading (most negative potential). From figures 4.2a and 4.2b it can be seen that the CO_2 and N_2 rates exhibit Langmuir-Hinshelwood behaviour and that increased levels of Na result in a small systematic increase in the CO partial pressure (P^*_{CO}) necessary for inhibition. That is, Na favours the chemisorption of NO relative to CO. The N_2O rate also exhibits Langmuir-Hinshelwood kinetics, but the effect of increased Na is somewhat different: in particular, high levels of Na suppress the N_2O rate and there is no systematic shift in P^*_{CO}. Thus increasing the sodium coverage causes an increase in the rates of formation of CO_2 and N_2 and a decrease in the rate of formation of N_2O resulting in the increase in the nitrogen selectivity shown in figure 4.2d. Figure 4.2a also shows that at high sodium loadings, high values of P_{CO} cause an overall decrease in the rate of formation of CO_2 in agreement with the results illustrated in figure 4.3a, as discussed below. Figure 4.2d shows that the nitrogen selectivity passes through a shallow maximum as P_{CO} increases, and that this effect becomes more pronounced as Na coverage increases.

Figures 4.3a−4.3d show corresponding results for the dependence of the rates of production of CO_2, N_2 and N_2O and the nitrogen selectivity on P_{NO} at fixed P_{CO} for three different values of catalyst potential. No rate maxima are observed within the accessible P_{NO} range. These results show that at lower partial pressures of NO, the N_2 and CO_2 reaction rates exhibit maxima as the sodium loading is increased (rate(highest Na)<rate(clean)<rate(moderate Na)). Figure 4.3d shows that the nitrogen selectivity is relatively insensitive to P_{NO}, other than at the highest Na coverage; in every case there is a very small overall decrease in selectivity, in accord with the results of Belton *et al.* [15]. Note also that the nitrogen selectivity of the unpromoted Rh film is 24% − a value that is fully consistent with those reported by Belton *et al.* [12] for the same reactants partial pressures and temperature, i. e. 40% over Rh(110), 26% over Rh(100) and 24% over Rh(111). Taken together, figures 4.2d and 4.3d illustrate the point that over the entire range of partial pressures explored, Na acts to increase selectivity.

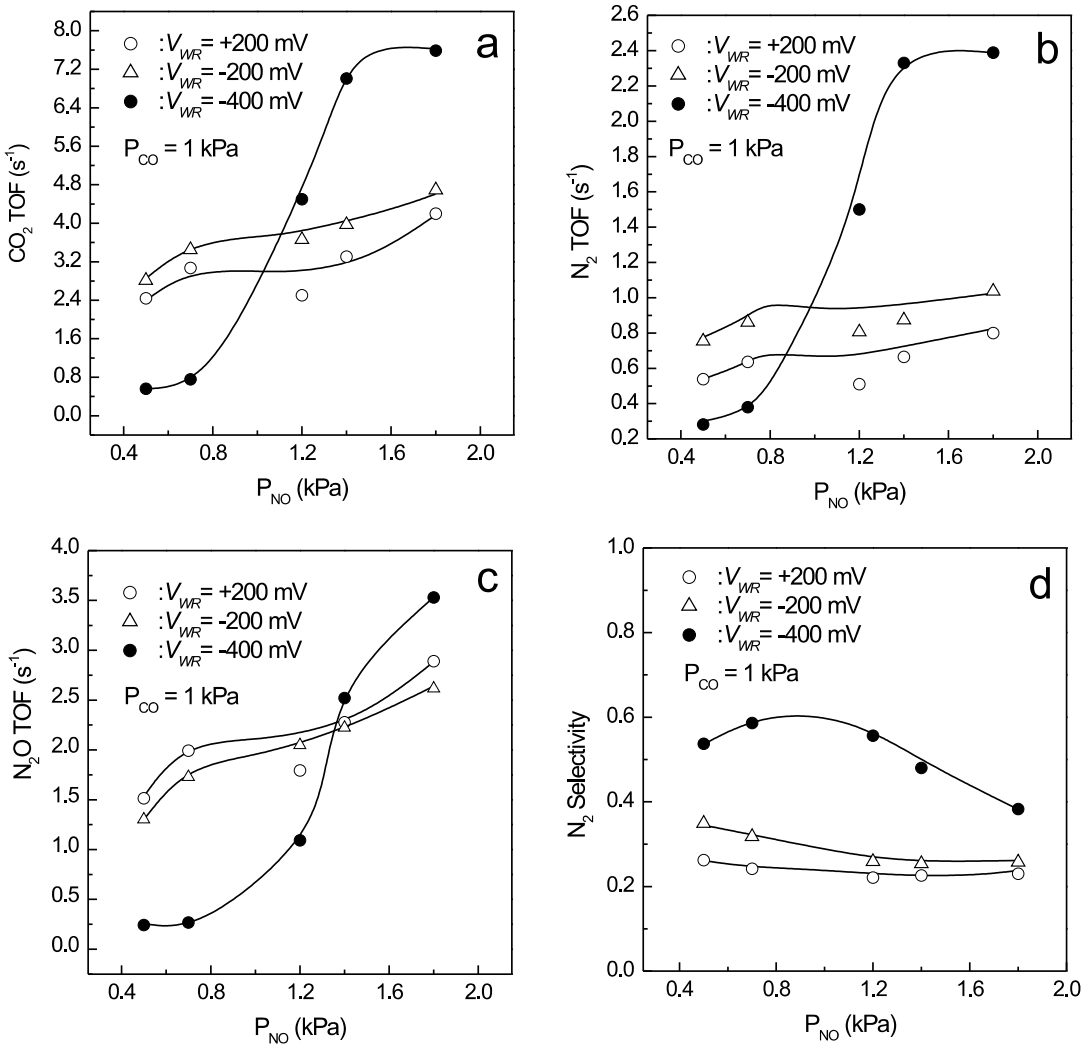

Figure 4.3: Effect of partial pressure of NO P_{NO} on the rates of CO_2 (a), N_2 (b), and N_2O (c) formation and on the selectivity of NO reduction to nitrogen(d), at three different fixed catalyst potentials. $T = 580\,\mathrm{K}$, $P_{\mathrm{CO}} = 1\,\mathrm{kPa}$.

4.5 Discussion

Our results are fully consistent with the view, advanced previously in regard to Pt-catalysed NO reduction [20, 26, 27], that Na acts to promote the rate limiting step and that this step is the dissociation of adsorbed NO. In the specific case of the Rh-catalysed NO + CO reaction the identity of the rate limiting step has been a matter of some controversy. The salient points are therefore considered here.

Belton *et al.* [12–17] carried out a series of detailed investigations in which they used Rh single crystal surfaces as model catalysts, operated at atmospheric pressure. They concluded that at high N coverages nitrogen desorption is not rate limiting, as previously proposed [17]. It was also shown that the NO dissociation rate decreases with increasing coverage [15] and that NO and N react to form only N_2O and not N_2 [14]. At moderate pressures, N_2 formation was accompanied by N_2O formation and there was no evidence that N_2O readsorption played a significant role [28]. They showed that the reaction is structure sensitive with rates increasing as metal surface atom density decreased, in the order: (111) < (100) < (110) [12].

On the other hand, studies performed under UHV conditions [9] led to the conclusion that N atom recombination was the rate-determining step. A comparison of these UHV results with the atmospheric pressure data of Belton *et al.* suggests that the relative contribution of the different elementary steps changes between the two pressure regimes. (Recall that no N_2O is produced under UHV conditions, whereas it is the main nitrogen-containing product at atmospheric pressures). This may be understood as follows. The NO dissociation rate is strongly dependent on NO coverage (due to the effects of lateral interactions and the availability of free sites). Under UHV conditions the steady state coverage is low, NO dissociation is extensive, the probability of the N + NO reaction is therefore small (no N_2O is observed) and the N recombination step is rate limiting. This situation is reversed under atmospheric pressure conditions: now, the steady state NO coverage is much higher, NO dissociation therefore becomes rate limiting, and, as a result, N_2O formation can occur. Given that the partial pressures and temperature conditions employed in our experiments are very similar to the those used by Belton *et al.*, it is reasonable to propose that the same mechanism prevails in the present case, i. e. that NO dissociation is rate limiting.

In the discussion that follows use is made of the term 'sodium coverage'. This does not imply that the promoter phase is thought to be present in the form of chemisorbed metallic sodium under reaction conditions. Decreasing the value of the catalysts potential under UHV conditions does indeed pump chemisorbed metallic sodium to the Rh surface, as we have shown in the previous chapter. As would be expected, and as

Tikhov *et al.* demonstrated previously [26], this electrochemically-supplied sodium is in the same chemical state as sodium deposited by vacuum evaporation. However, in the presence of a reactive atmosphere one expects the Na to be present as a surface compound(s) whose identity depends on the composition of the ambient gas. This too has been demonstrated previously and will be shown in the following chapters. In the case of EP of Pt-catalysed NO reduction by propene, XPS shows that alkali carbonate, nitrite and/or nitrate are present [26]; in the case of propene combustion XANES shows that the promoter phase consists of alkali carbonate [29].

All our results may be understood in terms of the promotion of NO dissociation induced by electro-pumped Na. Our XPS data presented in chapter 3 demonstrate directly the occurrence of this reversible spillover/backspillover effect which correlates very well with the reversible response of the catalytic system. The dissociation of adsorbed diatomic molecules in the electric field of adjacent alkali cations has received a detailed theoretical analysis [30]. The field lowers the energy of the NO antibonding orbital with respect to the Fermi level. This increases charge transfer from the metal to the NO π^* orbital, increasing the strength of the metal−N bond and decreasing the strength of the N−O bond. In the specific case of Rh/NO, studies on Rh(111)/K [31, 32] and on Rh(100)/Na [33] reveal the expected strengthening the metal−N bond and weakening of the N−O bond: both effects act to increase activity and selectivity.

The following reaction mechanism permits a rationalisation of EP by Na of the Rh-catalysed NO + CO reaction. It was previously proposed by Belton *et al.* [12] in regard to catalysis by Rh, by Lambert and Comrie [6] in regard to the CO + NO reaction over Pt, and by ourselves in regard to EP of the Pt-catalysed reaction [21].

$$\mathrm{CO(g) + S} \rightleftarrows \mathrm{CO(a)} \tag{4.2}$$

$$\mathrm{NO(g) + S} \rightleftarrows \mathrm{NO(a)} \tag{4.3}$$

$$\mathrm{NO(a) + S} \rightarrow \mathrm{N(a) + O(a)} \tag{4.4}$$

$$\mathrm{CO(a) + O(a)} \rightarrow \mathrm{CO_2(g) + 2S} \tag{4.5}$$

$$\mathrm{NO(a) + N(a)} \rightarrow \mathrm{N_2O(g) + 2S} \tag{4.6}$$

$$\mathrm{N(a) + N(a)} \rightarrow \mathrm{N_2(g) + 2S} \tag{4.7}$$

Where S represents a vacant site for adsorption. The adsorption and dissociation of the reactants depends on the availability of such free sites (reactions (4.2)−(4.4)). In this scheme, (4.4) is rate limiting, both (4.3) and (4.4) are enhanced by Na, and nitrogen selectivity depends on the relative rates of reactions (4.6) and (4.7). On this basis, Na

promotes activity and nitrogen selectivity as a result of accelerating the key reaction-initiating step (4.4). This leads to an increase in the coverages of N(a) and the O(a) and a decrease in that of NO(a). As a consequence, there is an increase in the rates of steps (4.5) and (4.7) and a decrease in the rate of step (4.6) yielding the observed increase in overall activity and nitrogen selectivity (figure 4.1). Additionally, the kinetic data (figure 4.2) demonstrate the beneficial effect of Na in increasing the adsorption strength of NO relative to CO such that higher CO partial pressures are required before CO poisoning sets in.

Figure 4.2d shows that the nitrogen selectivity exhibits a maximum as a function of P_{CO} for fixed P_{NO}. This may be understood as follows. Dissociation of NO(a) requires a nearest neighbour vacant site, therefore the nitrogen selectivity is expected to increase with the number of such sites. When P_{CO} is low, the surface will be mainly covered by O atoms, inhibiting NO dissociation; as P_{CO} increases, the coverage of O decreases due to formation of CO_2, freeing up sites for NO dissociation. Thus N_2 selectivity increases with P_{CO}. When P_{CO} is sufficiently high, N_2 selectivity eventually decreases because site blocking by CO begins to inhibit NO dissociation. Therefore the nitrogen selectivity passes through a maximum. The effect is more pronounced at higher sodium coverages as a result of enhanced NO dissociation induced by Na.

As noted previously, figures 4.3a−4.3b show that the reaction rates exhibit a maximum as the sodium loading is increased for low NO partial pressures at fixed CO partial pressure. This observation is consistent with the result displayed in figure 4.2a, namely that at the highest CO:NO ratio, rate(highest Na)<rate(clean)<rate(moderate Na). This may reflect the site blocking effect of islands of Na−CO surface complexes [34] that are known to be stable under these conditions. At sufficiently low CO:NO ratios there is a switch in behaviour: activity now increases with Na coverage. This may be rationalised in terms of increased coverage by NO and its dissociation products, especially O(a), which act to inhibit Na−CO complex formation and hence concomitant poisoning.

As noted earlier, reaction rates over the unpromoted catalyst exhibit maxima as a function of CO partial pressure (figure 4.2) and are approximately independent of NO partial pressure (figure 4.3). Such behaviour was observed for the NO + CO reaction over Pt [20]; it is also in good agreement with the results of Hendershot and Hansen [35] who studied the CO + NO reaction over Rh(100). Belton *et al.* [16] reported zero order in both CO and NO under conditions similar to those used in this study. However, close inspection of the data reveals no significant divergence between their findings and ours. Thus if we plot the results presented in figures 4.2 and 4.3 logarithmically, in the manner employed in reference [16], it becomes apparent that our data are in very good

agreement with those of Belton *et al.*; the variation of the unpromoted reaction rates with reactant partial pressures is rather small in the range of partial pressures studied.

EP by Na of the Rh-catalysed CO + NO reaction exhibits both similarities and differences compared with EP of the Pt-catalysed reaction [20]. In both cases increasing the sodium coverage causes an increase in the rates of formation of CO_2 and N_2 and results in a pronounced increase in the nitrogen selectivity. However, in the case of Pt, increasing the sodium coverage causes the rate of formation of N_2O to go through a maximum, whereas in the present case, under similar conditions, the N_2O rate always decreases with increasing Na loading. This reflects the fact that clean Rh surfaces are more efficient at dissociating NO than clean Pt surfaces. For example, NO dissociates on Rh(111) at low ϑ_{NO} (< 0.25) [36–38] whereas it does not dissociate on Pt(111) under the same conditions [6, 39].

4.6 Conclusions

1. The CO+NO reaction exhibits strong, reversible electrochemical promotion under Na pumping to the rhodium catalyst. This is due to the *in situ* control of sodium coverage over the catalyst surface.

2. Activity and selectivity towards N_2 formation are markedly improved by a factor of 3 and from 24% to 80%, respectively.

3. Na promotion of nitric oxide reduction is due to alkali-induced dissociation of chemisorbed NO, which process is the rate-limiting step. This factor is responsible for the Na-induced increase in activity and nitrogen selectivity.

4. Comparison of these EP results with corresponding data obtained using Pt/Na β"alumina EP samples corroborates that Rh surfaces are more efficient at dissociating NO than Pt surfaces.

Bibliography

[1] B. E. Nieuwenhuys, The surface science approach toward understanding automotive exhaust conversion catalysis at the atomic level, Advances in Catalysis **44**, 259–328 (2000).

[2] C. T. Campbell and J. M. White, Chemisorption and reactions of nitric oxide on rhodium, Applications of Surface Science **1**, 347–359 (1978).

[3] H. G. Lintz and T. Weisker, The oxidation of carbon monoxide on polycrystalline rhodium under Knudsen conditions. II. Reaction with nitrogen monoxide, Applied Surface Science **24**, 259–267 (1985).

[4] W. C. Hecker and A. T. Bell, Reduction of NO by CO over silica supported rhodium: infrared and kinetic studies, Journal of Catalysis **84**, 200–215 (1983).

[5] S. H. Oh, G. B. Fisher, J. E. Carpenter, and D. W. Goodman, Comparative kinetic studies of CO-O_2 and CO-NO reactions over single crystal and supported rhodium catalysts, Journal of Catalysis **100**, 360–376 (1986).

[6] C. M. Comrie and R. M. Lambert, The oxidation of CO by NO on Pt(111) and Pt(110), Surface Science **46**, 61–80 (1974).

[7] M. Aryafar and F. Zaera, Isothermal kinetic study of the decomposition of nitric oxide over Rh(111) surfaces, Journal of Catalysis **175**, 316–327 (1998).

[8] F. Zaera and C. S. Gopinath, Role of adsorbed nitrogen in the catalytic reduction of NO on rhodium surfaces, Journal of Chemical Physics **111**, 8088–8097 (1999).

[9] C. S. Gopinath and F. Zaera, A molecular beam study of the kinetics of the catalytic reduction of NO by CO on Rh(111) single crystal surfaces, Journal of Catalysis **186**, 387–404 (1999).

[10] C. S. Gopinath and F. Zaera, Transient kinetics during isothermal reduction of NO by CO on Rh(111) as studied with effusive collimated molecular beams, Journal of Physical Chemistry B **104**, 3194–3203 (2000).

[11] F. Zaera and C. S. Gopinath, Kinetics of NO reduction by CO on Rh(111): a molecular beam study, in *12th International congress on catalysis*, edited by A. Corma, F. V. Melo, S. Mendioroz, and J. L. G. Fierro, volume 130B of *Studies in Surface Science and Catalysis*, pages 1295–1300, Elsevier, Amsterdam, 2000.

[12] G. S. Herman, C. H. F. Peden, S. J. Schmieg, and D. N. Belton, A comparison of the NO-CO reaction over Rh(100), Rh(110) and Rh(111), Catalysis Letters **62**, 131–138 (1999).

[13] H. Permana, K. Y. S. Ng, C. H. F. Peden, S. J. Schmieg, D. K. Lambert, and D. N. Belton, Adsorbed species and reaction rates for NO-CO over Rh(111), Journal of Catalysis **164**, 194–206 (1996).

[14] D. N. Belton, C. L. DiMaggio, S. J. Schmieg, and K. Y. S. Ng, Reaction of coadsorbed nitric oxide and nitrogen atoms on Rh(111), Journal of Catalysis **157**, 559–568 (1995).

[15] C. H. F. Peden, D. N. Belton, and S. J. Schmieg, Structure sensitive selectivity of the NO-CO reaction over Rh(110) and Rh(111), Journal of Catalysis **155**, 204–218 (1995).

[16] H. Permana, K. Y. S. Ng, C. H. F. Peden, S. J. Schmieg, and D. N. Belton, Effect of NO pressure on the reaction of NO and CO over Rh(111), Journal of Physical Chemistry **99**, 16344–16350 (1995).

[17] D. N. Belton, C. L. DiMaggio, and K. Y. S. Ng, $N + N \rightarrow N_2$ reaction rates on Rh(111), Journal of Catalysis **144**, 273–284 (1993).

[18] V. P. Zhdanov, Mechanism and kinetics of the NO−CO reaction on Rh, Surface Science Reports **29**, 31–90 (1997).

[19] V. I. Pârvulescu, P. Grange, and B. Delmon, Catalytic removal of NO, Catalysis Today **46**, 233–316 (1998).

[20] A. Palermo, R. M. Lambert, I. R. Harkness, I. V. Yentekakis, O. Mar'ina, and C. G. Vayenas, Electrochemical promotion by Na of the platinum-catalysed reaction between CO and NO, Journal of Catalysis **161**, 471–479 (1996).

[21] F. J. Williams, C. M. Aldao, A. Palermo, and R. M. Lambert, A Monte Carlo simulation of the NO + CO reaction on Na-promoted platinum, Surface Science **412/413**, 174–183 (1998).

[22] Y. V. Yentekakis, R. M. Lambert, M. S. Tikhov, M. Konsolakis, and K. V., Promotion by sodium in emission control catalysis: A kinetic and spectroscopic study of the Pd-catalyzed reduction of NO by propene, Journal of Catalysis **176**, 82–92 (1998).

[23] M. Konsolakis, L. Nalbantian, N. M. Y. V. Yentekakis, and R. M. Lambert, Extraordinarily effective promotion by sodium in emission control catalysis: NO reduction by propene over Na-promoted $Pt/\gamma-Al_2O_3$, Applied Catalysis B: Environmental **22**, 123–133 (1999).

[24] M. Konsolakis, N. Macleod, J. Issac, Y. V. Yentekakis, and R. M. Lambert, Strong promotion by Na of Pt/γ-Al_2O_3 catalysts operated under simulated exhaust conditions, Journal of Catalysis **193**, 330–337 (2000).

[25] M. Shelef and G. W. Graham, Why rhodium in automotive three-way catalysts?, Catalysis reviews science and engineering **36**, 433–457 (1994).

[26] I. V. Yentekakis, A. Palermo, N. C. Filkin, M. S. Tikhov, and R. M. Lambert, *In situ* electrochemical promotion by sodium of the platinum-catalysed reduction of NO by propene, Journal of Physical Chemistry B **101**, 3759–3768 (1997).

[27] O. A. Mar'ina, I. V. Yentekakis, C. G. Vayenas, A. Palermo, and R. M. Lambert, *In situ* controlled promotion of catalyst surface via NEMCA: the effect of Na on the Pt-catalysed NO reduction by H_2, Journal of Catalysis **166**, 218–228 (1997).

[28] K. Y. S. Ng, D. N. Belton, S. J. Schmieg, and G. B. Fisher, NO-CO activity and selectivity over a $Pt_{10}Rh_{90}(111)$ alloy catalyst in the 10-Torr pressure range, Journal of Catalysis **146**, 394–406 (1994).

[29] N. C. Filkin, M. S. Tikhov, A. Palermo, and R. M. Lambert, A kinetic and spectroscopic study of the *in situ* electrochemical promotion by sodium of the platinum-catalysed combustion of propene, Journal of Physical Chemistry A **103**, 2680–2687 (1999).

[30] N. D. Lang, S. Holloway, and J. K. Nørskov, Electrostatic adsorbate-adsorbate interactions: the poisoning and promotion of the molecular adsorption reaction, Surface Science **150**, 24–38 (1985).

[31] L. Bugyi and F. Solymosi, Interaction of NO with clean and K-dosed Rh(111) surfaces. I. AES, TDS and work function studies, Surface Science **188**, 475–489 (1987).

[32] L. Bugyi, J. Kiss, K. Révéz, and F. Solymosi, Interaction of NO with clean and K-dosed Rh(111) surfaces. II. EELS and PES studies, Surface Science **233**, 1–11 (1990).

[33] H. Höchst and E. Colavita, The interaction of CO, NO and O_2 with sodium-promoted Rh(100) surfaces, Journal of Vacuum Science and Technology A **4**, 1442–1445 (1986).

[34] J. C. Bertolini, P. Delichere, and J. Massardier, The influence of potassium and the role of coadsorbed oxygen on the chemisortive properties of Pt(100), Surface Science **160**, 531–541 (1985).

[35] R. E. Hendershot and R. S. Hansen, Reduction of nitric oxide with carbon monoxide on the Rh(100) single crystal surface, Journal of Catalysis **98**, 150–165 (1986).

[36] H. J. Borg, J. F. C. J. M. Reijerse, R. A. van Santen, and J. W. Niemantsverdriet, The dissociation kinetics of NO on Rh(111) as studied by temperature programmed static secondary ion mass spectrometry and desorption, Journal of Chemical Physics **101**, 10052–10063 (1994).

[37] M. J. P. Hopstaken, W. J. H. van Gennip, and J. W. Niemantsverdriet, Reactions between NO and CO on rhodium (111): an elementary step approach, Surface Science **433/435**, 69–73 (1999).

[38] H. J. Borg, J. F. C. J. M. Reijerse, R. A. van Santen, and J. W. Niemantsverdriet, Kinetics of elementary surface reactions studied by static secondary ion mass spectrometry and temperature programmed reaction spectroscopy, Journal of Molecular Catalysis A: Chemical **131**, 199–208 (1998).

[39] C. M. Comrie, W. H. Weinberg, and R. M. Lambert, The adsorption of nitric oxide on Pt(111) and Pt(110) surfaces, Surface Science **57**, 619–631 (1976).

CHAPTER 5

The Rh–catalysed reduction of nitric oxide by propene

5.1 Introduction

Current automotive catalytic converters employ various combinations of Pt, Pd and Rh for the simultaneous removal of NO, CO and unburned hydrocarbons [1]. Of these metals, rhodium is the key component with respect to NO reduction due to its high activity to dissociate chemisorbed NO [2], which process seems likely to play an important role in the catalytic reduction of NO. Even so, Rh-based catalysts exhibit less than 100% selectivity towards nitrogen formation, substantial amounts of N_2O being produced as well. Although N_2O emission is not yet covered by legislation, it seems unlikely that this situation will persist as nitrous oxide is a powerful greenhouse gas. Attempts have therefore been made to improve the selectivity of Rh catalysts by doping either the component Rh itself [3], or the support material [4]. Interpretation of the observed effects remains, however largely speculative. Recently, MacLeod *et al.* showed that the catalytic performance of Rh particles supported on γ alumina in the reduction of NO by propene could be greatly improved by sodium promotion [5]. Though encouraging, a full understanding of these results is impeded by one of the most difficult problems that arises in studies of heterogeneous catalysis by dispersed metal particles, namely how is the promoter species distributed between the metal component and the support phase? Electrochemical Promotion (EP) of thin film metal catalysts offers a way forward.

As discussed in previous chapters, EP entails electrochemical pumping of ions from a solid electrolyte to the surface of a porous, catalytically active metal film with which it is in contact. Here we use Na β" alumina (a Na^+) conductor as the solid electrolyte.

As we have shown in chapter 3, controlling the catalyst potential with respect to a reference electrode V_{WR} controls the surface coverage of promoter species. Thus, we have a means of *in situ* control of alkali promoter levels on the working metal catalyst and the interpretation of the results is freed from ambiguities associated with possible effects of the alkali on the supported phase.

In this chapter we show that EP induces selectivity and activity improvements commensurate with those found with Na-promoted conventional dispersed Rh catalysts and a mechanism for Na promotion of Rh is proposed. XPS data illuminate the mode of action of EP. They also reveal the chemical identity of the Na-containing promoter phase and provide some insight into its morphology.

5.2 Experimental Methods

EP samples for catalytic testing and spectroscopic analyses were prepared and characterised by XRD, XPS and surface area measurements, as discussed in chapter 2. Rate data were acquired in the well-mixed reactor operated at atmospheric pressure described in chapter 2. Inlet and exit gas analysis was carried out by a combination of on-line gas chromatography (Shimadzu-14B; molecular sieve 13X and Haysep-N columns) and on-line mass spectrometry (Balzers QMG 064). N_2, N_2O, CO, CO_2 and C_3H_6 were measured by gas chromatography, and NO was monitored continuously by mass spectrometry after performing the necessary calibrations. NO (Distillers MG) and C_3H_6 (Distillers MG) were diluted in ultrapure He (99.996%) and fed to the reactor by mass flow controllers (Brooks 5850 TR). The total flow rate was kept constant in all experiments at $34 \times 10^{-5}\,\mathrm{mol{\cdot}s^{-1}}$ ($500\,\mathrm{cm^3(STP)/min}$). Reactant conversion was $< 15\%$ and control experiments were carried out in which the total flow was varied by a factor of 5 in order to verify that the observed changes in activity were indeed due to changes in actual surface reaction rates, unaffected by mass transfer limitations. Nitrogen and carbon mass balances always closed to within 5%. A galvanostat-potentiostat (Ionic Systems) was used in order to maintain a given potential difference (V_{WR}) between the working and reference electrodes (potentiostatic mode). All experiments were carried out in potentiostatic mode by following the effect of catalyst potential, i. e. the Na coverage (ϑ_{Na}), on the reaction rates. XPS experiments were performed under UHV conditions in a VG ADES 400 UHV spectrometer system. Details regarding system description, sample mounting, manipulation, and data acquisition are given in chapter 2. Quoted binding energies are referred to the Au $4f_{7/2}$ emission at 84 eV from the grounded Au wire that formed the electrical connection to the Rh working electrode.

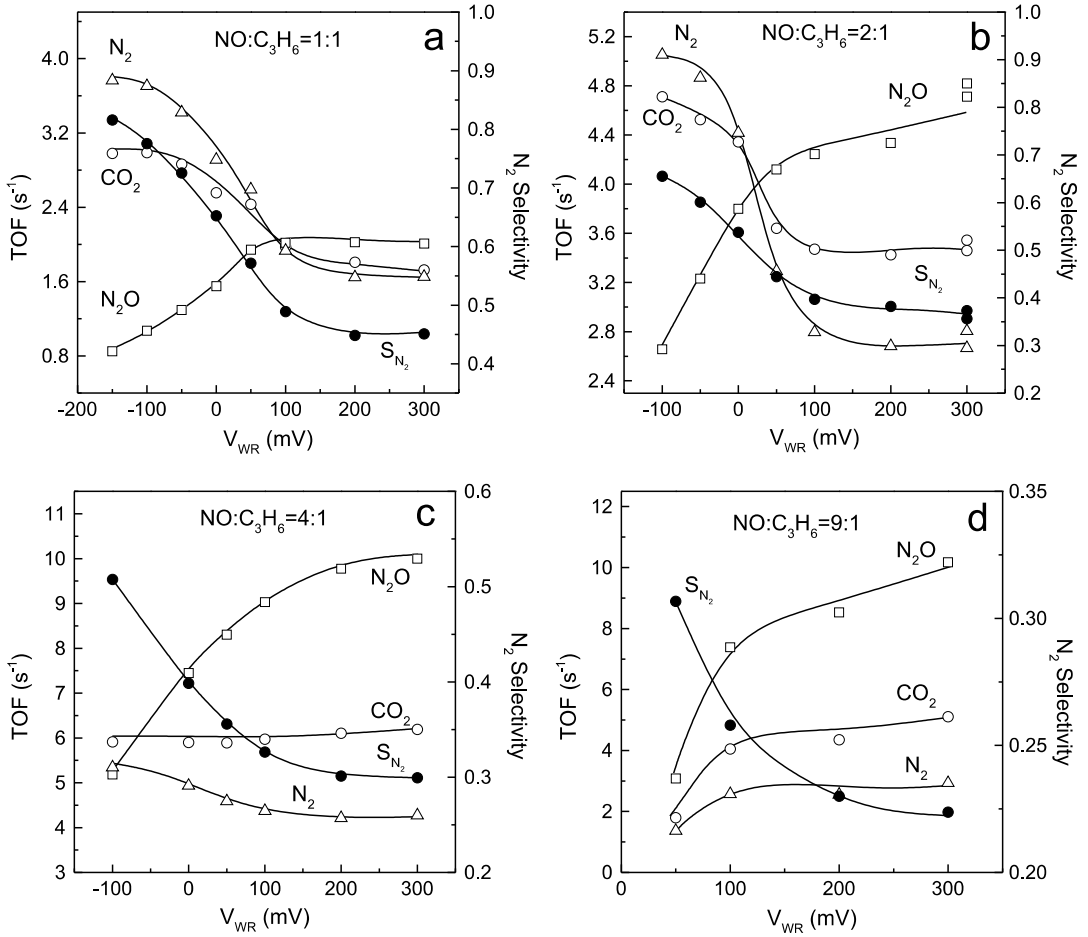

Figure 5.1: Effect of catalyst potential (V_{WR}) on CO_2, N_2 and N_2O formation rates and the nitrogen selectivity at 623 K for different NO and propene partial pressures. (a) $P^{\circ}_{\mathrm{NO}} = 1\,\mathrm{kPa}$, $P^{\circ}_{\mathrm{C_3H_6}} = 1\,\mathrm{kPa}$. (b) $P^{\circ}_{\mathrm{NO}} = 2\,\mathrm{kPa}$, $P^{\circ}_{\mathrm{C_3H_6}} = 1\,\mathrm{kPa}$. (c) $P^{\circ}_{\mathrm{NO}} = 4\,\mathrm{kPa}$, $P^{\circ}_{\mathrm{C_3H_6}} = 1\,\mathrm{kPa}$. (d) $P^{\circ}_{\mathrm{NO}} = 9\,\mathrm{kPa}$, $P^{\circ}_{\mathrm{C_3H_6}} = 1\,\mathrm{kPa}$.

5.3 Effect of catalyst potential on reaction rates

Figures 5.1a-5.1d show steady-state rate data for CO_2, N_2 and N_2O production as a function of V_{WR} at 623 K for different inlet pressures (P°_{NO}, $P^{\circ}_{\mathrm{C_3H_6}}$) of nitric oxide and propene, $P^{\circ}_{\mathrm{NO}} = 1\,\mathrm{kPa}$ and $P^{\circ}_{\mathrm{C_3H_6}} = 1\,\mathrm{kPa}$ (a), $P^{\circ}_{\mathrm{NO}} = 2\,\mathrm{kPa}$ and $P^{\circ}_{\mathrm{C_3H_6}} = 1\,\mathrm{kPa}$ (b), $P^{\circ}_{\mathrm{NO}} = 4\,\mathrm{kPa}$ and $P^{\circ}_{\mathrm{C_3H_6}} = 1\,\mathrm{kPa}$ (c), $P^{\circ}_{\mathrm{NO}} = 9\,\mathrm{kPa}$ and $P^{\circ}_{\mathrm{C_3H_6}} = 1\,\mathrm{kPa}$ (d). Under these conditions CO_2, N_2, N_2O and H_2O were the only products. Accurate measurement of the water production rate was not possible due to partial condensation within the sampling system. However, the behaviour of the H_2O rate was qualitatively the same as the CO_2 rate under all conditions. Rates are expressed as turnover frequency (TOF), i. e. molecules of product per Rh surface atom per second. Also shown in figure 5.1 is the V_{WR} dependence of the nitrogen selectivity ($S_{\mathrm{N_2}}$) defined as the ratio of nitrogen rate

Table 5.1: Effect of NO:C_3H_6 ratio on $\rho_i = r_i^p / r_i^u$ and nitrogen selectivity. u, p refer to unpromoted and optimally promoted cases, respectively.

$P^\circ_{NO} : P^\circ_{C_3H_6}$	ρ_{CO_2}	ρ_{N_2}	ρ_{N_2O}	$S^u_{N_2} \rightarrow S^p_{N_2}$
1 kPa : 1 kPa	1.7	2.4	0.4	45% → 82%
2 kPa : 1 kPa	1.4	1.9	0.6	36% → 66%
4 kPa : 1 kPa	1	1.3	0.5	30% → 51%
9 kPa : 1 kPa	0.35	0.5	0.3	22% → 31%

to the sum of the nitrogen + nitrous oxide rates, i. e. $S_{N_2} = r_{N_2}/(r_{N_2} + r_{N_2O})$. As can be seen from figure 5.1a, decreasing V_{WR} (Na pumping toward the Rh catalyst) causes an increase in the rate of CO_2 and N_2 formation and a decrease in the N_2O production. This induces a remarkable increase in the nitrogen selectivity. The same trends in overall catalytic activity and nitrogen selectivity are visible in figure 5.1b. Figure 5.1c shows that the effects of electro-pumping Na decrease as the NO:C_3H_6 ratio is increased, i. e. in this case decreasing V_{WR} causes little change in the CO_2 rate, a small increase in the N_2 rate, and a substantial decrease in the N_2O rate, resulting in a significant increase in the nitrogen selectivity. Figure 5.1d shows that as the NO:propene ratio increases further, decreasing V_{WR} causes a decrease in all reaction rates but still results in an increase in the nitrogen selectivity. Note that the reaction rates over the unpromoted catalyst ($V_{WR} = +300\,mV$) increased as the partial pressure of NO is increased from 1 kPa to 4 kPa (figures 5.1a-c) at fixed partial pressure of propene. However, further increasing P°_{NO} to 9 kPa caused the rates to decrease. This is in excellent agreement with the kinetic data discussed below (figures 5.3a-c).

In every case the system's behaviour was reversible: returning the catalyst potential to +300 mV (Na-free surface) restored the unpromoted reaction rates. It is apparent that the promotional effect increased as the gas composition became more reducing (lower NO:C_3H_6 ratios). This effect is illustrated in table 5.1 which shows the ratio (ρ) of the unpromoted and optimally promoted reaction rates as a function of the NO:C_3H_6 ratio. Also shown in table 5.1 is the variation of the unpromoted and optimally promoted values of the S_{N_2} with NO:propene ratio. It is evident that increasing the NO:propene ratio causes: (i) a decrease in all ρ values and (ii) a decrease in nitrogen selectivity for both the unpromoted and optimally promoted catalyst. These observations are also in good agreement with the kinetic measurements described below.

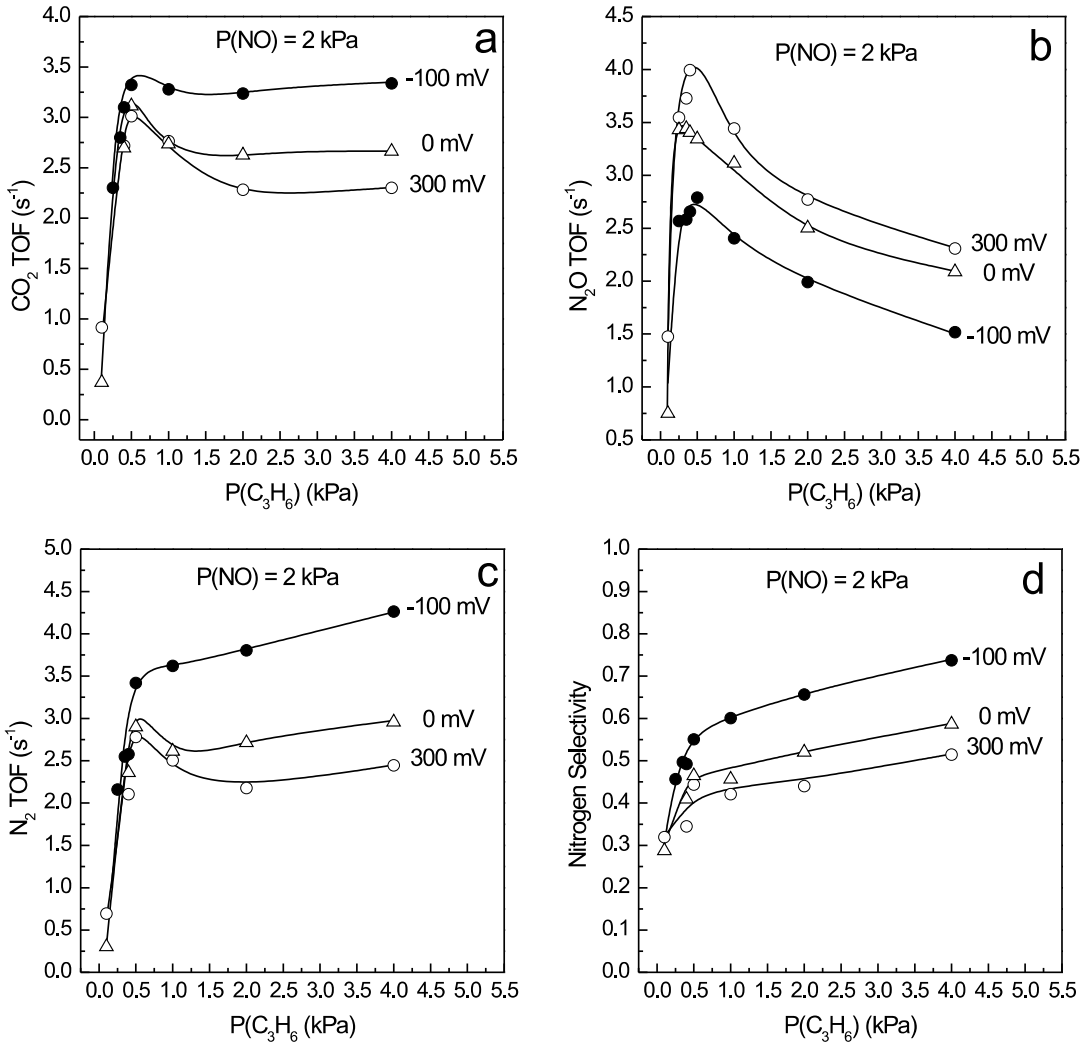

Figure 5.2: Effect of propene partial pressure on the rates of CO_2 (a), N_2 (b), and N_2O (c) formation and on nitrogen selectivity (d), for three different fixed catalyst potentials at 623 K and $P_{NO} = 2$ kPa.

5.4 Effect of partial pressures on reaction rates

Parts a, b and c of figure 5.2 show the turnover frequencies of CO_2, N_2O and N_2 production at 623 K for three different values of catalyst potential as a function of the of propene partial pressure, for a fixed NO partial pressure (2 kPa). Figure 5.2d shows corresponding results for the nitrogen selectivity. The observed rate variations show that the reaction follows Langmuir-Hinshelwood type kinetics, with the characteristic rate maximum reflecting competitive adsorption of the two reactants. It is apparent that as the catalyst potential was decreased to more negative values (increasing the sodium coverage), there was an increase in the CO_2 and N_2 production rates and a decrease in

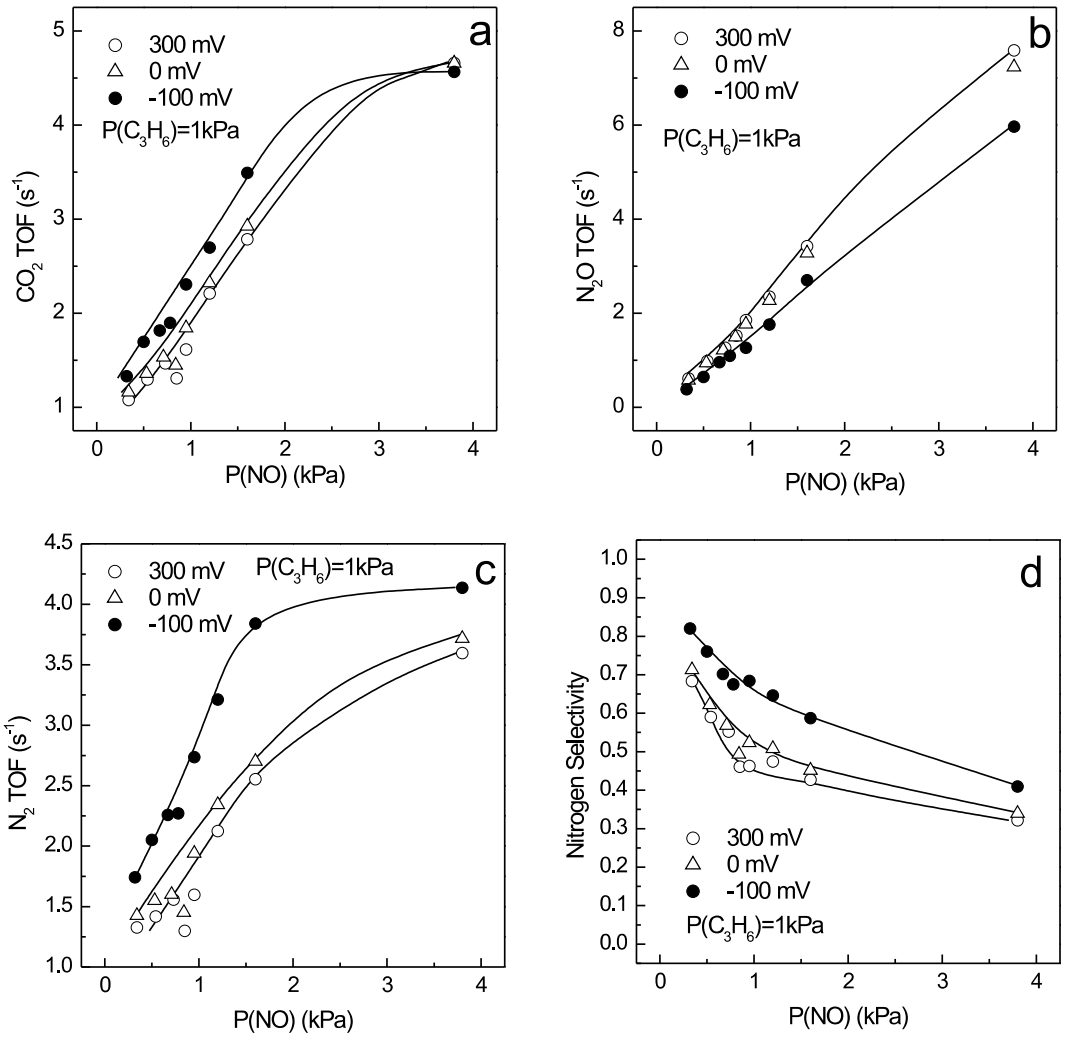

Figure 5.3: Effect of NO partial pressure on the rates of CO_2 (a), N_2 (b), and N_2O (c) formation and on nitrogen selectivity (d), for three different fixed catalyst potentials at 623 K and $P_{C_3H_6}$ = 1 kPa.

the N_2O rate. This resulted in an increase in nitrogen selectivity over the whole range of partial pressures (figure 5.2d). Figure 5.2d also shows that the nitrogen selectivity of the unpromoted and promoted catalyst increases as the C_3H_6:NO ratio is increased.

Figures 5.3a-d depict analogous results for the effect of NO at three different catalyst potentials for a fixed (1 kPa) partial pressure of propene. In this case the Langmuir-Hinshelwood rate maxima were inaccessible within the NO partial pressure range of our experiments, reflecting the weaker adsorption of NO relative to propene. In accord with the catalyst potential dependence of the reaction rates (figure 5.1), Figure 5.3a-d show that as the catalyst potential decreased the CO_2 and N_2 rates and nitrogen selectivity increased while the N_2O rate decreased.

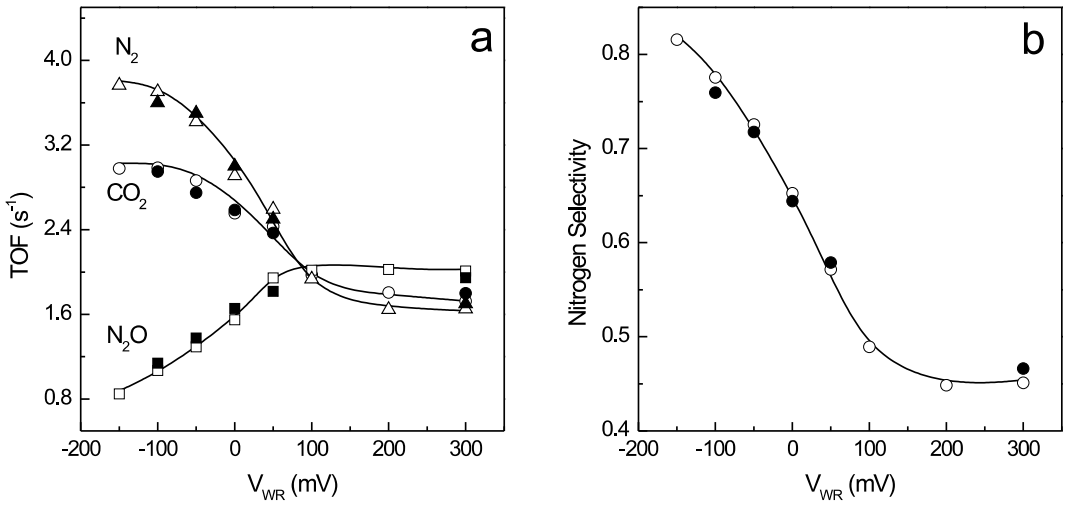

Figure 5.4: Effect of added CO_2 on the rates of CO_2, N_2, and N_2O formation (a) and on nitrogen selectivity (b). $P_{C_3H_6} = P_{NO} = 1\,\text{kPa}$, $T = 623\,\text{K}$ and $P_{CO_2} = 0\,\text{kPa}$ (open symbols) and $P_{CO_2} = 0.5\,\text{kPa}$ (closed symbols).

A comparison of the trends shown in figures 5.2 and 5.3 indicates that increasing amounts of sodium on the catalyst (decreasing V_{WR}) resulted in an increase in the CO_2 and N_2 formation rates, and a decrease in the N_2O rate. These effects are more pronounced at higher propene:NO ratios, in agreement with the results displayed in table 5.1 and described in the previous section. Note also that the nitrogen selectivity of the unpromoted and promoted catalysts decreased as the NO:propene ratio increased (figures 5.2d and 5.3d), in line with the data presented in table 5.1.

5.5 Effect of CO_2 partial pressure on reaction rates

As will be shown in the next section, spectroscopic data suggest that the chemical state of the promoter phase under reaction conditions is sodium carbonate. Therefore we investigated the effect of deliberately adding CO_2 to the reaction mixture. Figure 5.4a shows the steady-state rates of CO_2, N_2 and N_2O formation *versus* the catalyst potential at 623 K for a reaction mixture $P^\circ_{C_3H_6} = P^\circ_{NO} = 1\,\text{kPa}$. Figure 5.4b shows the corresponding nitrogen selectivity data. The open symbols correspond to $P^\circ_{CO_2} = 0\,\text{kPa}$, i. e. to the conditions corresponding to figure 5.1a (no CO_2), whereas the closed symbols correspond to $P^\circ_{CO_2} = 0.5\,\text{kPa}$. It is evident that CO_2 addition had no detectable effects.

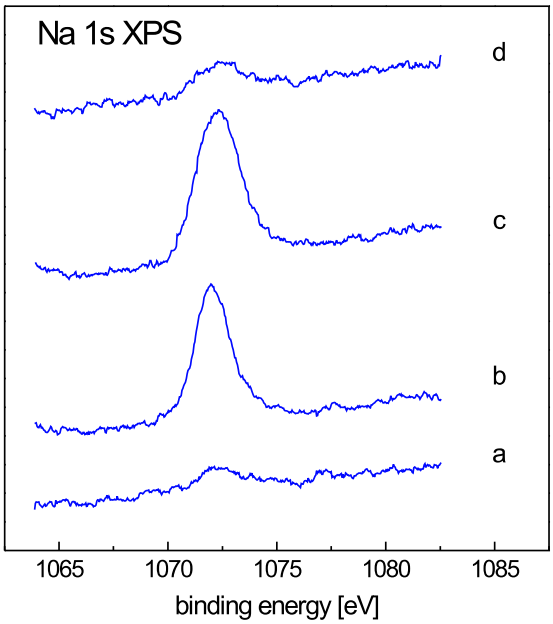

Figure 5.5: Na 1s XP spectra acquired after exposure to (1 kPa of propene + 1 kPa of NO) at 623 K with $V_{WR} = +600$ mV (a) and with $V_{WR} = -100$ mV (b). Spectrum (c) was acquired after spectrum (b) by heating to 623 K. Spectrum (d) was taken after heating at 623 K with $V_{WR} = +600$ mV.

5.6 X-ray Photoelectron Spectroscopy

XP spectra were obtained immediately after exposing the appropriately biased catalyst film to the conditions of temperature and reactants partial pressures typical of those encountered in the reactor, in order to determine what stable surface species were present under reaction conditions. During exposure of the catalyst to the reaction mixture, the V_{WR} values were such that the Rh film was either (i) electrochemically clean (+600 mV, unpromoted) or (ii) sodium promoted (−100 mV). A description of the procedure followed to obtained the post-reaction XP spectra can be found in chapter 2. Spectra were acquired after exposing the sample to a mixture of 1 kPa of propene + 1 kPa of NO, diluted in He, at 623 K and 1 bar total pressure. In every case Na 1s, Rh 3d, C 1s, O 1s, N 1s XP spectra were obtained under the following four sets of conditions: (i) after exposing the unpromoted sample to reaction gas (spectrum *a*); (ii) after exposing the promoted sample to reaction gas (spectrum *b*); (iii) after heating the post-reaction promoted sample in UHV at 623 K under open circuit conditions (spectrum *c*) and finally (iv) after cleaning the surface by imposing a positive bias ($V_{WR} = +600$ mV) at 623 K (spectrum *d*). Spectra *a* and *b* were acquired at room temperature under open circuit conditions; spectrum *c* at 623 K, open circuit; spectrum *d* at 623 K and +600 mV.

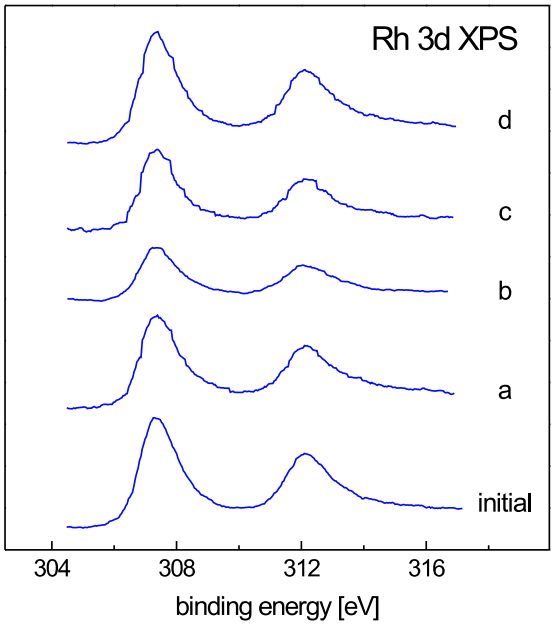

Figure 5.6: Rh 3d XP spectra acquired before exposing the sample to the reaction mixture (initial) and after exposure to (1 kPa of propene + 1 kPa of NO) at 623 K with $V_{WR} = +600$ mV (a) and with $V_{WR} = -100$ mV (b). Spectrum (c) was acquired after spectrum (b) by heating to 623 K. Spectrum (d) was taken after heating at 623 K with $V_{WR} = +600$ mV.

Figure 5.5 shows the resulting Na 1s XP spectra for each of the four conditions described above. Within the sampling depth of the technique (~ 12 Å, $\lambda = 5$ Å, photoelectron kinetic energy 180 eV), a small amount of sodium was detected after exposing the sample to the reaction mixture under unpromoted conditions (spectrum *a*). We have shown in chapter 3 and it has been also shown in the literature [6] that this residual Na signal is due to sodium in the β" alumina electrolyte which is spectroscopically visible through the cracks and imperfections in the porous rhodium film. The post-reaction promoted sample ($V_{WR} = -100$ mV) exhibits a march larger Na 1s signal (spectrum *b*). Heating the promoted sample to 623 K increased the Na 1s signal and broadened the peak to higher binding energy (spectrum *c*). These changes, which reflect a change in the nature of the sodium promoter phase, can be correlated with corresponding changes in the C 1s and O 1s emission, as discussed below. Electrochemical cleaning (catalyst potential held at +600 mV) caused a large decrease in Na 1s intensity, resulting in a spectrum essentially identical to spectrum *a*.

Rh 3d XP spectra are shown in figure 5.6. Two points should be noted. Firstly, the binding energy and lineshape are invariant, indicating that there was no oxidation of the rhodium film under any conditions. The second point concerns the degree of intensity attenuation which provides a measure of the amount of material present on

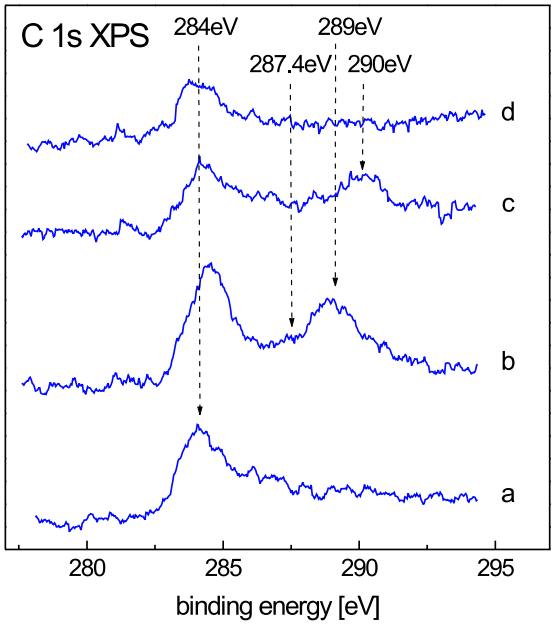

Figure 5.7: C 1s XP spectra acquired after exposure to (1 kPa of propene + 1 kPa of NO) at 623 K with $V_{WR} = +600$ mV (a) and with $V_{WR} = -100$ mV (b). Spectrum (c) was acquired after spectrum (b) by heating to 623 K. Spectrum (d) was taken after heating at 623 K with $V_{WR} = +600$ mV.

the surface. For purposes of comparison the clean surface spectrum taken before any exposure of the catalyst to reaction gas is also shown (labeled 'initial'). After exposing the unpromoted sample to reaction gas the Rh XPS signal was attenuated by 13%. This corresponds to a uniform layer of material ~ 2.6 Å thick covering about half the Rh surface ($\lambda = 11.62$ Å [7]). A substantial increase in attenuation of the Rh signal was observed when the promoted sample was exposed to reaction gas (spectrum *b*). The attenuation of 53% corresponds to a uniform layer of material ~ 7 Å thick covering the entire Rh surface. Spectrum *d* was acquired after heating and electrochemically cleaning the surface: note that the Rh signal recovered its initial intensity indicating complete removal of the alkali promoter phase. This is in agreement with the behaviour of the Na 1s emission, as discussed above, the C 1s, O 1s and N 1s emission as discussed below, and with the reactor data presented above.

Carbon 1s XP spectra provide information about the chemical identity of the Na compound(s) that are formed under reaction conditions (figure 5.7). These data suggest that Na is present on the surface of the working catalyst as a carbon-containing compound or compounds. The C 1s region comprises two principal features, one at lower binding energy (~284–285 eV) and the other at higher binding energy (~288–290 eV). The former is due to elemental carbon (284 eV [8]) and propene fragments (284–285 eV), whereas

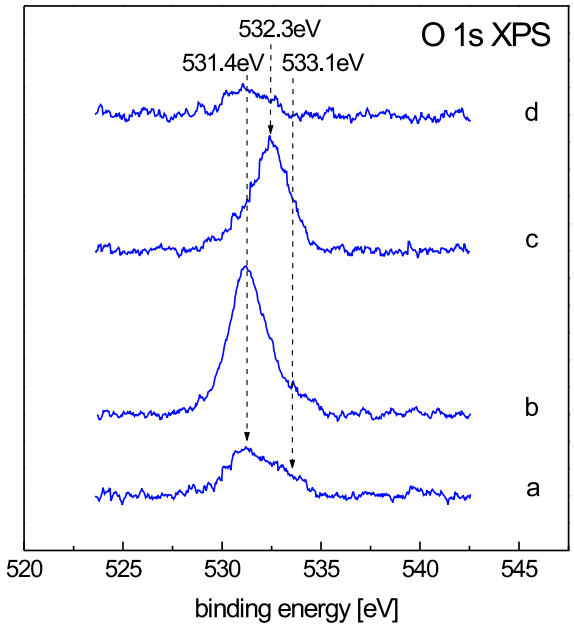

Figure 5.8: O 1s XP spectra acquired after exposure to (1 kPa of propene + 1 kPa of NO) at 623 K with $V_{WR} = +600$ mV (a) and with $V_{WR} = -100$ mV (b). Spectrum (c) was acquired after spectrum (b) by heating to 623 K. Spectrum (d) was taken after heating at 623 K with $V_{WR} = +600$ mV.

the latter corresponds to sodium carbonate (289 eV [9]). Exposure of the unpromoted catalyst to reaction gas (spectrum *a*) led to the appearance of a broad poorly resolved feature containing at least two components: (i) elemental carbon at 284 eV and (ii) propene fragments at 284–285 eV. Exposing the promoted catalyst to reaction mixture (spectrum *b*) caused the appearance of at least four features, as follows: (i) elemental carbon at 284 eV; (ii) propene fragments at 284–285 eV; (iii) a small but reproducible shoulder at 287.4 eV which may be due to partially oxidised propene fragments [8]; and (iv) a peak at 289 eV due to sodium carbonate. Heating this sample to 623 K under UHV and open circuit conditions resulted in spectrum *c* which exhibits the same low binding energy features as spectrum *b* (284 eV and 284–285 eV). However, there are two differences: (i) the peak at 287.4 eV is absent in spectrum *c* and (ii) the peak at 289 eV in spectrum *b* is replaced by a much smaller peak at 290 eV in spectrum *c*. The latter changes correlate with the changes observed in the Na 1s and O 1s regions, shortly to be described. Finally, setting V_{WR} to +600 mV (thus pumping Na away from the surface) caused the disappearance of 290 eV peak leaving only a very small amount of elemental carbon on the surface (spectrum *d*) in accord with the corresponding changes in the Rh 3d, O 1s and Na 1s regions.

The O1s spectral region (figure 5.8) contains three principal contributions. The

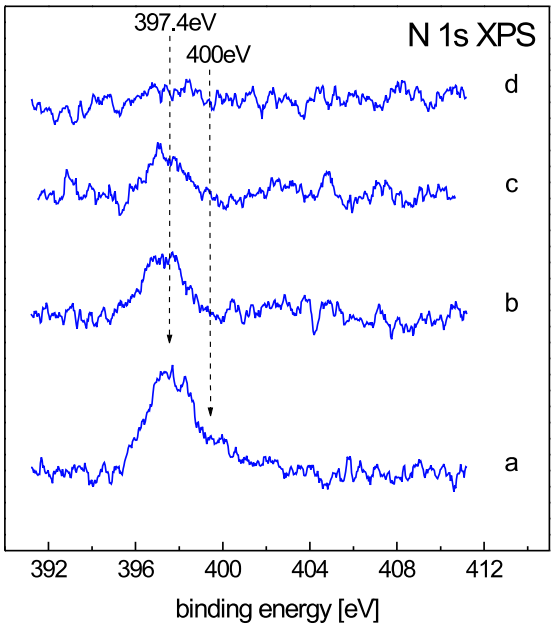

Figure 5.9: N 1s XP spectra acquired after exposure to (1 kPa of propene + 1 kPa of NO) at 623 K with $V_{WR} = +600$ mV (a) and with $V_{WR} = -100$ mV (b). Spectrum (c) was acquired after spectrum (b) by heating to 623 K. Spectrum (d) was taken after heating at 623 K with $V_{WR} = +600$ mV.

lower binding energy peak is due to chemisorbed oxygen (531.4 eV [10]) and carbonate (531.6 eV [11]). The intermediate binding energy peak (532.3 eV) must be associated with a sodium compound since it disappears under positive bias. The highest binding energy peak (533.1 eV) has previously been attributed to subsurface oxygen by Tolia *et al.* [10].

On the above basis we may make the following assignments. Exposing the unpromoted catalyst to reaction conditions generates chemisorbed oxygen and subsurface oxygen (spectrum *a*). Exposing the Na-promoted catalyst to reaction conditions generates chemisorbed oxygen, sodium carbonate and subsurface oxygen. Heating this surface under open circuit conditions results in a dramatic change in the O 1s spectrum which correlates with changes in the Na 1s lineshape and in the C 1s intensity and binding energy. Finally, cleaning the surface by applying a $V_{WR} = +600$ mV resulted in the disappearance of the O 1s emission due to sodium carbonate, leaving only a small amount of chemisorbed oxygen on the surface.

Figure 5.9 shows the corresponding N 1s XP spectra. Two main features are readily distinguished: (i) chemisorbed N at 397.4 eV [12] and (ii) chemisorbed NO at 400 eV [13]. That is, exposing the unpromoted sample to reaction conditions resulted in the presence of both chemisorbed N and NO (spectrum *a*). However, when the sample was promoted

with Na, only chemisorbed N was detected (spectrum *b*). Heating this surface to 623 K, under UHV led to eventual disappearance of the peak due to N(a) (spectrum *d*).

5.7 Discussion

The effects of controlled variations in Na loading on the catalytic behaviour of the rhodium film may be summarised as follows:

(i) Sodium causes an increase in the rate of CO_2 and N_2 formation for $P_{NO}/P_{C_3H_6} < 4$.

(ii) Sodium causes a decrease in the N_2O production rate.

(iii) Sodium causes an increase in the nitrogen selectivity under all the conditions explored.

Figures 5.1-5.3 and Table 5.1 show that the effectiveness of sodium promotion is strongly dependent on gas phase composition. The clean surface rate increased and the effect of sodium decreased as the NO:propene ratio increased (figure 5.3). Correspondingly, the promotional effect of sodium increased as the NO:propene ratio decreased (figure 5.2). These observations provide a strong indication as to the mode of action of the electro-pumped Na in promoting the reduction of NO by propene. As discussed below and suggested earlier in connection with previous work on EP of the $CO + NO$ reaction over Rh (see chapter 4) and Pt [14] and of the $NO+C_3H_6$ reaction over Pt [6], we propose that the promotional effect is due to enhanced NO chemisorption and dissociation induced by electrochemically-pumped sodium. NO dissociation triggers the reaction by producing the O(a) species responsible for initiating the ensuing oxidation reactions of adsorbed propene and propene fragments. The way in which Na enhances the strength of NO adsorption and decreases the activation energy to its dissociation is well understood theoretically [15]; it has also been demonstrated experimentally (see for example [16–19]).

The dependence of activity and selectivity on catalyst potential (V_{WR}) for different NO:propene ratios may be rationalised by considering the relative effect of Na on the surface chemistry of co-adsorbed propene and NO. For low NO:propene ratios and at high positive potential the Rh surface is free of sodium (figure 5.5, spectrum *a*) and covered mainly with propene. As the catalyst potential is decreased (pumping Na to the Rh surface), the electronic effect of the sodium promoter strengthens the Rh-N bond (increasing NO coverage) and weakens the $N-O$ bond (facilitating NO dissociation). Thus, the effect of the promoter is to enhance surface coverage by NO and its dissociation products. Our XPS data provide evidence in support of this view. Thus a comparison of

spectra *a* and *b* in figure 5.8 shows that the amount of chemisorbed oxygen (produced by NO dissociation) is greater when sodium is present on the catalyst. Strong corroboration is provided by spectra *a* and *b* in figure 5.9 which show that NO is only detected on the rhodium surface only when there is no Na present.

Sodium also enhances the selectivity toward N_2 formation. This quantity is determined by the competition between the following surface reactions

$$\mathrm{NO(a) + N(a) \rightarrow N_2O(g) + 2S} \tag{5.1}$$

$$\mathrm{N(a) + N(a) \rightarrow N_2(g) + 2S} \tag{5.2}$$

Where S represents a vacant site for adsorption and (a) and (g) stand for adatom and gas respectively. The observed increase in selectivity is a consequence of the Na-induced decrease and increase, respectively, in the amounts of molecularly adsorbed NO and atomic N on the surface, thus favouring the first reaction over the second. Qualitatively similar effects on nitrogen selectivity have been found for the sodium promoted NO reduction by CO (see chapter 4 and reference [14] and propene [6].

As noted above, the promotional effect of Na diminished as the NO:propene ratio increased. For example, figure 5.1d shows that at NO:propene = 9, decreasing the catalyst potential (increasing the sodium coverage) resulted in a decrease of all reaction rates. This may be understood in terms of the effect of sodium on the competitive adsorption of the reactants. Alkali decreases the chemisorption of propene (an electron donor) while enhancing the chemisorption of NO (an electron acceptor). Under reducing conditions (low NO:propene), self-poisoning due to excessive adsorption of propene and its decomposition products can be counteracted by the opposite effects of alkali on the adsorption of NO and propene. However, as the NO:propene ratio is increased beyond a certain point, alkali-enhanced adsorption of NO and alkali-decreased adsorption of propene deplete the surface from reductant species. Thus, the system now self-poisons due to excessive adsorption of NO resulting in the observed decrease in reaction rates.

The key assumption underlying much of the preceding discussion is that changes in V_{WR} result in reversible pumping of Na to/from the Rh from/to the solid electrolyte. Our XPS data (figure 5.5) convincingly demonstrate that such reversible transport of sodium between the solid electrolyte and the gas-exposed surface of the Rh film does indeed occur under the conditions of catalyst potential and temperature used for the reactor studies. This important observation substantiates our view of the mode of action of the EP system: it works by electrochemically controlled spillover or back-spillover of the promoter species between the electrolyte and the metal catalyst. Figure 5.5 illustrates

the direct correspondence between catalyst potential and sodium coverage. It also shows that the processes involved are fully reversible, since the original spectrum is restored upon electrochemically pumping Na away from the Rh surface. This is in excellent agreement with the reversible dependence of reaction rates on catalyst potential.

Controlling the catalyst potential controls the level of sodium promoter on the catalyst. In the presence of a reactive gas atmosphere, the promoter phase must be present as sodium-containing compounds. The XPS data reveal the chemical identity of the principal surface compounds that are present; they also provide some indication of the likely morphology of these compounds.

The Rh 3d XP spectra (figure 5.6) are revealing in regard to the extent of loading and morphology of the Na surface compounds. First, recall that the attenuation of Rh 3d emission from the post-reaction unpromoted surface corresponds to the presence of about half a monolayer of adsorbed material. That is, the metal surface is extensively covered with N, NO, O and propene fragments. The analogous data for the promoted catalyst nominally correspond to uniform coverage by a film ~ 7 Å thick, consisting mainly of the sodium promoter phase. However, since the promoted surface is even more active than the unpromoted surface, it follows that a substantial fraction of the former must consist of active metal sites. Therefore the material contained in the nominal ~ 7 Å thick layer must be distributed as 3D crystallites on an otherwise bare (promoted) metal surface. In other words our picture of the promoted working catalyst under steady state conditions is one of gas-exposed Rh sites modified by submonolayer amounts of the alkali promoter in co-existance with areas covered by crystallites of Na promoter compound. The size and distribution of these crystallites cannot of course be inferred from the XPS data; this would require the application of an imaging technique and such experiments are planned.

The C 1s and O 1s data shown in figure 5.7 (spectrum *b*) and figure 5.8 (spectrum *b*) provide strong evidence that the promoter phase consists principally, if not entirely, of Na_2CO_3. Heating this promoted surface under UHV conditions results variously in changes of lineshape, binding energy and/or intensity in the Na 1s, C 1s, O 1s and Rh 3d emission, as described in detail in Section 5.6. Here it is worth recalling that the literature contains a range of binding energies for sodium carbonate, depending on the nature of the sample. Quoted C 1s binding energies range from 289.4 eV for bulk sodium carbonate [20] to 290.4 eV for submonolayer quantities [21], the corresponding range for O 1s binding energies being 531.6 eV–532.2 eV. Therefore, we propose that the observed thermally induced changes under vaccum reflect changes in morphology and chemical state of the promoter phase. Thus partial evaporation of 3D crystallites of

sodium carbonate to yield thinner structures would account for the observed decrease in C 1s carbonate emission. Interestingly, the Na 1s emission actually increased, suggesting formation of some compound (possibly an oxide of sodium) that wets the Rh surface better than carbonate.

The present results are in excellent agreement with the work of MacLeod *et al.* on sodium promotion of NO reduction by propene over conventional dispersed Rh/γ alumina catalysts [5]. The Na-induced rate gains and selectivity improvements observed with the dispersed catalysts ($\rho_{N_2} = 3.3$, $\Delta S = 53\% \rightarrow 90\%$) are entirely comparable with those found here under similar conditions: $\rho_{N_2} = 2.4$, $\Delta S = 45\% \rightarrow 82\%$. Furthermore, the decrease in promotion with increasing the NO:propene ratio was also found with the sodium promoted dispersed catalysts [5]. Therefore we conclude that the mechanistic interpretations offered here also apply to the dispersed Rh catalysts. The EP approach eliminates ambiguities that arise with dispersed catalyst data due to the unknown distribution of the promoter between the metal and supported phases. Thus we may infer with some confidence that Na promotion of conventional dispersed Rh catalysts is due to effects on the surface chemistry of the metal component and that effects of the alkali on the support are not significant.

5.8 Conclusions

1. Electrochemical promotion of Rh is due to the reversible transport of ions between the solid electrolyte and the metal film catalyst with which it is in contact. The coverage of promoter species is controlled by the catalyst potential, measured with respect to a reference electrode.

2. In the present case, EP of Rh by Na can greatly enhance its catalytic performance with respect to both activity and nitrogen selectivity in the reduction of NO by propene. These improvements are most pronounced under reducing conditions, decreasing as the NO partial pressure rises. They are unaffected by deliberate addition of CO_2.

3. Promotion is due to the Na-induced dissociation of NO, the key reaction-initiating step.

4. Under reaction conditions, the sodium is present as a carbonate, some of which is in the form of 3D crystallites.

5. Comparison of these EP results with corresponding data obtained using conventional dispersed Rh catalysts shows that Na promotion of the practical materials

is due to the effects of alkali on the metal surface chemistry. Effects due to alkali on the support must be insignificant.

Bibliography

[1] K. C. Taylor, Nitric oxide catalysis in automotive exhaust systems, Catalysis reviews science and engineering **35**, 457–481 (1993).

[2] M. Shelef and G. W. Graham, Why rhodium in automotive three-way catalysts?, Catalysis reviews science and engineering **36**, 433–457 (1994).

[3] K. Tomishige, K. Asakura, and Y. Iwasawa, Observation of molecular reaction intermediate and reaction mechanism for NO dissociation and NO-H_2 reaction on Rh-Sn/SiO_2 catalysts, Journal of Catalysis **157**, 472–481 (1995).

[4] T. Chafik, A. M. Efstathiou, and X. E. Verykios, Effects of W^{+6} doping of TiO_2 on the reactivity of supported Rh toward NO: transient FTIR and mass spectroscopy studies, Journal of Physical Chemistry B **101**, 7968–7977 (1997).

[5] N. Macleod, J. Issac, and R. M. Lambert, Sodium promotion of the NO + C_3H_6 reaction over Rh/γ-Al_2O_3 catalysts, Journal of Catalysis **193**, 115–122 (2000).

[6] I. V. Yentekakis, A. Palermo, N. C. Filkin, M. S. Tikhov, and R. M. Lambert, *In situ* electrochemical promotion by sodium of the platinum-catalysed reduction of NO by propene, Journal of Physical Chemistry B **101**, 3759–3768 (1997).

[7] D. R. Penn, Quantitative chemical analysis by ESCA, Journal of Electron Spectroscopy and Related Phenomena **9**, 29–40 (1976).

[8] Z. Paål, R. Schlögl, and G. Ertl, Photoelectron spectroscopy of polycrystalline platinum catalysts, Journal of the Chemical Society, Faraday Transactions **88**, 1179–1189 (1992).

[9] T. Seyller, D. Borgmann, and G. Wedler, Interaction of CO_2 with Cs-promoted Fe(110) as compared to Fe(110)/K + CO_2, Surface Science **400**, 63–79 (1998).

[10] A. A. Tolia, R. J. Smiley, W. N. Delgass, C. G. Takoudis, and M. J. Weaver, Surface oxidation of rhodium at ambient pressures as probed by surface-enhanced Raman and X-ray photoelectron spectroscopies, Journal of Catalysis **150**, 56–70 (1994).

[11] C. D. Wagner, D. A. Zatko, and R. H. Raymond, Use of oxygen KLL Auger lines in identification of surface chemical states by electron spectroscopy for chemical analysis, Analytical Chemistry **52**, 1445–1451 (1980).

[12] R. J. Baird, R. C. Ku, and P. Wynblatt, The chemisorption of CO and NO on Rh(110), Surface Science **97**, 346–362 (1980).

[13] L. A. DeLouise and N. Winograd, Adsorption and desorption of NO from Rh(111) and Rh(331) surfaces, Surface Science **159**, 199–213 (1985).

[14] A. Palermo, R. M. Lambert, I. R. Harkness, I. V. Yentekakis, O. Mar'ina, and C. G. Vayenas, Electrochemical promotion by Na of the platinum-catalysed reaction between CO and NO, Journal of Catalysis **161**, 471–479 (1996).

[15] N. D. Lang, S. Holloway, and J. K. Nørskov, Electrostatic adsorbate-adsorbate interactions: the poisoning and promotion of the molecular adsorption reaction, Surface Science **150**, 24–38 (1985).

[16] I. R. Harkness and R. M. Lambert, Chemisorption and reactivity of nitric oxide on Na-dosed platinum(111), Journal of the Chemical Society, Faraday Transactions **93**, 1425–1429 (1997).

[17] L. Bugyi and F. Solymosi, Interaction of NO with clean and K-dosed Rh(111) surfaces. I. AES, TDS and work function studies, Surface Science **188**, 475–489 (1987).

[18] L. Bugyi, J. Kiss, K. Révéz, and F. Solymosi, Interaction of NO with clean and K-dosed Rh(111) surfaces. II. EELS and PES studies, Surface Science **233**, 1–11 (1990).

[19] H. Höchst and E. Colavita, The interaction of CO, NO and O_2 with sodium-promoted Rh(100) surfaces, Journal of Vacuum Science and Technology A **4**, 1442–1445 (1986).

[20] U. Gelius, P. F. Hedén, J. Hedman, B. J. Lindberg, R. Manne, R. Nordberg, C. Nordling, and K. Siegbahn, Molecular Spectroscopy by means of ESCA. III. Carbon compounds, Physica Scripta **2**, 70–80 (1970).

[21] J. Nerlov, S. V. Christensen, S. Weichel, E. H. Pedersen, and P. J. Møller, A photoemission study of the coadsorption of CO_2 and Na on TiO_2(110)-(1x1) and (1x2) surfaces: adsorption geometry and reactivity, Surface Science **371**, 321–336 (1997).

CHAPTER 6

The effect of oxygen on Rh–catalysed nitric oxide reduction

6.1 Introduction

The serious environmental implications of NO emission from automotive sources has stimulated a huge amount of pure and applied research directed at catalytic abatement of such emission. Although so-called three-way catalytic converters are very effective in oxidising CO and hydrocarbons, they are substantially less effective in reducing NO to nitrogen, producing N_2O in addition [1]. Although nitrous oxide is not yet a regulated pollutant, it is a powerful greenhouse gas, and future legislation is likely to include restrictions on N_2O emission. In this connection, note that over a wide range of engine operating conditions N_2O emission accounts for $60-80\%$ of the NO converted by current three-way converters [2]. Another important limitation of three-way converters is that they are ineffective for NO reduction in the presence of excess gaseous oxygen, because O_2 reacts faster with the available reductants than NO itself. This prevents the implementation of fuel-efficient, lean-burn spark ignition engines which would otherwise make a very significant contribution to reduced CO_2 emission. Two important fundamental questions arise. First, how can we improve the selectivity towards N_2 formation? Second, to what extent can any such improvements be sustained in the presence of gaseous oxygen?

Current automotive catalytic converters employ various combinations of Pt, Pd and Rh. MacLeod *et al.* have already shown that alkali metal additives substantially improve the catalytic activity and nitrogen selectivity of dispersed palladium and platinum catalysts under simulated three-way conditions [3, 4] . In chapters 4 and 5 we showed

that in the absence of gaseous oxygen, EP by Na of Rh thin film catalysts greatly enhanced both activity and selectivity towards N_2 production in the reduction of NO by CO and by propene. It follows the question of whether these improvements can still be present in the presence of oxygen.

Here we present the results of an EP study of the influence of gaseous oxygen on the alkali-promoted reduction of NO by CO and by propene, reactions that are of prime importance in practice. The effects of oxygen partial pressure and catalyst potential (sodium coverage) on the NO + CO + O_2 and NO + C_3H_6 + O_2 reactions have been investigated. Complementary post-reaction XPS data were acquired in order to monitor changes in the amount and chemical identity of the Na compounds present under a variety of conditions, and to determine changes in oxidation state of the rhodium film.

It is found that sodium does increase both the activity and nitrogen selectivity of rhodium in catalytic reduction of NO by CO or propene, even in the presence of oxygen. Increasing the oxygen partial pressure beyond a certain point decreases the effectiveness of alkali promotion, eventually resulting in a transition to a regime of alkali-induced poisoning. The chemical identity of the alkali surface compounds in the promoted and poisoned regimes is established; the mode of promoter action, the origin of poisoning, and the reaction mechanism are also discussed.

6.2 Experimental methods

The EP samples for catalytic testing and spectroscopic analysis were prepared by depositing a rhodium metal film on one face of a Na β" alumina wafer: this constituted the catalyst (working electrode). Gold counter and reference electrodes were deposited on the other face, all three electrodes being deposited by DC sputtering of Rh or Au in argon. Methods used for characterising the Rh film by XRD, XPS and surface area measurements have been described in chapter 2.

Reactor measurements were performed in a CST-reactor operated at atmospheric pressure. The EP sample was suspended in the reactor with all electrodes exposed to the reactant gas mixture. Inlet and exit gas analysis was carried out by a combination of on-line gas chromatography (Shimadzu-14B; molecular sieve 13X and Haysep-N columns), on-line mass spectrometry (Balzers QMG 064) and on-line non-dispersive infrared analysers (dual channel Siemens Ultramat 6 analysers calibrated for CO/CO_2 and NO/N_2O). N_2, N_2O, CO, CO_2, O_2 and C_3H_6 were separated and their concentrations determined by gas chromatography; additionally, N_2O, CO, CO_2 and NO were

also monitored continuously using the IR detectors after performing the necessary calibrations. Reaction gases (5%NO/He, 5%CO/He, 5%C_3H_6/He, 20%O_2/He, and He) were of ultra-high purity and were fed to the reactor by mass flow controllers (Brooks 5850 TR). The total flow rate was kept constant in all experiments at 34×10^{-5} mol·s^{-1} (500 cm^3(STP)/min). Reactant conversion was restricted to $< 20\%$ in order to avoid mass transfer limitations. Control experiments were carried out in which the total flow was varied by a factor of 5 in order to verify that the observed changes in activity were indeed due to changes in actual surface reaction rates, unaffected by mass transfer limitations. Nitrogen and carbon mass balances always closed to within 5%.

A galvanostat-potentiostat (Ionic Systems) was used to maintain a given potential difference between the working and reference electrodes (potentiostatic mode). All experiments were carried out in potentiostatic mode by following the effect of catalyst potential (V_{WR}, measured with respect to the reference electrode) on the reaction rates.

XPS experiments were performed under UHV conditions (base pressure $< 10^{-10}$ Torr) in a VG ADES 400 UHV spectrometer system equipped with a reaction cell. The EP sample was mounted on a manipulator that allowed translation between the reaction cell and the spectrometer chamber. Full details regarding sample mounting, manipulation, and data acquisition are given in chapter 2. Quoted binding energies are referred to the Au $4f_{7/2}$ emission at 84 eV from the grounded Au wire that formed the electrical connection to the Rh working electrode. Reference spectra for sodium carbonate and sodium nitrate were obtained by pressing small quantities of the pure compounds into the surface of a pure aluminum disc. This technique gave samples that did not exhibit electrostatic charging effects and were not free from carbon contamination as shown in chapter 2.

6.3 Results

6.3.1 Effect of V_{WR} and oxygen concentration on reaction rates

CO as reductant

Figures 6.1a-d show typical steady-state (potentiostatic) rate data obtained for the reduction of nitric oxide by carbon monoxide in the presence of oxygen. Turnover frequencies (TOF) are expressed as molecules of product per Rh surface atom per second. The rates of production of CO_2 (figure 6.1a), N_2O (figure 6.1b) and N_2 (figure 6.1c) at 595 K are shown as a function of catalyst potential V_{WR} for constant inlet pressures of NO and CO ($P^{\circ}_{CO} = P^{\circ}_{NO} = 0.9$ kPa) for a range of oxygen concentration (0, 0.2, 0.4 and 2 kPa). Figure 6.1d shows the effect of catalyst potential and oxygen concentration on

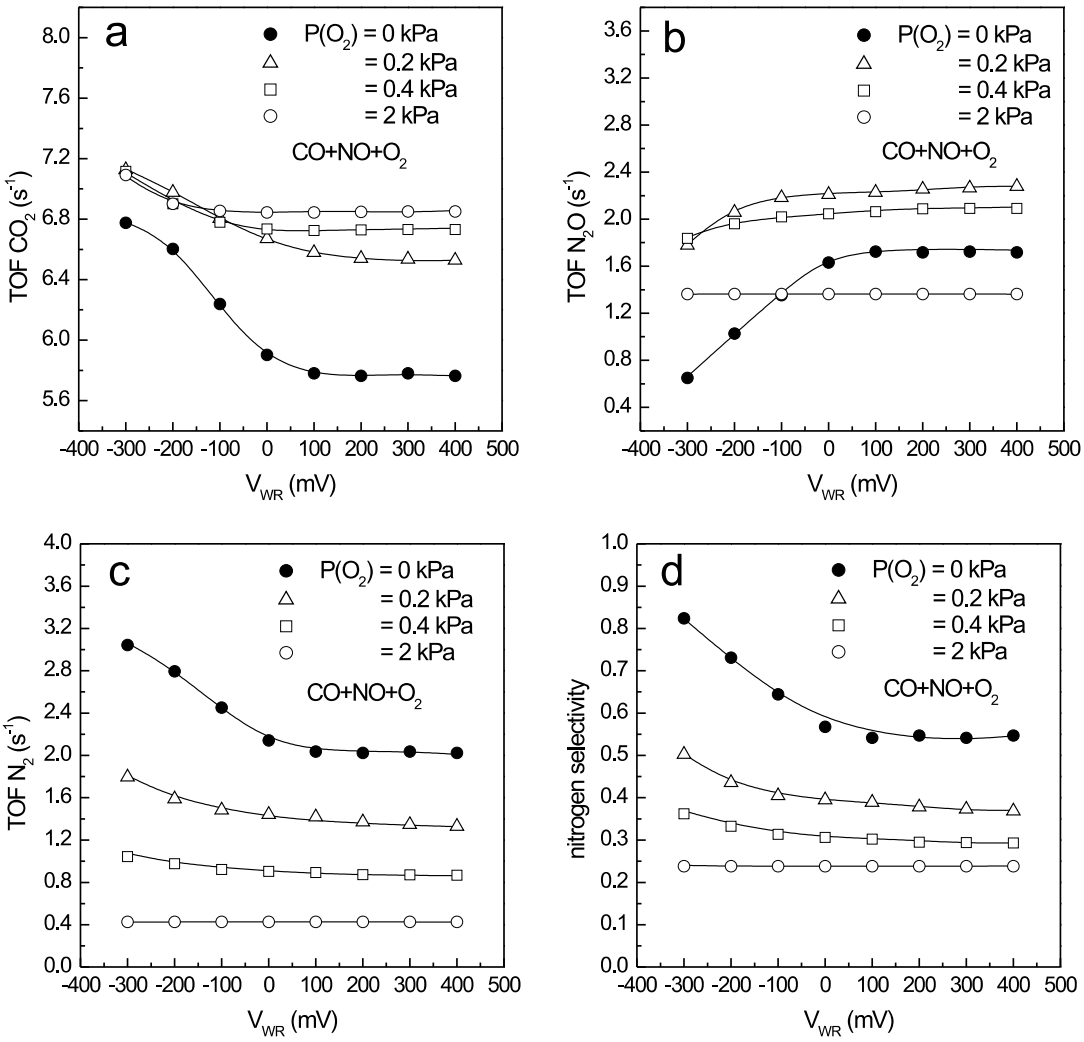

Figure 6.1: Effect of catalyst potential (V_{WR}) on CO_2 (a), N_2O (b), N_2 (c) formation rates and on nitrogen selectivity (d) for different partial pressures of oxygen. Conditions: $T = 595\,\mathrm{K}$, $P^{\circ}_{\mathrm{NO}} = P^{\circ}_{\mathrm{CO}} = 0.9\,\mathrm{kPa}$.

the nitrogen selectivity where this quantity is defined as the ratio of the nitrogen rate to the sum of the (nitrogen + nitrous oxide) rates. It is apparent that the CO_2, N_2O and N_2 reaction rates are dependent on catalyst potential and on the oxygen partial pressure. Decreasing the catalyst potential (thus increasing the sodium coverage) in the absence of gaseous oxygen (black circles) increased the rates of CO_2 and N_2 production. In contrast, the rate of formation of N_2O decreased with increasing sodium coverage. As a result, the selectivity towards nitrogen formation increased. As the oxygen partial pressure increased in the interval $0-0.4\,\mathrm{kPa}$, qualitatively similar results were obtained, but with progressive attenuation of the promoting effect of Na. However, at $P^{\circ}_{\mathrm{O}_2} = 2\,\mathrm{kPa}$ (open circles) the N_2 and N_2O rates (and hence the selectivity) became invariant with

Table 6.1: Effect of increasing the oxygen partial pressure on the Na-induced enhancement of reaction rates and nitrogen selectivities for the CO + NO reaction. u, p stand for unpromoted and optimally promoted, respectively. Conditions $P^{\circ}_{CO} = P^{\circ}_{NO} = 0.9\,\text{kPa}$, $T = 595\,\text{K}$

$P^{\circ}_{O_2}$	ρ_{CO_2}	ρ_{N_2}	ρ_{N_2O}	$S^{u}_{N_2} \rightarrow S^{p}_{N_2}$
0 kPa	1.2	1.5	0.38	54% → 82%
0.2 kPa	1.1	1.35	0.78	37% → 50%
0.4 kPa	1.06	1.2	0.88	30% → 36%
2 kPa	1.03	1	1	24% → 24%

Na loading whereas the CO_2 rate showed a small increase at the highest Na loadings. Table 6.1 summarises relative rate changes (ratios of maximally promoted/unpromoted reaction rates = ρ) and selectivity variations for the various oxygen concentrations. It should be noted that increasing the oxygen partial pressure causes changes in both the unpromoted ($V_{WR} = +400\,\text{mV}$) and promoted ($V_{WR} = -300\,\text{mV}$) conditions. For the unpromoted catalyst, progressively increasing P_{O_2} caused: (i) increased CO_2 rate, decreased N_2 rate, a maximum in the N_2O rate, and a decrease in the nitrogen selectivity. With the promoted catalyst, increasing P_{O_2} caused a progressive decrease in the effect of sodium on (i) reaction rates (all the ρ values tend to unity) and (ii) nitrogen selectivity.

Propene as reductant

Figures 6.2a-d illustrate the effect of sodium and oxygen on the reduction of nitric oxide by propene. The data were obtained at 623 K with $P^{\circ}_{C_3H_6} = P^{\circ}_{NO} = 1\,\text{kPa}$ and $P^{\circ}_{O_2}$ ranging from 0 kPa to 2 kPa. Under these conditions of partial pressures and temperature, CO_2, N_2, N_2O and H_2O were the only products. Figures 6.2a-c show steady-state rate data for CO_2 (a), N_2O (b) and N_2 (c) production as a function of V_{WR} for different (constant) values of oxygen pressure. Figure 6.2d shows the corresponding nitrogen selectivity data. Decreasing the catalyst potential (increasing the sodium coverage) in the absence of gaseous oxygen (filled circles) resulted in the following: (i) increased rates of CO_2 and N_2 formation, (ii) decreased N_2O production and (iii) a substantial increase in the selectivity towards nitrogen formation. In this respect the behaviour is qualitatively similar to that found for CO in the absence of oxygen. In the presence of gaseous oxygen, electro-pumping of Na to the catalyst surface in the oxygen pressure range up to 1 kPa again resulted in activity and selectivity promotion. That is, with increased Na loading, the CO_2 and N_2 rates increased, whereas the N_2O rate decreased, resulting in increased nitrogen selectivity. The effects of Na promotion diminished with

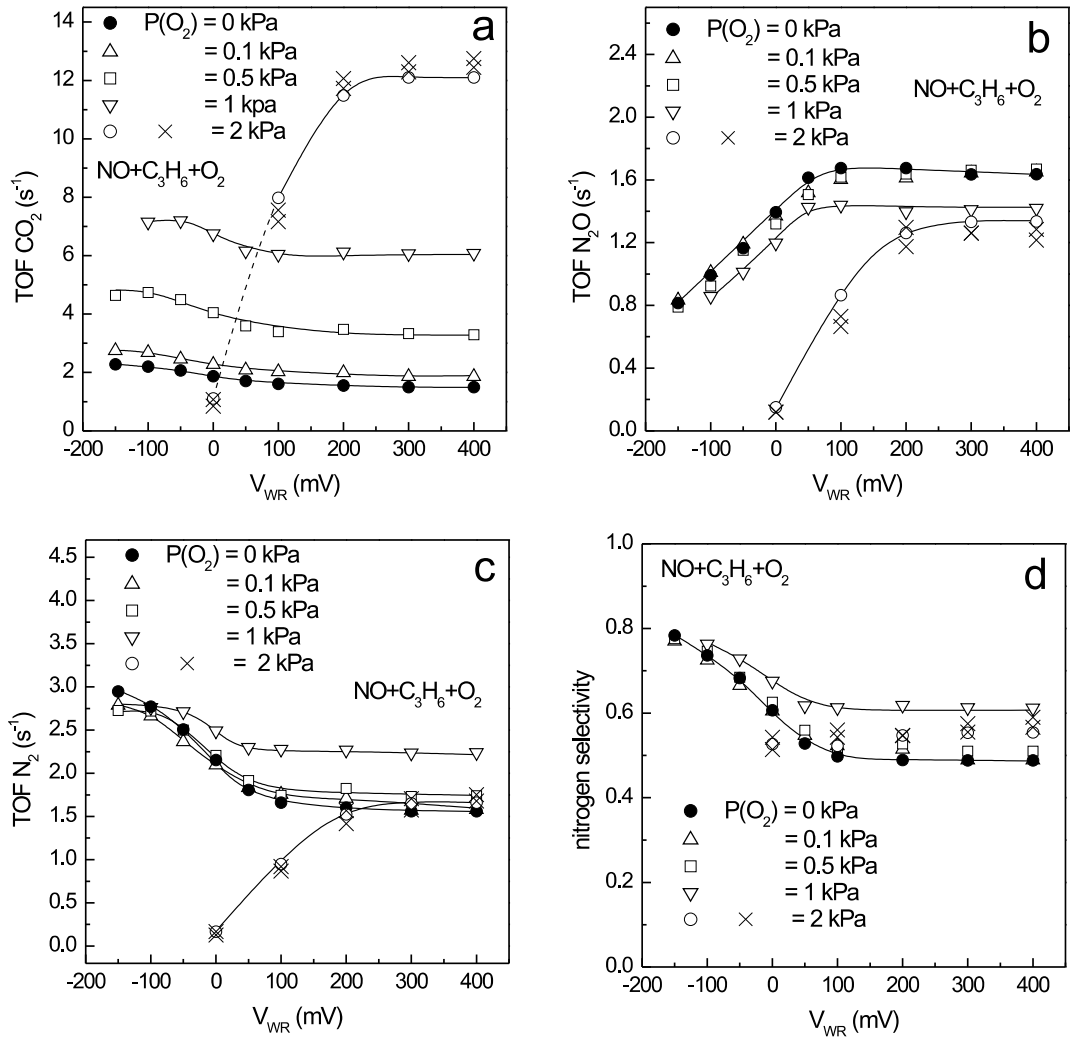

Figure 6.2: Effect of catalyst potential (V_{WR}) on CO_2 (a), N_2O (b), N_2 (c) formation rates and on nitrogen selectivity (d) for different partial pressures of oxygen. Conditions: $T = 623\,\mathrm{K}$, $P^{\circ}_{\mathrm{NO}} = P^{\circ}_{\mathrm{C_3H_6}} = 1\,\mathrm{kPa}$.

increasing oxygen partial pressure. However, at $P^{\circ}_{\mathrm{O_2}} = 2\,\mathrm{kPa}$, all rates decreased over the accessible range of Na loading, the effect being especially marked in the case of the major products (CO_2, N_2) which no longer exhibited any rate enhancement. In other words, as the oxygen pressure increased the system underwent a switch in behaviour. At lower oxygen pressures both rate and nitrogen selectivity were enhanced by Na. However, at 2 kPa oxygen, pumping Na to the surface resulted in marked activity loss, especially for the nitrogen-containing products, accompanied by a small loss in selectivity. Since this activity loss was so dramatic the experiment was repeated twice to check its reproducibility. The relevant data are shown as crosses in figures 6.2a-d from which it is evident that (i) the quenching behaviour was reproducible and (ii) that the

Table 6.2: Effect of increasing the oxygen partial pressure on the Na-induced enhancement of reaction rates and nitrogen selectivities for the $C_3H_6 + NO$ reaction. u, p stand for unpromoted and optimally promoted, respectively. Conditions $P^{\circ}_{C_3H_6} = P^{\circ}_{NO} = 1\,\text{kPa}$, $T = 623\,\text{K}$

$P^{\circ}_{O_2}$	ρ_{CO_2}	ρ_{N_2}	ρ_{N_2O}	$S^{u}_{N_2} \rightarrow S^{p}_{N_2}$
0 kPa	1.52	1.89	0.47	49% → 78%
0.1 kPa	1.47	1.76	0.5	49% → 77%
0.5 kPa	1.41	1.57	0.47	51% → 77%
1 kPa	1.17	1.23	0.6	61% → 76%
2 kPa	0.08	0.07	0.1	55% → 52%

electrochemical response was also reversible.

Table 6.2 shows the effect of sodium on the reaction at different oxygen partial pressures in terms of the relative rate changes (ρ) and the corresponding nitrogen selectivity variations. Note that under unpromoted conditions, progressively increasing the oxygen concentration resulted in a steady increase in the CO_2 rate whereas the N_2O, N_2 and the nitrogen selectivity passed through a maximum. The general trend is that the promotional effects of sodium on the reduction of NO by CO or propene become less significant as the oxygen partial pressure increases. This abatement of Na promotion is most pronounced when propene is the reductant: in this case the system eventually exhibits total poisoning of catalytic activity when the oxygen exceeds a certain threshold.

In order to understand these effects of oxygen on catalytic performance, post-reaction XPS analyses of the catalyst surface were carried out for the relevant range of oxygen partial pressures and for different catalyst potentials. The results presented refer to the reduction of NO by propene, the more complex of the two systems, because this is the critically important process for practical implementation of catalytic NO reduction in oxygen-containing environments [5].

6.3.2 Post-reaction XPS analysis

XP spectra were obtained immediately after exposing the appropriately biased catalyst film to the conditions of temperature and reactants partial pressures typical of those encountered in the reactor, in order to detect the various surface species present under reaction conditions. During exposure of the catalyst to the reaction mixture, the V_{WR} values were such that the Rh film was either (i) electrochemically clean (unpromoted) or (ii) sodium promoted. A full description of the procedure used to obtain the post-reaction XP spectra can be found in chapter 2.

XP spectra were taken after exposing the sample to a mixture of 1 kPa of propene + 1 kPa of NO + x kPa of O_2 at 623 K and 1 atmosphere total pressure (He carrier gas). Here, x = 0 kPa, 0.5 kPa (i. e. conditions under which sodium promotes the reaction) and 2 kPa (where sodium poisons the reaction). The three different reaction mixtures are designated 1, 2 and 3 for $x = 0,\ 0.5,\ 2.0$ kPa oxygen, respectively. Each reaction gas exposure was carried out for two different values of catalyst potential: (i) $V_{WR} = +600$ mV (unpromoted catalyst) and (ii) $V_{WR} = -100$ mV (promoted catalyst). XP spectra were thus acquired for the following six sets of conditions:

i. reaction mixture 1 (without oxygen); unpromoted (spectrum a).

ii. reaction mixture 1 (without oxygen); Na promoted (spectrum b).

iii. reaction mixture 2 ($P^{\circ}_{O_2} = 0.5$ kPa); unpromoted (spectrum c).

iv. reaction mixture 2 ($P^{\circ}_{O_2} = 0.5$ kPa); Na promoted (spectrum d).

v. reaction mixture 3 ($P^{\circ}_{O_2} = 2$ kPa); unpromoted (spectrum e).

vi. reaction mixture 3 ($P^{\circ}_{O_2} = 2$ kPa); Na promoted (spectrum f).

Figure 6.3 shows Na 1s XP spectra for the six different cases described above. It is apparent that a very small amount of sodium was detectable after exposing the unpromoted sample ($V_{WR} = +600$ mV) to the different reaction mixtures (spectra a, c and e). As we have shown in chapter 3, this residual emission is from Na in the underlying Na β" alumina spectroscopically visible through cracks and imperfections present in the porous rhodium film. In every case, electro-pumping Na to the catalyst ($V_{WR} = -100$ mV) resulted in a substantial increase in Na coverage of the Rh surface (spectra b, d and f). Note that the binding energy (BE) of the Na 1s XP signal in spectrum f is shifted ~ 1 eV towards higher BE with respect to spectra b and d. This reflects a change in the nature of the sodium compounds formed in reaction mixture 3. The top panel in figure 6.3 shows the Na KLL XAES spectra corresponding to the promoted cases of reaction mixtures 2 and 3, i. e. spectra d and f in the lower panel. (The dashed lines are reference Na KLL spectra for sodium carbonate and sodium nitrate). These Auger results confirm that the sodium compound present under reaction mixture 3 (spectrum f) is distinct from that present under reaction mixture 2. In addition, they show that the former is neither a carbonate nor a nitrate, whereas the latter (spectrum d) could be either.

Although the Na 1s BE does depend on the chemical identity of the particular sodium compound (e. g. Na_2CO_3 (1071.5 eV) [6], $NaHCO_3$ (1071.3 eV) [6], $NaNO_2$

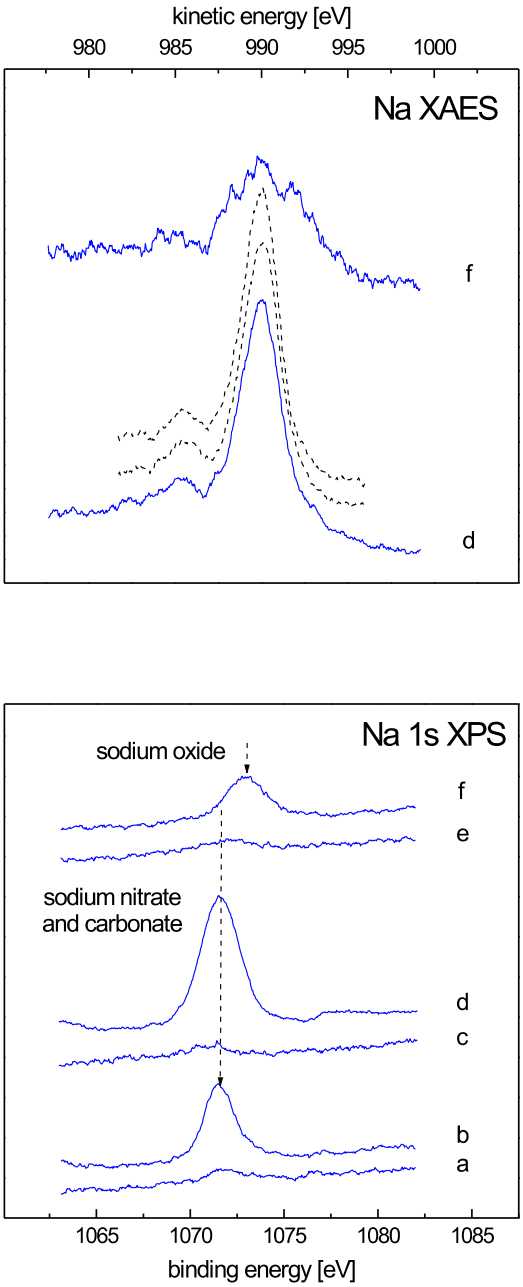

Figure 6.3: Sodium 1s XP spectra acquired after exposing the catalyst to 1 kPa of propene, 1 kPa of NO and varying partial pressures of oxygen at $T = 623\,\mathrm{K}$. $P^{\circ}_{O_2} = 0\,\mathrm{kPa}$, $V_{WR} = +600\,\mathrm{mV}$ (spectrum *a*) and $V_{WR} = -100\,\mathrm{mV}$ (spectrum *b*). $P^{\circ}_{O_2} = 0.5\,\mathrm{kPa}$, $V_{WR} = +600\,\mathrm{mV}$ (spectrum *c*) and $V_{WR} = -100\,\mathrm{mV}$ (spectrum *d*). $P^{\circ}_{O_2} = 2\,\mathrm{kPa}$, $V_{WR} = +600\,\mathrm{mV}$ (spectrum *e*) and $V_{WR} = -100\,\mathrm{mV}$ (spectrum *f*). The top panel shows Na KLL XAES spectra corresponding to: $P^{\circ}_{O_2} = 0.5\,\mathrm{kPa}$ and $V_{WR} = -100\,\mathrm{mV}$ (spectrum *d*) and $P^{\circ}_{O_2} = 2\,\mathrm{kPa}$ and $V_{WR} = -100\,\mathrm{mV}$ (spectrum *f*). Also shown in dashed lines are the Na KLL reference spectra corresponding to bulk sodium nitrate and carbonate samples.

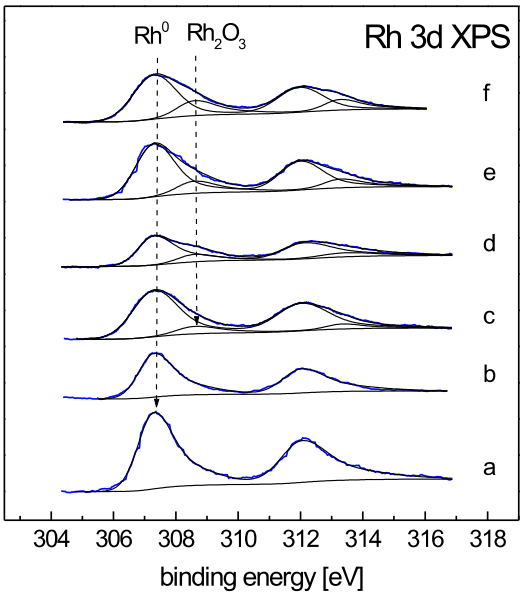

Figure 6.4: Rhodium 3d XP spectra acquired after exposing the catalyst to 1 kPa of propene, 1 kPa of NO and varying partial pressures of oxygen at $T = 623$ K.

(1071.6 eV) [7], $NaNO_3$ (1071.4 eV) [7], Na_2O 1072.5 eV [8]), this does not provide unambiguous chemical fingerprinting. We therefore identify the various Na compounds by making use of the corresponding C 1s, N 1s and O 1s spectra. As shown below, the sodium compounds formed may be identified as sodium carbonate (spectrum *b*), a mixture as sodium carbonate and sodium nitrate (spectrum *d*) and sodium oxide (spectrum *f*).

Rh 3d XP spectra are shown in figure 6.4. Note that under our conditions the inelastic mean free path of the Rh photoelectrons (kinetic energy 946 eV) was ~ 11 Å [9],

Table 6.3: Effect of increasing oxygen partial pressure and Na coverage on the oxidation of the Rh catalyst and on the attenuation of the Rh 3d XPS signal for the $C_3H_6 + NO + O_2$ reaction. Conditions $P^\circ_{C_3H_6} = P^\circ_{NO} = 1$ kPa, $T = 623$ K.

$P^\circ_{O_2}$ (kPa)	V_{WR} (mV)	oxidation (%)	attenuation (%)	film thickness (Å)
0 (spectrum *a*)	+600	0	13	1.3
0 (spectrum *b*)	−100	0	53	7
0.5 (spectrum *c*)	+600	14	38	4.6
0.5 (spectrum *d*)	−100	21	58	8.3
2 (spectrum *e*)	+600	23	36	4.3
2 (spectrum *f*)	−100	30	42	5.2

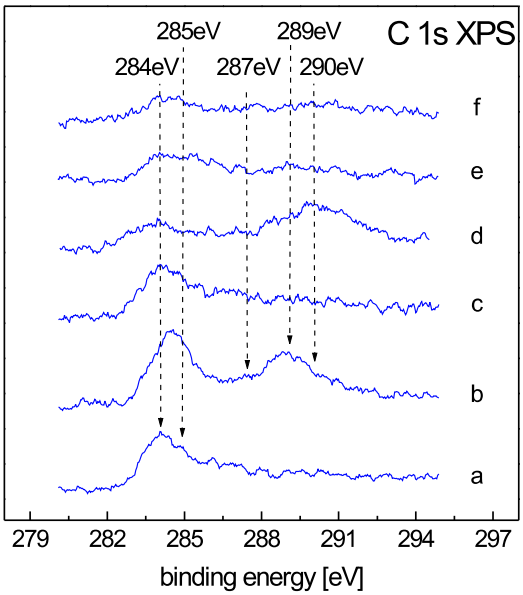

Figure 6.5: Carbon 1s XP spectra acquired after exposing the catalyst to 1 kPa of propene, 1 kPa of NO and varying partial pressures of oxygen at $T = 623$ K.

which provides the required surface sensitivity. These data illustrate two important points. Firstly, the BE shifts indicate changes in oxidation state of the rhodium film. Secondly, in any given case, the intensity attenuation provides a measure of the coverage of the metal by surface species. Two main contributions may be distinguished in the Rh 3d spectra: lower BE doublet at 307.3 and 312 eV corresponds to metallic rhodium whereas the higher BE doublet at 308.6 and 313.3 eV is due to Rh_2O_3 [10]. Within the XPS sampling depth, the fraction of the catalyst that had undergone oxidation under reaction conditions can be estimated from the ratio of the integrated intensity corresponding to the Rh_2O_3 to the total integrated intensity. The results of this procedure are given in table 6.3 which interprets the attenuation of Rh 3d emission in terms of the effective thickness of a hypothetical continuous film of overlying material. The first entry (1.3 Å) is of course physically unrealistic and is best thought of as equivalent to $\sim 1/3$ of a monolayer of adsorbate on an otherwise bare Rh surface. It is evident from table 6.3 that coverage of the post-reaction Rh catalyst by surface species is greater under promoted than under unpromoted conditions. The results in table 6.3 also show that the rhodium film undergoes oxidation only when there is O_2 present in the gas phase. It is also evident that the degree of oxidation of the rhodium film increased with (i) the oxygen partial pressure and (ii) Na loading.

Figure 6.5 shows carbon 1s XP spectra for the six different conditions described

above. These provide some information about the chemical identity of the Na compounds that are formed under reaction conditions. The C 1s region exhibits two main contributions, one at lower binding energy (∼284−285 eV) and the other at higher binding energy (∼288−290 eV). The former is due to elemental carbon (284 eV [11]) and to propene fragments (284−285 eV), whereas the latter is due to sodium carbonate (289 eV [12]). The small feature at ∼287 eV could be due to partially oxidised carbonaceous species [11]. After exposing the catalysts to reaction mixture 1 under unpromoted conditions (spectrum *a*), at least two peaks are apparent due to (i) elemental carbon and (ii) propene fragments. Exposing the catalyst to reaction mixture 1 under promoted conditions (spectrum *b*) generated at least four C 1s contributions, namely (i) elemental carbon (ii) propene fragments (iii) a shoulder at 287.4 eV, possibly due to partially oxidised carbonaceous species, as noted above and (iv) a peak at 289 eV due to sodium carbonate. Progressive addition of oxygen to the reaction gas resulted in a corresponding decrease in the amount of elemental carbon and carbonaceous species (spectra *c*−*f*). The emission at 289 eV−290 eV due to Na carbonate persists in spectrum *d* (reaction mixture 2, promoted conditions) but is eventually quenched (spectra *f* corresponding to reaction mixture 3, promoted conditions). Note that the peak ascribed to carbonate is upshifted by ∼ 1 eV between spectrum *b* and spectrum *d*. In summary, (i) the presence of gaseous oxygen decreases coverage by carbon and carbonaceous species (ii) carbonate is only present when the catalyst exhibits promotion by Na and (iii) carbonate is absent when the catalyst exhibits poisoning by Na.

Figure 6.6 shows corresponding N 1s XP spectra in which two contributions are readily apparent: chemisorbed N at 397.4 eV [13] and nitrate at 407.3 eV [14]. In addition, spectrum *a* exhibits a weak feature at 400 eV that may be ascribed to chemisorbed NO [15]. Thus exposure to reaction mixture 1 under unpromoted conditions results in the presence of both chemisorbed N and NO (spectrum *a*), whereas under promoted conditions only chemisorbed N is detected (spectrum *b*). When the reaction gas contains some oxygen (reaction mixture 2) only chemisorbed N is detected on the unpromoted surface (spectrum *c*). However Na promotion in reaction mixture 2 generates both N adatoms and nitrate (spectrum *d*). At the highest oxygen pressure (reaction mixture 3) no nitrogen containing adsorbates are detectable on both the unpromoted and promoted surfaces (spectra *e* and *f*).

The O 1s XP spectra shown in figure 6.7 contain three principal contributions. The lowest BE peak (529−530 eV) is due to rhodium oxide (530 eV [10]) and Na_2O (529.6 eV [8]). The 531.4 eV BE peak is due to chemisorbed oxygen [10] and carbonate (531.6 eV [16]). The highest BE peak (532.5 eV) must be associated with a sodium

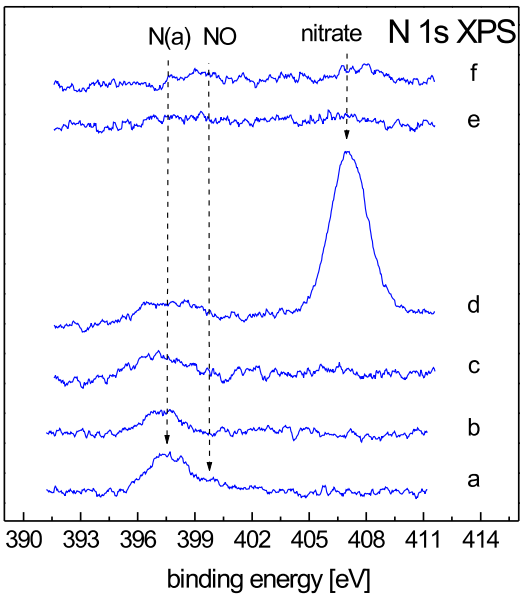

Figure 6.6: Nitrogen 1s XP spectra acquired after exposing the catalyst to 1 kPa of propene, 1 kPa of NO and varying partial pressures of oxygen at $T = 623$ K.

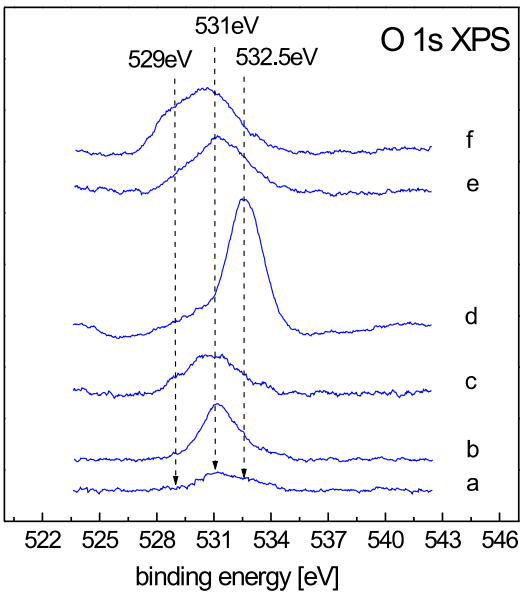

Figure 6.7: Oxygen 1s XP spectra acquired after exposing the catalyst to 1 kPa of propene, 1 kPa of NO and varying partial pressures of oxygen at $T = 623$ K.

compound since it disappears upon imposing a positive bias (thus pumping Na away from the Rh surface). We therefore assign it to and is due to sodium nitrate, in good agreement with the reported BE for this compound [17] and the corresponding N 1s spectrum shown in figure 6.6. It is possible that subsurface oxygen may make a small contribution at this BE [10]. Exposure of the unpromoted surface to oxygen-free reaction gas (mixture 1) under unpromoted conditions generates chemisorbed oxygen and subsurface oxygen (spectrum *a*). Alkali promotion in the same reaction gas (mixture 1) produces chemisorbed oxygen, sodium carbonate (cf the C 1s spectrum *b*) and subsurface oxygen. Addition of oxygen (mixtures 2 and 3) results in the appearance emission at 530 eV that correlates with the oxidation of the rhodium film detected in the Rh 3d spectra (figure 6.4). Accordingly, this O 1s emission is assigned to Rh_2O_3. Specifically, exposing the unpromoted surface to the oxygen-containing reaction mixture 2 produced rhodium oxide and chemisorbed oxygen (spectrum *c*); Na promotion in the same reaction gas produced Na nitrate in addition to Rh_2O_3 and O(a) (spectrum *d*). At the highest oxygen pressure (reaction mixture 3) rhodium oxide and chemisorbed oxygen are again present on the unpromoted conditions (spectrum *e*). This time, however, Na pumping to the catalyst resulted in poisoning, and the appearance of Na_2O rather than $NaNO_3$ (spectrum *f*).

It is worth noting that in every case application of $V_{WR} = +600\,mV$ at reaction temperature (pumping Na away from the catalyst) resulted in complete disappearance of the sodium compounds (variously carbonate, nitrate and oxide) leaving only a small amount of chemisorbed oxygen on the Rh surface. This provides confirmation of the overall validity of the spectral interpretations offered above, and the conclusions drawn on the catalytic behaviour, proposed below.

6.4 Discussion

Interpretation of our reactor data requires the explanation of two principal phenomena. First, there is a regime in which increasing the sodium coverage causes an increase in reaction rates and nitrogen selectivity. Second, as the oxygen content in the gas phase is increased the effects of sodium promotion on the nitrogen rate and selectivity progressively decrease. The effect is most pronounced in the case of the NO + propene reaction where all promotional effects are eventually suppressed and the system actually exhibits total poisoning of all catalytic activity. However, before discussing the effects of electrochemically supplied sodium it is necessary to consider the chemical state of the promoter phase under reaction conditions.

6.4.1 Chemical state of the alkali additive under reaction conditions

The post-reaction XPS demonstrate that the chemical identity of the sodium-containing promoting (or poisoning) phases is dependent on the gas atmosphere. When the gas phase consisted of equal amounts of NO and propene (spectra *b*) sodium was present as the carbonate. Addition of some oxygen (spectra *d*) resulted in a mixture of sodium carbonate and nitrate being formed. Ultimately, at the highest oxygen pressure (spectra *f*) sodium oxide was formed. These results are in excellent agreement with previous findings, in particular for the EP of Pt-catalysed NO reduction by propene, XPS shows that alkali nitrite, nitrate and/or carbonate are present depending on the different NO to propene ratios used [18]. In the case of Pt-catalysed propene combustion XPS and XANES show that under reducing conditions the promoter phase consists of sodium carbonate [19]. In all these cases as well as in the present case, the different sodium compounds adsorbed on the metal surface resulted in enhancing the catalytic properties of the catalyst film. This seems to indicate that the nature of the sodium counter-ion(s) (nitrite, nitrate, carbonate) might not be an important factor.

Alkali promotion on metal surfaces is understood in terms of the effect of the electric field due to the alkali cation on adjacent co-adsorbates [20]. In principle, co-adsorbed anions should exert the opposite influence to cations. However, as discussed above, all our experimental evidence indicates that the effect of the counter-ion in alkali promoted systems is secondary or negligible. Holloway *et al.* [21] showed using theoretical calculations that the range and absolute magnitude of the alkali-induced electrostatic potential is so much greater than the one for its counter-ion (they studied the effects of oxygen as a counter-ion) that the promoting effect of the alkali dominates over any poisoning due to its counter-ion. Therefore, all the experimental evidence as well as theoretical calculations indicate that promotion by sodium overwhelms poisoning by its counter-ion and, to a first approximation at least, the identity of the ion is not critically important in determining the promoting effect of Na. As mention above, we have shown in this work that under reaction conditions both $NaNO_3$ and Na_2CO_3 compounds act as strongly promoting species.

The Rh 3d XP spectra (figure 6.4) are revealing in regard to the extent of loading and morphology of the Na surface compounds. Under promoted conditions the Rh XP signal is attenuated by an overlayer consisting principally of sodium compounds. Since this surface is catalytically active, at least some of the surface must expose promoter-modified Rh sites while the rest is covered by the Na compound. Therefore, the nominal film thickness values given in table 6.3 (7, 8.3 and 5.2 Å) imply that under promoter

conditions the sodium compounds are present, at least in part, as 3-dimensional crystallites. The peaks at 289 eV and 290 eV in the C 1s XP spectra (figure 6.5, spectra *b*, *d*) have been assigned to sodium carbonate. This assignment is based on our own reference spectrum (BE = 289.5 eV) and on values reported in the literature. These latter range from 289.4 eV for bulk sodium carbonate samples [22] to 290.4 eV for submonolayer quantities of sodium carbonate on TiO_2 [23]. Therefore, we propose that the BE variations we observe reflect a change in the state of aggregation of the sodium carbonate, from largely three-dimensional to mainly two-dimensional.

6.4.2 Mode of alkali promotion

The reactor data clearly demonstrate the reversible dependence of reaction rates on catalyst potential. This is due to the reversible, potential-controlled, electro-pumping of sodium ions from the solid electrolyte to the rhodium catalyst. Equally, the post-reaction XPS data (figure 6.3) show the occurrence of reversible spillover/backspillover of Na to/from the surface of the Rh film. Decreasing the catalyst potential delivers Na to the surface, which, in the presence a reactive gas atmosphere, results in the formation of sodium compounds whose chemical identity depends on the composition of the gas phase. The resulting promotional effects of sodium on the reduction of NO by CO or propene may be understood in terms of the enhanced NO adsorption and dissociation induced by the co-adsorbed Na as discussed in previous chapters and as shown by surface science studies [24–26].

On the above basis, the following reaction mechanism permits a rationalisation of promotion by Na of the Rh-catalysed reduction of NO by CO or propene in the absence of oxygen.

$$\mathrm{NO(g) + S} \rightleftarrows \mathrm{NO(a)} \tag{6.1}$$

$$\mathrm{NO(a) + S} \rightarrow \mathrm{N(a) + O(a)} \tag{6.2}$$

$$\mathrm{NO(a) + N(a)} \rightarrow \mathrm{N_2O(g) + 2S} \tag{6.3}$$

$$\mathrm{N(a) + N(a)} \rightarrow \mathrm{N_2(g) + 2S} \tag{6.4}$$

$$\mathrm{O(a) + CO(a)\ (or\ propene)} \rightarrow \mathrm{CO_2(g)\ (+H_2O)} \tag{6.5}$$

Where S represents a vacant site for adsorption. Oxygen adatoms produced in the critical reaction-initiating step (6.2) react with adsorbed CO (or with hydrocarbon fragments, in the case of propene) to form CO_2. In this scheme, (6.2) is rate limiting and is promoted by Na as argued above. Nitrogen selectivity depends on the relative rates of reactions (6.3) and (6.4). Na promotes activity and nitrogen selectivity as a result

of accelerating (6.2), increasing N(a) and O(a) coverages and decreasing that of NO(a). As a result, there is an increase in the rates of N_2 and CO_2 production in steps (6.4) and (6.5), respectively, and a decrease in the rate of step (6.3), yielding the observed increase in overall activity and nitrogen selectivity (figures 6.1 and 6.2).

Consider now the effects of added oxygen. Figure 6.1 shows that in the case of the NO + CO reaction, increasing the oxygen partial pressure in the absence of Na promotion causes: (i) an increase in the CO_2 production rate, (ii) a decrease in the rate of N_2 production, (iii) a maximum in the rate of N_2O production and (iii) a decrease in nitrogen selectivity. These effects can be understood in terms of the competitive adsorption of oxygen and NO. Increasing the oxygen partial pressure causes an increase in the oxygen coverage, resulting in an increase CO_2 rate as observed. At the same time NO adsorption and dissociation are inhibited, resulting in a decrease in both the nitrogen rate and nitrogen selectivity. The maximum in the unpromoted N_2O rate as a function of increasing oxygen content may be understood as follows. When $P_{O_2} = 0$ the N_2O rate is low (see figure 6.1b) because NO dissociation is efficient. However, as the O_2 pressure increases up to 0.2 kPa, N_2O production increases because increased O(a) coverage inhibits NO dissociation, thus increasing ϑ_{NO} and favouring N_2O formation. Further increase in P_{O_2} decreases N_2O production due to decreased NO adsorption resulting from increased competition with O_2 for vacant sites.

The behaviour observed with propene as reductant is similar, though not indentical. As shown in figure 6.2, increasing the oxygen pressure in the absence of Na results in: (i) an increase in the CO_2 rate and (ii) the rate of nitrogen production and the nitrogen selectivity pass through a maximum. These effects may be rationalised as follows. Spectrum *a* in figure 6.5 shows that in the absence of gaseous oxygen the surface of the catalyst is covered mainly by hydrocarbon fragments. Increasing the oxygen partial pressure results in an increase in oxygen coverage, 'cleaning off' hydrocarbonaceous fragments (also shown in figure 6.5), and thus increasing the rate of CO_2 production. As a result, the number of free sites available for NO adsorption and dissociation increases, resulting in an increase in the rate of nitrogen production and in nitrogen selectivity. However, further increase in oxygen partial pressure eventually leads to a decrease in site availability for NO dissociation as the surface becomes over-populated by O(a). Therefore the nitrogen rate and nitrogen selectivity should both fall, so that the maximum exhibited by both these quantities is understandable.

6.4.3 Oxygen-induced inhibition of alkali promotion

Here we discuss the consequences of increasing the oxygen partial pressure under promoted conditions. As shown in figures 6.1 and 6.2, the promotional effects of sodium on the reduction of NO by both CO and propene decrease as the oxygen partial pressure is increased. This occurs to the extent that they disappear (when CO was used as the reductant) or they result in a decrease in reaction rates (when propene was used as the reductant) when oxygen is increased above a certain threshold. This behaviour is explicable in terms of the effect of alkali modifiers on the competitive adsorption of the reactants. Sodium is an electropositive adsorbate and should therefore decrease the strength of chemisorption of electron donating adsorbates (propene); conversely, it should strengthen the chemisorption of electron acceptors (CO, NO and O(a)). The post-reaction XP data are in accord with this view: spectra *c*, *d*, *e* and *f* in figures 6.5 and 6.7 show that sodium increases the steady state coverage of oxygen-containing species at the expense of adsorbed hydrocarbon fragments.

Thus progressive suppression of the promoting effect of sodium promotion by addition of gaseous oxygen is due to alkali-enhanced adsorption of oxygen at the expense of propene: the system self-poisons by excessive adsorption of one of the reactants. The other consequence of alkali-enhanced oxygen adsorption is oxidation of the rhodium catalyst itself (figure 6.4). Alkali-enhanced oxidation of silicon is well known [27] and it will be shown in the case of copper in chapter 7.

It is known that sodium enhances the adsorption and dissociation of CO, NO and O_2 when co-adsorbed separately with these species on rhodium [26]. However, the effect of sodium on the competitive adsorption of CO, NO and O_2 it is not known. Our data show that the unpromoted nitrogen rate decreases as the partial pressure of oxygen increases. As discussed above, this implies decreased NO adsorption and dissociation resulting from increased competition with O_2 for vacant sites. Our data also shows that the Na-promoted nitrogen rate decreases as P_{O_2} increases. This suggests that sodium enhances oxygen adsorption more strongly than that of nitric oxide. On this basis, increasing the partial pressure of oxygen under promoted conditions will result in a relative increase of the surface coverage of oxygen adatoms at expenses of both free sites and NO molecules, therefore resulting in a decrease in the level of promotion. This is, alkali enhanced NO-dissociation would be diminished because the probability for NO(a) to interact with a Na-promoted Rh site decreases as O(a) increases.

Why oxygen-inhibited alkali promotion is more pronounced in the case of NO reduction by propene (where poisoning is observed) than NO reduction by CO? When using CO as the reductant adding O_2 decreased the promotional effects of sodium. As

discussed above, this is due to a decreased probability for NO(a) to interact with a Na-promoted Rh site as O(a) increases. However, when using propene as the reductant adding sodium poisoned all reaction rates at the maximum oxygen pressure. This difference in behaviour is understandable in terms of the opposite effects of sodium on the chemisorption of the two reductants. Thus, sodium enhances the adsorption of CO whereas it decreases the adsorption strength of propene. As a result, at sufficiently high oxygen pressures, the propene + NO reaction is strongly inhibited by two effects that work in the same direction. Alkali-enhanced NO dissociation is suppressed, as discussed above, and propene adsorption is also suppressed. With CO the second effect does not occur, shown by the fact that although sodium stops promoting NO dissociation it still promotes the oxidation of carbon monoxide (reflecting the alkali increased coverage of oxygen adatoms).

It is worth noting that the behaviour of this EP system closely parallels that found with classically-promoted conventional dispersed catalysts. Thus, MacLeod *et al.* found that although sodium promotes that reduction of NO by propene over Rh/γ-alumina catalysts [28], it actually poisons the system under three-way conditions [29], i. e. in the presence of substantial amounts of oxygen. This provides further support for the view that EP studies on model thin film catalysts provide insight into the behaviour of the corresponding practical dispersed catalysts.

6.5 Conclusions

1. Electrochemically supplied sodium can promote both the catalytic activity and nitrogen selectivity in the rhodium-catalysed reduction of NO by CO or propene, even in the presence of oxygen. This is understandable in terms of alkali-enhanced NO dissociation.

2. Under promoted conditions, the alkali surface phase consists of carbonate, nitrate, or both, depending on the gas composition. To a first approximation the chemical identity of the counter anion appears not to play a significant role. Some of this material is present as three-dimensional crystallites.

3. With increasing oxygen partial pressure the promotional effects of sodium are progressively decreased. This is understandable in terms of alkali-enhanced adsorption of oxygen and subsequent suppression of NO adsorption and dissociation.

4. When using propene as the reductant, drastic poisoning by sodium at the highest oxygen partial pressures is due to strong alkali-inhibition of propene adsorption,

resulting in the observed excessive formation of Na_2O, and oxidation of Rh to Rh_2O_3.

5. The markedly different behaviour of CO and propene as reductants is due to opposite effects of co-adsorbed alkali on the electronegative or electropositive adsorbate, respectively.

Bibliography

[1] K. C. Taylor, Nitric oxide catalysis in automotive exhaust systems, Catalysis reviews science and engineering **35**, 457–481 (1993).

[2] N. W. Cant, D. E. Angove, and D. C. Chambers, Nitrous oxide formation during the reaction of simulated exhaust streams over rhodium, platinum and palladium catalysts, Applied Catalysis B: Environmental **17**, 63–73 (1998).

[3] N. Macleod, J. Issac, and R. M. Lambert, Promotion by Na of Pd/γ-Al_2O_3 catalysts operated under simulated exhaust conditions, Journal of Catalysis, submitted .

[4] M. Konsolakis, N. Macleod, J. Issac, Y. V. Yentekakis, and R. M. Lambert, Strong promotion by Na of Pt/γ-Al_2O_3 catalysts operated under simulated exhaust conditions, Journal of Catalysis **193**, 330–337 (2000).

[5] R. Burch, P. J. Millington, and A. P. Walker, Mechanism of the selective reduction of nitrogen monoxide on platinum-based catalysts in the presence of excess oxygen, Applied Catalysis B: Environmental **4**, 65–94 (1994).

[6] C. D. Wagner, Photoelectron and Auger energies and the Auger parameter: a data set, in *Practical surface analysis by Auger and X-ray photoelectron spectroscopy*, edited by D. Briggs and M. P. Seah, Wiley, New York, 1983.

[7] C. D. Wagner, Chemical shifts of Auger lines and the Auger parameter, Discussions of the Faraday Society **60**, 291–300 (1975).

[8] A. Barrie and F. J. Street, An Auger and X-ray photoelectron spectroscopic study of sodium metal and sodium oxide, Journal of Electron Spectroscopy and Related Phenomena **7**, 1–31 (1975).

[9] D. R. Penn, Quantitative chemical analysis by ESCA, Journal of Electron Spectroscopy and Related Phenomena **9**, 29–40 (1976).

[10] A. A. Tolia, R. J. Smiley, W. N. Delgass, C. G. Takoudis, and M. J. Weaver, Surface oxidation of rhodium at ambient pressures as probed by surface-enhanced Raman and X-ray photoelectron spectroscopies, Journal of Catalysis **150**, 56–70 (1994).

[11] Z. Paål, R. Schlögl, and G. Ertl, Photoelectron spectroscopy of polycrystalline platinum catalysts, Journal of the Chemical Society, Faraday Transactions **88**, 1179–1189 (1992).

[12] T. Seyller, D. Borgmann, and G. Wedler, Interaction of CO_2 with Cs-promoted Fe(110) as compared to Fe(110)/K + CO_2, Surface Science **400**, 63–79 (1998).

[13] R. J. Baird, R. C. Ku, and P. Wynblatt, The chemisorption of CO and NO on Rh(110), Surface Science **97**, 346–362 (1980).

[14] B. Folkesson, ESCA studies on the charge distribution in some dinitrogen complexes of rhenium, iridium, ruthenium and osmium, Acta Chemica Scandinavica **27**, 287–302 (1973).

[15] L. A. DeLouise and N. Winograd, Adsorption and desorption of NO from Rh(111) and Rh(331) surfaces, Surface Science **159**, 199–213 (1985).

[16] C. D. Wagner, D. A. Zatko, and R. H. Raymond, Use of oxygen KLL Auger lines in identification of surface chemical states by electron spectroscopy for chemical analysis, Analytical Chemistry **52**, 1445–1451 (1980).

[17] C. Bandis, L. Scudiero, S. C. Langford, and J. T. Dickinson, Photoelectron emission studies of cleaved and excimer laser irradiated single-crystal surfaces of $NaNO_3$ and $NaNO_2$, Surface Science **442**, 413–419 (1999).

[18] I. V. Yentekakis, A. Palermo, N. C. Filkin, M. S. Tikhov, and R. M. Lambert, *In situ* electrochemical promotion by sodium of the platinum-catalysed reduction of NO by propene, Journal of Physical Chemistry B **101**, 3759–3768 (1997).

[19] N. C. Filkin, M. S. Tikhov, A. Palermo, and R. M. Lambert, A kinetic and spectroscopic study of the *in situ* electrochemical promotion by sodium of the platinum-catalysed combustion of propene, Journal of Physical Chemistry A **103**, 2680–2687 (1999).

[20] N. D. Lang, S. Holloway, and J. K. Nørskov, Electrostatic adsorbate-adsorbate interactions: the poisoning and promotion of the molecular adsorption reaction, Surface Science **150**, 24–38 (1985).

[21] S. Holloway, J. K. Nørskov, and N. D. Lang, Electrostatic interactions and their role in coadsorption phenomena, Journal of the Chemical Society, Faraday Transactions I **83**, 1935–1943 (1987).

[22] U. Gelius, P. F. Hedén, J. Hedman, B. J. Lindberg, R. Manne, R. Nordberg, C. Nordling, and K. Siegbahn, Molecular Spectroscopy by means of ESCA. III. Carbon compounds, Physica Scripta **2**, 70–80 (1970).

[23] J. Nerlov, S. V. Christensen, S. Weichel, E. H. Pedersen, and P. J. Møller, A photoemission study of the coadsorption of CO_2 and Na on TiO_2(110)-(1x1) and (1x2) surfaces: adsorption geometry and reactivity, Surface Science **371**, 321–336 (1997).

[24] L. Bugyi and F. Solymosi, Interaction of NO with clean and K-dosed Rh(111) surfaces. I. AES, TDS and work function studies, Surface Science **188**, 475–489 (1987).

[25] L. Bugyi, J. Kiss, K. Révéz, and F. Solymosi, Interaction of NO with clean and K-dosed Rh(111) surfaces. II. EELS and PES studies, Surface Science **233**, 1–11 (1990).

[26] H. Höchst and E. Colavita, The interaction of CO, NO and O_2 with sodium-promoted Rh(100) surfaces, Journal of Vacuum Science and Technology A **4**, 1442–1445 (1986).

[27] M. Riehlchudoba, K. M. Schirm, L. Surnev, and P. Soukiassian, The role of alkali-metal layers in the oxidation of Si and Ge surfaces - a comparative study, Surface Science **333**, 375–380 (1995).

[28] N. Macleod, J. Issac, and R. M. Lambert, Sodium promotion of the NO + C_3H_6 reaction over Rh/γ-Al_2O_3 catalysts, Journal of Catalysis **193**, 115–122 (2000).

[29] N. Macleod, J. Issac, and R. M. Lambert, in preparation.

CHAPTER 7

The Cu–catalysed reduction of nitric oxide by carbon monoxide

7.1 Introduction

Copper-based catalysts for NO reduction have been studied for many years because their low cost offers large potential economic benefits in the field of emission control catalysis [1]. Extensive research on the use of such catalysts for NO reduction carried out in the 1960s and early 1970s (e. g. [2, 3]) has been reviewed by Shelef [4]. In this connection, the CO + NO reaction has received the most attention because of its simplicity and relative ease of investigation; a recent comprehensive review is available [5]. There is no generally agreed reaction mechanism, and there are divergent opinions about the nature of the catalytically active site or sites. An important issue concerns the oxidation state of the catalytically active surface. It seems likely that, at least in part, disagreements in the literature reflect the sensitivity of the copper/oxygen system to changes in oxidation potential of the gas phase. With oxygen as oxidant, small changes in O_2 partial pressure can result in abrupt phase transitions between Cu metal, Cu_2O and CuO, accompanied by pronounced changes in catalytic behaviour [6–10]. Furthermore, depending on the rates of oxygen transfer to and from the solid, the catalyst composition may not be uniform as one proceeds from surface to bulk. With NO as oxidant, similar effects are to be expected, although less pronounced than in the case of O_2. In this connection, it is noteworthy that the steady state reaction kinetics are essentially the same, regardless of whether the starting material is Cu metal or Cu_2O [5]. A variety of reaction mechanisms has been proposed, often containing a large number of postulated elementary steps and adsorbed species. Some authors have proposed that Cu^0, Cu^+ and Cu^{++} sites are all

involved in catalytic turnover [11]. Others have suggested [12] that adsorbed nitrogen oxyanions participate in the reaction, although infrared spectra [11] indicate that such species are not present on the active catalyst.

Single crystal data obtained under ultra high vacuum conditions provide valuable basic information. They show that NO dissociates completely on both smooth and Cu stepped surfaces [13–16] accompanied by facile desorption of N_2 and incipient oxidation of the metal. The same is observed in the case of reduced copper supported catalysts [17]. This suggests that at much higher reactant pressures it is unlikely that Cu^0 metal sites survive in a net oxidising environment. Key information regarding the oxidation state of alumina-supported Cu catalysts under reaction conditions at atmospheric pressure comes from an *in situ* XANES study carried out by Fernández-García *et al.* [18]. Their results indicate that both Cu^+ and Cu^{++} sites participate in the overall process, with Cu^+ being involved in the rate limiting step.

Here we report on the electrochemical promotion (EP) by Na of the CO+NO reaction over a copper film catalyst supported on Na β" alumina solid electrolyte which acts as the source of electro-pumped spillover Na. This is the first time that EP has been observed with a base metal catalyst. The results shed light on the chemical composition of the catalytically active surface and on the way in which this composition varies as the CO:NO ratio varies from net reducing to net oxidising conditions. In addition, we address certain aspects of the reaction mechanism and identify the chemical state of the Na promoter. In agreement with London and Bell [11] it is found that Cu nitrate is not present on the active surface. In agreement with Fernández-García *et al.* [18], we show that the latter consists of Cu(I) and Cu(II) oxides, at least within the sampling depth of the XP spectra ($\sim 1\,\mathrm{nm}$). Comparison with our EP study of the Rh-catalysed $CO + NO$ reaction (see chapter 4) is instructive and allows conclusions to be drawn about active sites and the mechanism of promotion in the Cu system.

7.2 Experimental methods

Details regarding sample preparation and characterisation can be found in chapter 2. Inlet and exit gas analysis was carried out by a combination of on-line gas chromatography (Shimadzu-14B; molecular sieve 5A and Porapak-N columns) and on-line mass spectrometry (Balzers QMG 064). N_2, N_2O, CO and CO_2 were measured by gas chromatography, and NO was monitored continuously by mass spectrometry after performing the required calibrations. Reactants were pure NO (Distillers MG) and CO (Distillers MG) diluted in ultrapure He (99.996%) and fed to the reactor by mass-flow controllers (Brooks 5850

TR). The total flow rate was kept constant in all experiments at 6.8×10^{-5} mol·s^{-1} (100 cm^3(STP)/min), with partial pressures P_{NO} and P_{CO} varying between 0.5-6 kPa and 1.5-2.5 kPa, respectively and P_{He} giving a total pressure of 1 atmosphere in every case. Conversion of the reactants was restricted to $< 15\%$ in order to avoid mass transfer limitations. Control experiments were carried out in which the total flow was varied by a factor of 2 in order to verify that the observed changes in activity were due to actual changes in surface reaction rates and not due to mass transfer limitations. Nitrogen and carbon mass balances always closed to within 2%.

XPS experiments were performed as described in chapter 2. XPS analysis of the as-deposited Cu electrode showed a measurable C 1s signal (binding energy 284 eV) corresponding to a submonolayer quantity of carbon. After exposure to reaction gas, the C 1s intensity was reduced to an undetectable level.

7.3 Effect of Catalyst Potential on Reaction Rates

Figures 7.1a-d show steady-state (potentiostatic) rate data for CO_2, N_2, and N_2O production as a function of catalyst potential V_{WR} at 648 K for a range of reactant gas compositions determined by (fixed) inlet pressures (P°_{CO}, P°_{NO}) as follows: (figure 7.1a) $P^\circ_{CO} = 2.5$ kPa, $P^\circ_{NO} = 0.5$ kPa (CO:NO=5:1), (figure 7.1b) $P^\circ_{CO} = 2$ kPa, $P^\circ_{NO} = 1$ kPa (CO:NO=2:1), (figure 7.1c) $P^\circ_{CO} = 1$ kPa, $P^\circ_{NO} = 1$ kPa (CO:NO=1:1) and (figure 7.1d) $P^\circ_{CO} = 1.5$ kPa, $P^\circ_{NO} = 6$ kPa (CO:NO=1:4). Turnover frequencies (TOF) are expressed as molecules of product per Cu surface atom per second. Also shown in figures 7.1a-d is the dependence of N_2 selectivity on catalyst potential, where selectivity is defined as $S_{N_2} = r_{N_2}/(r_{N_2} + r_{N_2O})$.

These data show that all rates (CO_2, N_2 and N_2O) increase with decreasing V_{WR}, which corresponds to progressively increasing the sodium loading of the Cu catalyst surface. Two features are evident: (i) for values of V_{WR} between +100 mV and −100 mV the reaction rates are almost constant (unpromoted regime) and (ii) there is a sharp increase in activity as V_{WR} is reduced below −100 mV (promoted regime). This behaviour was reproducible and fully reversible. The rate enhancement ratios (ρ) and the unpromoted and promoted values of the nitrogen selectivity are shown in table 7.1 as a function of the CO:NO ratio. It is apparent that decreasing V_{WR} not only caused substantial increases in all reaction rates, but also appreciable enhancement of the nitrogen selectivity in every case.

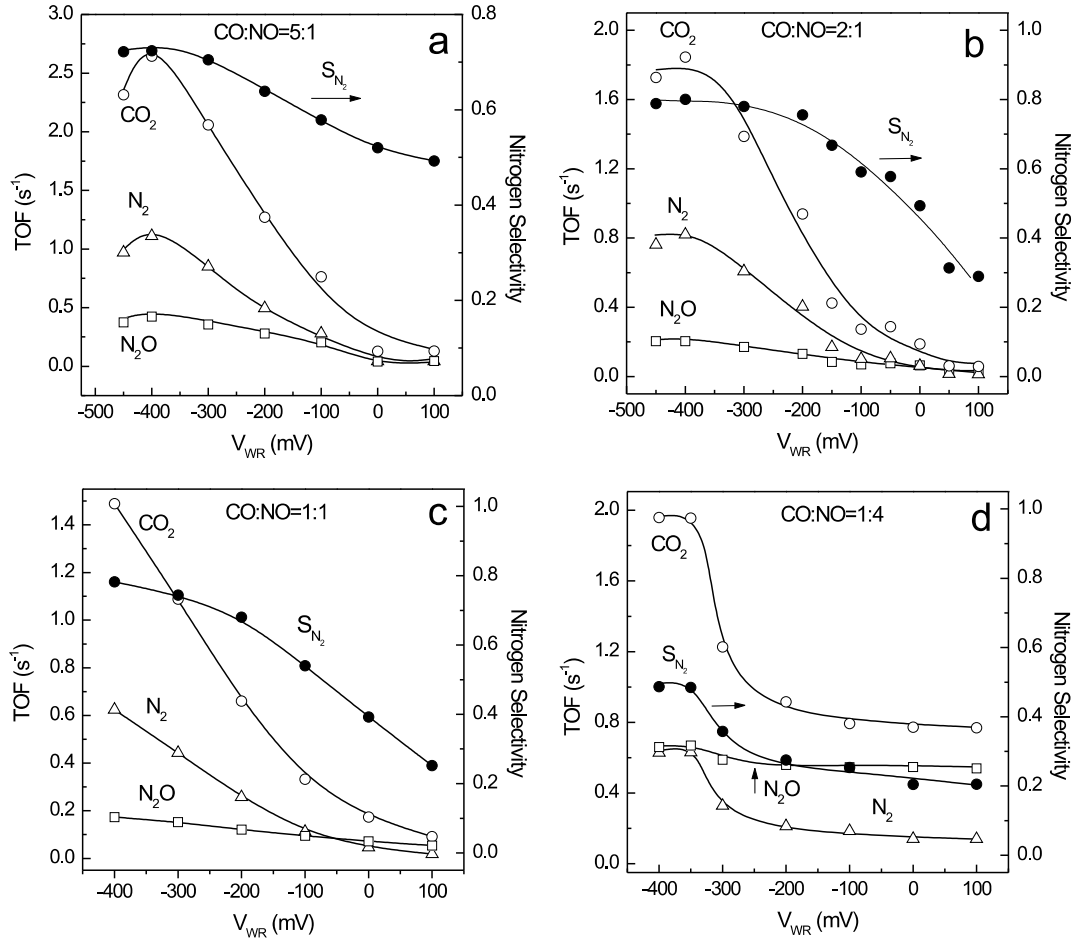

Figure 7.1: Effect of catalyst potential V_{WR} on the CO_2, N_2 and N_2O formation rates and the selectivity of NO reduction to nitrogen for different CO:NO ratios. Conditions are $T = 648\,\mathrm{K}$, (a) CO:NO=5:1, (b) CO:NO=2:1, (c) CO:NO=1:1 and (d) CO:NO=1:4.

Table 7.1: Effect of CO:NO ratio on $\rho_{\mathrm{i}} = r_{\mathrm{i}}^{p}/r_{\mathrm{i}}^{u}$ and nitrogen selectivity. u, p refer to unpromoted and optimally promoted cases, respectively.

CO : NO	ρ_{CO_2}	ρ_{N_2}	ρ_{N_2O}	$S^{u}_{N_2} \rightarrow S^{p}_{N_2}$
5 : 1	20	26	11	50% → 75%
2 : 1	26	66	9	29% → 80%
1 : 1	16	34	3.2	25% → 75%
1 : 4	2.5	4.4	1.2	20% → 50%

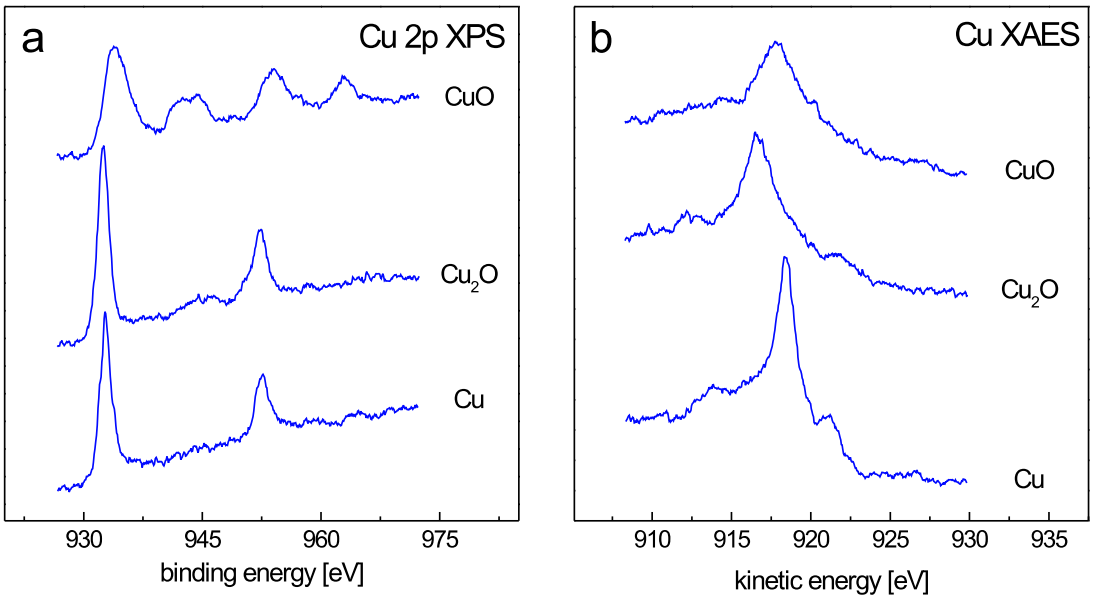

Figure 7.2: (a) Cu 2p XPS and (b) Cu LMM XAES for metallic Cu, Cu_2O and CuO.

7.4 Post-Reaction XPS Studies of the EP catalyst

XPS and Auger spectra were acquired after sample transfer to the electron spectrometer chamber following exposure to appropriate reaction gas environments in the reactor cell. For comparison purposes, we acquired reference Cu 2p XP and Cu LMM AE reference spectra for Cu, Cu_2O and CuO using the procedure described by Poulston *et al.* [19]. These are illustrated in figure 7.2. Post-reaction XP/AE spectra were obtained after exposing the catalyst film to the same conditions of temperature and reactant partial pressures as those used in the CST reactor. A description of the procedure employed can be found in chapter 2.

These post-reaction XP/AE experiments were performed in order to shed light on several important issues. (i) What evidence is there for the reversible transport of Na between electrolyte and catalyst under reaction conditions? (ii) What differences in catalyst surface composition are there between the unpromoted and promoted regimes? (iii) What surface species are formed by Na pumping to the Cu catalyst at reaction temperature in the presence of the reactant gases? (iv) What is the oxidation state of the Cu catalyst? We therefore exposed the sample to the same conditions as those used in the reactor, all at 648 K, 1 bar total pressure, as follows: (i) CO:NO=5:1, (ii) CO:NO=2:1 and (iii) CO:NO=1:4 under unpromoted ($V_{WR} = +100\,mV$) and promoted ($V_{WR} = -400\,mV$) conditions. After these gas exposures the sample was transferred to the spectrometer chamber, and the XP spectra recorded.

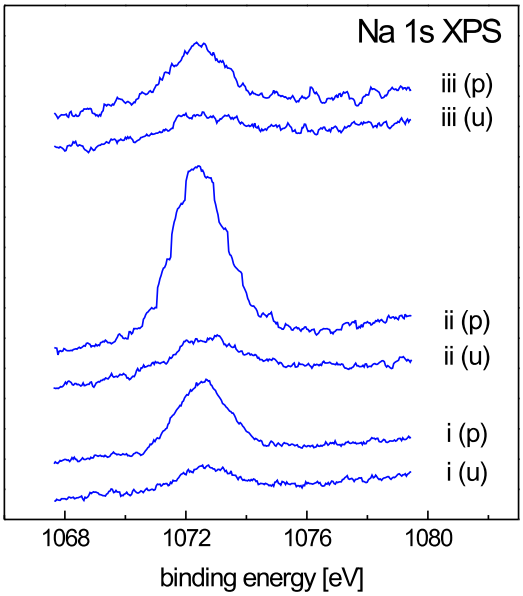

Figure 7.3: Na 1s XP spectra of the catalyst film after exposure to different reaction mixtures at reaction temperature. The results refer to unpromoted (u) and promoted (p) conditions for different CO:NO ratios: (i) CO:NO=5:1, (ii) CO:NO=2:1 and (iii) CO:NO=1:4.

A combination of Cu XP and XAE spectra is required in order to distinguish between Cu metal, Cu_2O and CuO [10, 19]. Thus CuO is characterised by high intensity shake-up satellites at 9 eV higher binding energy than the main $2p_{3/2}$ and $2p_{1/2}$ peaks. Additionally, the CuO main lines are shifted 1.2 eV towards higher binding energy and broadened compared to Cu_2O and Cu metal [20]. Cu metal and Cu_2O are best distinguished by their X-ray excited Cu LMM Auger spectra since their Cu 2p transitions differ by only ~ 0.2 eV. We therefore recorded appropriate reference spectra and these data are shown in figure 7.2.

Figure 7.3 shows Na 1s XP spectra of the catalyst film taken after exposure to three different reaction mixtures under both unpromoted and promoted conditions. These results clearly demonstrate that the value of V_{WR} is directly correlated with the loading of Na on the catalyst surface under reaction conditions: decreasing the catalyst potential ($V_{WR} = -400$ mV) causes an increase in the amount of Na. It is important to note that these spectral changes were fully reversible as a function of catalyst potential.

Analogous Cu 2p XPS and Cu LMM Auger spectra are shown in figures 7.4a and 7.4b respectively. Several features are apparent from figures 7.4a and 7.4b and may be summarised as follows: (1) initially, before use, the surface of the catalyst film consists of metallic Cu alone; (2) for a given catalyst potential, as the CO:NO ratio decreases (i. e. as the gaseous environment becomes more oxidising) the oxidation state of the

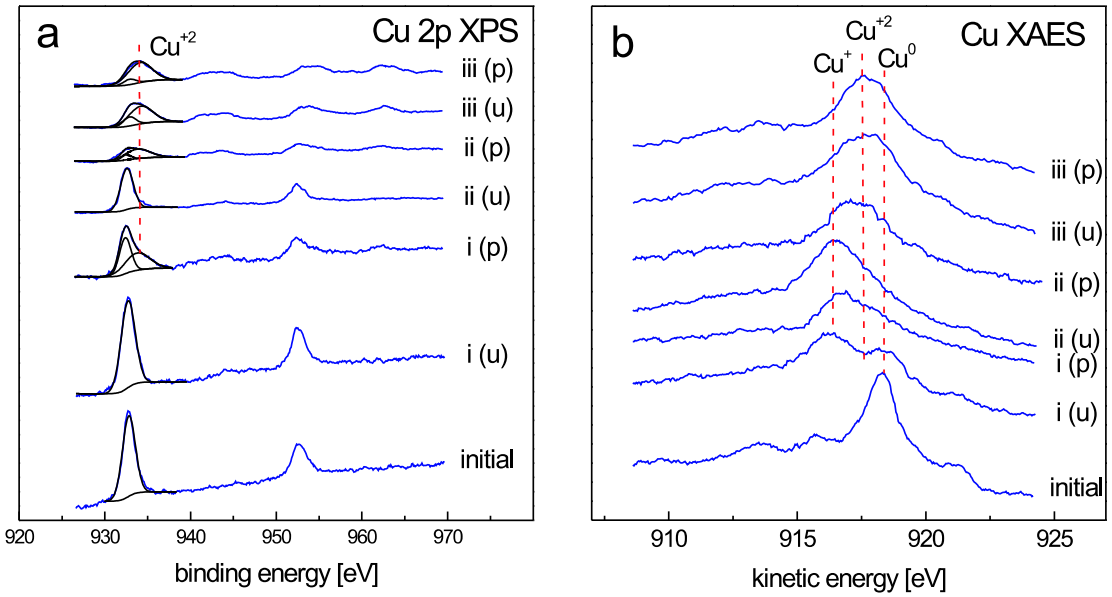

Figure 7.4: (a)Cu 2p XP spectra and (b) Cu LMM XAES spectra of the catalyst film after exposure to different reaction mixtures at reaction temperature. The results refer to unpromoted (u) and promoted (p) conditions for different CO:NO ratios: (i) CO:NO=5:1, (ii) CO:NO=2:1 and (iii) CO:NO=1:4.

copper increases; (3) for a given CO:NO ratio, as the sodium coverage increases, the oxidation state of the copper is increased. Thus, the bottom spectra of figures 7.4a and 7.4b show the Cu 2p and Cu LMM XAES spectra of the catalyst 'as received'. The sharp peak present at ~ 918.5 eV kinetic energy in the Cu LMM spectra and the shape and binding energy positions of the Cu $2p_{3/2}$ and Cu $2p_{1/2}$ demonstrate that the initial oxidation state of the Cu in the catalyst is zero, as comparison with the reference spectra in figure 7.2 confirms. Exposing this 'as received' film to the same conditions of pressure and temperature as those used in the CST reactor with CO:NO=5:1 under unpromoted conditions causes an increase in oxidation state of the Cu catalyst. The catalyst consists of Cu metal and Cu_2O as determined from the relevant Cu 2p XP and Cu LMM XAES spectra. Exposing the Cu film in the same initial condition as before to the same gas environment and temperature but under promoted conditions causes a further increase in the oxidation state of the Cu film. In this case, the catalyst surface consists of Cu_2O and CuO. The same general trends were observed when the procedure was repeated with gas composition CO:NO=2:1. In this case, the unpromoted catalyst consists of Cu_2O, whereas under promoted conditions the catalyst surface consists of Cu_2O and CuO, no Cu^0 being detectable. With CO:NO=1:4 the unpromoted surface consists of CuO and a small amount of Cu_2O; the promoted surface consists almost entirely of CuO. These

Table 7.2: Determination of surface oxidation state using Cu 2p XP and Cu LMM XAE spectra.

CO : NO	$V_{WR} = +100\,mV$ (unpromoted)	$V_{WR} = -400\,mV$ (promoted)
5 : 1	Cu^0+Cu_2O (48%+52%)	Cu_2O+CuO (67%+33%)
2 : 1	Cu_2O (100%)	Cu_2O+CuO (28%+72%)
1 : 4	Cu_2O+CuO (19%+81%)	Cu_2O+CuO (13%+87%)

findings are summarised in table 7.2. Quantification was achieved by estimating the integrated intensity of the Cu^0, Cu^+ and Cu^{2+} components and by assuming that (i) the photoionisation cross section of Cu 2p is independent of oxidation state and (ii) the sampled volume is unaffected by the state of oxidation of the Cu film. Although these are not gross approximations, the estimated compositions should be regarded as no more than indicative.

Figures 7.5 and 7.6 show the O 1s XP spectra and N 1s XP spectra respectively, taken after exposing the film to exactly the same range of conditions as those pertaining to figures 7.4a and 7.4b. It is evident that (i) in all the unpromoted cases the O 1s signal exhibits only one feature at 530 eV binding energy and (ii) when sodium is present on the surface, a second feature appears at 532.5 eV binding energy. The 530 eV may be attributed with confidence to the oxides of copper [21, 22] present on the surface under both unpromoted and promoted conditions. No carbonate species were present as judged by the complete absence of C 1s emission. Since the O 1s peak at 532.5 eV appeared only when sodium was present on the surface, we assign it to a sodium compound. We now show that this compound is $NaNO_3$. Figure 7.6 shows relevant N 1s XP spectra: this signal was detectable at all CO:NO ratios, but only after the catalyst had been run under promoted conditions. The binding energy (407 eV) corresponds to sodium nitrate [23]. Moreover, in any given case, the ratio of the intensity of the O 1s higher binding energy component to that of the corresponding N 1s emission was 2.86 (after normalisation to take account of photoionization cross section [24]). This provides strong quantitative support for the view that under promoted conditions sodium is present on the surface as $NaNO_3$. The binding energies observed in the Cu 2p spectra rule out the presence of copper nitrate [25] under all conditions. Heating the promoted catalyst in vacuum to 483 K and applying a positive catalyst potential causes the disappearance of both the higher binding energy O 1s signal, the N 1s peak and the Na 1s peak, restoring clean surface conditions in agreement with the reversibility observed in the kinetic measurements.

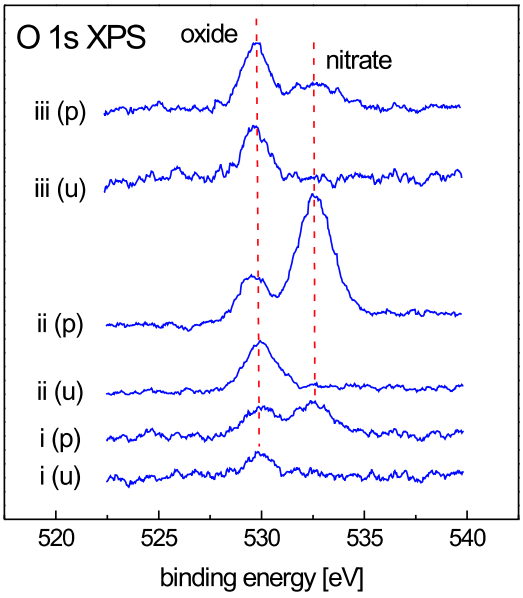

Figure 7.5: O 1s XP spectra of the catalyst film after exposure to different reaction mixtures at reaction temperature. The results refer to unpromoted (u) and promoted (p) conditions for different CO:NO ratios: (i) CO:NO=5:1, (ii) CO:NO=2:1 and (iii) CO:NO=1:4.

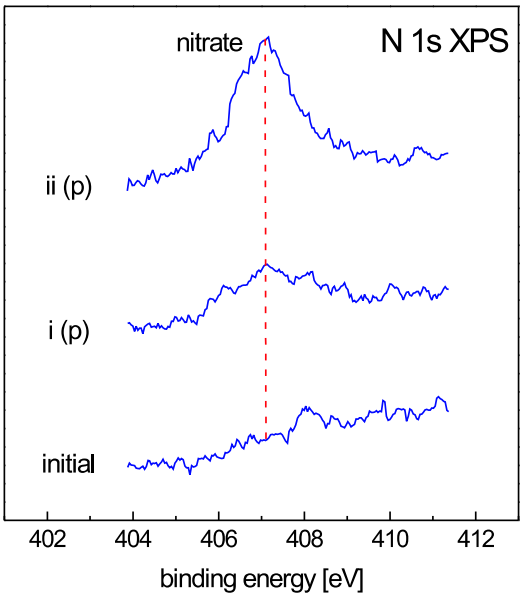

Figure 7.6: N 1s XP spectra of the catalyst film after exposure to different reaction mixtures at reaction temperature. The results refer promoted (p) conditions for different CO:NO ratios: (i) CO:NO=5:1 and (ii) CO:NO=2:1.

7.5 Discussion

Given the lack of sensitivity of the CO + NO reaction toward the details of surface structure [13–16] it is reasonable to take the view that our data and those obtained with conventional dispersed catalysts should be interpretable on the same general basis.

It is useful to summarise the overall pattern of behaviour illustrated in figures 7.1a-d. First, regardless of reaction gas composition and Na loading, sodium promotion always leads to enhancement of both activity and N_2 selectivity. Second, the Na-induced enhancement in activity is very large under reducing conditions ($\rho \sim 20$ for CO:NO = 5:1 and 2:1) and an order of magnitude smaller under oxidising conditions ($\rho \sim 2.5$, CO:NO = 1:4). Third, on the clean surface ($V_{WR} = +100\,mV$) the nitrogen selectivity decreases with decreasing CO:NO ratio.

The spectroscopic data show clearly that promotion is associated with the pumping of Na to the catalysts surface (figure 7.3). They also establish that under reaction conditions (i) this sodium is present as the nitrate (figures 7.5 and 7.6) (ii) no alkali carbonate is formed (iii) no copper nitrate is present (iv) the promoted catalyst surface consists of Cu oxides. In view of (iii) we rule out participation of Cu nitrate in the overall catalytic process, in agreement with London and Bell [11] and at variance with Dekker *et al.* [12].

In the work presented in chapters 4 and 5 on NO reduction by CO or propene over rhodium, we proposed that EP results from acceleration of the key reaction-initiating step: dissociation of adsorbed NO. In the case of a pure metal surface, we argued as follows. As the catalyst potential is decreased (pumping Na to the surface) the electronic effect of the sodium promoter on adsorbed NO strengthens the metal−N bond and weakens the N−O bond facilitating NO dissociation. These effects are caused by the electric field of the alkali cation which lowers the energy of the π^* orbital in the adjacent diatomic molecule with respect to the metal Fermi level [26]. This results in an increased electron density in the π^* orbital (i) strengthening the metal−N bond and (ii) weakening the N−O bond facilitating dissociation of the molecule. Thus, Na promotion produces large increases in both activity and N_2 selectivity as a result of accelerating the dissociation of adsorbed NO.

What happens in the present case, which is complicated by the effects of Cu metal oxidation? There is little agreement in the literature regarding the question of which types of Cu sites are involved in catalytic turnover and which types of site adsorb NO, CO or other possible adsorbates under reaction conditions. For example, on the basis of their transient isotope reactor measurements, Dekker *et al.* [12] concluded that strongly bound NO is associated with Cu^+ sites. This is at variance with the proposal by Fu *et*

al. [27], based on low temperature IR data, namely that CO and NO adsorb on both Cu^{+} and Cu^{++}, with NO adsorbed somewhat more strongly on Cu^{++} and CO adsorbed somewhat more strongly on Cu^{+}. London and Bell [11] invoke Cu^{0}, Cu^{+} and Cu^{++} in the process of catalytic turnover; most other authors consider that only Cu^{+} and Cu^{++} sites are involved. Our results cannot resolve all these issues, but they do provide answers to some of them. As argued below, they demonstrate that Na promotion of NO dissociation accounts for the observed effects of EP on activity and selectivity in a natural way. In addition, they clearly demonstrate that the chemical composition of the active surface is strongly dependent on the composition of the reaction gas mixture, an issue that previously has not been investigated systematically. We therefore suggest that in the present case the reaction mechanism and mode of promotion are analogous to those proposed to explain the behaviour of Pt and Rh catalysts undergoing EP of NO reduction (see chapters 4 and 5 and references [28, 29]).

The post-reaction XP and Auger spectra (figures 7.4a and 7.4b) indicate that the promoted surface does not contain detectable Cu^{0}. It consists of a mixture of Cu^{++} and Cu^{+} sites: the number density of the latter is relatively small under strongly oxidising conditions. This is in line with the observations of Fu *et al.* [27] whose IR/XPS data obtained with CuO/alumina catalysts indicated the simultaneous presence of Cu^{++} and Cu^{+} at the surface. We therefore propose that the reaction is triggered by the Na-induced dissociation of NO adsorbed on Cu^{+} as follows:

$$Cu^{+} - NO + Cu^{+} \rightarrow Cu^{+} - N + Cu^{2+} - O^{-} \tag{7.1}$$

Cu^{+} rather than Cu^{++} is suggested as the principal site for NO activation on the grounds of the 3d electron density. This d electron density should favour NO dissociation on Cu^{+} (relative to Cu^{++}) and thus enhance the effect of Na promotion. This view is supported by the observation that the effects of Na promotion on both selectivity and activity are most pronounced when the Cu^{+} content of the clean (unpromoted) surface are highest (figures 7.1a-d, 7.4a, 7.4b and table 7.2). It is also in accord with the findings of Fernández-García *et al.* [18], whose XANES data led them to conclude that NO adsorption and dissociation at Cu^{+} sites is the rate limiting step for the unpromoted reaction.

The identity of the NO activating site(s) deserves further comment. We propose that Cu^{+} rather than Cu^{++} as the key site in dissociating NO. This selection is based on the following reasoning (also mention above). In order for the N−O bond to be broken it is anticipated that it will be necessary to first weaken the bond through the addition of an electron into the antibonding orbital of the molecule. Adsorption on a Cu^{+} site

should facilitate this step since it should be easier to withdraw an electron from Cu^{+} than from Cu^{++}. However, Shelef and Gandhi have shown [30] that NO adsorbs faster at Cu^{++} sites than it does at Cu^{+} sites. Preferential adsorption of NO at Cu^{++} sites may be rationalised in terms of the unpaired spins on adsorbate and adsorbent [30]. Our suggestion is based on adsorbed NO acting as a σ donor π^{*} acceptor. Recent calculations [31, 32] show that NO does indeed bond to Cu^{+} by a σ/π^{*} mechanism. With respect to mechanism, a key issue is the activation energy to dissociation of NO on the two types of Cu site. The weight of theoretical [26], and experimental evidence [27, 33] suggests that this quantity should be lowest on Cu^{+}, consistent with our model. Thus the observation [33] of a substantially lower N−O stretching frequency (1765 cm^{-1}) for $Cu^{+} - NO$ than for $Cu^{++} - NO$ (1880 cm^{-1}) points to a reduced activation energy for NO dissociation in the former case. These values are in agreement with the ones determined by Bijsterbosch [34], i. e. $Cu^{+} - NO$ (1747 cm^{-1}) and $Cu^{++} - NO$ (1867 cm^{-1}).

Therefore, on balance, we agree with Fernández-García *et al.* [18] that NO reduction over copper based catalysts proceeds via a mechanism of reduction and oxidation of the surface. Thus, the process of catalytic turnover may be written as the following redox mechanism:

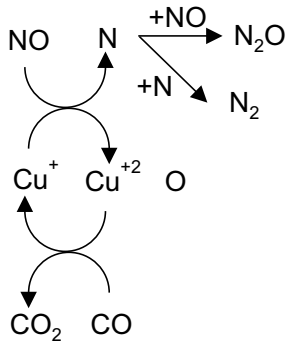

This mechanism accounts for the observed consequences of sodium promotion as follows. As mention above, the role of sodium is to increase the N−O dissociation step (the proposed rate determining step [18]) resulting in (i) larger reaction rates and nitrogen selectivity values and (ii) higher oxidation of copper. The mechanism is also in line with the fact that increasing the NO:CO ratio increases the overall oxidation state of copper under unpromoted conditions.

Figures 7.1a-d show that the nitrogen selectivity of the unpromoted ($V_{WR} = +100\,mV$)

catalyst decreases while decreasing the CO:NO ratio. This may be rationalised as follows. The mode of NO chemisorption on Cu^0, Cu^+ and Cu^{++} is linear bonding through the nitrogen atom. The conventional view of this process is the donation/backdonation model [35] involving the π^* level of NO and d-orbitals of the metal. Net electron transfer may thus vary from $M^{\delta-} - NO^{\delta+}$ to $M^{\delta+} - NO^{\delta-}$. On this basis, and in agreement with observation [13–15, 17], one expects the efficacy of Cu species for NO dissociation to lie in the order $Cu^0 > Cu^+ > Cu^{++}$. The spectroscopic data show that decreasing the CO:NO ratio causes an increase in overall oxidation state of the copper. This in turn should result in a decrease in NO dissociation and hence a decrease in nitrogen selectivity.

7.6 Conclusions

1. In the catalytic reduction of NO by CO, the reactive behaviour, surface composition and response to electrochemical promotion of Cu film catalysts are a strong function of the composition of the reactant gas, consistent with a redox mechanism.

2. Under reducing or fairly oxidising conditions the Cu-catalysed CO + NO reaction exhibits strong electrochemical promotion of both activity and selectivity. Under strongly oxidising conditions, promotion is still observed, but the effects are much less pronounced.

3. The spectroscopic data indicate that these effects are due to pumping of Na to the catalyst where, under reaction conditions, it is present as $NaNO_3$ on an oxidised Cu surface. Na_2CO_3 and Cu nitrate are not detectable.

4. The spectroscopic and reactor data indicate that Cu^0 sites are not of catalytic significance under the conditions explored. In this regard, the weight of evidence suggests that Cu^+ is the principal site for NO dissociation. EP is due to Na-induced enhancement of the dissociation of NO at these sites.

Bibliography

[1] K. C. Taylor, Nitric oxide catalysis in automotive exhaust systems, Catalysis reviews science and engineering **35**, 457–481 (1993).

[2] M. Shelef and K. Otto, Appearance of N_2O in the catalytic reduction of NO by CO, Journal of Catalysis **10**, 408–412 (1968).

[3] M. Shelef, K. Otto, and H. Ghandi, The oxidation of CO by O_2 and by NO on supported chromium oxide and other metal oxide catalysts, Journal of Catalysis **12**, 361–375 (1968).

[4] M. Shelef, Nitric oxide: surface reactions and removal from auto exhaust, Catalysis reviews science and engineering **11**, 1–40 (1975).

[5] V. I. Pârvulescu, P. Grange, and B. Delmon, Catalytic removal of NO, Catalysis Today **46**, 233–316 (1998).

[6] H. H. Hildenbrand and H. G. Lintz, Phase composition and selectivity: solid electrolyte potentiometry aided study of the oxidation of propene on copper oxides, Applied Catalysis **65**, 241–252 (1990).

[7] H. H. Hildenbrand and H. G. Lintz, Solid electrolyte potentiometry aided study of the influence of promotors on the phase transitions in copper oxide catalysts under working conditions, Catalysis Today **9**, 153–160 (1991).

[8] H. H. Hildenbrand and H. G. Lintz, Phase composition and oxygen activity of oxidic catalysts under working conditions, Berichte der Bunsen Gesellschaft Physical Chemistry Chemical Physics **95**, 1191–1196 (1991).

[9] J. Bruck, M. Brust, and H. G. Lintz, Solid electrolyte potentiometry at oxidic catalysts, Berichte der Bunsen Gesellschaft Physical Chemistry Chemical Physics **99**, 1509–1513 (1995).

[10] G. G. Jernigan and G. A. Somorjai, Carbon monoxide oxidation over three different oxidation states of copper: metallic copper, copper (I) oxide, and copper (II) oxide: a surface science and kinetic study, Journal of Catalysis **147**, 567–577 (1994).

[11] J. W. London and A. T. Bell, A simultaneous infrared and kinetic study of the reduction of nitric oxide by carbon monoxide over copper oxide, Journal of Catalysis **31**, 96–109 (1973).

[12] F. H. M. Dekker, S. Kraneveld, A. Bliek, F. Kapteijn, and J. A. Moulijn, NO reduction over alumina supported Cu and Cu-Cr studied with the step-response method, Journal of Catalysis **170**, 168–180 (1997).

[13] A. R. Balkenende, O. L. J. Gijzeman, and J. W. Geus, The interaction of NO and CO with Cu(111), Applied Surface Science **37**, 189–200 (1989).

[14] A. R. Balkenende, H. Dendaas, M. Huisman, O. L. J. Gijzeman, and J. W. Geus, The interaction of NO, O_2 and CO with Cu(100) and Cu(110), Applied Surface Science **47**, 341–353 (1991).

[15] A. R. Balkenende, R. Hoogendam, T. Debeer, O. L. J. Gijzeman, and J. W. Geus, The interaction of NO, O_2 and CO with Cu(710) and Cu(711), Applied Surface Science **55**, 1–9 (1992).

[16] A. T. S. Wee, J. Lin, A. C. H. Huan, F. C. Loh, and K. L. Tan, SIMS study of NO and CO adsorption on Cu(100) and Cu(210) surfaces, Surface Science **304**, 145–158 (1994).

[17] A. R. Balkenende, C. J. G. van der Grift, E. A. Meulenkamp, and J. W. Geus, Characterisation of the surface of a Cu/SiO_2 catalyst exposed to NO and CO using IR spectroscopy, Applied Surface Science **68**, 161–171 (1993).

[18] M. F. García, C. M. Alvarez, I. R. Ramos, A. G. Ruíz, and G. L. Haller, New insights on the mechanism of the NO reduction with CO over alumina supported copper catalysts, Journal of Physical Chemistry **99**, 16380–16382 (1995).

[19] S. Poulston, P. M. Parlett, P. Stone, and M. Bowker, Surface oxidation and reduction of CuO and Cu_2O studied using XPS and XAES, Surface and Interface Analysis **24**, 811–820 (1996).

[20] J. A. Leiro, M. H. Heinonen, F. Werfel, E. G. Nordström, and K. H. Karlsson, X-ray photoemission study of $NaCuO_2$, Philosophical Magazine Letters **68**, 153–157 (1993).

[21] F. Parmigiani, L. E. Depero, T. Minerva, and J. B. Torrance, The fine structure of the Cu $2p_{3/2}$ X-ray photoelectron spectra of copper oxide based compounds, Journal of Electron Spectroscopy and Related Phenomena **58**, 315–323 (1992).

[22] F. Parmigiani, G. Pacchioni, F. Illas, and P. S. Bagus, Studies of the Cu−O bond in cupric oxide by X-ray photoelectron spectroscopy and *ab initio* electronic structure models, Journal of Electron Spectroscopy and Related Phenomena **59**, 255–269 (1992).

[23] H. C. Allen, J. M. Laux, R. Vogt, B. J. F. Pitts, and J. C. Hemminger, Water-induced reorganization of ultrathin nitrate films on NaCl: implications for the tropospheric chemistry of sea salt particles, Journal of Physical Chemistry **100**, 6371–6375 (1996).

[24] J. J. Yeh and I. Lindau, Atomic subshell photoionisation cross sections and asymmetry parameters: $1 \leq Z \leq 103$, Atomic Data and Nuclear Data Tables **32**, 1–155 (1985).

[25] C. D. Wagner, Photoelectron and Auger energies and the Auger parameter: a data set, in *Practical surface analysis by Auger and X-ray photoelectron spectroscopy*, edited by D. Briggs and M. P. Seah, Wiley, New York, 1983.

[26] N. D. Lang, S. Holloway, and J. K. Nørskov, Electrostatic adsorbate-adsorbate interactions: the poisoning and promotion of the molecular adsorption reaction, Surface Science **150**, 24–38 (1985).

[27] Y. Fu, Y. Tian, and P. Lin, A low temperature IR spectroscopy study of selective adsorption of NO and CO on CuO/γ-Al_2O_3, Journal of Catalysis **132**, 85–91 (1991).

[28] A. Palermo, R. M. Lambert, I. R. Harkness, I. V. Yentekakis, O. Mar'ina, and C. G. Vayenas, Electrochemical promotion by Na of the platinum-catalysed reaction between CO and NO, Journal of Catalysis **161**, 471–479 (1996).

[29] I. V. Yentekakis, A. Palermo, N. C. Filkin, M. S. Tikhov, and R. M. Lambert, *In situ* electrochemical promotion by sodium of the platinum-catalysed reduction of NO by propene, Journal of Physical Chemistry B **101**, 3759–3768 (1997).

[30] H. S. Ghandi and M. Shelef, The adsorption of nitric oxide on copper oxides, Journal of Catalysis **28**, 1–7 (1973).

[31] M. Casarin, C. Maccato, and A. Vittadini, A comparative study of CO and NO chemisorption on $Cu_2O(111)$ and $Ag_2O(111)$ non-polar surfaces, Chemical Physics Letters **280**, 53–58 (1997).

[32] M. Casarin and A. Vittadini, A theoretical study of the CO and NO chemisorption on $Cu_2O(111)$, Surface Science **387**, L1079–L1084 (1997).

[33] A. Sepúlveda, C. Márquez, I. R. Ramos, A. G. Ruíz, and J. L. G. Fierro, Spectroscopic studies of surface copper spinels: influence of pretreatments on chemical state of copper, Surface and Interface Analysis **20**, 1067–1074 (1993).

[34] J. Bijsterbosch, *Copper based catalysts for CO oxidation and NO reduction*, PhD thesis, University of Amsterdam, Amsterdam, 1993.

[35] G. Blyholder and M. A. Allen, Infrared spectra and molecular orbital model for carbon monoxide adsorbed on metals, Journal of the American Chemical Society **91**, 3158–3162 (1969).

CHAPTER 8

The Fischer-Tropsch synthesis

8.1 Introduction

As shown in chapter 3, Electrochemical Promotion (EP) is a unique method for the *in situ* control of promoter concentration at the surface of a working metal catalyst. As such, it may be used to investigate reaction mechanisms and to guide the development of classically promoted dispersed catalysts. Examples of the former are provided by previous chapters on the EP of NO reduction over Rh and Cu. Examples of the latter include effective alkali-promoted catalysts for NO reduction under realistic (simulated exhaust) conditions [1]. The EP technique entails electrochemical pumping of ions from a solid electrolyte to the surface of a porous, catalytically active metal film with which it is in contact. The catalyst is at the same time the working electrode of a solid state electrochemical cell. With Na β" alumina (a Na^+ conductor) as the solid electrolyte, controlling the catalyst potential measured with respect to a reference electrode (V_{WR}) controls the sodium coverage (ϑ_{Na}) and consequently the reactive behaviour of the catalyst surface [2].

The present investigation of Fischer-Tropsch synthesis (FTS) was undertaken with three principal objectives. First, to broaden the applicability of EP in the study of heterogeneous catalysis. With one exception (the selective hydrogenation of acetylene over Pt [3]), all the earlier work in this field has involved oxidation reactions; none of it has involved C−C bond forming reactions. Second, to investigate the effects of Na promotion on FTS with a view to contributing to our understanding of the mechanism. Third, to establish whether such EP data are of relevance to the behaviour and understanding

of classical dispersed FTS catalysts.

The effective FTS catalysts are Ru, Fe, Co and Rh. Ruthenium was chosen for this exploratory study at atmospheric pressure because it exhibits high intrinsic activity for linear α–olefins production and because alkali promotion of conventional Ru FTS catalysts has already been studied [4–8]. There is broad agreement with respect to the consequences of alkali promotion, although the explanation of these effects remains controversial. Ensemble effects [5], electronic effects [6, 7] and a decrease in the surface coverage and in the mobility of H adatoms [8, 9] have been variously invoked, whereas Lahtinen and Somorjai [10] proposed that the principal effect of K is to inhibit graphite formation.

We conclude that CO dissociation is not rate limiting, that alkali promotion increases the probability of chain growth, and that electronic effects must play a significant role in the promoted reaction.

8.2 Experimental methods

The Ru catalyst (working electrode, W) consisted of a porous continuous thin film deposited by thermal decomposition of a solution of $Ru_3(CO)_{12}$ in acetone at 573 K in a nitrogen atmosphere on one face of a 45 mm×15 mm×1 mm wafer of a Na β" alumina solid electrolyte. Au reference (R) and counter (C) electrodes were deposited on the other face by Au sputtering in argon. The sample was suspended in a quartz, atmospheric pressure well-mixed reactor with all electrodes exposed to the reactant gas mixture. The system behaved as a single pellet, well mixed reactor as described in chapter 2 and in reference [11].

Quantitative analysis of the reaction products was carried out by on-line gas chromatography (Shimadzu-14B ;Porapak-N; flame ionisation detector). The detector was calibrated using standards of known concentration. Reactants were pure CO (Distillers MG) and pure H_2 (Distillers MG) and were fed to the reactor by mass-flow controllers (Brooks 5850 TR). A galvanostat-potentiostat (Ionic Systems) was used to maintain a difference potential between the working and reference electrodes (potentiostatic mode). All experiments were carried out in potentiostatic mode by following the effect of catalyst potential (V_{WR}, measured with respect to the reference electrode) on the reaction rates. Decreasing the catalyst potential below the value corresponding to the electrochemically clean surface (+400 mV) resulted in electro-pumping of Na to the Ru surface, thereby increasing ϑ_{Na}. Our previous work (chapter 3) showed that ϑ_{Na} increased linearly with decreasing V_{WR}.

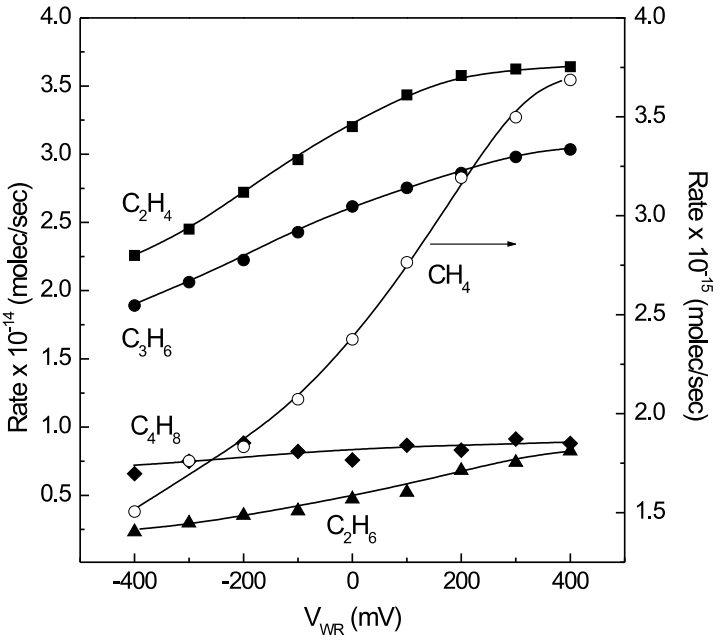

Figure 8.1: Effect of catalyst potential V_{WR} on the reaction rates of the formation of products. Note that the CH_4 rate is represented on the right axes. Conditions $P^{\circ}_{\mathrm{CO}} = 25.33\,\mathrm{kPa}$, $P^{\circ}_{\mathrm{H_2}} = 76\,\mathrm{kPa}$, $T = 473\,\mathrm{K}$.

8.3 Effect of catalyst potential on reaction rates

CO was hydrogenated to hydrocarbons over the Ru EP model catalyst at 473 K and 1 bar total pressure. Linear alkenes and alkanes of carbon number up to 4 were the only products. Figure 8.1 shows steady-state (potentiostatic) rate data for hydrocarbon production as a function of catalyst potential (V_{WR}) for inlet gas composition $P^{\circ}_{\mathrm{CO}} = 25.33\,\mathrm{kPa}$, $P^{\circ}_{\mathrm{H_2}} = 76\,\mathrm{kPa}$ (H_2: CO = 3). Reaction rates are expressed as molecules of product per second. It is apparent that all rates decrease with increasing ϑ_{Na} (decreasing V_{WR}). Figure 8.2 shows the dependence of product selectivity on catalyst potential, where selectivity is defined as:

$$S_i = \frac{r_i}{\sum\limits_j r_j} \tag{8.1}$$

where r_i is the rate of formation of the product i. Figure 8.2 shows that the selectivity towards ethene, propene and 1-butene production increases while the selectivity towards methane and ethane formation decreases with increasing ϑ_{Na} (decreasing V_{WR}). The catalytic response of the system was reproducible and reversible with respect to the catalyst potential, i. e. returning V_{WR} to its original value restored the original values of the reaction rates.

It is apparent from figures 8.1 and 8.2 that while the effect of alkali is to reduce the

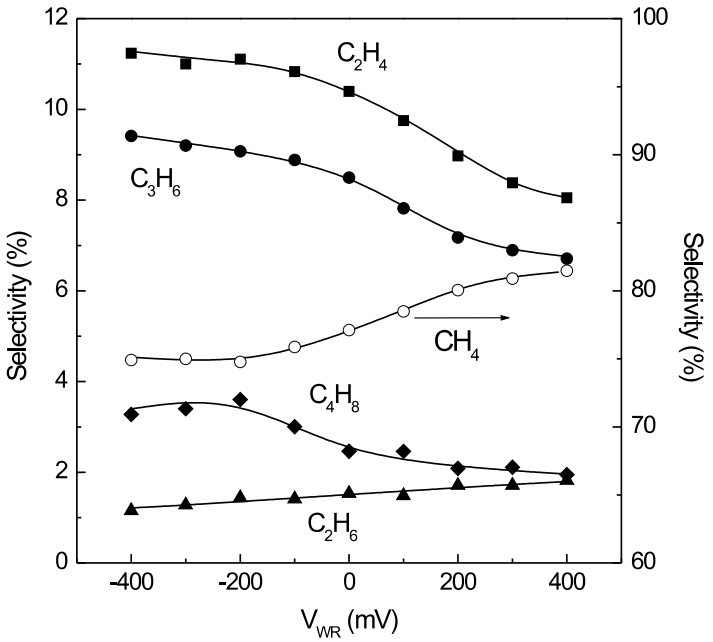

Figure 8.2: Effect of catalyst potential V_{WR} on the product selectivity. Note that the selectivity towards CH_4 production is represented on the right axes. Conditions $P^{\circ}_{\mathrm{CO}} = 25.33\,\mathrm{kPa}$, $P^{\circ}_{\mathrm{H_2}} = 76\,\mathrm{kPa}$, $T = 473\,\mathrm{K}$.

Table 8.1: Changes in rate (Δr) and selectivity (ΔS) between clean and optimally promoted catalyst divided by unpromoted rate ($r_\circ$) and unpromoted selectivity ($S_\circ$) respectively.

product	$\Delta r/r_\circ$	$\Delta S/S_\circ$
methane	-59	-8
ethene	-38	$+40$
ethane	-72	-33
propene	-38	$+40$
1-butene	-25	$+70$

rates of all catalytic reactions, the rates of formation of the higher alkenes are reduced less than the rates of formation of methane and ethane. The result is an increase in selectivity towards the higher alkenes. These results are presented numerically in table 8.1 which shows the relative changes in reaction rates and in selectivity for methane, ethene, ethane, propene, and 1-butene as one proceeds from the alkali free ruthenium catalyst to the optimally promoted ruthenium catalyst. It is clear that the formation of higher alkenes is favoured by sodium promotion, a result that will be discussed below.

8.4 Effect of catalyst potential on chain growth

The Anderson-Flory-Schulz distribution for the FTS reaction yield [12] is given by:

$$n(i) = n(1) \cdot \alpha^{i-1} \tag{8.2}$$

where i indicates the carbon number, α the chain growth probability and $n(i)$ the molar fraction of linear products with carbon number i (i. e. $n(1)$ is the molar fraction of C_1 product, methane). This relation implies a polymerisation reaction that proceeds via addition of a single carbon monomer with α independent of the carbon number of the growing species. Equation 8.2 predicts a linear relationship between $\ln[n(i)/n(1)]$ and $i-1$, whence α can be obtained from the slope. Our data have been plotted according to this relationship (figure 8.3). It can be seen that: (i) the experimental distribution deviates from the Anderson-Flory-Schulz distribution at C_2 and (ii) the calculated chain growth probability increases with ϑ_{Na} (decreasing V_{WR}). Significant deviations from the Anderson-Flory-Schulz distribution are reported in the literature [13]. The C_2 anomaly found here is in very good agreement with the results of Quyoum *et al.* [14] who reported exactly the same effect for FTS over Ru supported on SiO_2. The C_2 anomaly has been rationalised in terms of secondary reactions, including (i) incorporation of ethene in growing chains [15], (ii) rapid readsorption of ethene [16] and (iii) hydrogenolysis of ethene [16].

As noted above, figure 8.3 shows that the slope of the distribution increases with increasing ϑ_{Na} (decreasing V_{WR}). The implications of this are made apparent in figure 8.4 where the chain growth probability is plotted against catalyst potential. It is evident that α increases with ϑ_{Na} (decreasing V_{WR}): the chain growth probability for the optimally promoted catalyst is much greater than that for the unpromoted catalyst ($-400\,\mathrm{mV}$ *versus* $+400\,\mathrm{mV}$). Figure 8.5 shows the effect of catalyst potential on the alkene to alkane ratio for C_2 products. Decreasing the catalyst potential, i. e. increasing ϑ_{Na} causes an increase in the rate of production of ethene relative to ethane, with a

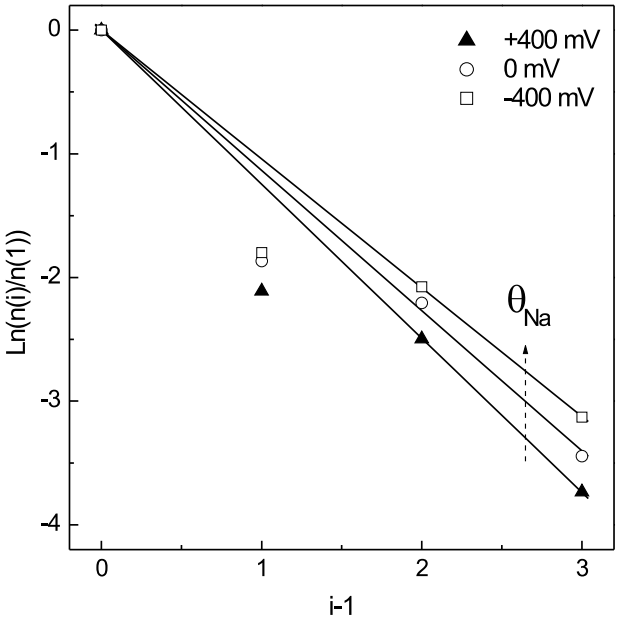

Figure 8.3: Experimental molecular distribution of the reaction products obtained at different catalysts potential. The solid lines represent the (theoretical) Anderson-Flory-Schulz distribution for a stepwise polymerisation of methylenes. $n(i)$ is the molar fraction of molecules having carbon number i.

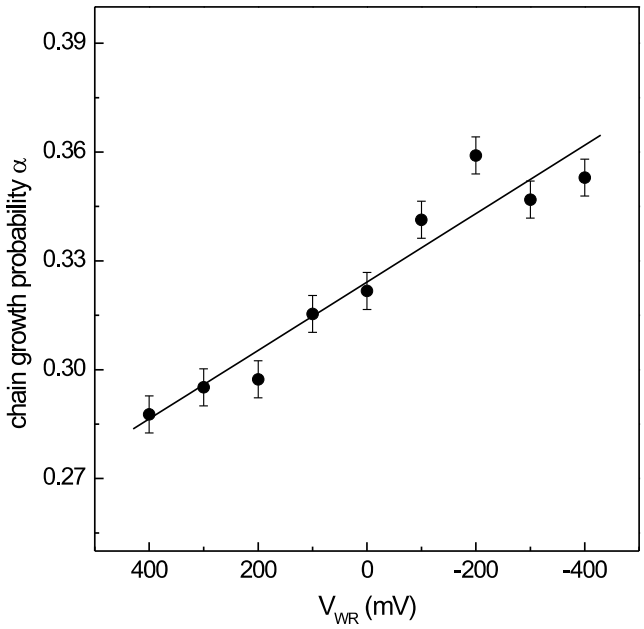

Figure 8.4: Effect of catalyst potential V_{WR} on the probability of chain growth. The error was calculated from the error in the linear regression shown in figure 8.3.

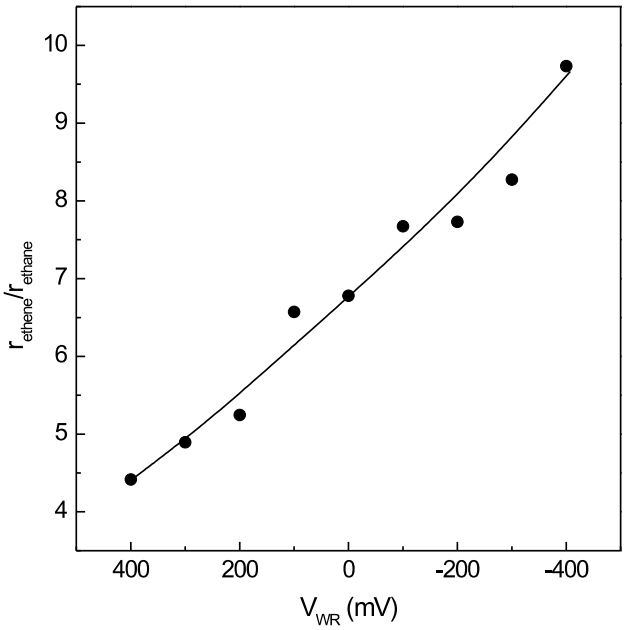

Figure 8.5: Effect of catalyst potential V_{WR} on the olefin to paraffin ratio for C_2 products.

maximum increase of 122%.

8.5 Discussion

The effects of increased alkali loading on the reaction may be summarised as follows:

(i) a decrease in all reaction rates.

(ii) an increase in the selectivity towards longer hydrocarbons.

(iii) an increase in the chain growth probability.

(iv) an increase in the alkene to alkane ratio.

We may rationalise these observations in terms of a model based on that proposed by Kellner and Bell [17, 18], modified to account for water formation via a sequence of Langmuir-Hinshelwood steps rather than a single concerted Eley-Rideal step. Complexities introduced by possible alkene reincorporation [19] and chain branching do not affect the overall validity of the argument.

The surface catalysed polymerisation uses CH_2 monomers, formed by hydrogenation of adsorbed CO in order to produce hydrocarbons. Chain growth occurs by addition of surface methylene species to adsorbed alkyl groups. These alkyl groups can undergo β-hydrogen abstraction to form α-olefins or hydrogen addition to form n-paraffins [20].

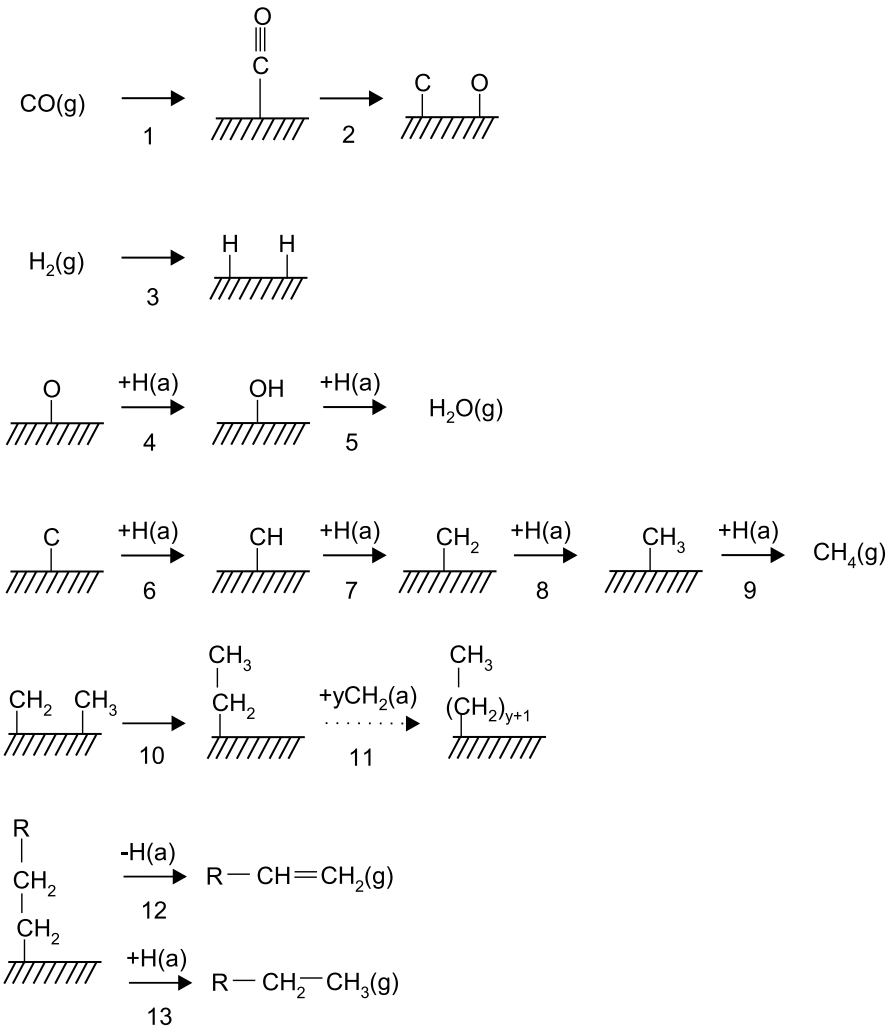

Figure 8.6: Proposed mechanism of hydrocarbon synthesis modified from references [17] and [18].

Figure 8.6 depicts the initiation, growth and termination of chains according to this mechanism. CO adsorbs (step 1) and dissociates (step 2) whereas H_2 is assumed to adsorb dissociatively (step 3). Adsorbed oxygen and hydrogen react to form water (steps 4 and 5). Chain initiation occurs when carbon adatoms react with hydrogen adatoms (steps 6,7, and 8) to form CH, CH_2 (monomer) and CH_3 (chain initiator). Methane formation takes place when CH_3 is hydrogenated (step 9). Chain growth occurs by insertion of the monomer in a growing alkyl species (step 10 and 11). Termination occurs by β-hydrogen elimination yielding an α-olefin (step 12) or by addition of hydrogen to form an n-alkane (step 13).

It is generally accepted that the rate-limiting step is C hydrogenation rather than CO dissociation [17, 21]. This view is consistent with the fact that whereas alkali metals facilitate the dissociation of adsorbed CO, alkali promotion nevertheless decreases all rates in FTS. Therefore alkali promotion data, such as those presented here, provide additional evidence that the rate limiting step cannot be CO dissociation.

All the effects of sodium promotion ((i) to (iv) above) may be understood by postulating that the effect of alkali is to inhibit the hydrogenation steps. If hydrogenation is rate limiting, this would decrease all reaction rates (observation (i)). Because methanation is more hydrogen demanding than the FTS, the CH_4 rate is more strongly suppressed than those of the higher hydrocarbons. This results in increased selectivity towards higher hydrocarbons, implying increased chain growth probability (observations (ii) and (iii)). Finally, since termination to form alkanes involves consumption of hydrogen adatoms (H(a)), whereas β-hydrogen elimination to form alkenes generates H(a), alkali-induced decrease in the hydrogenation rate should result in an increase of the alkene/alkane ratio, as found (observation (iv)).

How does Na decrease the rate of the hydrogenation steps? Broadly speaking, there are two possibilities. Alkali may act to (i) reduce the availability of H(a), or (ii) modify the intrinsic rate at which hydrogen adds to C adatoms. The first of these could reflect an ensemble effect due to blocking of adsorption sites; it could also reflect an electronic effect [22]. Both effects would act to decrease ϑ_H and their relative importance cannot be decided on the basis of available results, both here and in the literature [5, 8, 9]. The second possibility implies a change in metal−C bonding, as suggested by McClory *et al.* [5, 7]. There is no direct experimental evidence nor any theoretical support for this (plausible) suggestion. Indirect evidence is provided by vibrational spectroscopy data which show that on metal surfaces electropositive and electronegative co-adsorbates decrease [23] and increase [6], respectively, the strength of the C−O bond, implying a corresponding increase or decrease, respectively, in the metal−C bond strength. This

would be at least consistent with an alkali-induced reduction in the intrinsic hydrogenation rate.

In this connection the work of Okuhara *et al.* [6] is of interest. They studied the effect of K and P on FTS over alumina-supported ruthenium catalysts and found, in agreement with our work and earlier reports, that K increased the chain growth probability, decreased the reaction rate and increased the olefin to paraffin ratio. They also showed that P induced the opposite changes, i. e. decreased the chain growth probability, increased rate and decreased the alkene to alkane ratio.

This argues against ensemble effects being the sole cause of alkali-increased chain growth in FTS. The strong implication is that there are also significant electronic effects. We propose that such alkali-induced electronic effects could very well include another contribution, considered also by Okuhara *et al.*, though overlooked by others. As noted above, co-adsorbed alkalis increase the metal-C bond strength in chemisorbed CO. This is well established experimentally [23] and well understood theoretically [24]. Thus under any given conditions of temperature and pressure, alkalis should increase ϑ_{CO} at the expense of ϑ_H thus providing another factor favouring both chain growth and alkene production.

As noted above, in addition to increasing ϑ_{CO} alkali also promotes CO dissociation, thus increasing ϑ_O and ϑ_C. This effect should act to decrease ϑ_H even more. In this connection it is interesting to note that calculations by Baetzold show that although hydrogenation is rate limiting in FTS, the rate constant for CO dissociation determines hydrocarbon chain length: longer chains form if CO dissociation is accelerated [25].

In summary, it seems likely that alkali promotion of selectivity in FTS is the result of more than a single effect. The availability of hydrogen adatoms and the strength of the metal-C bond could both be affected, though we have no direct evidence for the latter. In addition, alkali-induced changes in ϑ_{CO} and its degree of dissociation, both well-documented effects, would also operate in the direction necessary to cause the observed behaviour.

There is a close correspondence between our results and those obtained with classically promoted dispersed Ru catalysts. We conclude that the effects of alkali promotion in FTS synthesis over Ru may be ascribed to modification of the metal surface chemistry, as discussed above. To first approximation, alkali-induced modification of the support or of the metal/support interaction appears not to be an important issue. Having demonstrated the utility of EP in the study of promoter effects in FTS carried out at 1 bar, future work will be carried out at ~ 100 bar and complemented by post-reaction electron spectroscopic studies of surface species.

8.6 Conclusions

1. Electrochemical promotion can be applied to C−C bond forming reactions and is a useful mechanistic probe in such systems.

2. The EP behaviour of thin film Ru model catalysts in FTS under Na promotion closely parallels that of classically promoted dispersed catalysts. Activity, selectivity and the C_2 anomaly are all reproduced. Support effects are therefore not of prime importance.

3. Na causes a substantial increase in chain growth probability reflected by increased selectivity toward higher hydrocarbons. It also increases the alkene:alkane ratio.

4. The effects of alkali promotion demonstrate that CO dissociation is not rate limiting and that effects in addition to purely geometrical ones must be taken into account. Such electronic effects may in part reflect alkali enhancement of CO chemisorption at the expense of hydrogen chemisorption.

Bibliography

[1] M. Konsolakis, N. Macleod, J. Issac, Y. V. Yentekakis, and R. M. Lambert, Strong promotion by Na of Pt/γ-Al_2O_3 catalysts operated under simulated exhaust conditions, Journal of Catalysis **193**, 330–337 (2000).

[2] F. J. Williams, A. Palermo, M. S. Tikhov, and R. M. Lambert, The origin of Electrochemical Promotion in heterogeneous catalysis: Photoelectron spectroscopy of solid state electrochemical cells, Journal of Physical Chemistry B **104**, 615–621 (2000).

[3] S. Tracey, J. P. Holgado-Vazquez, A. Palermo, and R. M. Lambert, *In situ* electrochemical promotion by sodium of the selective hydrogenation of acetylene over platinum, Journal of Catalysis **179**, 231–240 (1998).

[4] R. D. Gonzalez and H. Miura, Methanation and Fischer-Tropsch studies on potassium-promoted silica-supported Ru catalysts, Journal of Catalysis **77**, 338–347 (1982).

[5] M. M. McClory and R. D. Gonzalez, The role of alkali metals as promoters in the methanation and Fischer-Tropsch reaction: an *in situ* study, Journal of Catalysis **89**, 392–403 (1984).

[6] T. Okuhara, H. Tamura, and M. Misono, Effect of potassium and phosphorus on the hydrogenation of CO over alumina-supported ruthenium catalyst, Journal of Catalysis **95**, 41–48 (1985).

[7] T. E. Hoost and J. G. Goodwin, Reaction analysis of potassium promotion of Ru-catalyzed CO hydrogenation using steady-state isotopic transients, Journal of Catalysis **137**, 22–35 (1992).

[8] T. Komaya, A. T. Bell, Z. Weng-Sieh, R. Gronsky, F. Engelke, T. S. King, and M. Pruski, Effects of sodium on the structure and Fischer-Tropsch synthesis activity of Ru/TiO_2, Journal of Catalysis **152**, 350–359 (1995).

[9] D. O. Uner, M. Pruski, B. C. Gerstein, and T. S. King, Hydrogen chemisorption on potassium promoted supported ruthenium catalysts, Journal of Catalysis **146**, 530–536 (1994).

[10] J. Lahtinen and G. A. Somorjai, The effects of promoters in carbon monoxide hydrogenation on cobalt foil model catalysts, Journal of Molecular Catalysis A: Chemical **130**, 255–260 (1998).

[11] I. V. Yentekakis and S. Bebelis, Study of the NEMCA effect in a single-pellet catalytic reactor, Journal of Catalysis **137**, 278–283 (1992).

[12] H. Schulz and M. Claeys, Kinetic modelling of Fischer-Tropsch product distributions, Applied Catalysis A: General **186**, 91–107 (1999).

[13] G. P. van der Laan and A. A. C. M. Beenackers, Kinetics and selectivity of the Fischer-Tropsch synthesis: a literature review, Catalysis reviews science and engineering **41**, 255–318 (1999).

[14] R. Quyoum, V. Berdini, M. L. Turner, H. C. Long, and P. M. Maitlis, Mechanistic studies of methylene chain propagation in the Fischer-Tropsch synthesis, Journal of Catalysis **173**, 355–365 (1998).

[15] S. Novak, R. J. Madon, and H. Suhl, Secondary effects in the Fischer-Tropsch synthesis, Journal of Catalysis **77**, 141–151 (1982).

[16] T. Komaya and A. T. Bell, Estimates of rate coefficients for elementary processes occurring during Fischer-Tropsch synthesis over Ru/SiO_2, Journal of Catalysis **146**, 237–248 (1994).

[17] C. S. Kellner and A. T. Bell, The kinetics and mechanism of carbon monoxide hydrogenation over alumina-supported ruthenium, Journal of Catalysis **70**, 418–432 (1981).

[18] A. T. Bell, Catalytic synthesis of hydrocarbons over group VIII metals, a discussion of the reaction mechanism, Catalysis reviews science and engineering **23**, 203–232 (1981).

[19] E. Iglesia, S. L. Soled, and R. A. Fiato, Fischer-Tropsch synthesis on cobalt and ruthenium. Metal dispersion and support effects on reaction rate and selectivity, Journal of Catalysis **137**, 212–224 (1992).

[20] E. Iglesia, Design, synthesis, and use of cobalt-based Fischer-Tropsch synthesis catalysts, Applied Catalysis A: General **161**, 59–78 (1997).

[21] Y. Kobori, H. Yamasaki, S. Naito, T. Onishi, and K. Tamaru, Mechanistic study of carbon monoxide hydrogenation over ruthenium catalysts, Journal of the Chemical Society, Faraday Transactions I **78**, 1473–1490 (1982).

[22] S. C. Gebhard and B. E. Koel, Influence of potassium on the adsorption of hydrogen on Pt(111), Journal of Physical Chemistry **96**, 7056–7063 (1992).

[23] R. A. de Paola, J. Hrbek, and F. M. Hoffmann, Potassium promoted C−O bond weakening on Ru(001). I. Through-metal interaction at low potassium precoverage, Journal of Chemical Physics **82**, 2484–2498 (1985).

[24] N. D. Lang, S. Holloway, and J. K. Nørskov, Electrostatic adsorbate-adsorbate interactions: the poisoning and promotion of the molecular adsorption reaction, Surface Science **150**, 24–38 (1985).

[25] R. C. Baetzold, A theoretical model of hydrocarbon formation from CO and H_2, Journal of Physical Chemistry **88**, 5583–5589 (1984).

CHAPTER 9

Concluding remarks and future outlook

The aims of this work were (i) to study the phenomena that underlie the EP effect, (ii) to exploit EP as a tool to study alkali promotion in heterogeneous catalysis and (iii) to diversify the catalytic chemistry that can be addressed by EP.

From the present work a more complete understanding of the mechanism of EP is possible. We have demonstrated using photoelectron spectroscopies that EP is due to the potential controlled sodium coverage over thin film catalysts; it follows that this is the reason for the observed rate changes upon electrochemical modification. We have also found that eventually catalyst potential uncouples from the sodium coverage: once the catalyst is sodium free and reaction rates return to unpromoted values a further increase in catalyst potential does not modify the sodium coverage as expected, and therefore reaction rates remain at their unpromoted values. This finding fundamentally challenges Vayenas view of EP, according to which changes in the measured potential difference between working and reference electrode are controlled by changes in catalyst work function. This view is not supported by our experimental findings and the theoretical work of others.

The resulting advances in fundamental understanding have been used to exploit EP in the catalytic control of toxic emissions. Reactor measurements along with post-reaction photoelectron spectroscopies were used in order to: (i) establish the mechanism of reaction, (ii) determine the mode of promoter action and (iii) identify the chemical state of the promoter phase, in the Na-promoted catalytic reduction of NO over rhodium surfaces. Very large increases both in activity and in selectivity of the catalysts were

achieved. Our data point towards NO dissociation as the rate-limiting step and indicate that promotion is due to sodium-enhanced dissociation of chemisorbed NO. We have shown that under working conditions the promoter phase is present on the catalyst surface as a sodium-containing compound. Moreover, we have determined that the nature of the compound depends on gas atmosphere and that it can be removed from the catalyst surface by electrochemically pumping sodium away from the catalyst film. As a consequence, unpromoted conditions are restored. Most importantly, we have also shown that the beneficial effects of sodium in the Rh-catalysed nitric oxide reduction can be sustained in the presence of gaseous oxygen. However, this finding is not promising since under realistic conditions sodium poisons the rhodium catalyst. Our data indicates that this is due to (i) alkali-enhanced adsorption of O_2 against NO and (ii) alkali-inhibited adsorption of propene.

These catalytic results allowed the design and development of entirely new conventional catalytic systems. Close comparison with our results demonstrates that EP can be used as a tool to study alkali promotion of metal catalysts. The main advantages of using EP samples rather than dispersed catalysts is that they permit *in situ* control of promoter levels over the working catalyst and are amenable to study by surface science techniques. In this manner, it is possible to eliminate uncertainties due to (i) location of the promoter phase, (ii) possible modification of the support and (iii) variations in surface area from sample to sample.

Finally we have expanded the catalytic chemistry that can be studied with EP. We demonstrated for the first time that the EP effect can be induced over Cu catalysts. In particular we studied the Na-promoted Cu-catalysed nitric oxide reduction by carbon monoxide. Although, on the basis of published work the reaction mechanism can be regarded as controversial, our data indicates that the reaction involves dissociation of adsorbed NO over Cu^+ sites. We have also broadened the utility of EP by studying the CO hydrogenation polymerisation reaction over Ru catalysts. Our findings indicate that alkali promotion of selective formation of longer hydrocarbons is due to a combination of factors, all of which result in a lower hydrogenation rate: (i) alkali-enhanced CO adsorption, (ii) alkali-inhibited H_2 adsorption and (iii) alkali-enhanced CO dissociation. Our data also show that the rate-limiting step can not be CO dissociation. The excellent agreement between our Fischer-Tropsch EP studies and those carried out using sodium-promoted dispersed catalysts demonstrates that support effects are not of great importance in the latter case and it also illustrates the use of EP as a tool to study alkali promotion in heterogeneous catalysis.

After describing what has been achieved in this work, a natural question arises,

where to proceed next. The work on electrochemical promotion can be further extended and developed, including (i) fundamental studies of the phenomenon, (ii) new fields of catalytic chemistry, (iii) studies at very high pressure and (iv) application of new materials.

Although EP using alkali conductors can be rationalised in light of the findings of this thesis, the nature of the effect when using oxygen conductors remains controversial. On one hand Vayenas claimed that the spillover oxygen species are different from oxygen adsorbed from the gas phase, whereas Imbihl *et al.* have experimentally demonstrated their identity. Clarifying this controversy calls for controlled spectroscopic experiments on well-characterised films. Moreover, advanced spectroscopic techniques, like Fast-XPS, can be used to study the time dependence of the spillover process.

The use of new solid electrolytes in electrochemical promotion opens up many new possibilities. Instead of controlling the surface concentration of 'conventional' Na or K promoters, Pb or Ag solid electrolytes (e. g. Pb β" alumina and Ag β" alumina, which are good Pb^{2+} and Ag^{+} conductors) can be used to control the concentration of these metals at the surface of a platinum metal. This should make possible the study of catalysis by alloys, using electrochemical control to vary the surface composition of the alloy under reaction conditions. Thus, EP provides a huge and never previously exploited advantage: the catalytic response of the system to changes in alloy composition can be followed *in situ*. Furthermore, these EP samples are well suited to investigation by advanced spectroscopic techniques, both laboratory and synchrotron based, as demonstrated by the present research work. The *in situ* power of the EP approach, coupled with directly relevant spectroscopic data on the active catalyst surface, should permit to make new an useful contributions to the subject of catalysis by alloys.

Nothing is known about the behaviour of electrochemically promoted catalysts at very high pressures. Our atmospheric study of the Fischer-Tropsch reaction provides an useful starting point towards the study of EP at high pressures. Reaction rates and product chain length distributions should be studied as a function of pressure and promoter level. The study of the EP phenomenon at high pressures would contribute towards providing new insights in the Fischer-Tropsch reaction mechanism and extending the range of application of the EP technique.